Spectroscopic Characterization of Spatial and Temporal Patterns in Foliar Biochemistry

By
Adam Chlus

A dissertation submitted in partial fulfillment of
the requirements for the degree of

Doctor of Philosophy
(Forestry)

at the
UNIVERSITY OF WISCONSIN - MADISON
2020

Date of final oral examination: 11/2/2020

The dissertation is approved by the following members of the Final Oral Committee:

- Philip A. Townsend, Professor, Forest and Wildlife Ecology
- Eric L. Kruger, Professor, Forest and Wildlife Ecology
- Ankur Desai, Professor, Atmospheric and Oceanic Sciences
- Keith Krause, PhD, Battelle Memorial Institute
- Erika Marin-Spiotta, Professor, Geography

Acknowledgments

First and foremost, I want to thank Phil Townsend for taking me on as graduate student and providing me with the opportunities and tools to succeed during my time at UW. I have learned a lot from Phil and am extremely grateful for his support and patience over the past five years. I also want to thank my committee, Eric Kruger, Ankur Desai, Keith Krause and Erika Marin-Spiotta, for their input, guidance and feedback which greatly improved this dissertation.

This dissertation would not have been possible without help from fellow graduate students, postdocs, staff and undergraduates in the Townsend Lab including Abby Walther, Aditya Singh, Aidan Mazur, Alex Brito, Alex Horvath, Andrew Jablonski, Andy Ciurro, Angad Dhariwal, Ashley Seufzer, Beckett Hills, Ben Spaier, Ben Townsend, Brendan Heberlein, Clayton Kingdon, Dewi Radin Umar, Dianna Guerra, Erin Wagner, Grady Munroe, Hailey Knight, Hannah Manninan, Ittai Herrmann, Jacob Gold, James Gui, Jillian Seablom, John Clare, John Couture, Katie Gold, Lake White, Liza Rick, Matt Garcia, Nanfeng Lui, Natalie Queally, Prabu Ravindran, Rachel Kent, Rachel Kranz, Raina Eddy, Robi Phetteplace, Ryan Geygan, Sam Jaeger, Sara Esa, Sarika Mittra, Tedward Erker, Ting Zheng, Venkat Lakshmanan, Will Arrett, Zhihui Wang, Zhiwei Ye, Zhixing Xu and many others. I am especially grateful to Tedward Erker, Ben Spaier, Alex Horvath, Aidan Mazur and Andrew Jablonski for their outsized contribution to this dissertation.

I also want to thank the staff at the NEON, the Wisconsin Department of Natural Resources and Upham Woods for providing technical and logistical support, and the funding agencies, USDA, NASA and NSF, that made this research possible. Finally, I would like to thank my family and friends for their support during my graduate studies.

Table of contents

List of tables

List of supplemental tables

List of figures

List of supplemental figures

Introduction

Foliar biochemistry varies through space and time and is linked to a number of important ecosystem processes including primary productivity and nutrient cycling (de Bello et al. 2010). Sometimes referred to as 'functional traits' or simply 'traits', they include properties related photosynthesis, such as chlorophyll and nitrogen content, structure and decomposition, including carbon and lignin content, and defense, like condensed tannins and phenolic compounds. Characterizing the spatiotemporal variability in biochemical traits is important for accurately parameterizing ecosystem process models (Reichstein et al. 2014). Most studies that have used functional traits to assess patterns in community composition and ecological function generally use mean trait values for species (Albert et al. 2011). However foliar biochemical traits are known to show a significant amount of intra-specific variability that is scale dependent and driven by both genetic and environmental factors (Albert et al. 2010; Messier et al. 2010; Messier et al. 2017). Trait-based ecology has become increasingly common due the relative ease with which traits can be measured compared to underlying physiologic processes they are related to. However, in spite of this, there is a limit to the density of measurements, spatial extent and temporal richness at which functional traits can be quantified using traditional field techniques before efforts become prohibitively costly.

Over the past several decades, spectroscopy has emerged as a valuable technology for expanding the scales at which foliar biochemical traits can be measured. Spectroscopic estimation of foliar traits is predicated on the development of relationships between light reflectance, absorbance and/or transmittance and a biochemical quantity. Driving these relationships are the presence of spectral absorption features associated with electron transitions and bending and stretching in chemical bonds (e.g., C-H, C-O, N-H and O-H) within compounds that comprise plant materials (Curran 1989). Research in the 1950's and 60's in agronomy first demonstrated to utility of spectroscopy for the retrieval of biochemical properties, where it provided an alternative method for characterizing forage quality (Norris et al. 1976; Shenk 1979; Shenk and Westerhaus 1994). Since then, the catalog of biochemical compounds estimated from spectroscopic measurements has come to include minerals (Clark et al. 1987), trace elements (Clark et al. 1989), carbohydrates (Ramirez et al. 2015), secondary metabolites (Smyth and Cozzolino 2011; Couture et al. 2016) and pigments (Gitelson and Merzlyak and 1996). Historically, spectroscopic estimation of foliar biochemistry has utilized dried and ground foliar samples (Norris et al. 1976; Wessman et al. 1988a). However fresh leaf spectra can also be used to estimate foliar biochemistry (Asner et al. 2008; Serbin et al. 2019). Unlike dry ground spectra, fresh spectra can be collected nondestructively without removing leaves from a plant to allow for repeat measurements. However, the presence of water in fresh leaves can obscure molecular absorption features.

Despite the widespread use of chemometric models for estimating foliar biochemistry from both fresh and dry spectra data, generalized models which can be used with confidence are lacking. Models tend to be developed using a small number of species (Vazquez et al. 1995; Ourcival et al. 1999) or at a single point in the growing season (Roelofsen et al. 2014; Serbin et al. 2014). These perform well so long as the model is applied within the constraints of the data used to generate it. Models that generalize well must be developed using data that cover the range of plausible leaf characteristics and are thus able to leverage generalized features in the spectrum.

While both dry and fresh spectral models provide rapid and reliable measurements of foliar biochemistry, the scales on which they can be applied is limited. Early research in the

1980’s demonstrated the capability of imaging spectroscopy to map canopy-level biochemistry including nitrogen and lignin (Wessman et al. 1988b), and further research by Martin and Aber (1997) and Ollinger and Smith (2005) linked remotely sensed canopy biochemistry to ecosystem processes, especially primary production. By developing relationships between canopy spectra and field measured foliar traits, maps of these traits can be generated at large spatial scales, and with repeat collections both seasonally and from year-to-year, temporal patterns can also be observed. Despite the demonstrated value of imaging spectroscopy to map canopy biochemistry, it has not become widely used largely due to the lack of availability of imagery and the challenges of working with the high-dimensional data. With the exception of the satellite-borne EO-1 Hyperion sensor (2001-2017), most available spectroscopy data until recently have been from aircraft campaigns over specific targeted areas and collected in support of limited scientific objectives. For the most part, ecosystem studies using multiple sites or years have focused on characterizing mid-season (i.e., peak greenness) foliar characteristics (Martin et al. 2018, Singh et al. 2015, Wang et al. 2020) at single time intervals. Other large-scale studies (Asner and Martin 2009; Chadwick and Asner 2018) have been mostly concentrated in the tropics and only a single study (Matson et al. 1994) has specifically targeted intra-seasonal utilization of imaging spectroscopy for mapping canopy biochemistry.

Foliar traits vary not just horizontally, but also vertically within canopies (Niinemets et al. 1997; Cavaleri et al. 2010; Coble et al. 2014), which may be important to how we utilize mapped traits to parameterize photosynthetic function within models (Cavaleri et al. 2010; Coble et al. 2014; Rogers et al. 2017). Although this variation has been noted in spectral studies (e.g., Serbin et al. 2014), and some studies have endeavored to characterize “whole canopy” traits such as nitrogen (Smith et al. 2002; Martin et al. 2008), no published studies have explicitly addressed within-canopy trait variation in mapping studies using imaging spectroscopy. The ability to address variations in foliar traits has expanded beyond single “peak greenness” applications with the availability of new data sets such as NEON’s Aerial Observation Platform (AOP).

In my dissertation, I address these gaps in the course of three chapters. In my first chapter I developed generalized spectroscopic models to estimate 27 biochemical traits including pigments, macro- and micronutrients, structural and defensive compounds using spectra from both fresh leaf and dried and ground samples. Models were built using broadleaf and graminoid samples collected across the entire growing season representing over 100 species. I also investigated the extent to which known spectral features are associated with specific traits. In the second chapter I combined extensive field data with coincident imaging spectroscopy and lidar data to model and map the three-dimensional patterns in leaf mass per area (LMA) in a broadleaf deciduous forest. In the third chapter of my dissertation, I used a time series of imaging spectroscopy data collected over the course of a single growing season coupled with field data to map intra-annual patterns in nine foliar biochemical traits. I used the resulting maps to characterize the extent to which phenology, taxonomy and environment drive variation in foliar biochemistry.

Chapter overviews

Chapter 1. Fresh vs. dry: A comparison of generalized spectroscopic models for estimating broadleaf and graminoid biochemistry.

Chlus, A., Erker, T., Wang, Z., Kruger, E.L., & Townsend, P.A.

To be submitted to *Methods in Ecology and Evolution.*

Field spectroscopy has become increasingly prevalent for the rapid estimation of foliar biochemistry (Asner and Martin 2008; Cheng et al. 20011; Nunes et al. 2017). In the past spectral measurements of dry ground foliar samples have been the predominant method used in lab-based near-infrared spectroscopy (NIRS) (Norris et al. 1976; Shenk 1979). While spectral measurements on dried and ground samples can provide accurate estimates for numerous biochemical properties, they also have limitations in that they require destructive sampling of foliar tissue and transport of samples from the field, either of which can be infeasible. However, fresh leaf reflectance using a leaf clip can be made rapidly in situ and often without detaching foliage, allowing for repeat measurements. For some traits, especially those with absorption features obscured by water absorption bands, dry spectra models outperform fresh spectra models (Lacaze and Jofre 1994; Martin and Aber 1994; Jacquemoud et al. 1995), but for many traits these differences have not been assessed. Regardless of measurement type (fresh leaf or dried and ground), accurate, generalized spectroscopic models require data that are representative of the range of conditions that drive the variability in foliar biochemistry, including time (i.e., phenology), geography (i.e., environmental variation), ontogeny, plant and/or leaf developmental stage and taxonomy/phylogeny (Yang et al 2016).

To develop generalized models and assess the relative merits of each approach, I performed a comprehensive analysis in which I aggregated linked fresh and dry ground spectra, and wet chemistry data for 27 foliar biochemical properties including pigments (chlorophylls, carotenoids and xanthophylls), macronutrients (N, P, K, Ca, Mg and S), micronutrients (B, Cu, Fe, Mn, Z), aluminum, carbohydrates, structural and defensive biochemical traits. This dataset consisted of broadleaf and graminoid samples, totaled over 100 species and included samples collected across the course of the growing season and throughout the continental United States. I built paired PLSR models for each trait using both fresh leaf and dry ground spectra and compared their performances and tested the impact of wavelength region on predictive ability. Finally, to assess the relationships between spectra and traits I performed a correlation analysis using a wavelet transform of the reflectance spectrum.

I found that Ca, N, cellulose, lignin, sugars and total phenolics were estimated with high confidence using dry spectra (validation R^2: > 0.6), while chlorophylls A and B and leaf mass per area were estimated with high accuracy using fresh spectral measurements. Other biochemical properties including B, K, P, Mg, flavonoids and carotenoid pigments were estimated with moderate confidence (R^2: > 0.4). With the exception of pigments, the top performing models for each trait utilized the SWIR (1000-2500 nm) regions of the spectrum, while all pigment models utilized the VNIR region (400-1000 nm). Generally, pairwise correlations between spectrally derived traits retained the same directionality as pairwise correlations between laboratory derived traits, but correlations increased in magnitude with spectral estimates, i.e., positive correlations became more strongly positive and negative correlations more negative.

Using the wavelet transform to assess the relationships between spectra (fresh leaf or dried and ground) and traits, I found that for N, phenolic compounds, carbohydrates and chlorophyll, wavelengths associated with electron transitions or molecular bonds present in these compounds were strongly correlated to laboratory measurements, but some features were obscured by water absorption bands in the fresh leaf spectra. In contrast, other traits, including P and K, which lack strong or known absorption features, were correlated at wavelengths with absorption features attributed to proteins, carbohydrates or phenolics, indicating their retrieval was a consequence of their correlation with these compounds, a result of their role in regulating their production or transport.

The results of this chapter highlight that neither fresh nor dry spectral measurements are optimal for estimating the full suite of traits, but together can be used in conjunction with traditional analytical techniques (for validation) as a reasonable approach to estimate traits for extensive sample data sets.

Chapter 2. Mapping three-dimensional variation in leaf mass per area with imaging spectroscopy and lidar in a temperate broadleaf forest

Chlus, A., Kruger, E. L., & Townsend, P. A. (2020)
Remote Sensing of Environment, *250*, 112043.

Increasingly, imaging spectroscopy data are used to characterize horizontal patterns in foliar biochemical traits. However, in forest ecosystems foliar biochemical traits are also known to vary vertically through the canopy, as well as horizontally. The need for vertically detailed maps of canopy traits has been identified in recent research as important for more accurately parameterizing ecological models (Cavaleri et al. 2010, Rogers et al. 2017). Multi-layer canopy photosynthesis models, which incorporate variation in physiologically important traits throughout the canopy, can provide more accurate estimates of assimilation rates than more generalized methods like big-leaf models (Raulier et al. 1999). Luening et al. (1995) found that the choice of canopy nitrogen profiles resulted in a 10% difference in assimilation rate among models. However, these more complex models are difficult to apply due to the lack of sufficient information to accurately parameterize vertical trait distributions. One of the most widely studied and characterized biophysical properties in the context of within-canopy patterns is leaf mass per area (LMA), the ratio between the projected leaf area and dry mass, which is largely comprised of structural and nonstructural carbohydrates, proteins, lignin and minerals (Poorter et al., 2009). LMA—or its inverse, specific leaf area (SLA)—is a central component of the leaf economic spectrum (LES) representing the tradeoff between growth and defense (Wright et al. 2004; Poorter et al., 2009).

LMA decreases with depth into the canopy, largely a result of attenuation of light and a decrease in height-mediated hydraulic constraints (Cavaleri et al. 2010; Niinemets, 2015). Environmental factors including temperature, wind exposure and humidity, which co-vary with incident radiation and height, also influence within-canopy LMA (Niinemets 2001; Poorter et al. 2009; Petter et al. 2016; Wu et al. 2016). While numerous studies have explored within-canopy patterns in LMA through individual tree canopies (Ellsworth and Reich 1993; Aranda et al. 2004), few studies have explored patterns of LMA in vertically heterogenous canopies where both species composition and architecture vary within the vertical profile.

A lack of vertically explicit maps of canopy traits like LMA is largely due to the limitations of passive optical sensors in seeing through a canopy surface. Although sub-canopy elements contribute to the top-of-canopy signal, disentangling them is challenging. Active sensors like LiDAR are able to detect reflected radiation within a canopy, which can then be linked to a three-dimensional point distribution in space. However, these signals, while valuable for reconstructing canopy structure and light environment, provide little information about important spectral features that are correlated with foliar biochemistry as most LiDAR sensors are monochromatic. Hyperspectral lidar has been proposed for addressing this shortcoming (Martinez-Ramirez et al. 2012), and, although promising, the technology is still emerging with current systems being ground-based and limited to measuring small samples (Hakala et al. 2012, Nevalainen et al. 2014, Du et al. 2016). As such, traditional imaging spectroscopy provides the most direct approach to foliar trait estimation, although it is primarily sensitive to top-of-canopy characteristics. Hyperspectral imagery and lidar are complementary and have been fused in previous studies (Clark et al. 2011, Puttonen et al., 2010), especially for species identification (Jones et al. 2010; Dalponte et al. 2012; Naidoo et al. 2012). However, when used together, lidar data have typically been "flattened" and incorporated as additional explanatory variables to model a two-dimensional space (i.e. Thomas et al. 2008) rather than being used to extend modeling to an additional dimension.

In this chapter, I used the demonstrated capabilities of hyperspectral remote sensing to estimate top-of-canopy LMA and lidar to model canopy environmental conditions related to variation in LMA (i.e., light transmittance and height) to extend LMA estimates through the canopy. I collected field data in 2016 and 2017 in the broadleaf deciduous forests of northern Wisconsin and the Upper Peninsula of Michigan. Plot-level field sampling involved the collection of branches throughout the vertical extent of the canopy. I measured the height above ground of all sampled branches and calculated the mean branch-level LMA. Field sampling was coincident with overflights of NEON's Airborne Observation Platform (AOP) which collected high resolution imaging spectroscopy and lidar data simultaneously.

To map three dimensional patterns in LMA I first used the imaging spectroscopy data coupled with field measurements of LMA to estimate LMA at the top of the canopy using partial least squares regression (PLSR). During PLSR model development I also tested how wavelength range impacted model performance. I then used the lidar data to calculate several within-canopy variables: absolute height, relative height and metrics of lidar transmittance. Next I tested a series of models in a regression framework beginning with univariate models and sequentially increasing model complexity by including additional predictors. These models included combinations of top-of-canopy LMA, absolute height, relative height, a lidar transmittance metric.

I found that top-of-canopy LMA was predicted with the highest accuracy using the shortwave infrared region of the spectrum (2000-2450 nm) (R^2: 0.57, RMSE 10.8 g m^{-2}) while the model which included the full range (400-2450 nm) performed the poorest (R^2: 0.39, RMSE 12.7 g m^{-2}). All three within canopy variables, absolute height, relative height and lidar transmittance, were significantly correlated with within-canopy LMA ($p < .01$). The top performing within-canopy LMA model used the top-of-canopy estimate of LMA as a starting point for LMA and was decremented as a function of both a lidar transmittance metric and the relative height within the canopy (R^2: 0.78, RMSE 8.3 g m^{-2}). The coupled models accurately estimated LMA throughout the canopy without taking into account species composition (R^2 : 0.82, RMSE: 8.5 g m^{-2}). While previous work has demonstrated species-agnostic determination of top-of-canopy LMA using imaging spectroscopy data, the results here also demonstrate the ability estimate within-canopy LMA despite vertical species-turnover where top-of-canopy species differ from understory species.

As part of my analysis I also tested the impact of spatial window size on calculating the lidar transmittance metric for each data point and subsequent effect on within-canopy model performance. I found in dense canopies, like those of sugar maples, few lidar returns reached the understory which in turn resulted in an underestimation of transmittance in the lower canopy. This impact was reduced by increasing the window size to a diameter of 20 m, which increased the number of returns in the lower canopy used to calculate lidar transmittance.

Chapter 3. Characterizing seasonal variation in foliar biochemistry in a temperate broadleaf forest using imaging spectroscopy

Chlus A., Kruger E. L., & Townsend P. A.

To be submitted to *Remote Sensing of Environment*

Ecosystems are not static, especially those with strong seasonal patterns like temperate deciduous forests. The functioning of these ecosystems varies during the course of a growing season from leaf out to senescence (Wehr et al. 2016), but measurement of functional variation, beyond greenness, especially using remote sensing, is uncommon. However, not accounting for functional variation can result in biases in ecosystem models (Ito et al. 2006). Direct measurements of ecosystem functions such as primarily productivity are logistically difficult to make and/or map, but foliar biochemical traits can serve as proxies for a number of important ecosystem processes including growth and defense.

Studying intra-annual patterns in foliar biochemical traits at scales greater than the plot level is challenging due to the extensive field sampling required to capture the temporal and spatial variability of both explanatory and response variables. Remote sensing provides a means to extend field level measurements to landscape and larger scales and characterize environmental gradients with fine spatial resolution. Traditionally, remote sensing of phenology has been studied within the context of greenness with the normalized difference vegetation index (NDVI), a metric of vegetative vigor (Duchemin et al. 1999), and in this chapter I extend the study of phenology to foliar functional traits.

Full range (400-2500 nm) imaging spectroscopy, with its high spectral resolution, provides the ability to resolve narrowband absorption features associated with biochemical traits not discernible from broadband sensors (Curran 1989). Past studies using imaging spectroscopy to map foliar traits have largely focused on a single point in time, namely the peak of the growing season, whereas foliar traits are known to vary throughout the course of the growing season and are most dynamic during leaf out and senescence (Martin and Aber 1997; Asner et al. 2008; Asner et al. 2015; Singh et al. 2015). Only a single study to date (Matson et al. 1994) has used airborne imaging spectroscopy data to map foliar biochemistry seasonally but was largely limited to coniferous species and imagery was collected at coarse resolution (20 m) precluding the assessment of species-specific patterns.

Recent research using leaf-level spectroscopy has indicated that relationships between spectra and traits vary across the course of the growing season, and that predictive models built at one point in the growing season may induce a bias when applied at a different phenological stage (Yang et al. 2016). This pattern is expected to transfer to canopy-level spectroscopy, indicating that accurately mapping intra-seasonal patterns in foliar biochemistry will require spectroscopic models built with data collected across the course of a growing season, something not currently available.

The overarching goal of this chapter was to develop spectroscopic models to map foliar biochemistry across the course of a growing season in a temperate broadleaf forest. As part of this analysis, I also sought to test the influence on seasonality on model performance; that is, can a model built using data collected in one time of the year accurately predict traits at another time of year? Using the resulting maps coupled with maps of species composition and soil maps I then characterized the sources of variation in biochemical traits and compared patterns in interannual trait trajectories across species.

Between May and October of 2018, we collected high resolution (1 m) imaging spectroscopy data over Blackhawk Island, Wisconsin, USA at eight time points during the growing season. Coincident with overflights, I conducted fieldwork to collect top-of-canopy foliage samples, which, along with fresh and dry spectroscopic models, were used to estimate nine foliar traits related to ecophysiological function: chlorophyll content, leaf mass per area, and concentrations of nitrogen, lignin, fiber, phenolics, calcium, phosphorus and potassium. Combining spectra extracted from the imagery with field data, I developed predictive (PLSR) models applicable to all dates to produce canopy-level trait maps. In addition to these full season models, I also developed and tested models using seasonal subsets from the beginning, middle and end of the growing season.

The accuracy of the full-season models varied across traits (R^2: 0.55-0.93). Traits with well-defined absorption features were retrieved with the highest accuracy, including chlorophyll

(R^2: 0.93; %RMSE: 8.0) and total phenolics (R^2: 0.86; %RMSE: 11.0). Despite the relatively poor performance of some models, the mapped intra-annual patterns for all traits followed patterns reported in literature and displayed expected species ordering. In testing models built using seasonal subsets varied by traits, I found that some traits required data collected across the entire growing season to develop general predictive models (e.g N, Ca), indicating that trait-spectra relationships vary across the growing season and need to be considered when developing broad applications.

In testing the primary drivers of trait variation, I found that phenology (date) explained the greatest amount of variation for all traits except total phenolics, for which species explained 75% of the variation. Macronutrients (N, P and K) showed general trends of decreasing concentration over the course of the year, reflecting dilution by carbon-rich compounds during the growing season and resorption during senescence. Conversely, recalcitrant compounds including lignin, fiber and calcium increased until late summer, after which they stabilized. Except for phenolics, seasonal trait trajectories were generally consistent among species, although the pace of accumulation (or resorption) differed.

Significance

The world's ecosystems are rapidly changing, and as those ecosystems respond to new environmental conditions, we need to better characterize how the functioning of those ecosystems is responding. New techniques and datasets are necessary for measuring and understanding the impacts of climate and other anthropogenic drivers, and to accurately model future scenarios. Forest ecosystems provide multiple important benefits to society including provisioning and regulating services that are related to functional trait diversity. Leveraging the power of remote sensing, and imaging spectroscopy in particular, can provide a comprehensive understanding of the patterns and processes effecting those services and traits (Jetz et al. 2016; Schimel at al. 2019).

In the first chapter of my dissertation I developed and compared generalized PLSR models using spectra both from fresh leaves and dried and ground samples to estimate 27 foliar biochemical traits. The use of models to predict traits from fresh and dry spectra were essential to this dissertation. While only a subset of foliar samples were measured using traditional wet chemistry techniques, and generalized models like the ones developed here were critical for estimating biochemistry on full set of field samples, which were then in turn used to develop canopy level models from imagery reported in Chapters 2 and 3. Increasingly, such models are essential in remote sensing beyond my study, as laboratory based measurements are impractical to collect at broad spatial extents. I found the selection of measurement type -- fresh vs. dry spectra -- as well as the wavelength range used in model development have a significant impacts on the resulting predictive performance of the spectroscopic models. Using a wavelet transform to assess trait spectra-relationships, I found that many biochemicals shared common spectral features. This provides new, unique insights into the basis for our ability to predict traits for which known absorption features either had not been reported or were not known to the remote sensing community. One useful outcome of this effort is that I provide readers with an assessment of each trait, its robustness of prediction, and the extent to which users of spectroscopic trait models should consider estimate of a trait to be an index of other traits to which it is correlated. I provide functional interpretations of prediction capacity, for instance that spectroscopic prediction of potassium is based on its role in synthesis of other traits that are detectable. The database of spectra and trait measurements collected here is unprecedented in its scope and consists of over 15,000 spectra which cover a multiple axes of trait variation including taxonomy, phenology and environment. It will provide a foundational data set for the analysis of foliar traits using spectra paired to laboratory measurements, across seasons and using a range of instrumentation.

Next, I demonstrate a methodology to estimate within-canopy variation of leaf mass per area (LMA) using top-of-canopy estimates from imaging spectroscopy and lidar representations of within-canopy structure. As lidar data become more widely available, there is the potential to link lidar and spectral data to develop whole-canopy (rather than sunlit-crown) estimates of characteristics important to predicting ecosystem function. For example, current ecosystem models do not represent within-canopy variation in foliar traits with any level of sophistication, if at all. As modelers come to understand the new mapping capabilities and test the sensitivities of models to within-canopy trait variation, work such as this may help provide motivation to update approaches to canopy mapping with more detailed three-dimensional representation of aboveground traits. This mapping of 3D patterns in LMA has the potential to be coupled with modeled vertical LAI profiles and leaf area density using lidar as an basis for estimating full canopy foliar biomass and nutrient content. Although LMA is likely the most significant trait that varies vertically in canopies, my work can also be expanded to include traits other than LMA. This will provide the basis to tackle a range of ecological questions beyond nutrient and carbon cycling, for example links to trophic dynamics, relationships with arthropods and birds, as well as disturbance processes. In summary, this work demonstrates the potential for global mapping through the fusion of spaceborne imaging spectrometers and lidar, which can provide opportunities to better quantify full-canopy ecological and physiological variation in ecosystems that are not possible with in-situ measurements.

Finally, I used an unprecedented dense time series of imaging spectroscopy data collected during a single growing season to map intra-annual patterns in foliar biochemistry. Such work is essential to how we characterize functional variation in ecosystems, including functional diversity (which may vary spatially) and other processes that link to foliar traits. From a remote sensing perspective, this is the first paper to investigate the seasonal variation in foliar traits in a mixed temperate forest ecosystem using high-resolution hyperspectral imagery and expands on the diversity of traits mapped seasonally. By coupling maps of foliar biochemistry with species maps, I demonstrated that phenology was a significant driver of variation for most traits, but that for others, like phenolics, variation is largely driven by taxonomic identity. Importantly, this study demonstrates that seasonal trait variation is consistent neither by trait nor by species.

The research presented in this dissertation was largely conducted with an eye to towards the future when high-fidelity, year-round, global imaging spectroscopy data will be collected by spaceborne imagers. In a rapidly changing world these sensors will be critical to monitoring ecosystem health. Specifically, the measurement and detection of changes in foliar biochemistry will be an important component in monitoring ecosystem structure, diversity and functioning. Despite the enormous potential of spaceborne imaging spectroscopy for global characterization of foliar biochemistry, continued research is needed to fully realize it. My dissertation contributes to this need by expanding on existing methodologies and demonstrating new applications of imaging spectroscopy for mapping foliar biochemistry.

References

Albert, C. H., Thuiller, W., Yoccoz, N. G., Douzet, R., Aubert, S., & Lavorel, S. (2010). A multi-trait approach reveals the structure and the relative importance of intra-vs. interspecific variability in plant traits. *Functional Ecology*, *24*(6), 1192-1201.

Albert, C. H., Grassein, F., Schurr, F. M., Vieilledent, G., & Violle, C. (2011). When and how should intraspecific variability be considered in trait-based plant ecology?. *Perspectives in Plant Ecology, Evolution and Systematics*, *13*(3), 217-225.

Asner, G. P., & Martin, R. E. (2008). Spectral and chemical analysis of tropical forests: Scaling from leaf to canopy levels. *Remote Sensing of Environment*, *112*(10), 3958-3970.

Asner, G. P., & Martin, R. E. (2009). Airborne spectranomics: mapping canopy chemical and taxonomic diversity in tropical forests. *Frontiers in Ecology and the Environment*, *7*(5), 269-276.

Aranda, I., Pardo, F., Gil, L., & Pardos, J. A. (2004). Anatomical basis of the change in leaf mass per area and nitrogen investment with relative irradiance within the canopy of eight temperate tree species. *Acta Oecologica*, *25*(3), 187-195.

Cavaleri, M. A., Oberbauer, S. F., Clark, D. B., Clark, D. A., & Ryan, M. G. (2010). Height is more important than light in determining leaf morphology in a tropical forest. *Ecology*, *91*(6), 1730-1739.

Chadwick, K. D., & Asner, G. P. (2018). Landscape evolution and nutrient rejuvenation reflected in Amazon forest canopy chemistry. *Ecology letters*, *21*(7), 978-988.

Cheng, T., Rivard, B., & Sanchez-Azofeifa, A. (2011). Spectroscopic determination of leaf water content using continuous wavelet analysis. *Remote Sensing of Environment*, *115*(2), 659-670.

Clark, D. H., Mayland, H. F., & Lamb, R. C. (1987). Mineral Analysis of Forages with near Infrared Reflectance Spectroscopy 1. *Agronomy Journal*, *79*(3), 485-490.

Clark, D. H., Cary, E. E., & Mayland, H. F. (1989). Analysis of trace elements in forages by near infrared reflectance spectroscopy. *Agronomy Journal*, *81*(1), 91-95.

Clark, M. L., Roberts, D. A., Ewel, J. J., & Clark, D. B. (2011). Estimation of tropical rain forest aboveground biomass with small-footprint lidar and hyperspectral sensors. *Remote Sensing of Environment*, *115*(11), 2931-2942.

Coble, A. P., Autio, A., Cavaleri, M. A., Binkley, D., & Ryan, M. G. (2014). Converging patterns of vertical variability in leaf morphology and nitrogen across seven Eucalyptus plantations in Brazil and Hawaii, USA. *Trees*, *28*(1), 1-15.

Couture, J. J., Singh, A., Rubert-Nason, K. F., Serbin, S. P., Lindroth, R. L., & Townsend, P. A. (2016). Spectroscopic determination of ecologically relevant plant secondary metabolites. *Methods in Ecology and Evolution*, *7*(11), 1402-1412.

Curran, P. J. (1989). Remote sensing of foliar chemistry. *Remote sensing of environment*, *30*(3), 271-278.

Dalponte, M., Bruzzone, L., & Gianelle, D. (2008). Fusion of hyperspectral and LIDAR remote sensing data for classification of complex forest areas. *IEEE Transactions on Geoscience and Remote Sensing*, *46*(5), 1416-1427.

de Bello, F., Lavorel, S., Díaz, S., Harrington, R., Cornelissen, J. H., Bardgett, R. D., ... & da Silva, P. M. (2010). Towards an assessment of multiple ecosystem processes and services via functional traits. *Biodiversity and Conservation*, *19*(10), 2873-2893.

Du, L., Gong, W., Shi, S., Yang, J., Sun, J., Zhu, B., & Song, S. (2016). Estimation of rice leaf nitrogen contents based on hyperspectral LIDAR. *International journal of applied earth observation and geoinformation*, *44*, 136-143.

Duchemin, B., Goubier, J., & Courrier, G. (1999). Monitoring phenological key stages and cycle duration of temperate deciduous forest ecosystems with NOAA/AVHRR data. *Remote Sensing of Environment*, *67*(1), 68-82.

Ellsworth, D. S., & Reich, P. B. (1993). Canopy structure and vertical patterns of photosynthesis and related leaf traits in a deciduous forest. *Oecologia*, *96*(2), 169-178.

Gitelson, A. A., Merzlyak, M. N., & Lichtenthaler, H. K. (1996). Detection of red edge position and chlorophyll content by reflectance measurements near 700 nm. *Journal of plant physiology*, *148*(3-4), 501-508.

Hakala, T., Suomalainen, J., Kaasalainen, S., & Chen, Y. (2012). Full waveform hyperspectral LiDAR for terrestrial laser scanning. *Optics express*, *20*(7), 7119-7127.

Ito, A., Muraoka, H., Koizumi, H., Saigusa, N., Murayama, S., & Yamamoto, S. (2006). Seasonal variation in leaf properties and ecosystem carbon budget in a cool-temperate deciduous broad-leaved forest: simulation analysis at Takayama site, Japan. *Ecological Research*, *21*(1), 137-149.

Jacquemoud, S., Verdebout, J., Schmuck, G., Andreoli, G., & Hosgood, B. (1995). Investigation of leaf biochemistry by statistics. *Remote Sensing of Environment*, *54*(3), 180-188.

Jetz, W., Cavender-Bares, J., Pavlick, R., Schimel, D., Davis, F. W., Asner, G. P., ... & Schaepman, M. E. (2016). Monitoring plant functional diversity from space. *Nature plants*, *2*(3), 1-5.

Jones, T. G., Coops, N. C., & Sharma, T. (2010). Assessing the utility of airborne hyperspectral and LiDAR data for species distribution mapping in the coastal Pacific Northwest, Canada. *Remote Sensing of Environment*, *114*(12), 2841-2852.

Lacaze, B., & Joffre, R. (1994). Extracting biochemical information from visible and near infrared reflectance spectroscopy of fresh and dried leaves. *Journal of plant physiology*, *144*(3), 277-281.

Leuning, R., Kelliher, F. M., De Pury, D. G. G., & Schulze, E. D. (1995). Leaf nitrogen, photosynthesis, conductance and transpiration: scaling from leaves to canopies. *Plant, Cell & Environment*, *18*(10), 1183-1200.

Martin, M. E., & Aber, J. D. (1994). Analyses of forest foliage III: Determining nitrogen, lignin and cellulose in fresh leaves using near infrared reflectance data. *Journal of Near Infrared Spectroscopy*, *2*(1), 25-32.

Martin, M. E., & Aber, J. D. (1997). High spectral resolution remote sensing of forest canopy lignin, nitrogen, and ecosystem processes. *Ecological applications*, *7*(2), 431-443.

Martin, Mary E., Lucie C. Plourde, Scott V. Ollinger, M-L. Smith, and B. E. McNeil. "A generalizable method for remote sensing of canopy nitrogen across a wide range of forest ecosystems." *Remote Sensing of Environment* 112, no. 9 (2008): 3511-3519.

Martin, R., Chadwick, K., Brodrick, P., Carranza-Jimenez, L., Vaughn, N., & Asner, G. (2018). An approach for foliar trait retrieval from airborne imaging spectroscopy of tropical forests. *Remote Sensing*, *10*(2), 199.

Matson, P., Johnson, L., Billow, C., Miller, J., & Pu, R. (1994). Seasonal patterns and remote spectral estimation of canopy chemistry across the Oregon transect. *Ecological Applications*, *4*(2), 280-298.

Martinez-Ramirez, D., Buller, G., McCarthy, A., Ren, X., Morak, A. W. S., Nichol, C., & Woodhouse, I. (2012). Developing hyperspectral lidar for structural and biochemical analysis of forest data. In *Proc. EARSEL Conf. Adv. Geosci.* (pp. 1-11).

Messier, J., McGill, B. J., & Lechowicz, M. J. (2010). How do traits vary across ecological scales? A case for trait-based ecology. *Ecology letters*, *13*(7), 838-848.

Messier, J., McGill, B. J., Enquist, B. J., & Lechowicz, M. J. (2017). Trait variation and integration across scales: is the leaf economic spectrum present at local scales?. *Ecography*, *40*(6), 685-697.

Naidoo, L., Cho, M. A., Mathieu, R., & Asner, G. (2012). Classification of savanna tree species, in the Greater Kruger National Park region, by integrating hyperspectral and LiDAR data in a Random Forest data mining environment. *ISPRS journal of Photogrammetry and Remote Sensing*, *69*, 167-179.

Nevalainen, O., Hakala, T., Suomalainen, J., Mäkipää, R., Peltoniemi, M., Krooks, A., & Kaasalainen, S. (2014). Fast and nondestructive method for leaf level chlorophyll estimation using hyperspectral LiDAR. *Agricultural and Forest Meteorology*, *198*, 250-258.

Niinemets, Ü. (1997). Distribution patterns of foliar carbon and nitrogen as affected by tree dimensions and relative light conditions in the canopy of Picea abies. *Trees*, *11*(3), 144-154

Niinemets, Ü. (2001). Global-scale climatic controls of leaf dry mass per area, density, and thickness in trees and shrubs. *Ecology*, *82*(2), 453-469.

Niinemets, Ü., Keenan, T. F., & Hallik, L. (2015). A worldwide analysis of within-canopy variations in leaf structural, chemical and physiological traits across plant functional types. *New Phytologist*, *205*(3), 973-993.

Norris, K. H., Barnes, R. F., Moore, J. E., & Shenk, J. S. (1976). Predicting forage quality by infrared replectance spectroscopy. *Journal of animal science*, *43*(4), 889-897

Nunes, M., Davey, M., & Coomes, D. (2017). On the challenges of using field spectroscopy to measure the impact of soil type on leaf traits.

Ollinger, S. V., & Smith, M. L. (2005). Net primary production and canopy nitrogen in a temperate forest landscape: an analysis using imaging spectroscopy, modeling and field data. *Ecosystems*, *8*(7), 760-778.

Ourcival, J. M., Joffre, R., & Rambal, S. (1999). Exploring the relationships between reflectance and anatomical and biochemical properties in Quercus ilex leaves. *The New Phytologist*, *143*(2), 351-364.

Petter, G., Wagner, K., Wanek, W., Sánchez Delgado, E. J., Zotz, G., Cabral, J. S., & Kreft, H. (2016). Functional leaf traits of vascular epiphytes: vertical trends within the forest, intra-and interspecific trait variability, and taxonomic signals. *Functional Ecology*, *30*(2), 188-198.

Poorter, H., Niinemets, Ü., Poorter, L., Wright, I. J., & Villar, R. (2009). Causes and consequences of variation in leaf mass per area (LMA): a meta-analysis. *New phytologist*, *182*(3), 565-588.

Puttonen, E., Suomalainen, J., Hakala, T., Räikkönen, E., Kaartinen, H., Kaasalainen, S., & Litkey, P. (2010). Tree species classification from fused active hyperspectral reflectance and LIDAR measurements. *Forest Ecology and Management*, *260*(10), 1843-1852.

Ramirez, J. A., Posada, J. M., Handa, I. T., Hoch, G., Vohland, M., Messier, C., & Reu, B. (2015). Near-infrared spectroscopy (NIRS) predicts non-structural carbohydrate concentrations in different tissue types of a broad range of tree species. *Methods in Ecology and Evolution*, *6*(9), 1018-1025.

Raulier, F., Bernier, P. Y., & Ung, C. H. (1999). Canopy photosynthesis of sugar maple (Acer saccharum): comparing big-leaf and multilayer extrapolations of leaf-level measurements. *Tree Physiology*, *19*(7), 407-420.

Reichstein, M., Bahn, M., Mahecha, M. D., Kattge, J., & Baldocchi, D. D. (2014). Linking plant and ecosystem functional biogeography. *Proceedings of the National Academy of Sciences*, *111*(38), 13697-13702.

Roelofsen, H. D., van Bodegom, P. M., Kooistra, L., & Witte, J. P. M. (2014). Predicting leaf traits of herbaceous species from their spectral characteristics. *Ecology and evolution*, *4*(6), 706-719.

Rogers, A., Medlyn, B. E., Dukes, J. S., Bonan, G., Von Caemmerer, S., Dietze, M. C., ... & Prentice, I. C. (2017). A roadmap for improving the representation of photosynthesis in Earth system models. *New Phytologist*, *213*(1), 22-42.

Schimel, D., Schneider, F. D., & JPL Carbon and Ecosystem Participants. (2019). Flux towers in the sky: global ecology from space. *New Phytologist*, *224*(2), 570-584.

Serbin, S. P., Singh, A., McNeil, B. E., Kingdon, C. C., & Townsend, P. A. (2014). Spectroscopic determination of leaf morphological and biochemical traits for northern temperate and boreal tree species. *Ecological Applications*, *24*(7), 1651-1669.

Serbin, S. P., Wu, J., Ely, K. S., Kruger, E. L., Townsend, P. A., Meng, R., ... & Rogers, A. (2019). From the Arctic to the tropics: multibiome prediction of leaf mass per area using leaf reflectance. *New Phytologist*, *224*(4), 1557-1568.

Shenk, J. S., Westerhaus, M. O., & Hoover, M. R. (1979). Analysis of forages by infrared reflectance. *Journal of Dairy Science*, *62*(5), 807-812.

Shenk, J. S., & Westerhaus, M. O. (1994). The application of near infrared reflectance spectroscopy (NIRS) to forage analysis. *Forage quality, evaluation, and utilization*, 406-449.

Shenk, J. S., Westerhaus, M. O., & Hoover, M. R. (1979). Analysis of forages by infrared reflectance. *Journal of Dairy Science*, *62*(5), 807-812.

Singh, A., Serbin, S. P., McNeil, B. E., Kingdon, C. C., & Townsend, P. A. (2015). Imaging spectroscopy algorithms for mapping canopy foliar chemical and morphological traits and their uncertainties. *Ecological Applications*, *25*(8), 2180-2197.

Smith, M. L., Ollinger, S. V., Martin, M. E., Aber, J. D., Hallett, R. A., & Goodale, C. L. (2002). Direct estimation of aboveground forest productivity through hyperspectral remote sensing of canopy nitrogen. *Ecological applications*, *12*(5), 1286-1302.

Smyth, H., & Cozzolino, D. (2011). Applications of infrared spectroscopy for quantitative analysis of volatile and secondary metabolites in plant materials. *Current Bioactive Compounds*, *7*(2), 66-74.

Thomas, V., Treitz, P., Mccaughey, J. H., Noland, T., & Rich, L. (2008). Canopy chlorophyll concentration estimation using hyperspectral and lidar data for a boreal mixedwood forest in northern Ontario, Canada. *International Journal of Remote Sensing*, *29*(4), 1029-1052.

Vázquez de Aldana, B. R., García Criado, B., & Pérez Corona, M. E. (1995). Estimation of mineral content in natural grasslands by near infrared reflectance spectroscopy.

Wang, Z., Chlus, A., Geygan, R., Ye, Z., Zheng, T., Singh, A., ... & Townsend, P. A. (2020). Foliar functional traits from imaging spectroscopy across biomes in eastern North America. *New Phytologist*.

Wehr, R., Munger, J. W., McManus, J. B., Nelson, D. D., Zahniser, M. S., Davidson, E. A., ... & Saleska, S. R. (2016). Seasonality of temperate forest photosynthesis and daytime respiration. *Nature*, *534*(7609), 680.

Wessman, C. A., Aber, J. D., Peterson, D. L., & Melillo, J. M. (1988a). Foliar analysis using near infrared reflectance spectroscopy. *Canadian Journal of Forest Research*, *18*(1), 6-11.

Wessman, C. A., Aber, J. D., Peterson, D. L., & Melillo, J. M. (1988b). Remote sensing of canopy chemistry and nitrogen cycling in temperate forest ecosystems. *Nature*, *335*(6186), 154-156.

Wu, C., Niu, Z., Tang, Q., Huang, W., Rivard, B., & Feng, J. (2009). Remote estimation of gross primary production in wheat using chlorophyll-related vegetation indices. *Agricultural and Forest Meteorology*, *149*(6-7), 1015-1021.

Wright, I. J., Reich, P. B., Westoby, M., Ackerly, D. D., Baruch, Z., Bongers, F., ... & Flexas, J. (2004). The worldwide leaf economics spectrum. *Nature*, *428*(6985), 821.

Yang, X., Tang, J., Mustard, J. F., Wu, J., Zhao, K., Serbin, S., & Lee, J. E. (2016). Seasonal variability of multiple leaf traits captured by leaf spectroscopy at two temperate deciduous forests. *Remote Sensing of Environment*, *179*, 1-12.

1. Fresh vs. dry: A comparison of generalized spectroscopic models for estimating broadleaf and graminoid biochemistry.

Contributors: Adam Chlus, Tedward Erker, Zhihui Wang, Eric L. Kruger & Philip A. Townsend

Abstract

The use of field spectroscopy has increased in prominence for the rapid estimation of foliar biochemistry, especially in ecology. Historically, spectral measurements of dried and ground foliar samples have been used in lab-based near-infrared spectroscopy (NIRS). While spectral measurements on dry samples can provide accurate estimates for numerous biochemical properties, they also have limitations in that they require destructive sampling of foliar tissue and transport of samples from the field, either of which can be infeasible. Conversely, measurements of fresh leaf reflectance using a leaf clip can be made rapidly *in situ* and often without detaching foliage, allowing for repeat measurements. To assess the relative merits of each approach, we performed a comprehensive analysis in which we aggregated linked fresh and dry spectra with wet chemistry data for 27 foliar biochemical properties including pigments (chlorophylls, carotenoids and xanthophylls), macronutrients (N, P, K, Ca, Mg and S), micronutrients (B, Cu, Fe, Mn, Z), aluminum, carbohydrates, structural and defensive biochemical traits. We built paired PLSR models for each trait using spectra on both fresh leaf and ground dry samples, compared their performances and tested the impact of wavelength region on predictive ability. Using spectral measurements on dried and ground samples, Ca, N, cellulose, lignin, sugars and total phenolics could be estimated with high confidence (validation $R^2 > 0.6$), while chlorophylls A and B and leaf mass per area were estimated with high accuracy using fresh spectral measurements. Other biochemical properties including B, K, P, Mg, flavonoids and carotenoid pigments were estimated with moderate confidence ($R^2 > 0.4$). We also used a wavelet transform to assess the relationships between spectra (fresh leaf and dry ground) and traits. We found that for N, phenolic compounds, carbohydrates and chlorophyll, strong correlations emerged for wavelengths associated with electron transitions or molecular bonds present in these compounds, although some features were obscured by water absorption bands in the fresh leaf spectra. Other traits, including P and K, which lack strong or known absorption features, were correlated at wavelengths with absorption features attributed to proteins, carbohydrates or phenolics, indicating their retrieval was a consequence of their correlation with these compounds, likely as a result of their role in regulating their production or transport. Neither fresh nor dry spectral measurements are optimal for estimating the full suite of traits, but together represent a reasonable approach to estimate traits for extensive sample data sets, when used in conjunction with traditional analytical techniques for validation.

Introduction

Rapid, reliable and repeatable measurements of foliar biochemistry are essential for a number of disciplines including ecology, plant science, agriculture and geology. The chemical composition of leaves affects decomposition (Melillo et al. 1982), plant-insect interactions (Agrawal et al. 2009) and photosynthesis/photosynthetic capacity (Evans and Seeman 1989). Foliar biochemistry can also be used to infer soil properties (Dunn 2011), detect the presence of pollutants (Sager et al. 2005) and pathogens (Gold et al. 2020) and characterize crop status (Blackmer and Scheper 1994; Waskom et al. 1994) and forage quality (Norris et al. 1976; Shenk and Westerhaus 1994). Wet chemistry techniques like high performance liquid chromatography (HPLC), mass spectrometry, combustion analysis and colorimetric assays are generally used to quantify the chemical composition of leaves (Dixon and Kuja 1995; Trotter et al. 2002; Da Silveira et al. 1989; Ainsworth and Gillipsie 2007). While these methods can provide accurate measurements of biochemical profiles, they are often costly in terms of both equipment and materials, time consuming, require advanced training for operation and can produce hazardous chemical waste. Beginning in the 1950's and 60's, the use of spectroscopy gained increasing acceptance for measuring foliar biochemistry, particularly in the agricultural industry where it provided an alternative method for characterizing forage quality, including the estimation of protein, oil and fiber content (Norris et al. 1976; Shenk 1979; Shenk and Westerhaus 1985). Since then, the catalog of biochemical compounds estimated from spectroscopic measurements has come to include minerals (Clark et al. 1987), trace elements (Clark et al. 1989), carbohydrates (Card et al. 1988; Ramirez et al. 2015), secondary metabolites (Smyth and Cozzolino 2011; Couture et al. 2016) and pigments (Gitelson et al. 1996; Merzlyak et al. 2003)

Spectroscopic determination of foliar biochemistry is predicated on the development of a relationship between spectra and the chemical trait of interest. Early research largely relied on the use of stepwise linear regression in which a subset of the spectrum -- usually including fewer than 10 wavelengths -- was selected to develop calibration equations (Norris et al. 1976; Shenk 1979; Wessman et al. 1989). However stepwise regression has largely fallen out of use in favor of more advanced chemometric techniques like principal components regression (PCA) and partial least squares regression (PLSR, Wold et al. 2001) due to the potential for identifying spurious relationships (Grossman et al. 1996). Physics-based radiative transfer models (RTM) including LIBERTY (Dawson et al. 1998) and PROSPECT (Jacquemond and Baret 1990) and their descendants have also been used to derive estimates of foliar biochemistry by inverting leaf spectra using absorption profiles of leaf constituents including pigments, proteins, water and structural compounds. However, RTMs are limited to inverting compounds with known and well-defined absorption profiles, although recent versions of PROSPECT retrieve nitrogen and leaf mass per area (LMA) using semi-empirical formulations (Wang et al. 2015; Feret et al. 2019). Underlying both empirically and physically based methods is the presence of spectral absorption features associated with electron transitions and bending and stretching in chemical bonds (C-H, C-O, N-H and O-H) within compounds that comprise plant materials (Curran 1989). Other important chemistries, including many minerals, do not have spectral signatures in the visible through shortwave infrared (400-2500 nm) (Workman and Weyer 2008), although compounds in which these are present may have spectral features associated with other molecular bonds within the compound. However, in general, the ability to estimate minerals using reflectance spectroscopy is a result of correlations with other chemical constituents that do possess spectral signatures (Clark et al. 1987; Ciavarella et al. 1998).

Historically, spectroscopic estimation of foliar biochemistry has utilized dried and ground foliar samples (Norris et al. 1976; Wessman et al. 1988). Drying removes water which has major absorption features in the infrared that obscure weaker absorptions of other foliar compounds, while grinding homogenizes samples and exposes the inner leaf material. Increasingly, fresh leaf spectra are used to estimate foliar biochemistry, which generally involves the use of a leaf clip or integrating sphere to measure reflectance (Asner and Martin 2008; Nunes et al. 2017; Serbin et al. 2019). Early work by Curran et al. (1992) demonstrated the ability to estimate chlorophyll, sugars and water content using fresh leaf spectra, which has since been expanded to estimate quantities of macro- and micronutrients, defensive compounds and carbohydrates (Martin and Aber 1994; Yoder and Pettigrew 1995; Jacquemoud et al. 1996; Asner et al. 2011). Unlike dry ground spectra, measurements of fresh spectra do not require subsequent sample processing, can be performed nondestructively without removing leaves from a plant to allow repeat measurements and, with properly calibrated models, can provide near-instantaneous estimates of biochemistry. For some traits, especially those with absorption features obscured by water absorption bands, dry spectra models outperform fresh spectra models (Lacaze and Jofre 1994; Martin and Aber 1994; Jacquemoud et al. 1995), but for many traits these differences have not been assessed.

Regardless of measurement type (fresh leaf or dry ground) accurate, generalized spectroscopic models require data that are representative of the range of conditions that drive the variability in foliar biochemistry, including time (i.e., phenology), geography (i.e., environmental variation), ontogeny, plant and/or leaf developmental stage and taxonomy/phylogeny. Many applications of spectroscopy tend to predict chemical constituents using models specific to a species or a small number of closely related species (Vazquez et al. 1995; Ourcival et al. 1999; Yuan et al. 2016; Fernàndez-Martínez et al. 2017). These perform well so long as the model is applied within the constraints of the data used to generate it. However, this presents challenges for estimating foliar chemistry on a novel species where it may be unknown whether the species spectral and chemical profile is bounded by the data used to build the model. A further complication is that seasonality – i.e. leaf phenology or developmental stage – also impacts model performance (Yang et al. 2016), as the specific absorption features related to the chemical compounds may change over the course of a season because both leaf structure and chemical composition also evolve seasonally. For those studies that incorporate a large number of species, sample collection is largely limited to peak of the growing season (Roelofsen et al. 2014; Serbin et al. 2014). Accurate estimates of chemistry from reflectance spectroscopy require models developed using data that cover the range of plausible leaf characteristics and are thus able to leverage generalized features in the spectrum, rather than features that may be expressed at particular developmental stages. The alternative is to develop season- or species- specific models, which may be more accurate, but are not generalizable to ecological studies spanning species and ecosystem types.

In this study we linked spectral and biochemistry data from four datasets covering specimens collected from a range of vegetation types (trees, shrubs, forbs, grasses), geographic extents and leaf developmental (phenological) stages to generate spectroscopic models to estimate 27 biochemical properties including pigments, carbohydrates, minerals, and phenolic compounds, as well as leaf mass per area. For each foliar trait we developed and compared predictive performance of models developed using both fresh and dry ground spectral models. For each model type and trait, we also compared models built using different regions of the spectrum. Finally, we performed a series of analyses to identify the relationships between spectra and foliar biochemistry, specifically to assess the extent to which determination of chemistries using spectra was a consequence of spectral features unique to a particular trait and how they vary between fresh and dry spectra.

Methods

Data

The data used in this study was compiled from four datasets (Table 1.1), including data specific to this study. The species sampled in these datasets cover a wide range vegetation types, including trees, forbs and grasses, leaf developmental (phenological) stages and geographic extent. See the individual studies for details on the dataset collection.

Data unique to this study were collected in Madison, WI, USA on the campus of the University of Wisconsin, in the adjacent university-owned Lakeshore Nature Preserve and at the University of Wisconsin Arboretum (43.0766° N, 89.4125° W). Sampling occurred in 2016 and 2017 on a weekly basis, spanning June to November in 2016 and April and May in 2017. Sampling followed a three-week cycle: during each week in the cycle we collected foliage from a set of 20-25 broadleaf trees, 10-20 forbs and 3-5 graminoid species. This cycle was repeated throughout the study period, such that the same set of species (except ephemerals or those that had senesced) were sampled at least every three weeks. Over the course of the growing season, a total of 211 unique species were sampled, including 89 tree species, 104 forbs and vines and 18 graminoid species. Sampled species included native, ornamental and invasive species. We sampled two individuals of each species. For trees, we collected two sets of samples per individual including one set from sun leaves and one from shade leaves. For tall trees we used extendable pole pruners to collect branches at the top of the canopy. Between 10 – 20 leaves were collected per sample set. For forb and graminoid species leaves came from multiple individuals growing in close proximity to each other to ensure sufficient sample material (10 g dry matter per sample). After collection leaves were placed in plastic bags with a damp paper towel which were placed in a cooler on ice.

Samples were brought back to the lab within 1.5 hours for spectral and structural measurements. At the lab petioles were removed from all leaves, any dirt, debris or moisture was wiped off and each sample set was photographed. Six leaves were chosen from each sample for leaf-level measurements and the remaining leaves were retained for bulk chemical analysis. Individual leaf area was measured using a LI-3100 leaf area meter (LI-COR Biosciences, Lincoln, NE, USA) and fresh weight was measured using a precision balance (0.0001 g).

Spectral measurements were then made using two spectrometers: a PSR 3500+ spectrometer (Spectral Evolution, Boston, MA, USA) and Fieldspec 3 spectrometer (Analytical Spectral Devices, Boulder, CO, USA), hereafter referred to as PSR and ASD respectively. Each spectrometer was equipped with a manufacturer-provided leaf clip and measurements were referenced against a 99% Spectralon panel (Labsphere, North Sutton, NH, USA) to derive relative reflectance. The six leaves were measured in the same order on all spectrometers to enable comparison of individual leaf spectra. For homogeneously colored leaves, one spectrum was collected per leaf, while, for heterogeneously colored leaves (e.g. those undergoing senescence), between 2-6 spectra were averaged per leaf depending on leaf size and degree of heterogeneity. Graminoid species for which individual leaf blades did not fill the field of view of the leaf clip were aligned in parallel to create a non-overlapping mat using the six leaves, and six measurements were then made of the mat. For all samples, the six leaves were stored in individually labeled envelopes and placed in a paper bag with the remaining foliage ("bulk sample"). The sampled leaves were then frozen in liquid nitrogen and stored in a -20° C freezer until further processing. A subset of individual leaf samples (n = 279) from across the growing season were selected for pigment content determination. Pigment content was measured using HPLC as per Schweiger et al. (2020). Pigments measured included chlorophyll A and B, beta-carotene, lutein, antheraxanthin, neoxanthin, violaxanthin and zeaxanthin.

With the exception of the subset of samples analyzed for pigment content, all samples were freeze-dried in a lyophilizer (> 120 hr). Individual leaves measured for leaf area were weighed on a precision balance (0.0001g). Leaf mass per area (LMA) was calculated by dividing the leaf dry mass by fresh leaf area and was averaged for each sample set of 6 leaves. Samples were then ground using a Wiley Mill equipped with a #20 mesh (1mm). A subset of ground samples was then measured for elemental concentration (N, P, K , Ca, Mg, Al, B, Zn, Mn, Cu) (n = 195), sugars and starch (n =213), total phenolics (n = 115), flavonoids (n=115), cellulose and acid detergent lignin (ADL) (n = 207). Nitrogen concentration was determined using combustion analysis while all other elemental concentrations were measured using inductively coupled plasma emission spectroscopy (Gavlak et al. 2004). Total phenolics concentration was determined using the Folin-Ciocalteu method (Ainsworth and Gillepsie 2007) and flavonoids were determined using aluminum chloride colorimetry (Baba and Malik 2015). Lignin and cellulose concentrations were determined using a hot-acid detergent extraction (Couture et al. 2012) and sugar and starch concentrations were determined using a colorimetric quantification (Lindroth et al. 2002). Dry spectral reflectance measurements were made on all samples using an ASD Fieldspec 3 spectrometer equipped with a press to ensure consistent foreoptic position and pressure following Serbin et al. (2014). Prior to measurements, ground samples were stored in a drying oven (> 24 hr) to remove residual moisture collected during storage. Six spectra were measured per dry sample and were averaged to produce a single spectrum per sample.

Spectral preprocessing

ASD spectra were 'jumped corrected' to align mismatches in reflectance between detectors using the SWIR1 detector as the reference (Dorigo et al. 2006). For both the PSR and ASD, we excluded reflectance data below 400 nm due to a low signal-to-noise ratio. Each spectrum was vector normalized to minimize brightness differences between spectra (Xing et al. 2007).

With the exception of fresh spectra collected by Serbin et al. (2014), which used an ASD spectrometer, all samples had spectral measurements made using a PSR. Because of differences in spectrometer design, including leaf clip geometry and internal optics, reflectance measurements made on the same leaves do not match exactly (Figure 1.1). To match ASD fresh spectra with PSR fresh spectra we used the method of Meireles et al. (2020) to develop a response matrix to convert ASD to PSR spectra. Using over 11,000 paired ASD and PSR individual leaf reflectance measurements made in this study we developed and validated a response matrix using partial least-squares regression (PLSR, Wold et al. 2001). Because some graminoid samples were made using mats and individual measurements between spectrometers could not be linked (due to different view area in which one spectrometer may see multiple leaves in a mat, and the other only one), they were excluded from development of the response matrix. First, we divided the data randomly 50:50 into validation and calibration, and withheld validation data from subsequent model development. The calibration data were then used to select the optimal number of model components by minimizing the cross-validated predicted residual sum of squares statistic (PRESS). A PLSR model was then developed for the calibration data using the selected optimal number of components and applied to the validation dataset. To compare improvement in agreement between the observed PSR spectra and predicted PSR spectra from ASD (PSR_{ASD}), we calculated the difference between vector-normalized spectra before and after the transform was applied to the validation dataset (Figure 1.1). Finally, we applied the transform to the ASD fresh spectra collected by Serbin et al. (2014) for use in subsequent analyses.

Spectroscopic model development

Predictive models to estimate foliar biochemistry from fresh and dry spectra were built using PLSR. PLSR is a commonly used technique used for chemometric applications due to its ability to handle highly colinear, hyper-dimensional data, core characteristics of spectroscopic reflectance data (Wold et al. 2001). Modeling was implemented using the Python library ‘scikit-learn’ (Pedregosa et al. 2011). Other data-driven modeling frameworks have been used for estimating foliar biochemistry from spectroscopic data including multiple linear regression (Min et al. 2006), random forest regression (Abdel-Rahman et al. 2013), neural networks (Mutanga and Skidmore 2004) and gaussian process models (Verrelst et al. 2012). However, we selected PLSR due to its relatively low computational requirements, wide use and acceptance, and interpretability of model coefficients.

For each trait, we developed spectroscopic models using both fresh leaf and dry ground spectra, to ensure comparability between models we only used data points with paired fresh and dry spectra for model development. With the exception of pigments, both fresh and dry spectra were collected on multiple leaves per sample; we assumed that, for pigments, the single leaf measured using HPLC was representative of the sample from which it was a subset of. To test the impact of wavelength region on model performance, we built three models for each trait using the entire spectrum (400-2500 nm), VNIR spectrum (400-1000 nm) and the SWIR (1000 - 2500 nm).

Prior to model development, we performed a Bonferroni corrected outlier test ($p < 0.05$) to identify and remove influential data points (Cousineau and Chartier 2010). On average, across all traits, 1% of data points were labeled outliers. After outlier removal, the data were randomly split into calibration and validation (70:30). The optimal number of model components for PLSR of each trait was identified by building PLSR models on the calibration dataset using up to 30 components and selecting the number of components that minimized the jackknifed PRESS (Tarpey 2000). Next, using the calibration dataset a series of 500 models were built for each trait using a random 70% subset of the calibration data. These permuted models were applied to both the fully withheld validation and the calibration datasets and the mean and standard deviation of the 500 predictions were calculated to generate one predicted value (mean of 500) and its uncertainty (standard deviation). We also calculated R^2, root mean squared error (RMSE), normalized RMSE (NRSME) and bias on the calibration and validation predictions. After validation, final models, fresh and dry ground, for application were built, we used the validation R^2 to select the optimum wavelength range for each model. Final models were built using all the data using the same 500-model, 70% permutation approach used for developing the calibration model. The models were then applied to the entire dataset, yielding fresh and dry ground spectroscopic measurements for each trait.

Trait-spectra relationships

We used Pearson product-moment correlation to evaluate correlations among traits for those samples having multiple trait measurements. We did this for trait measurements derived both from laboratory assays as well as from spectrally predicted traits. For traits derived using laboratory measurements, correlations were only calculated for paired traits with more than 10 samples; for spectrally derived traits, correlations were calculated using all paired samples used in model development (n= 2,713).

To assess the relationships between spectra and foliar biochemistry, we utilized Pearson product-moment correlation to identify wavelengths associated with each biochemical property. Specifically, we calculated Pearson's r between trait values and a continuous wavelet transform (CWT) of the reflectance spectrum on both the fresh and dry ground samples. CWT is a signal processing technique used to decompose a signal into a series of subcomponents defined by a mother wavelet (Barache et al. 1997; Dinc and Baleanu 2008). A number of wavelet families exist for performing signal decomposition; here we used the Mexican-hat wavelet which closely approximates a gaussian response curve and has been used for characterizing spectral features related to foliar nitrogen (Wang et al. 2016; Kalacska et al. 2015), water content (Cheng et al. 2011) and chlorophyll content (Liao et al. 2013). The wavelet transform is calculated by convolving the selected wavelet with the original spectrum, the resulting coefficients provide a measure of agreement between the wavelet and the localized spectrum (Kalacska et al. 2015). The wavelet is defined by both a translation and scale that correspond to the wavelet center and stretch. Transforms were calculated in Python using 'PyWavelets' (Lee et al. 2019). For each scale and translation, we calculated Pearson’s r between the trait and the wavelet coefficient. This resulted in a *t* by s matrix of correlation coefficients, where *t* is the number of translations and *s* is the number scales. The number of translations was equal to the number of wavelengths (2100) and 20 scales were computed per translation. Typically, wavelet coefficients, or correlations, are displayed using a 2D matrix commonly referred to as a scalogram. To better visualize the magnitude and locations of spectral features, the correlations were displayed along single dimension, translation, and each scale was plotted as a separate line (Figure S1.1).

Results

The datasets used in this study consisted of between 171 and 2277 samples with laboratory-derived biochemical traits or LMA and paired fresh and dry ground spectral measurements (Table 1.2). With the exception of the pigment zeaxanthin, which was not detectable in a majority of samples, each biochemistry had at least 300 samples representing 99 - 138 genera and 170 - 192 species. Sample collection dates were largely concentrated in the middle of the growing season between day of year 150 and 250, but extended from April to November (Figure 1.2).

Spectroscopic models

Models for estimating pigments, potassium and LMA had the best predictive performance when developed using spectra on fresh green leaves (hereafter “fresh spectra” or “fresh models”); for all other traits models built using spectra of dried and ground foliage (“dry spectra/models”) exhibited stronger performances (Figure 1.3). The difference between fresh and dry model performance varied by trait and was greatest for calcium, lignin and chlorophyll B. Aluminum, copper, zinc, zeaxanthin and antheraxanthin all performed poorly regardless of spectral measurement type ($R^2 < 0.2$). All R^2 values reported are for the withheld validation samples.

Model performance varied across pigments and was dependent on the wavelength range used, although chlorophyll A and B were estimated with the highest accuracy (Figure 1.4). The top performing fresh spectral model for each pigment included the VNIR region of the spectrum, either 400-1000 nm or 400 - 2400 nm, however the difference in performance between the two wavelength ranges was generally small. Dry spectra models for pigments were generally poor ($R^2 < 0.5$) and validated best for neoxanthin using the full spectrum (R^2: 0.47, NRMSE 0.13). Among foliar element concentrations, N and Ca were estimated with the highest accuracies using dry spectra (R^2: 0.9 and 0.8, NRMSE 0.06 and 0.1, respectively). All models of foliar elemental concentration incorporated the SWIR region of the spectrum and, with the exception of nitrogen, performed poorly when using only the VNIR ($R^2 \leq 0.31$). Among models of elements developed using fresh spectra, N was estimated with the highest accuracy followed by K and Ca and, like the dry models, the best model for each included the SWIR region. Structural and defensive compounds, including total phenolics, sugars, lignin, cellulose and LMA were all estimated with high accuracy (R^2: 0.74 - 0.93), each using either the full or SWIR region of the spectrum and with the exception of LMA top performing models used the dry spectra for estimation.

Trait correlations

For spectrally derived traits, correlation patterns generally matched the relationships derived from laboratory assays and correlations generally became stronger in spectrally derived traits (i.e. negative correlations in the lab data became more negative in the spectral predictions and vice versa; Figures 1.5 and 1.6).

From HPLC measurements, contents of beta-carotene, chlorophylls A and B, lutein and neoxanthin were highly correlated (r: 0.83; $p <.01$) and moderately correlated with violaxanthin (r: 0.57 - 0.65) (Figure 1.5). Similar patterns were observed with spectroscopically derived pigments but with stronger correlations for all pigment pairs, correlations were highest between chlorophyll A and chlorophyll B (r: 0.99) and lutein and neoxanthin (r: 0.99). For both laboratory-measured and spectroscopically derived pigments, correlations with other traits were weak. Macronutrients including N, P, K and S were all positively correlated whether derived using laboratory assays (r: 0.45 - 0.55) or spectral models (r : 0.57 - 0.87) and were generally negatively correlated with carbohydrates, lignin and LMA. Total phenolics and flavonoids were both positively correlated with sugars using both laboratory-derived and spectral estimates.

Wavelet correlations

In our interpretations of the correlations of wavelength-by-wavelength wavelet transformations with foliar traits, we treat the observation of a negative correlation at a wavelength as evidence of an absorption feature and thus these are our focus (Figure 1.7). In addition, by comparing the wavelet correlations across all wavelengths between all pairs of traits, we could identify those traits whose relationships with spectra leverage common absorption (or reflectance) features (Figure S1.2). Specifically, in Figure S1.2 higher positive correlations between traits indicate that the pair of traits share strong correlations with many common absorption features, while strong negative correlations indicate that wavelengths with absorption features for one trait in the pair being compared are matched by reflectance features in the other trait. Combined, these analyses enable comparison with absorption features reported elsewhere in the literature, as well as identifying those traits for whom reasonable spectroscopic predictions may be a function of inter-trait correlations rather than the presence of known absorption features (see Discussion).

All pigments with the exception of zeaxanthin and antheraxanthin, exhibited near identical patterns in correlations using the wavelet transforms of both dry and fresh spectra, and were highly correlated with each another (r: 0.76- 0.99) (Figure 1.7; Figure S1.2). For these pigments, the strongest negative correlation (i.e. absorption feature) was observed at the red edge near 710 nm. Correlations with the SWIR region of the spectrum were generally weak but exhibited minima (i.e., negative wavelet correlation indicating a possible absorption feature) at 2050 nm and 2170 nm in both the fresh and dry spectra with slightly stronger correlations in the dry spectra (Figure 1.8a). For zeaxanthin and antheraxanthin, which were poorly estimated using

PLSR models, wavelet correlations were weak across the entire spectrum ($r < 0.3$) (Figures S1.2 and S1.9).

Patterns in correlations for elements exhibited two general groupings, each of which showed similar relationships between trait measurements and wavelet transforms (Figure 1.7). The first group, including Cu, Fe, N, K, P and S, exhibited the strongest negative correlations near 1520, 1980 and 2170 in the dry spectra, whereas correlations were weaker and less consistent among traits in the fresh spectra (Figures 1.7 and 1.8). The second group, which included Ca, B and Mg, showed nearly identical patterns across the spectrum. As well, wavelet correlations across wavelengths were also highly correlated among the three minerals ($r > 0.94$ - 0.98; Figure S1.2), indicating that spectroscopic prediction for these traits likely leverages common features; Ca, B and Mg are also highly correlated with each other in the laboratory measurements (Figure 1.5, upper diagonal). For dry spectra the region 1910-2010 nm exhibited the strongest correlations in all three traits however for the fresh spectra, correlations were weak across the entire spectrum (Figures 1.7 and 1.8c). Al and Z exhibited correlation patterns that were uncorrelated with all other traits and were weak across the spectrum (Figures S1.10 and S1.21). Manganese was unique in that unlike all other elemental traits, whose wavelet correlations were strongly aligned across wavelengths, it was negatively correlated with other elements, especially Mg and P ($r < -0.81$) (Figure S1.2). Notably, Mn was generally uncorrelated with the other elements in the laboratory data (Figure 1.5).

Total phenolics and flavonoids were negatively correlated with dry spectra wavelet features near 1130, 1470, 1660 and 2150 nm (Figure S1.28-1.29). However total phenolics features at 1130 and 1470 nm were absent in the wavelet correlations with fresh spectra (Figure 1.8d). In both the fresh and dry spectra, cellulose was negatively correlated with features at 1240 and 2260 nm. Lignin exhibited strong correlation with wavelet features in the dry spectra across the spectrum, and was strongest at 510, 710, 1730, and 2150 nm, but for fresh spectra correlated features were generally limited to the SWIR region (Figure S1.26). Sugars and starch displayed similar patterns in correlations with wavelet features and had the strongest correlation near 1200, 1440 and 2140 nm. LMA was most strongly negatively correlated with dry and fresh wavelet features at 1200, 1420 and 2150 nm, but also exhibited sharp peaks of positive correlation (i.e., with reflectance rather than absorption) in the fresh spectra at 950 and 1140 nm that were absent in the correlations with dry spectra (Figure S1.27)

Discussion

In this study we developed models to estimate foliar biochemical traits from leaf reflectance data from both fresh intact leaves and dried/ground samples. Our models were built using a comprehensive dataset that included samples from over 100 species of tree, shrubs, forbs and grass that were collected across the growing season, covered a wide geographic extent and included both sun and shade leaves. We found that for pigments, LMA and K, models using fresh spectra provided the most accurate estimates. Ca, Mg, N, P, K, S, defensive and structural compounds were most accurately estimated using dry spectral models. However, Al, Cu, Fe, Z, zeaxanthin and antheraxanthin were poorly estimated regardless of the measurement type used.

For both the fresh and dry models we found that choice of spectral range impacted the model performance. For all traits with the exception of pigments, including the SWIR region resulted in the best model performance. Conversely the VNIR region was important for estimating pigments accurately. Generally, for traits that were well estimated ($R^2 > 0.5$) inclusion of other regions beyond only marginally changed model performance, i.e. VNIR was sufficient for pigments and SWIR sufficient for the rest. There are some benefits to constraining the spectral range for prediction, as it reduces the likelihood of introducing error due to confounding features, and – in many cases – limits the predictions to wavelengths where known absorption features exist (i.e., more physically realistic). Some of the traits have long been estimated using reflectance spectroscopy, e.g. due to known absorption features at visible wavelengths for pigments, or from decades-old research that is the foundation for using spectra to estimate proteins (i.e., nitrogen), fiber and carbohydrates in forage. However, many of the traits that are widely estimated from reflectance spectroscopy do not exhibit strong spectral absorbance signatures to provide a basis for estimation (for example, many elements). Yet, estimations from leaf spectral measurements have formed the basis for numerous studies (Asner and Martin 2008, Asner et al. 2009, Doughty et al. 2011; Singh et al. 2015; Wang et al. 2019, 2020), especially studies that link traits to remote sensing data for mapping, where laboratory chemistry needed to calibrate such models is impractical at the scale of imagery. This begs the question whether the retrieval of certain traits for leaf level estimates using data-driven chemometric methods such as PLSR is a consequence of spurious correlations or trait-trait correlations where one trait has a strong correlation feature that is leveraged to predict another, highly correlated trait. In our discussion, we review the basis for estimating these traits from spectroscopy.

Among plant biochemicals pigments are the most well characterized spectrally due to their role in converting sunlight into chemical energy used to fix carbon. Chlorophylls are the primary light absorbing pigments found in plants. Other pigments, including carotenoids and xanthophylls are also present, where they play a photoprotective role (Lambers et al. 1998). Pigments absorb strongly in the visible spectrum (400-700nm), but it is worth noting that Clark et. (1987) measured the NIR-SWIR spectrum of extracted chlorophyll and reported additional spectral features at 1768, 1850, 2304 and 2350 nm. For all pigments which were well estimated with PLSR coefficients, wavelet correlations were strongest at the red edge (710 -720 nm) and a similar pattern was displayed in the PLSR coefficients (Figures S1.3-S1.8). Correlations were stronger in fresh versus dry spectra, which is expected due to the denaturing effects of oven drying, but a negative correlation was still present at the red edge in dry spectra. The red edge is commonly used to estimate chlorophyll content as saturation occurs at the chlorophyll absorption maximum (660-680 nm) (Horler et al. 1983; Gitelson et al. 1996). The presence of this correlation in non-chlorophyll pigments, which generally absorb light at wavelengths < 550nm, indicates that the ability to estimate these pigments is largely driven their strong correlation with chlorophyll content (Figure 1.5) and is demonstrated by similar PLSR coefficient structure for all pigments (Figures S1.2-S1.8). Interestingly though, in the dry spectra, wavelet correlation features associated with non-chlorophyll pigments become apparent near 440 and 470 nm (Clementson and Wojtasiewicz 2019), suggesting differential levels of denaturing by different pigments in response to oven drying. Cui et al. (2004) found that 70% of carotenoids were retained after oven drying compared to 40% for chlorophylls. While correlations were strongest in the visible region of spectrum, features in the SWIR associated with nitrogen at 2061 and 2172 nm were also correlated with pigment content, indicating a correlative relationship between pigments and other N-containing compounds like proteins in the photosystems and light harvesting complex.

In foliage, Ca is present in a number of forms including ionic Ca^{2+}, in the middle lamella in the form of calcium pectate and in various salts including calcium oxalate, calcium carbonate, calcium sulfate and calcium citrate (Krieger et al. 2016). In its ionic form Ca is not known to have absorption features in the infrared (Workman and Weyer 2008). However, calcium pectate and calcium salts have infrared signatures (Titok et al. 2010; Applin et al. 2016). Petisco et al. (2005) reported that for a mix of woody species, wavelengths in the 1900 nm region of the spectrum were most important for estimating calcium, and others have reported similar results with absorption features at wavelengths greater than 1800nm (Shenk et al. 1979; Valdes et al. 1985; Clark et al. 1987). Among its non-ionic forms, Ca is commonly found in the form of calcium oxalate (CaOx), which can constitute up to 80% of the Ca in a leaf (Francesci and Nakata 2005). Chandler (1937) found that foliar CaOx content was correlated with total foliar calcium. CaOx serves multiple role in plants including storage of excess Ca, in the formation of defensive structures and as a chelating agent (Franeschi and Horner 1980; Nakata 2003; Mazen 2004). CaOx exhibits sharps absorption peaks centered at 1957 and 2002 nm that are not present in other calcium salts. These spectral features closely align with regions of maximum negative correlation with wavelet transforms (Figure 1.9). Moreover, the coefficients of the dry spectra PLSR model for Ca have large negative weights in those regions as well (Figure S1.13), indicating a potential mechanism for the ability to estimate Ca concentration from reflectance spectra. Of note, this feature is absent in the fresh spectra correlations, a possible result of obscuration by water absorption (Figure 1.8c).

Nitrogen is a key plant nutrient that is closely tied with the photosynthetic apparatus, where it is found largely in the form of proteins, including the enzyme RuBisCO which can contain up to 30% of total leaf nitrogen. N is also present in amino acids, lipids, the cell wall and in pigments (Evans and Seemann 1989; Makino 2003; Onoda et al. 2004). Spectral estimation of nitrogen is often used as a surrogate for photosynthetic capacity and its detection is thus also the basis for spectroscopic estimation of metabolic traits such as Vcmax (Serbin et al. 2012; Dechant et al. 2017). N and proteins and are generally well estimated from dry spectra due the absorption features in the SWIR resulting from N-H bonding (Curran 1989; Kokaly 2001). In our dataset wavelengths with large negative dry ground wavelet correlations were all near absorption features related to nitrogen including N-H bonds present proteins (1515, 1980, 2050 and 2170 nm) (Curran 1989; Osborne et al. 1993; Workman and Weyer 2008; Figure 1.8b). However, in the fresh leaf PLSR model only features near 2050 and 2170 nm were leveraged, a possible consequence of leaf water absorption in regions with N absorption features (Figure 1.8b).

Phosphorus is present in a number of compounds critical to plant growth including ATP and DNA (Schachtman et al. 1998), and is involved in regulating enzymatic activity (Mills and Jones 1996). Weak absorption features related to P are present in the SWIR regions of the spectrum due to P-H (1891 and 1908 nm) and P-SH bonds (1970 and 1999 nm) (Workman and Weyer 2008) but were not evident in our wavelet or PLSR coefficients. In both the wavelet correlations and the PLSR model, positive coefficient maxima are observed at 1429 and 1438 nm respectively (Figure S1.19). Robert and Cadet (1998) report a sharp absorption peak for polysaccharides at 1437nm while Boulley et al. (2015) report a sugar absorption band at 1432nm. P is involved in starch metabolism (Qiu and Israel 1992), and Brahim et al. (1996) found that P deficiency resulted in a decrease in foliar phosphorus concentration and increase in foliar starch and glucose accumulation in pine seedings. Thus, the positive correlation peaks may reflect the increasing accumulation of carbohydrates with decreasing concentrations of phosphorus. Conversely wavelengths with negative correlation coefficients included those associated with N-H bonds in proteins (1525 and 1990 nm). In our dataset phosphorus was most strongly correlated with nitrogen ($r = 0.55$ in lab measurements and $r = 0.73$ from spectroscopic determination). Likewise, PLSR coefficients for the P model leveraged nitrogen features at 2050 and 1985 nm and the starch feature at 1438 nm. We conclude that the estimation of P from reflectance spectroscopy leverages a range of absorption features associated with correlated N-containing compounds and other chemistries (e.g., nonstructural carbohydrates) for which P plays a role in metabolism. P can be reasonably estimated from spectroscopy but estimates from reflectance spectroscopy should be interpreted with caution as its uncertainty (14%) is much higher than N (6%). In any given data set, spectroscopic predictions of phosphorus should be carefully compared to other constituents to determine whether its accurate estimation does not simply track a correlation with foliar N.

Potassium plays a number of roles in plants including controlling opening of stomates via osmoregulation, translocation of sugars and starch, and cellulose formation (Cochrane and Cochrane 2009; Mills and Jones 1996). As with Ca, K has no known signature in the infrared in its ionic form (Shenk et al. 1979). Ciavarella et al. (1998) noted that K concentration was closely correlated with spectral regions related to sugars, starch and cellulose, indicating that the ability to estimate potassium spectrally is related to its influence on other organic compounds with known spectral signatures. Using dry spectra, spectral regions with strong negative wavelet correlations with K included those associated within N bonds (1515 and 1985 nm) and proteins (1690 nm) (Workman and Weyer 2008), which is unsurprising given the positive correlation of K with N in the lab data ($r = 0.51$; $r = 0.57$ in the spectroscopic estimates). Spectral regions that were positively correlated with K are associated with starches (1450 nm, 990 nm), which were weakly negatively correlated with K in the lab data, and aromatic compounds (1670 and 2140 nm). The correlation with starch features is notable as symptoms of K deficiency include built up of carbohydrates (Mills and Jones 1996). Lacking known absorptions feature, the spectroscopic estimation of K clearly leverages correlated features related to non-K containing compounds, but those correlated features are related to many compounds and spread throughout the spectrum, meaning that K predictions from spectroscopy may be reliable, but are based on the complex interactions among multiple compounds influenced by K.

Magnesium acts a cofactor for enzymes and is found in chlorophyll (Mills and Jones 1996). In our dataset Mg was poorly correlated with chlorophyll content but was strongly correlated with calcium using both laboratory and spectrally derived measurements ($r \geq 0.7$). Correlations with wavelet features using both fresh and dry spectra revealed nearly identical patterns when compared to those identified in calcium (r: 0.8 and 0.97). Shenk et al. (1979) reported low predictability of Mg in dry forage while Nunes et al. (2017) estimated Mg using fresh leaf spectra and reported similar results to our own fresh leaf models (R^2: 0.40 here vs 0.49 in Nunes et al. 2017). Like other minerals it is not known to have a spectral signature in the near infrared in its ionic form and its estimation likely a result of correlations with other compounds, like Ca-containing complexes.

Sulfur is a component of multiple amino acids that are building blocks for a number of proteins; symptoms of S deficiency include decreases in chlorophyll and proteins, and increases in starch (Droux 2004; Marschner 2011). Like P, a weak absorption feature is present in the SWIR region of the spectrum associated with S-H bonding (1980 nm) (Workman and Weyer 2008). Wavelet correlation patters for S closely match those for N (r: 0.83) and align with known features associated with proteins, indicating the ability to estimate S is likely a function of its correlation with N (r: 0.51).

Micronutrients (B, Cu, Fe, Mn, Zn) are essential elements that are found in small quantities in plant tissues that are important to the regulation of enzymatic activity, metabolism and the production of structural and defensive compounds (Marschner 2011). Al is not known to be an essential nutrient and is generally considered to be toxic to many plants (Bojorquez-

Quintal et al. 2017), and its concentration in foliage is sometimes used as an indicator of soil acidity. Few studies have attempted to estimate micronutrients or trace minerals from a diverse group of species using either dry ground and or fresh leaf spectra. Using single species calibrations, Clark et al. (1989) estimated aluminum with moderate accuracy (R^2: 0.69-0.78) for three forage types, but found that important wavelengths varied across species. Galvez-Sola et al. (2015) developed PLSR equations for *Citrus* species and reported "moderate" accuracies for Zn and Fe, but found that B, Cu and Mn were poorly estimated. Here, trace elements, with the exception of B, were poorly estimated using fresh or dry spectra models. Moreover, the wavelet correlation patterns in B were nearly identically followed those of Ca (r: 0.98). B and Ca are known to be closely associated (Bolanos et al. 2004) and are similarly immobile within plants. Cu and Fe were weakly to moderately positively correlated with N and exhibited common patterns in wavelet correlation features that are associated with N and protein absorption bands. Mn is known to be a cofactor for enzymes that produce lignin and phenolic compounds (Marschner 2011) and was negatively correlated with wavelengths associated with phenolic compounds (1130, 1450, 1660 and 2150 nm). In addition, lignin and Mn wavelet features showed a strong correlation in both the fresh leaf and dry spectra (r: 0.92 and 0.87), indicating that detection of Mn from spectra likely tracks its role in lignin synthesis.

Sugars and starch, products of photosynthesis, have well-characterized absorption features in the infrared that are a result of C-H and O-H bonds present in these compounds (Workman and Weyer 2008). Robert and Cadet (1998) found that that these spectral features are generally shifted by 25-130 nm in polysaccharides (starches) compared to monosaccharides (sugars), which may enable relative determination of starch vs. sugar concentration. In both the wavelet correlations and the PLSR coefficients these features are evident near 1200 nm and 1450 nm for starches (Figure S1.24). For sugars, the absorption feature at 1450 nm was present in the wavelet correlations, but it was absent in the PLSR coefficients (Figure S1.23). Among the other wavelet features correlated with sugars were 1668, 1148 and 2150 nm, which are wavelengths associated with aromatics and phenolic compounds (Buback 1993; Workman and Weyer 2008), but not specifically with sugars. Phenolic compounds are often found linked with glucose (Harborne 1989). In our dataset sugars and starch were positively correlated with both total phenolics and flavonoids ($r \geq 0.46$ in spectroscopic estimates), a positive relationship observed elsewhere (Ibrahim et al. 2011) that indicates that the ability to measure sugars is may be driven in part by its correlation with phenolic compounds. The independent validation R^2 for sugars was high (R^2: 0.65) supporting the use of reflectance spectroscopy for estimation of sugar concentration, although validation of predictions of starch concentrations was much poorer (R^2: 0.24; NRMSE 16%), a possible consequence of a lower average concentration in foliage (3.3%) compared to sugars (17.9%). We conclude that the estimation of nonstructural carbohydrates is well supported by the presence of distinct spectral features, but that spectral estimation may also leverage a range of features associated with compounds that correlate with sugars and starches.

Phenolics are a class of secondary metabolites including condensed tannins that are generally associated with plant defense but also play a role in photoprotection and cold acclimation (Appel et al. 2001; Close and McArthur 2002). Phenolic composition varies across taxonomic groups, and individual species can produce of over 100 phenolic compounds (Harborne 1989; Li and Seeram 2018). Due to their similar molecular structure consisting of an aromatic ring, phenolic compounds share a number of absorption features in infrared region of the spectrum (Workman and Weyer 2008). However, Couture et al. (2016) demonstrate that the specific phenols present in closely related species will both share absorption features and exhibit unique features. Thus, the exact location of spectral features may be shifted as a function of the presence of specific phenolics whose identities are species-dependent or whose absorption features may shift in location in the presence of other compounds (Workman and Weyer 2008; Kokaly and Skidmore 2015). For instance, in our dataset wavelet correlation features were shifted to longer wavelengths (~10nm) in flavonoids compared to total phenolics (Figure 1.10). However, large negative coefficients appeared around 1660 nm in both the wavelet correlations and PLSR models for both total phenolics and flavonoids (Figure 1.8d and 1.10; Figures S1.27-1.28), matching the presence of a major absorption feature at 1660 nm present in a number of phenolic compounds including gallic acid and tannic acids (Kokaly and Skidmore 2015). Other absorption features associated with phenolic compounds including 1132, 1460 and 2135 nm were also evident in wavelet correlation plots and PLSR coefficients (Buback 1993; Workman and Weyer 2008). The detection of phenolic compounds from reflectance spectroscopy is very strongly supported by the presence of absorption features, but because the specific phenolic compounds in species differ, caution should be exercised when making specific inference about the roles that spectroscopically determined phenolics play in the functioning of any given observation. Nevertheless, there is also evidence that diversity in phenolic compounds can also be detected (Couture et al. 2016), but this requires careful laboratory discrimination of the multitude of phenolics present, which may be impractical across a large number of species having distinct phenolic profiles.

Cellulose and lignin are structural compounds that constitute the cell wall and provide rigidity, increase tensile strength and waterproof the cell (Delmer and Amor 1995; Boerjan et al. 2003; Somerville 2006). Similar to nonstructural carbohydrates, cellulose and lignin are composed of bonded C-H and O-H molecules and have well characterized absorption features in the near through shortwave infrared (Osborne et al. 1993; Workman and Weyer 2008). For cellulose, O-H features at 1490 and 2270 nm were present in both the PLSR and wavelet coefficients (Figure S1.25). Lignin, which consists of aromatic subunits, exhibited negative wavelet correlations with features associated with aromatic rings including 1135 and 1670 nm. Interestingly, lignin was also strongly correlated with wavelengths in the visible region of the spectrum (Figure S1.26). However, lignin is not known to contain any absorption features in the visible wavelengths and the relationship may be a result of correlation with pigments (Figure 1.5) or due to lignin autofluorescence (Donaldson 2020).

LMA is a composite measure of a plant's investment in biomass per unit area and is widely used in ecology as a measure of resource allocation strategy because of its low cost and ease of measurement. Spectroscopic estimates of LMA provide the additional benefits of rapid and non-destructive measurement and multiple studies have shown that LMA can be measured with high accuracy from fresh leaf spectra (Ourcival et al 1999; Asner et al. 2011; Serbin et al. 2019). Using both dry and fresh spectra, LMA was strongly correlated wavelet features in the NIR regions at 1000, 1200 and 1450 nm (Figure S1.27). These regions are associated with absorption by starch, sugars, cellulose and lignin, compounds which constitute a large proportion of the leaf dry matter content that comprises LMA. The estimation of LMA from reflectance spectroscopy is due to the relationship between the many carbon compounds associated with leaf structure, and thus is entirely correlative in application. However, it is also the leaf trait that can be most robustly estimated from reflectance spectroscopy ($R^2 > 0.9$, uncertainty < 5%), as was demonstrated by Serbin et al. (2019) for species spanning the tropics to Arctic.

A limiting factor in developing highly reliable, generalizable spectroscopic models is the accuracy of wet chemistry procedures. With the exception of LMA, which was measured directly, and lignin and cellulose, which were determined gravimetrically, no other traits were directly quantified. There can be a considerable amount of uncertainty in wet chemistry analysis that is dependent on the analytical technique, reagents, standards and exact methodology used (Young et al. 1994; Appel et al. 2001; Thorsen and Hildebrandt 2003). Quentin et al. (2015) found that measures of nonstructural carbohydrates were not comparable between different labs. Similarly, Brinkman et al. (2002) found that measurements of lignin concentrations were dependent on analytical method. In our own dataset we found that the same samples measured for cellulose and lignin at different labs using the same analytical technique yielded inconsistent results (Figure S1.30): measurements were either poorly correlated (lignin, R^2: 0.31) or contained significant outliers (cellulose, with outliers R^2: 0.34, without outliers R^2: 0.97). Even gravimetric methods have limitations, namely the complete isolation of the compounds of interest. For example, Brinkman et al. (2002) found and that acid detergent lignin (ADL), the method used in this study, contained up to 18% bound proteins, resulting in an overestimation of lignin compared to other methods.

The models developed here used data from plants in the United States and despite containing a diverse collection species (native, invasive and cultivated) and phenological stages do not represent the global diversity of plant types and spectral and biochemical profiles. For example, we did not include conifer species, whose structure and chemical profiles vary significantly from broadleaf species and graminoids. Conifers also present challenges for making fresh spectra measurements due their small and narrow shapes (Daughtry et al. 1989). Although numerous studies have advocated for approaches to sampling conifer needles, especially using mats (Daughtry et al. 1989, but see also alternative method in Wang et al. 2020), work is still needed to enable linkage of fresh spectra from broadleaf and conifers (e.g. Rautiainen et al.

2018). Dry spectral measurements from conifers can be integrated with broadleaf data, but incorporation of fresh spectra may be challenging due to differences in measurement techniques. As an additional caveat, the integration of conifer with broadleaf samples for spectroscopic determination does risk inflating accuracy of spectral models. Because conifers and broadleaf species differ considerably in foliar chemistry and spectral characteristics, there is the risk of developing predictive models that simply fit to clusters of much different spectra from conifer vs. broadleaf species, when in fact these lack the ability to characterize within leaf-type variation in foliar chemistry.

We note that our dataset included samples covering the range of phenological stages (Figure 1.2). Addressing phenology has been demonstrated to be important to generation of accurate models, including both leaf spectra (Yang et al. 2016) and image spectra (Chapter 3). This necessitates adequately sampling across developmental stages to ensure that the range of differing combinations of biochemical concentrations among traits is captured. As well, our dataset included leaves from both sunlit and shaded canopy positions. Light environment strongly influences leaf optical properties (Niinemets et al. 1998) and especially traits such as LMA (Chapter 2) and pigments, and thus models should include samples that adequately represent this dimension of variation. Finally, for completeness, factors such as the ontogeny of a sample and other environmental controls such as soil fertility and climate should be considered for their influence on different samples from common species. While not all of these factors can be or need to be addressed for all species, an adequate representation across species whose traits are being predicted using spectroscopy ensures more robust application to new samples. This is especially important if these data are being used as a substitute for traditional measurements.

As such, continued work is needed to broaden the diversity of samples used in model development. Creation of such a global database would allow for the development of truly global models that can be applied with confidence irrespective of species and would also present the opportunity to develop more localized models tailored to given species or spectral type (Sinnaeve et al. 1994). Ultimately, the most accurate predictive models may be those that are taxonomically (species, genus or family) specific, with generalized models utilized to predict for additional samples lacking taxonomically constrained models.

Conclusion

Using an unprecedented dataset that covered multiple axes of variation driving variability in foliar biochemistry, including taxonomy, phenology and geography, we developed empirical models to estimate 27 foliar biochemical traits using both fresh leaf and dried and ground spectra. We found that using dry spectral measurements Ca, N, cellulose, lignin, sugars and total phenolics could be estimated with high confidence ($R^2 > 0.6$), while chlorophylls A and B and LMA were estimated with high accuracy using fresh spectra. Other biochemical properties including B, K, P, Mg, flavonoids and carotenoid pigments were estimated with moderate confidence ($R^2 > 0.4$), but estimates should be treated with caution. Reviewing the literature, we also explored the extent to which correlative patterns underlying trait-spectra relationships could be explained by electron transitions and bending and stretching in chemical bonds (C-H, C-O, N-H and O-H) of closely related compounds. Our results highlight the tradeoffs between using spectra from intact leaves (fresh) versus dried and ground samples for estimating foliar traits and that neither method on its own is optimal for estimating the full suite of traits measured here.

Ideally a combination of the two methods should be used, coupled with traditional analytical techniques for model validation.

Acknowledgments

Thank you to all the members of the Townsend Lab who assisted with fieldwork and sample processing, especially Aidan Mazur and Alex Horvath.

References

Abdel-Rahman, E. M., Ahmed, F. B., & Ismail, R. (2013). Random forest regression and spectral band selection for estimating sugarcane leaf nitrogen concentration using EO-1 Hyperion hyperspectral data. *International Journal of Remote Sensing*, *34*(2), 712-728.

Agrawal, A. A., Fishbein, M., Jetter, R., Salminen, J. P., Goldstein, J. B., Freitag, A. E., & Sparks, J. P. (2009). Phylogenetic ecology of leaf surface traits in the milkweeds (Asclepias spp.): chemistry, ecophysiology, and insect behavior. *New Phytologist*, *183*(3), 848-867.

Ainsworth, E. A., & Gillespie, K. M. (2007). Estimation of total phenolic content and other oxidation substrates in plant tissues using Folin–Ciocalteu reagent. *Nature protocols*, *2*(4), 875-877.

Appel, H. M., Govenor, H. L., D'ascenzo, M., Siska, E., & Schultz, J. C. (2001). Limitations of Folin assays of foliar phenolics in ecological studies. *Journal of chemical ecology*, *27*(4), 761-778.

Applin, D. M., Izawa, M. R., & Cloutis, E. A. (2016). Reflectance spectroscopy of oxalate minerals and relevance to Solar System carbon inventories. *Icarus*, *278*, 7-30.

Asner, G. P., & Martin, R. E. (2008). Spectral and chemical analysis of tropical forests: Scaling from leaf to canopy levels. *Remote Sensing of Environment*, *112*(10), 3958-3970.

Asner, G. P., Martin, R. E., Ford, A. J., Metcalfe, D. J., & Liddell, M. J. (2009). Leaf chemical and spectral diversity in Australian tropical forests. *Ecological Applications*, *19*(1), 236-253.

Asner, G. P., Martin, R. E., Knapp, D. E., Tupayachi, R., Anderson, C., Carranza, L., ... & Weiss, P. (2011). Spectroscopy of canopy chemicals in humid tropical forests. *Remote Sensing of Environment*, *115*(12), 3587-3598.

Baba, S. A., & Malik, S. A. (2015). Determination of total phenolic and flavonoid content, antimicrobial and antioxidant activity of a root extract of Arisaema jacquemontii Blume. *Journal of Taibah University for Science*, *9*(4), 449-454.

Barache, D., Antoine, J. P., & Dereppe, J. M. (1997). The continuous wavelet transform, an analysis tool for NMR spectroscopy. *Journal of Magnetic Resonance*, *128*(1), 1-11.

Blackmer, T. M., & Schepers, J. S. (1994). Techniques for monitoring crop nitrogen status in corn. *Communications in soil science and plant analysis*, *25*(9-10), 1791-1800.

Boerjan, W., Ralph, J., & Baucher, M. (2003). Lignin biosynthesis. *Annual review of plant biology*, *54*(1), 519-546.

Bojórquez-Quintal, E., Escalante-Magaña, C., Echevarría-Machado, I., & Martínez-Estévez, M. (2017). Aluminum, a friend or foe of higher plants in acid soils. *Frontiers in plant science*, *8*, 1767.

Bolaños, L., Lukaszewski, K., Bonilla, I., & Blevins, D. (2004). Why boron?. *Plant Physiology and Biochemistry*, *42*(11), 907-912.

Boulley, L., Schulte, H., & Pierson, J. F. (2015). Near-infrared optical spectroscopy of sugar-based mixtures–A snapshot to identify issues of influence. *of Materials*, 27.

Brahim, M. B., Loustau, D., Gaudillère, J. P., & Saur, E. (1996). Effects of phosphate deficiency on photosynthesis and accumulation of starch and soluble sugars in 1-year-old seedlings of maritime pine (Pinus pinaster Ait). In *Annales des sciences forestières* (Vol. 53, No. 4, pp. 801-810). EDP Sciences.

Brinkmann, K., Blaschke, L., & Polle, A. (2002). Comparison of different methods for lignin determination as a basis for calibration of near-infrared reflectance spectroscopy and implications of lignoproteins. *Journal of chemical ecology*, *28*(12), 2483-2501.

Buback, M., & Vögele, H. P. (1993). *FT-NIR atlas*. John Wiley & Son Ltd.

Card, D. H., Peterson, D. L., Matson, P. A., & Aber, J. D. (1988). Prediction of leaf chemistry by the use of visible and near infrared reflectance spectroscopy. *Remote Sensing of Environment*, *26*(2), 123-147.

Chandler Jr, R. F. (1937). Certain relationships between the calcium and oxalate content of foliage of certain forest trees. *Journal of Agricultural Research*, *55*, 393.

Cheng, T., Rivard, B., & Sanchez-Azofeifa, A. (2011). Spectroscopic determination of leaf water content using continuous wavelet analysis. *Remote Sensing of Environment*, *115*(2), 659-670.

Ciavarella, S., Batten, G. D., & Blakeney, A. B. (1998). Measuring potassium in plant tissues using near infrared spectroscopy. *Journal of Near Infrared Spectroscopy*, *6*(A), A63-A66.

Clark, D. H., Mayland, H. F., & Lamb, R. C. (1987). Mineral Analysis of Forages with near Infrared Reflectance Spectroscopy 1. *Agronomy Journal*, *79*(3), 485-490.

Clark, D. H., Cary, E. E., & Mayland, H. F. (1989). Analysis of trace elements in forages by near infrared reflectance spectroscopy. *Agronomy Journal*, *81*(1), 91-95.

Clementson, L. A., & Wojtasiewicz, B. (2019). Dataset on the absorption characteristics of extracted phytoplankton pigments. *Data in brief*, *24*, 103875.

Close, D. C., & McArthur, C. (2002). Rethinking the role of many plant phenolics–protection from photodamage not herbivores?. *Oikos*, *99*(1), 166-172.

Cloutis, E. (2015). CTAPE Mineral and rock sample database [5_Master_Carbonates_oxalates.xls: PIG204]. Retrieved from https://ctape.uwinnipeg.ca/Sample_Database/

Cochrane, T. T., & Cochrane, T. A. (2009). The vital role of potassium in the osmotic mechanism of stomata aperture modulation and its link with potassium deficiency. *Plant signaling & behavior*, *4*(3), 240-243.

Cousineau, D., & Chartier, S. (2010). Outliers detection and treatment: a review. *International Journal of Psychological Research*, *3*(1), 58-67.

Couture, J. J., Meehan, T. D., & Lindroth, R. L. (2012). Atmospheric change alters foliar quality of host trees and performance of two outbreak insect species. *Oecologia*, *168*(3), 863-876.

Couture, J. J., Singh, A., Rubert-Nason, K. F., Serbin, S. P., Lindroth, R. L., & Townsend, P. A. (2016). Spectroscopic determination of ecologically relevant plant secondary metabolites. *Methods in Ecology and Evolution*, *7*(11), 1402-1412.

Cui, Z.-W., Xu, S.-Y., & Sun, D.-W. (2004). *Effect of Microwave-Vacuum Drying on the Carotenoids Retention of Carrot Slices and Chlorophyll Retention of Chinese Chive Leaves. Drying Technology, 22(3), 563–575.* doi:10.1081/drt-120030001

Curran, P. J. (1989). Remote sensing of foliar chemistry. *Remote sensing of environment*, *30*(3), 271-278.

Curran, P. J., Dungan, J. L., Macler, B. A., Plummer, S. E., & Peterson, D. L. (1992). Reflectance spectroscopy of fresh whole leaves for the estimation of chemical concentration. *Remote Sensing of Environment*, *39*(2), 153-166.

Da Silveira, L., Sternberg, L., Mulkey, S. S., & Wright, S. J. (1989). Ecological interpretation of leaf carbon isotope ratios: influence of respired carbon dioxide. *Ecology*, *70*(5), 1317-1324.

Daughtry, C. S. T., Biehl, L. L., & Ranson, K. J. (1989). A new technique to measure the spectral properties of conifer needles. *Remote Sensing of Environment*, *27*(1), 81-91

Dawson, T. P., Curran, P. J., & Plummer, S. E. (1998). LIBERTY—Modeling the effects of leaf biochemical concentration on reflectance spectra. *Remote sensing of environment*, *65*(1), 50-60.

Dechant, B., Cuntz, M., Vohland, M., Schulz, E., & Doktor, D. (2017). Estimation of photosynthesis traits from leaf reflectance spectra: Correlation to nitrogen content as the dominant mechanism. *Remote Sensing of Environment*, *196*, 279-292.

Delmer, D. P., & Amor, Y. (1995). Cellulose biosynthesis. *The plant cell*, *7*(7), 987.

Dinç, E., & Baleanu, D. (2008). Application of Haar and Mexican hat wavelets to double divisor-ratio spectra for the multicomponent determination of ascorbic acid, acetylsalicylic acid and paracetamol in effervescent tablets. *Journal of the Brazilian Chemical Society*, *19*(3), 434-444.

Dixon, M. J., & Kuja, A. L. (1995). Effects of simulated acid rain on the growth, nutrition, foliar pigments and photosynthetic rates of sugar maple and white spruce seedlings. *Water, Air, and Soil Pollution*, *83*(3-4), 219-236.

Donaldson, L. (2020). Autofluorescence in Plants. *Molecules*, *25*(10), 2393.

Dorigo, W., Bachmann, M., & Heldens, W. (2006). AS Toolbox & Processing of field spectra. *User's manual, German Aerospace Center (DLR), Oberpfaffenhofen*.

Doughty, C. E., Asner, G. P., & Martin, R. E. (2011). Predicting tropical plant physiology from leaf and canopy spectroscopy. *Oecologia*, *165*(2), 289-299.

Droux, M. (2004). Sulfur assimilation and the role of sulfur in plant metabolism: a survey. *Photosynthesis Research*, *79*(3), 331-348.

Dunn, C. E. (2011). *Biogeochemistry in mineral exploration*. Elsevier.

Evans, J. R., & Seemann, J. R. (1989). The allocation of protein nitrogen in the photosynthetic apparatus: costs, consequences, and control. *Photosynthesis*, *8*, 183-205.

Féret, J. B., Le Maire, G., Jay, S., Berveiller, D., Bendoula, R., Hmimina, G., ... & De Boissieu, F. (2019). Estimating leaf mass per area and equivalent water thickness based on leaf optical properties: Potential and limitations of physical modeling and machine learning. *Remote sensing of environment*, *231*, 110959.

Fernàndez-Martínez, J., Joffre, R., Zacchini, M., Fernández-Marín, B., García-Plazaola, J. I., & Fleck, I. (2017). Near-infrared reflectance spectroscopy allows rapid and simultaneous evaluation of chloroplast pigments and antioxidants, carbon isotope discrimination and nitrogen content in Populus spp. leaves. *Forest Ecology and Management*, *399*, 227-234.

Franceschi, V. R., & Horner, H. T. (1980). Calcium oxalate crystals in plants. *The Botanical Review*, *46*(4), 361-427.

Franceschi, V. R., & Nakata, P. A. (2005). Calcium oxalate in plants: formation and function. *Annu. Rev. Plant Biol.*, *56*, 41-71.

Galvez-Sola, L., García-Sánchez, F., Pérez-Pérez, J. G., Gimeno, V., Navarro, J. M., Moral, R., ... & Nieves, M. (2015). Rapid estimation of nutritional elements on citrus leaves by near infrared reflectance spectroscopy. *Frontiers in plant science*, *6*, 571.

Gavlak, R., Horneck, D., Miller, R. O., & Kotuby-Amacher, J. (2003). Soil, plant and water reference methods for the western region. *WCC-103 Publication, Fort Collins, CO.*

Gitelson, A. A., Merzlyak, M. N., & Lichtenthaler, H. K. (1996). Detection of red edge position and chlorophyll content by reflectance measurements near 700 nm. *Journal of plant physiology*, *148*(3-4), 501-508.

Gold, K. M., Townsend, P. A., Chlus, A., Herrmann, I., Couture, J. J., Larson, E. R., & Gevens, A. J. (2020). Hyperspectral measurements enable pre-symptomatic detection and differentiation of contrasting physiological effects of late blight and early blight in potato. *Remote Sensing*, *12*(2), 286.

Grossman, Y. L., Ustin, S. L., Jacquemoud, S., Sanderson, E. W., Schmuck, G., & Verdebout, J. (1996). Critique of stepwise multiple linear regression for the extraction of leaf biochemistry information from leaf reflectance data. *Remote Sensing of Environment*, *56*(3), 182-193.

Harborne, J. B. (1989). General procedures and measurement of total phenolics. *Methods in plant biochemistry*, *1*, 1-28.

Horler, D. N. H., Dockray, M., Barber, J., & Barringer, A. R. (1983). Red edge measurements for remotely sensing plant chlorophyll content. *Advances in Space Research*, *3*(2), 273-277.

Ibrahim, M. H., Jaafar, H. Z., Rahmat, A., & Rahman, Z. A. (2011). The relationship between phenolics and flavonoids production with total non structural carbohydrate and photosynthetic rate in Labisia pumila Benth. under high CO2 and nitrogen fertilization. *Molecules*, *16*(1), 162-174.

Jacquemoud, S., & Baret, F. (1990). PROSPECT: A model of leaf optical properties spectra. *Remote sensing of environment*, *34*(2), 75-91.

Jacquemoud, S., Verdebout, J., Schmuck, G., Andreoli, G., & Hosgood, B. (1995). Investigation of leaf biochemistry by statistics. *Remote Sensing of Environment*, *54*(3), 180-188.

Jacquemoud, S., Ustin, S. L., Verdebout, J., Schmuck, G., Andreoli, G., & Hosgood, B. (1996). Estimating leaf biochemistry using the PROSPECT leaf optical properties model. *Remote sensing of environment*, *56*(3), 194-202.

Kalacska, M., Lalonde, M., & Moore, T. R. (2015). Estimation of foliar chlorophyll and nitrogen content in an ombrotrophic bog from hyperspectral data: Scaling from leaf to image. *Remote Sensing of Environment*, *169*, 270-279.

Kokaly, R. F. (2001). Investigating a physical basis for spectroscopic estimates of leaf nitrogen concentration. *Remote Sensing of Environment*, *75*(2), 153-161.

Kokaly, R. F., & Skidmore, A. K. (2015). Plant phenolics and absorption features in vegetation reflectance spectra near 1.66 µm. *International Journal of Applied Earth Observation and Geoinformation*, *43*, 55-83.

Krieger, C., Calvaruso, C., Morlot, C., Uroz, S., Salsi, L., & Turpault, M. P. (2017). Identification, distribution, and quantification of biominerals in a deciduous forest. *Geobiology*, *15*(2), 296-310.

Lacaze, B., & Joffre, R. (1994). Extracting biochemical information from visible and near infrared reflectance spectroscopy of fresh and dried leaves. *Journal of plant physiology*, *144*(3), 277-281.

Lambers, H., CHAPIN, F., & Pons, T. L. (1998). Plant physiological ecology Springer Verlag. *New York, USA*.

Li, C., & Seeram, N. P. (2018). Ultra-fast liquid chromatography coupled with electrospray ionization time-of-flight mass spectrometry for the rapid phenolic profiling of red maple (Acer rubrum) leaves. *Journal of separation science*, *41*(11), 2331-2346.

Lee, G. R., Gommers, R., Waselewski, F., Wohlfahrt, K., & O'Leary, A. (2019). PyWavelets: A Python package for wavelet analysis. *Journal of Open Source Software*, *4*(36), 1237.

Liao, Q., Wang, J., Yang, G., Zhang, D., Lii, H., Fu, Y., & Li, Z. (2013). Comparison of spectral indices and wavelet transform for estimating chlorophyll content of maize from hyperspectral reflectance. *Journal of Applied Remote Sensing*, *7*(1), 073575.

Lindroth, R. L., Osier, T. L., Barnhill, H. R. H., & Wood, S. A. (2002). Effects of genotype and nutrient availability on phytochemistry of trembling aspen (Populus tremuloides Michx.) during leaf senescence. *Biochemical Systematics and Ecology*, *30*(4), 297-307

Makino, A. (2003). Rubisco and nitrogen relationships in rice: leaf photosynthesis and plant growth. *Soil Science and Plant Nutrition*, *49*(3), 319-327.

Marschner, H. (2011). *Marschner's mineral nutrition of higher plants*. Academic press.

Martin, M. E., & Aber, J. D. (1994). Analyses of forest foliage III: Determining nitrogen, lignin and cellulose in fresh leaves using near infrared reflectance data. *Journal of Near Infrared Spectroscopy*, *2*(1), 25-32.

Mazen, A. M. A. (2004). Calcium oxalate deposits in leaves of Corchorus olitorius as related to accumulation of toxic metals. *Russian Journal of Plant Physiology*, *51*(2), 281-285.

Meireles, J. E., Cavender-Bares, J., Townsend, P. A., Ustin, S., Gamon, J. A., Schweiger, A. K., ... & Schrodt, F. (2020). Leaf reflectance spectra capture the evolutionary history of seed plants. *New Phytologist*, *228*(2), 485-493.

Melillo, J. M., Aber, J. D., & Muratore, J. F. (1982). Nitrogen and lignin control of hardwood leaf litter decomposition dynamics. *Ecology*, *63*(3), 621-626.

Merzlyak, M. N., Gitelson, A. A., Chivkunova, O. B., Solovchenko, A. E., & Pogosyan, S. I. (2003). Application of reflectance spectroscopy for analysis of higher plant pigments. *Russian journal of plant physiology*, *50*(5), 704-710.

Mills, H. A., & Jones Jr, J. B. (1996). *Plant analysis handbook II: A practical sampling, preparation, analysis, and interpretation guide* (No. 581.13 M657).

Min, M., Lee, W. S., Kim, Y. H., & Bucklin, R. A. (2006). Nondestructive detection of nitrogen in Chinese cabbage leaves using VIS–NIR spectroscopy. *HortScience*, *41*(1), 162-166.

Mutanga, O., & Skidmore, A. K. (2004). Integrating imaging spectroscopy and neural networks to map grass quality in the Kruger National Park, South Africa. *Remote sensing of environment*, *90*(1), 104-115.

Nakata, P. A. (2003). Advances in our understanding of calcium oxalate crystal formation and function in plants. *Plant Science*, *164*(6), 901-909.

Niinemets, Ü., Kull, O., & Tenhunen, J. D. (1998). An analysis of light effects on foliar morphology, physiology, and light interception in temperate deciduous woody species of contrasting shade tolerance. *Tree physiology*, *18*(10), 681-696.

Norris, K. H., Barnes, R. F., Moore, J. E., & Shenk, J. S. (1976). Predicting forage quality by infrared replectance spectroscopy. *Journal of animal science*, *43*(4), 889-897

Nunes, M., Davey, M., & Coomes, D. (2017). On the challenges of using field spectroscopy to measure the impact of soil type on leaf traits.

Onoda, Y., Hikosaka, K., & Hirose, T. (2004). Allocation of nitrogen to cell walls decreases photosynthetic nitrogen-use efficiency. *Functional Ecology*, 419-425.

Osborne, B. G., Fearn, T., & Hindle, P. H. (1993). *Practical NIR spectroscopy with applications in food and beverage analysis*. Longman scientific and technical.

Ourcival, J. M., Joffre, R., & Rambal, S. (1999). Exploring the relationships between reflectance and anatomical and biochemical properties in Quercus ilex leaves. *The New Phytologist*, *143*(2), 351-364.

Pedregosa, F., Varoquaux, G., Gramfort, A., Michel, V., Thirion, B., Grisel, O., ... & Vanderplas, J. (2011). Scikit-learn: Machine learning in Python. *the Journal of machine Learning research*, *12*, 2825-2830.

Petisco, C., García-Criado, B., De Aldana, B. V., Zabalgogeazcoa, I., & Mediavilla, S. (2005). Use of near-infrared reflectance spectroscopy in predicting nitrogen, phosphorus and calcium contents in heterogeneous woody plant species. *Analytical and Bioanalytical Chemistry*, *382*(2), 458-465.

Qiu, J., & Israel, D. W. (1992). Diurnal starch accumulation and utilization in phosphorus-deficient soybean plants. *Plant Physiology*, *98*(1), 316-323.

Quentin, A. G., Pinkard, E. A., Ryan, M. G., Tissue, D. T., Baggett, L. S., Adams, H. D., ... & Gibon, Y. (2015). Non-structural carbohydrates in woody plants compared among laboratories. *Tree physiology*, *35*(11), 1146-1165.

Ramirez, J. A., Posada, J. M., Handa, I. T., Hoch, G., Vohland, M., Messier, C., & Reu, B. (2015). Near-infrared spectroscopy (NIRS) predicts non-structural carbohydrate concentrations in different tissue types of a broad range of tree species. *Methods in Ecology and Evolution*, *6*(9), 1018-1025.

Rautiainen, M., Lukeš, P., Homolova, L., Hovi, A., Pisek, J., & Mõttus, M. (2018). Spectral properties of coniferous forests: A review of in situ and laboratory measurements. *Remote Sensing*, *10*(2), 207.

Robert, C., & Cadet, F. (1998). Analysis of near-infrared spectra of some carbohydrates. *Applied Spectroscopy Reviews*, *33*(3), 253-266.

Roelofsen, H. D., van Bodegom, P. M., Kooistra, L., & Witte, J. P. M. (2014). Predicting leaf traits of herbaceous species from their spectral characteristics. *Ecology and evolution*, *4*(6), 706-719.

Sager, E. P. S., Hutchinson, T. C., & Croley, T. R. (2005). Foliar phenolics in sugar maple (Acer saccharum) as a potential indicator of tropospheric ozone pollution. *Environmental monitoring and assessment*, *105*(1-3), 419-430.

Schachtman, D. P., Reid, R. J., & Ayling, S. M. (1998). Phosphorus uptake by plants: from soil to cell. *Plant physiology*, *116*(2), 447-453.

Serbin, S. P., Dillaway, D. N., Kruger, E. L., & Townsend, P. A. (2012). Leaf optical properties reflect variation in photosynthetic metabolism and its sensitivity to temperature. *Journal of Experimental Botany*, *63*(1), 489-502.

Serbin, S. P., Singh, A., McNeil, B. E., Kingdon, C. C., & Townsend, P. A. (2014). Spectroscopic determination of leaf morphological and biochemical traits for northern temperate and boreal tree species. *Ecological Applications*, *24*(7), 1651-1669.

Serbin, S. P., Wu, J., Ely, K. S., Kruger, E. L., Townsend, P. A., Meng, R., ... & Rogers, A. (2019). From the Arctic to the tropics: multibiome prediction of leaf mass per area using leaf reflectance. *New Phytologist*, *224*(4), 1557-1568.

Shenk, J. S., Westerhaus, M. O., & Hoover, M. R. (1979). Analysis of forages by infrared reflectance. *Journal of Dairy Science*, *62*(5), 807-812.

Shenk, J. S., & Westerhaus, M. O. (1985). Accuracy of Nirs instruments to analyze forage and grain 1. *Crop science*, *25*(6), 1120-1122.

Shenk, J. S., & Westerhaus, M. O. (1994). The application of near infrared reflectance spectroscopy (NIRS) to forage analysis. *Forage quality, evaluation, and utilization*, 406-449.

Singh, A., Serbin, S. P., McNeil, B. E., Kingdon, C. C., & Townsend, P. A. (2015). Imaging spectroscopy algorithms for mapping canopy foliar chemical and morphological traits and their uncertainties. *Ecological Applications*, *25*(8), 2180-2197.

Sinnaeve, G., Dardenne, P., & Agneessens, R. (1994). Global or local? A choice for NIR calibrations in analyses of forage quality. *Journal of near infrared spectroscopy*, *2*(3), 163-175.

Smyth, H., & Cozzolino, D. (2011). Applications of infrared spectroscopy for quantitative analysis of volatile and secondary metabolites in plant materials. *Current Bioactive Compounds*, *7*(2), 66-74.

Somerville, C. (2006). Cellulose synthesis in higher plants. *Annu. Rev. Cell Dev. Biol.*, *22*, 53-78.

Tarpey, T. (2000). A note on the prediction sum of squares statistic for restricted least squares. *The American Statistician*, *54*(2), 116-118.

Thorsen, M. A., & Hildebrandt, K. S. (2003). Quantitative determination of phenolic diterpenes in rosemary extracts: aspects of accurate quantification. *Journal of Chromatography A*, *995*(1-2), 119-125.

Titok, V., Leontiev, V., Yurenkova, S., Nikitinskaya, T., Barannikova, T., & Khotyleva, L. (2010). Infrared spectroscopy of fiber flax. *Journal of natural fibers*, *7*(1), 61-69.

Trotter, G. M., Whitehead, D., & Pinkney, E. J. (2002). The photochemical reflectance index as a measure of photosynthetic light use efficiency for plants with varying foliar nitrogen contents. *International Journal of Remote Sensing*, *23*(6), 1207-1212.

Valdes, E. V., Young, L. G., McMillan, I., & Winch, J. E. (1985). Analysis of hay, haylage and corn silage samples by near infrared reflectance spectroscopy. *Canadian Journal of Animal Science*, *65*(3), 753-760.

Vázquez de Aldana, B. R., García Criado, B., & Pérez Corona, M. E. (1995). Estimation of mineral content in natural grasslands by near infrared reflectance spectroscopy.

Verrelst, J., Alonso, L., Caicedo, J. P. R., Moreno, J., & Camps-Valls, G. (2012). Gaussian process retrieval of chlorophyll content from imaging spectroscopy data. *IEEE Journal of Selected Topics in Applied Earth Observations and Remote Sensing*, *6*(2), 867-874.

Wang, Z., Skidmore, A. K., Wang, T., Darvishzadeh, R., & Hearne, J. (2015). Applicability of the PROSPECT model for estimating protein and cellulose+ lignin in fresh leaves. *Remote Sensing of Environment*, *168*, 205-218.

Wang, Z., Townsend, P. A., Schweiger, A. K., Couture, J. J., Singh, A., Hobbie, S. E., & Cavender-Bares, J. (2019). Mapping foliar functional traits and their uncertainties across three years in a grassland experiment. *Remote Sensing of Environment*, *221*, 405-416.

Wang, Z., Chlus, A., Geygan, R., Ye, Z., Zheng, T., Singh, A., ... & Townsend, P. A. (2020). Foliar functional traits from imaging spectroscopy across biomes in eastern North America. *New Phytologist*.

Wang, Z., Skidmore, A. K., Wang, T., Darvishzadeh, R., Heiden, U., Heurich, M., ... & Hearne, J. (2017). Canopy foliar nitrogen retrieved from airborne hyperspectral imagery by correcting for canopy structure effects. *International journal of applied earth observation and geoinformation*, *54*, 84-94.

Waskom, R. M., Westfall, D. G., Spellman, D. E., & Soltanpour, P. N. (1996). Monitoring nitrogen status of corn with a portable chlorophyll meter. *Communications in Soil Science and Plant Analysis*, *27*(3-4), 545-560.

Wessman, C. A., Aber, J. D., Peterson, D. L., & Melillo, J. M. (1988). Foliar analysis using near infrared reflectance spectroscopy. *Canadian Journal of Forest Research*, *18*(1), 6-11.

Wold, S., Sjöström, M., & Eriksson, L. (2001). PLS-regression: a basic tool of chemometrics. *Chemometrics and intelligent laboratory systems*, *58*(2), 109-130.

Workman Jr, J., & Weyer, L. Practical Guide to Interpretive Near-infrared Spectroscopy, 2008.

Xing, J., Ngadi, M., Gunenc, A., Prasher, S., & Gariepy, C. (2007). Use of visible spectroscopy for quality classification of intact pork meat. *Journal of food engineering*, *82*(2), 135-141.

Yang, X., Tang, J., Mustard, J. F., Wu, J., Zhao, K., Serbin, S., & Lee, J. E. (2016). Seasonal variability of multiple leaf traits captured by leaf spectroscopy at two temperate deciduous forests. *Remote Sensing of Environment*, *179*, 1-12.

Yoder, B. J., & Pettigrew-Crosby, R. E. (1995). Predicting nitrogen and chlorophyll content and concentrations from reflectance spectra (400–2500 nm) at leaf and canopy scales. *Remote sensing of environment*, *53*(3), 199-211.

Young, M. W., Davies, H. V., & MacKerron, D. K. L. (1993). Comparison of techniques for nitrogen analysis in potato crops. In *Optimization of Plant Nutrition* (pp. 7-11). Springer, Dordrecht.

Yuan, M., Couture, J. J., Townsend, P. A., Ruark, M. D., & Bland, W. L. (2016). Spectroscopic determination of leaf nitrogen concentration and mass per area in sweet corn and snap bean. *Agronomy Journal*, *108*(6), 2519-2526.

Tables

Table 1.1 Datasets used in this study.

Study	Traits	Measurement	Instrument	Season	Location	Vegetation type
This study	N, P, K, Ca, Mg, Al, B, Zn, Mn, Cu, sugars, starch, flavonoids total phenolics, lignin, cellulose, pigments, leaf mass per area	Dry ground Fresh leaf	PSR 3500+ (Fresh) ASD Fieldspec 3 (Fresh and dry)	Full season	Madison, WI, USA	Trees, shrubs, forbs, grasses
Serbin et al. 2014	N, fiber, lignin, cellulose	Dry ground Fresh leaf	ASD Fieldspec 3	Summer	Upper Midwest and Eastern USA	Trees and shrubs
Wang et al. 2020	N, P, K, Ca, Mg, Al, B, Zn, Mn, Cu, sugars, starch, flavonoids total phenolics, lignin, cellulose, pigments	Dry ground Fresh leaf	PSR 3500+ (Fresh) ASD Fieldspec 3 (Dry)	Summer	Continental USA	Trees, shrubs forbs, grasses
Chapter 3[1]	N, P, K, Ca, Mg, Al, B, Zn, Mn, Cu, sugars, starch, flavonoids total phenolics, lignin, cellulose, pigments	Dry ground Fresh leaf	PSR 3500+ (Fresh) ASD Fieldspec 3 (Dry)	Full season	Blackhawk Island, WI, USA	Trees

[1] Although not noted cellulose, sugar and starch concentrations were measured using the same wet chemistry techniques employed in this study.

Table 1.2 Sample chemistry summary.

	Trait	**Units**	**Samples**	**Mean**	**Range**	**Genera**	**Species**
Pigments	Antheraxanthin	μmol • m^{-2}	476	3.53	0.34 - 15.95	118	189
	Beta-Carotene	μmol • m^{-2}	480	34.79	0.72 - 77.7	117	188
	Chlorophyll A	μmol • m^{-2}	485	342.97	1.52 - 909.83	118	189
	Chlorophyll B	μmol • m^{-2}	483	106.54	0.75 - 289.89	118	189
	Lutein	μmol • m^{-2}	488	59.77	3.14 - 153.78	117	189
	Neoxanthin	μmol • m^{-2}	488	18.42	0.48 - 51.19	117	189
	Violaxanthin	μmol • m^{-2}	488	23.09	0.79 - 66.32	118	190
	Zeaxanthin	μmol • m^{-2}	171	7.98	0.88 - 28.25	65	108
Elements	Aluminum	ppm	347	51.85	4.4 - 1410.0	109	175
	Boron	ppm	349	33.83	1.6 - 135.5	109	176
	Calcium	% dry mass	348	1.4	0.05 - 5.05	108	176
	Copper	ppm	348	7.23	1.0 - 22.0	109	177
	Iron	ppm	346	58.28	17.7 - 157.0	110	176
	Magnesium	% dry mass	348	0.32	0.08 - 1.06	109	176
	Manganese	ppm	345	241.9	4.8 - 2040.0	110	177
	Nitrogen	% dry mass	513	2.5	0.48 - 5.06	109	183
	Phosphorus	% dry mass	350	0.24	0.03 - 0.72	110	178
	Potassium	% dry mass	348	1.23	0.16 - 4.74	108	176
	Sulfur	% dry mass	344	0.19	0.04 - 0.6	108	176
	Zinc	ppm	344	31.51	3.5 - 196.0	110	178
Carbohydrates	Sugars	% dry mass	384	17.94	4.12 - 40.09	115	192
	Starch	% dry mass	386	3.3	0.34 - 10.65	115	192
Structure	Cellulose	% dry mass	396	15.42	4.44 - 39.49	114	190
	Lignin	% dry mass	400	12.62	0.0 - 42.12	114	190
	Leaf Mass per Area	g • m^{-2}	2277	60.51	15.8 - 148.59	138	183
Phenolics	Flavonoids	% dry mass	319	6.67	0.67 - 26.01	99	170
	Total phenolics	% dry mass	323	7.22	1.26 - 25.65	101	173

Table 1.3 PLSR calibration and validation metrics for predicting pigments using fresh and dry spectra. 'C' indicates number of model components.

		Fresh							**Dry**						
			R^2		**RMSE**		**NRMSE**			**R^2**		**RMSE**		**NRMSE**	
	Wavelengths	**C**	**Cal.**	**Val.**	**Cal.**	**Val.**	**Cal.**	**Val.**	**C**	**Cal.**	**Val.**	**Cal.**	**Val.**	**Cal.**	**Val.**
Antheraxanthin	400 - 1000 nm	2	0.05	0.14	2.86	2.56	0.19	0.16	1	0.01	0.01	2.93	2.7	0.2	0.17
	1000 - 2500 nm	1	0.03	0.14	2.9	2.56	0.2	0.17	5	0.12	0.11	2.75	2.56	0.19	0.16
	400 - 2500 nm	3	0.06	0.16	2.85	2.53	0.19	0.16	6	0.14	0.13	2.73	2.55	0.18	0.16
Beta-Carotene	400 - 1000 nm	4	0.71	0.59	7.74	8.96	0.1	0.13	4	0.28	0.16	12.07	12.98	0.16	0.19
	1000 - 2500 nm	7	0.55	0.3	9.59	11.79	0.12	0.17	9	0.39	0.29	11.18	11.79	0.15	0.17
	400 - 2500 nm	5	0.72	0.59	7.59	8.9	0.1	0.13	11	0.46	0.36	10.45	11.16	0.14	0.16
Chlorophyll A	400 - 1000 nm	8	0.74	0.65	82.38	92.75	0.09	0.12	11	0.44	0.33	120.94	128.48	0.13	0.17
	1000 - 2500 nm	10	0.57	0.44	105.8	130.23	0.12	0.17	8	0.43	0.36	122.21	126.6	0.13	0.16
	400 - 2500 nm	7	0.77	0.66	78.3	91.32	0.09	0.12	12	0.55	0.44	108.52	118.23	0.12	0.15
Chlorophyll B	400 - 1000 nm	7	0.7	0.65	27.37	31.22	0.09	0.11	10	0.46	0.39	36.93	40.73	0.13	0.15
	1000 - 2500 nm	6	0.43	0.33	37.79	42.99	0.13	0.15	9	0.44	0.32	37.6	42.84	0.13	0.15
	400 - 2500 nm	8	0.75	0.71	25.01	28.1	0.09	0.1	11	0.54	0.4	34.07	40.62	0.12	0.14
Lutein	400 - 1000 nm	7	0.55	0.48	16.52	17.74	0.13	0.12	3	0.27	0.28	21.11	20.86	0.17	0.15
	1000 - 2500 nm	6	0.38	0.22	19.48	21.75	0.15	0.15	8	0.35	0.31	20.04	20.38	0.16	0.14
	400 - 2500 nm	10	0.64	0.46	14.92	18.39	0.12	0.13	12	0.46	0.37	18.2	19.4	0.14	0.14
Neoxanthin	400 - 1000 nm	8	0.65	0.6	5.06	5.7	0.11	0.11	5	0.33	0.43	6.99	6.8	0.15	0.13
	1000 - 2500 nm	10	0.52	0.35	5.91	7.36	0.13	0.15	10	0.42	0.38	6.51	7.08	0.14	0.14
	400 - 2500 nm	7	0.69	0.6	4.74	5.72	0.1	0.11	13	0.51	0.47	5.97	6.59	0.13	0.13
Violaxanthin	400 - 1000 nm	4	0.27	0.29	10.61	10.52	0.18	0.17	3	0.19	0.14	11.22	11.56	0.19	0.19
	1000 - 2500 nm	6	0.29	0.34	10.45	10.19	0.18	0.17	9	0.32	0.21	10.27	11.11	0.17	0.18
	400 - 2500 nm	5	0.33	0.36	10.19	9.97	0.17	0.16	13	0.41	0.29	9.57	10.5	0.16	0.17
Zeaxanthin	400 - 1000 nm	2	0.1	0.01	4.86	5.27	0.2	0.19	1	0.02	0.02	5.06	5.2	0.2	0.19
	1000 - 2500 nm	1	0.03	0	5.05	5.28	0.2	0.19	1	0.07	0.07	4.94	5.07	0.2	0.19
	400 - 2500 nm	4	0.23	0.08	4.5	5.11	0.18	0.19	1	0.07	0.05	4.94	5.11	0.2	0.19

Table 1.4 PLSR calibration and validation metrics for predicting elemental traits using fresh and dry spectra. 'C' indicates number of model components.

		Fresh							Dry						
			R^2		RMSE		NRMSE			R^2		RMSE		NRMSE	
	Wavelengths	**C**	**Cal.**	**Val.**	**Cal.**	**Val.**	**Cal.**	**Val.**	**C**	**Cal.**	**Val.**	**Cal.**	**Val.**	**Cal.**	**Val.**
Aluminum	400 - 1000 nm	1	0.02	0	101.59	151.72	0.07	0.12	1	0.06	0.04	99.17	148.01	0.07	0.11
	1000 - 2500 nm	1	0.01	0	101.86	151.81	0.07	0.12	2	0.08	0.08	98.35	145.07	0.07	0.11
	400 - 2500 nm	1	0.02	0	101.37	151.95	0.07	0.12	1	0.07	0.05	99.08	147.72	0.07	0.11
Boron	400 - 1000 nm	2	0.12	0.14	25.46	24.28	0.19	0.19	6	0.27	0.27	23.28	22.32	0.17	0.17
	1000 - 2500 nm	9	0.34	0.32	22.04	21.49	0.16	0.17	7	0.39	0.43	21.2	19.77	0.16	0.15
	400 - 2500 nm	3	0.14	0.15	25.21	24.09	0.19	0.19	9	0.45	0.48	20.13	18.97	0.15	0.15
Calcium	400 - 1000 nm	2	0.08	0.15	0.9	0.89	0.19	0.21	11	0.43	0.17	0.71	0.9	0.15	0.21
	1000 - 2500 nm	11	0.55	0.5	0.63	0.67	0.13	0.16	17	0.85	0.8	0.36	0.43	0.07	0.1
	400 - 2500 nm	11	0.45	0.44	0.7	0.71	0.14	0.17	11	0.75	0.62	0.47	0.58	0.1	0.14
Copper	400 - 1000 nm	3	0.13	0.01	3.32	3.68	0.16	0.21	3	0.25	0.14	3.08	3.36	0.15	0.19
	1000 - 2500 nm	11	0.4	0.12	2.76	3.52	0.13	0.2	8	0.31	0.14	2.95	3.36	0.14	0.19
	400 - 2500 nm	4	0.2	0.09	3.17	3.46	0.15	0.2	5	0.31	0.18	2.95	3.3	0.14	0.19
Iron	400 - 1000 nm	3	0.11	0	22.68	28.02	0.17	0.21	3	0.04	0.02	23.59	26.62	0.17	0.2
	1000 - 2500 nm	3	0.14	0.06	22.29	26.14	0.16	0.2	4	0.15	0.16	22.22	24.63	0.16	0.18
	400 - 2500 nm	3	0.14	0	22.3	27.82	0.16	0.21	7	0.22	0.24	21.24	23.48	0.15	0.18
Magnesium	400 - 1000 nm	2	0.13	0.01	0.17	0.21	0.17	0.24	6	0.31	0.24	0.15	0.17	0.16	0.19
	1000 - 2500 nm	15	0.71	0.4	0.1	0.16	0.1	0.17	16	0.73	0.59	0.1	0.13	0.1	0.14
	400 - 2500 nm	9	0.45	0.1	0.14	0.2	0.14	0.22	11	0.64	0.53	0.11	0.14	0.11	0.15
Manganese	400 - 1000 nm	1	0.05	0.06	386.42	328.17	0.19	0.24	10	0.29	0.24	333.68	298.29	0.17	0.22
	1000 - 2500 nm	8	0.39	0.3	308.91	284.39	0.15	0.21	15	0.56	0.38	263.06	299.68	0.13	0.22
	400 - 2500 nm	4	0.2	0.15	353.31	312.62	0.18	0.23	7	0.38	0.37	312.37	267.18	0.16	0.19
Nitrogen	400 - 1000 nm	5	0.26	0.26	0.73	0.73	0.17	0.16	26	0.75	0.64	0.42	0.5	0.1	0.11
	1000 - 2500 nm	12	0.71	0.66	0.45	0.49	0.1	0.11	16	0.91	0.9	0.25	0.26	0.06	0.06
	400 - 2500 nm	19	0.75	0.65	0.43	0.5	0.1	0.11	20	0.93	0.9	0.23	0.26	0.05	0.06
Phosphorus	400 - 1000 nm	7	0.2	0.25	0.13	0.12	0.18	0.18	3	0.2	0.31	0.13	0.11	0.18	0.17
	1000 - 2500 nm	7	0.45	0.44	0.1	0.1	0.15	0.15	6	0.45	0.52	0.1	0.09	0.15	0.14
	400 - 2500 nm	5	0.39	0.37	0.11	0.11	0.16	0.16	6	0.46	0.51	0.1	0.1	0.15	0.14
Potassium	400 - 1000 nm	5	0.21	0.3	0.7	0.67	0.15	0.17	9	0.3	0.28	0.66	0.67	0.14	0.17
	1000 - 2500 nm	5	0.47	0.55	0.58	0.54	0.13	0.14	15	0.73	0.5	0.41	0.58	0.09	0.15
	400 - 2500 nm	5	0.5	0.58	0.56	0.52	0.12	0.13	10	0.64	0.5	0.47	0.57	0.1	0.14
Sulfur	400 - 1000 nm	2	0.08	0.02	0.09	0.1	0.17	0.21	3	0.15	0.06	0.09	0.1	0.16	0.2
	1000 - 2500 nm	3	0.27	0.22	0.08	0.09	0.15	0.19	8	0.42	0.38	0.07	0.08	0.13	0.17
	400 - 2500 nm	5	0.32	0.21	0.08	0.09	0.14	0.19	7	0.39	0.32	0.08	0.09	0.14	0.17
Zinc	400 - 1000 nm	1	0.01	0	30.66	29.85	0.16	0.16	1	0.05	0	30.1	30.49	0.16	0.16
	1000 - 2500 nm	2	0.03	0.02	30.42	29.65	0.16	0.16	2	0.08	0	29.62	31.03	0.15	0.17
	400 - 2500 nm	1	0.01	0.01	30.61	29.7	0.16	0.16	1	0.07	0	29.74	30.82	0.15	0.17

Table 1.5 PLSR calibration and validation metrics for predicting carbohydrates, structural traits and phenolic compounds using fresh and dry spectra. 'C' indicates number of model components.

		Fresh							Dry						
			R^2		RMSE		NRMSE			R^2		RMSE		NRMSE	
	Wavelengths	**C**	**Cal.**	**Val.**	**Cal.**	**Val.**	**Cal.**	**Val.**	**C**	**Cal.**	**Val.**	**Cal.**	**Val.**	**Cal.**	**Val.**
Sugars	400 - 1000 nm	5	0.24	0.26	6.39	6.02	0.18	0.2	4	0.2	0.29	6.53	5.88	0.18	0.19
	1000 - 2500 nm	18	0.79	0.5	3.33	5.37	0.09	0.18	16	0.77	0.65	3.48	4.16	0.1	0.14
	400 - 2500 nm	4	0.36	0.28	5.83	6.04	0.16	0.2	14	0.71	0.62	3.97	4.31	0.11	0.14
Starch	400 - 1000 nm	9	0.27	0.07	1.78	2.2	0.19	0.21	3	0.07	0	2.02	2.27	0.21	0.22
	1000 - 2500 nm	9	0.41	0.19	1.6	2.02	0.17	0.2	10	0.37	0.22	1.66	1.97	0.17	0.19
	400 - 2500 nm	10	0.44	0.19	1.57	2.03	0.16	0.2	13	0.43	0.24	1.58	1.97	0.16	0.19
Cellulose	400 - 1000 nm	4	0.24	0.29	5.3	5.31	0.16	0.15	5	0.15	0.18	5.6	5.74	0.17	0.16
	1000 - 2500 nm	15	0.73	0.67	3.14	3.67	0.09	0.1	14	0.81	0.82	2.64	2.75	0.08	0.08
	400 - 2500 nm	16	0.7	0.59	3.33	4.15	0.1	0.12	17	0.82	0.76	2.57	3.18	0.08	0.09
Lignin	400 - 1000 nm	3	0.18	0.14	7.6	8.19	0.17	0.2	17	0.66	0.3	4.89	8.14	0.11	0.2
	1000 - 2500 nm	13	0.56	0.42	5.53	6.72	0.13	0.17	14	0.76	0.73	4.08	4.57	0.09	0.11
	400 - 2500 nm	5	0.33	0.32	6.84	7.25	0.16	0.18	19	0.81	0.74	3.62	4.44	0.08	0.11
LMA	400 - 1000 nm	23	0.82	0.81	10.05	10.81	0.07	0.08	29	0.7	0.68	12.99	13.83	0.1	0.1
	1000 - 2500 nm	16	0.93	0.93	6.15	6.58	0.05	0.05	19	0.69	0.7	13.21	13.35	0.1	0.1
	400 - 2500 nm	14	0.93	0.92	6.54	6.74	0.05	0.05	30	0.79	0.77	10.93	11.7	0.08	0.09
Flavonoids	400 - 1000 nm	1	0.01	0.03	4.8	4.49	0.2	0.18	3	0.04	0.08	4.73	4.38	0.2	0.17
	1000 - 2500 nm	1	0.02	0.11	4.79	4.38	0.2	0.17	11	0.3	0.45	4.05	3.41	0.17	0.13
	400 - 2500 nm	3	0.08	0.17	4.64	4.2	0.19	0.17	2	0.03	0.05	4.77	4.44	0.2	0.18
Total phenolics	400 - 1000 nm	4	0.16	0.04	4.38	4.9	0.18	0.21	6	0.22	0.18	4.23	4.47	0.18	0.19
	1000 - 2500 nm	11	0.77	0.64	2.27	3.05	0.09	0.13	13	0.8	0.76	2.16	2.52	0.09	0.11
	400 - 2500 nm	10	0.7	0.55	2.63	3.46	0.11	0.15	19	0.82	0.73	2	2.66	0.08	0.11

Figures

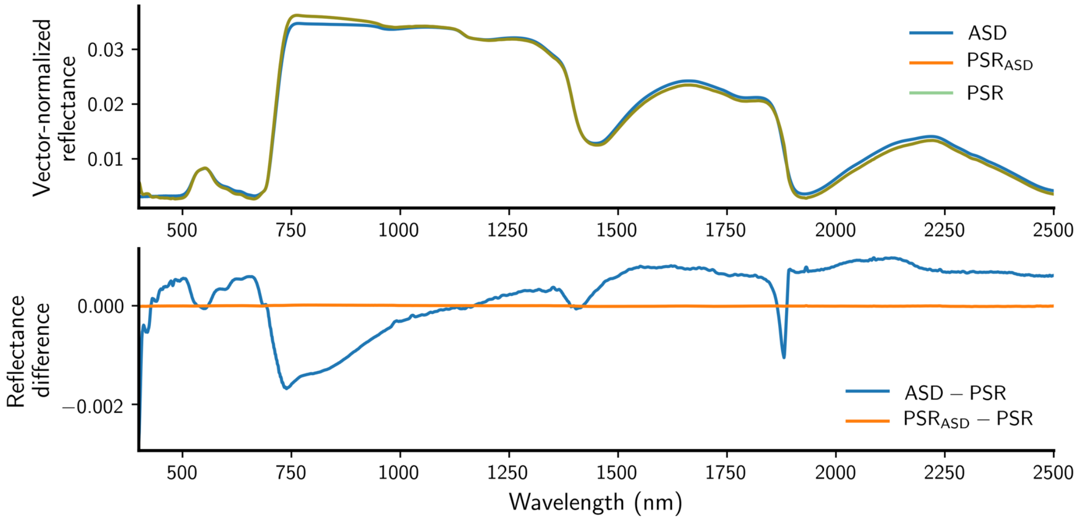

Figure 1.1 Results of ASD to PSR spectral transformation. Top: Average vector normalized reflectance spectra of validation dataset (n > 5,000), the PSR spectrum is displayed with transparency as not to obscure the transformed ASD spectrum (PSR$_{ASD}$). Bottom: Average difference in vector normalized reflectance between validation PSR spectra and ASD spectra before (ASD- PSR) and after (PSR$_{ASD}$ - PSR) the spectral transform was applied.

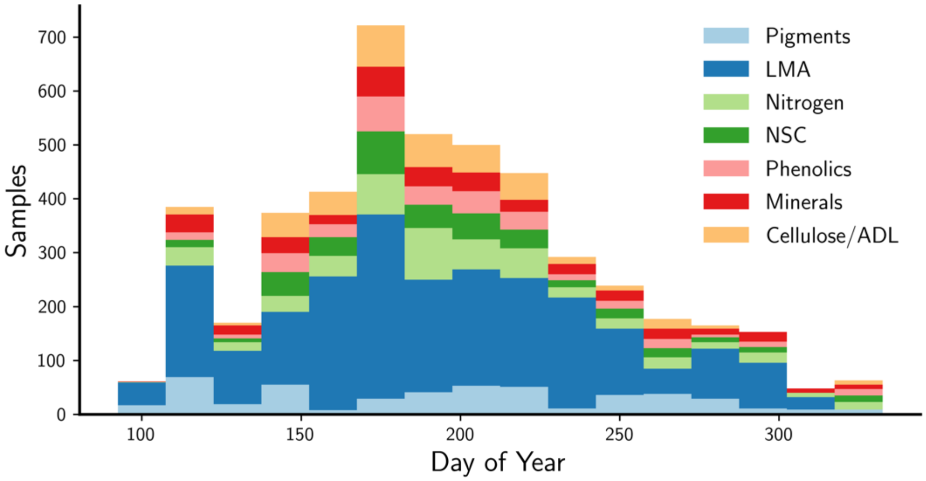

Figure 1.2 Temporal distribution of samples used in this study. Collection date of samples in last column is unknown

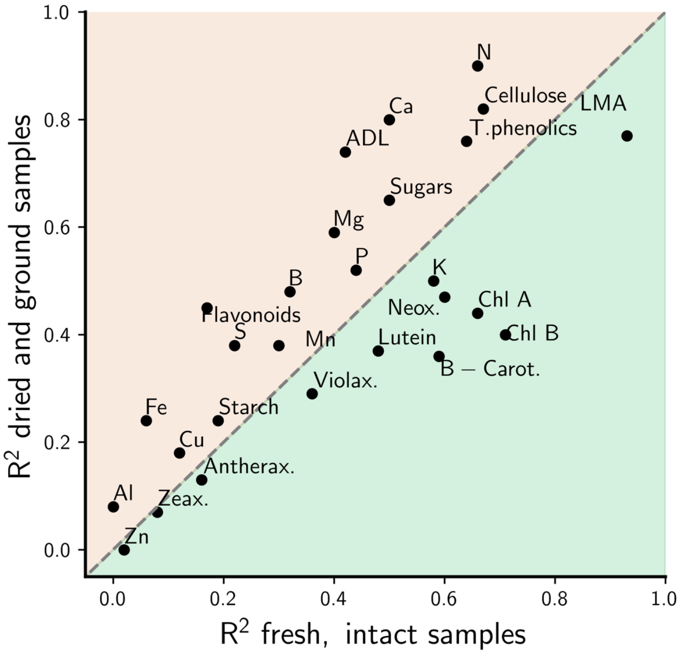

Figure 1.3 Comparison of fresh, whole leaf and dried and ground spectroscopic model performances (R^2). For each measurement type (fresh or dry) the model result from the top performing wavelength range (VNIR, SWIR or Full) is shown. Points in the green region indicate better performance using fresh spectra models and those in the orange region indicate better predictive performance using dry ground spectra

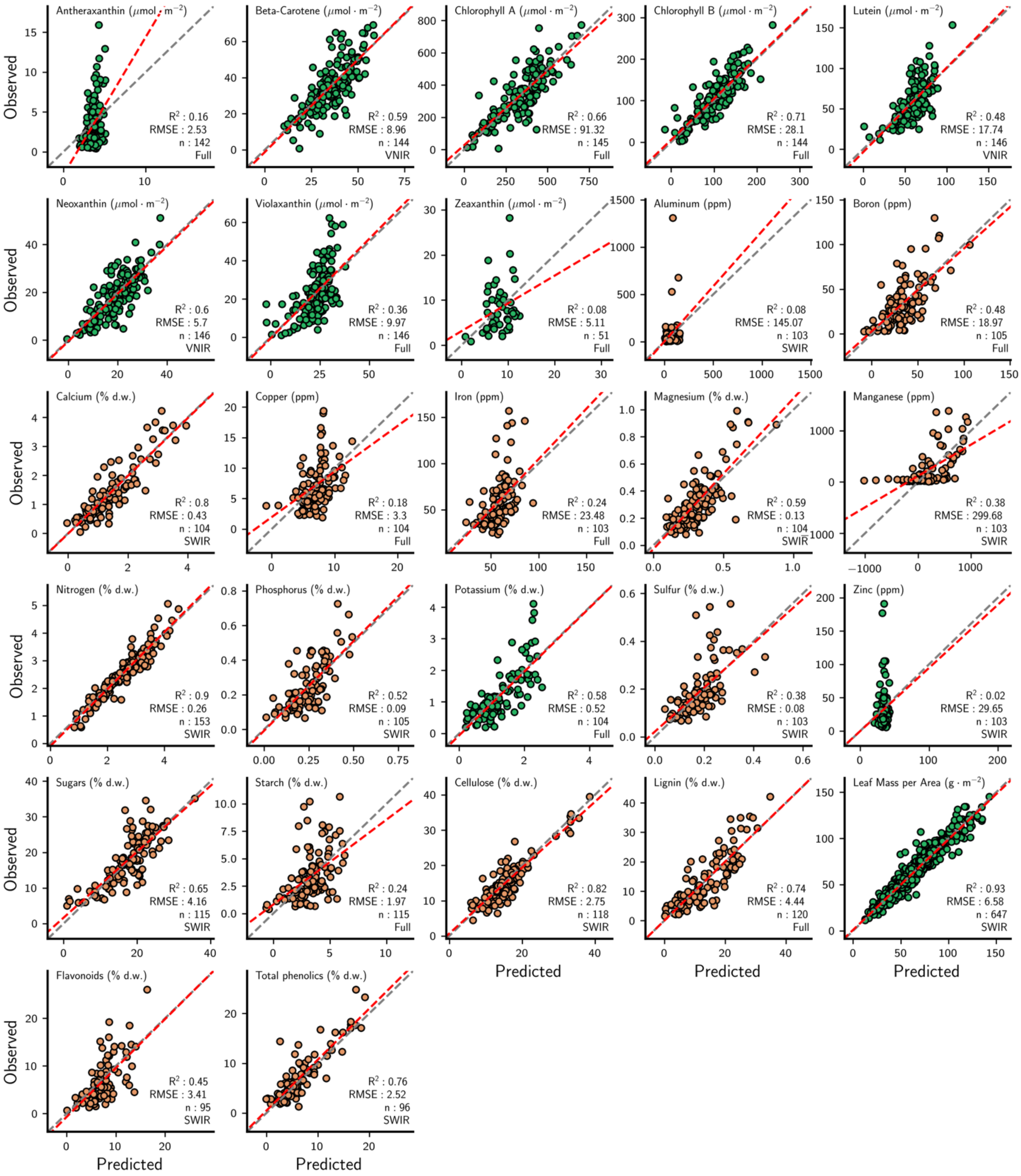

Figure 1.4 Independent validation scatterplots for top performing model for each trait. Green points indicate fresh leaf model and orange points indicate dry ground model. In each plot the wavelength range used in model building is listed in the lower right corner. Grey dashed lines are 1:1 lines, red dashed lines are linear fits between the predicted and observed values.

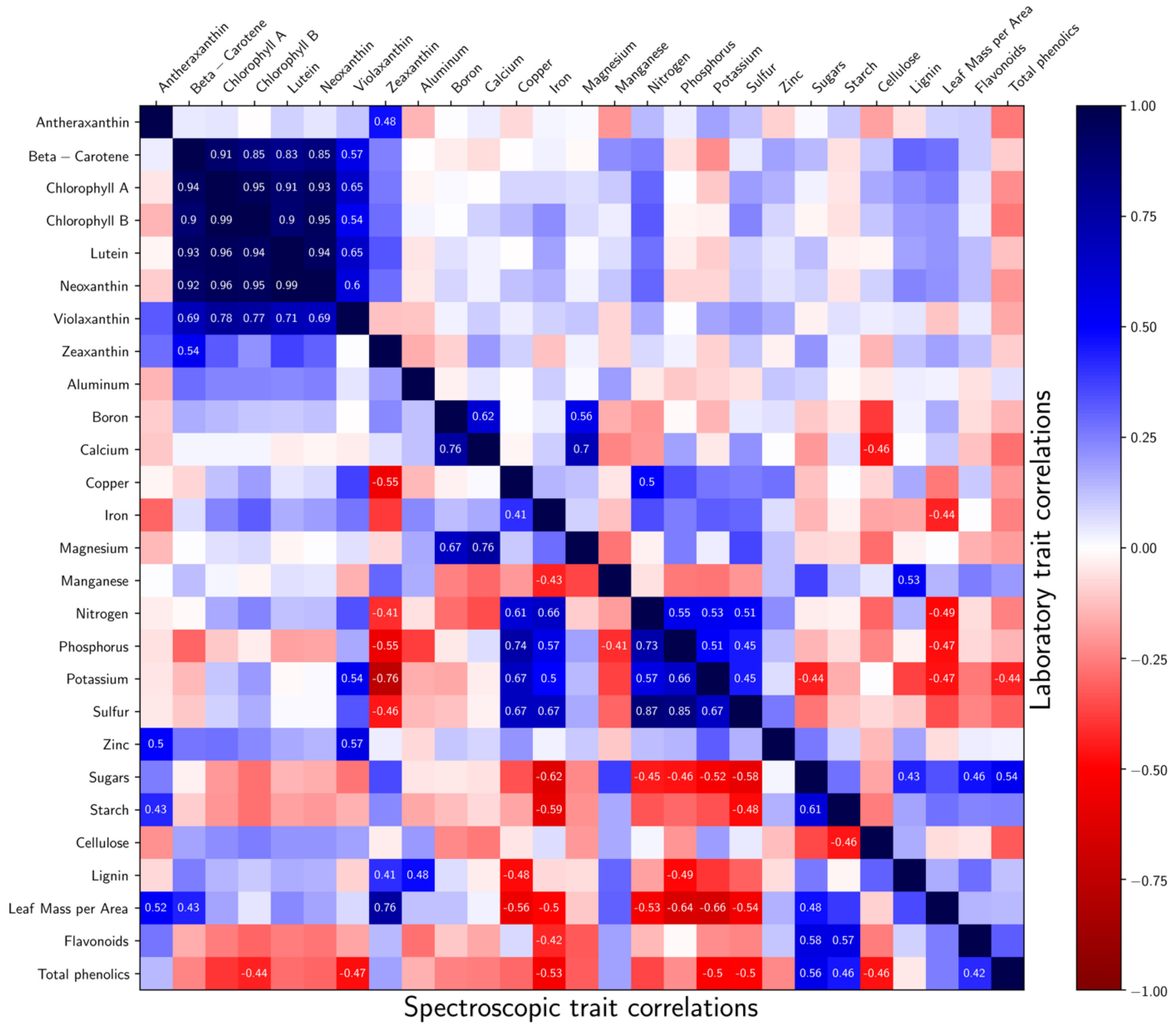

Figure 1.5 Pairwise trait correlation (Pearson's r) matrix. Upper diagonal: correlations between laboratory measured traits, only those pairs with greater than 10 common samples are shown. Lower diagonal: correlations between spectroscopically derived traits, best performing model for each trait was used for prediction (Figure 4). Labeled correlations indicate p <.01 and absolute r > 0.4.

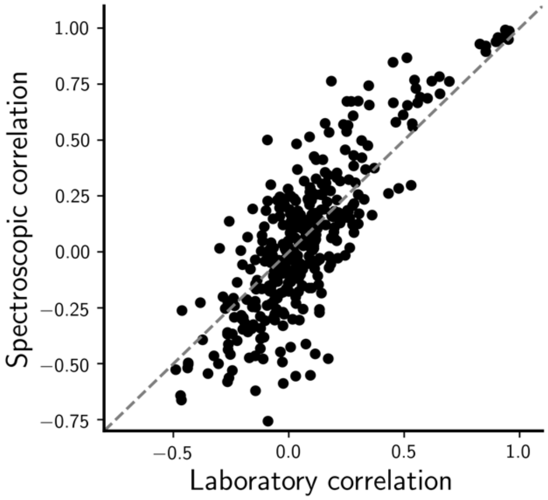

Figure 1.6 . Scatter plot between pairwise laboratory and spectroscopic trait correlations. Gray line indicates 1:1 line.

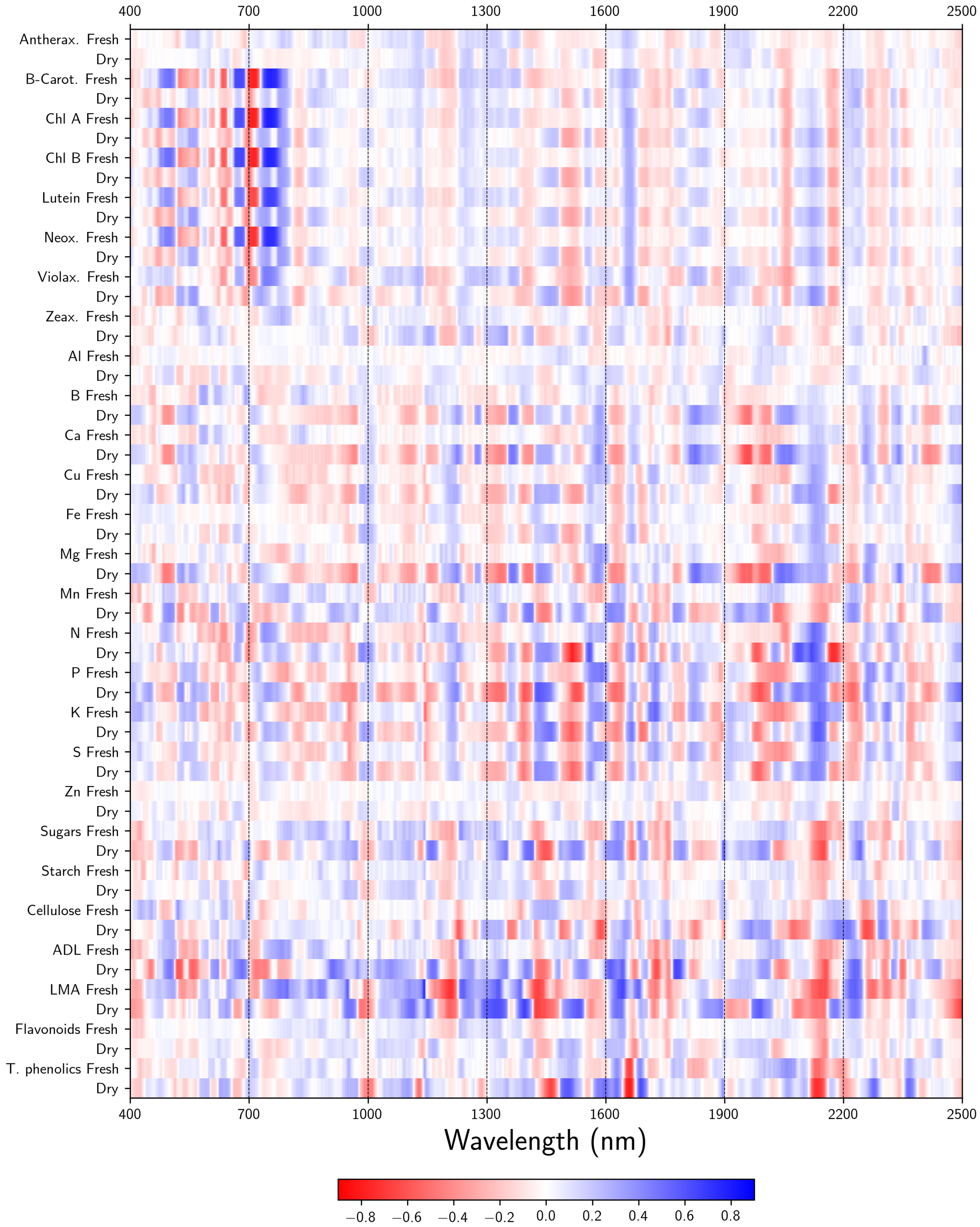

Figure 1.7 Correlation matrix showing mean wavelet correlations across all scales for each trait and spectral measurement type.

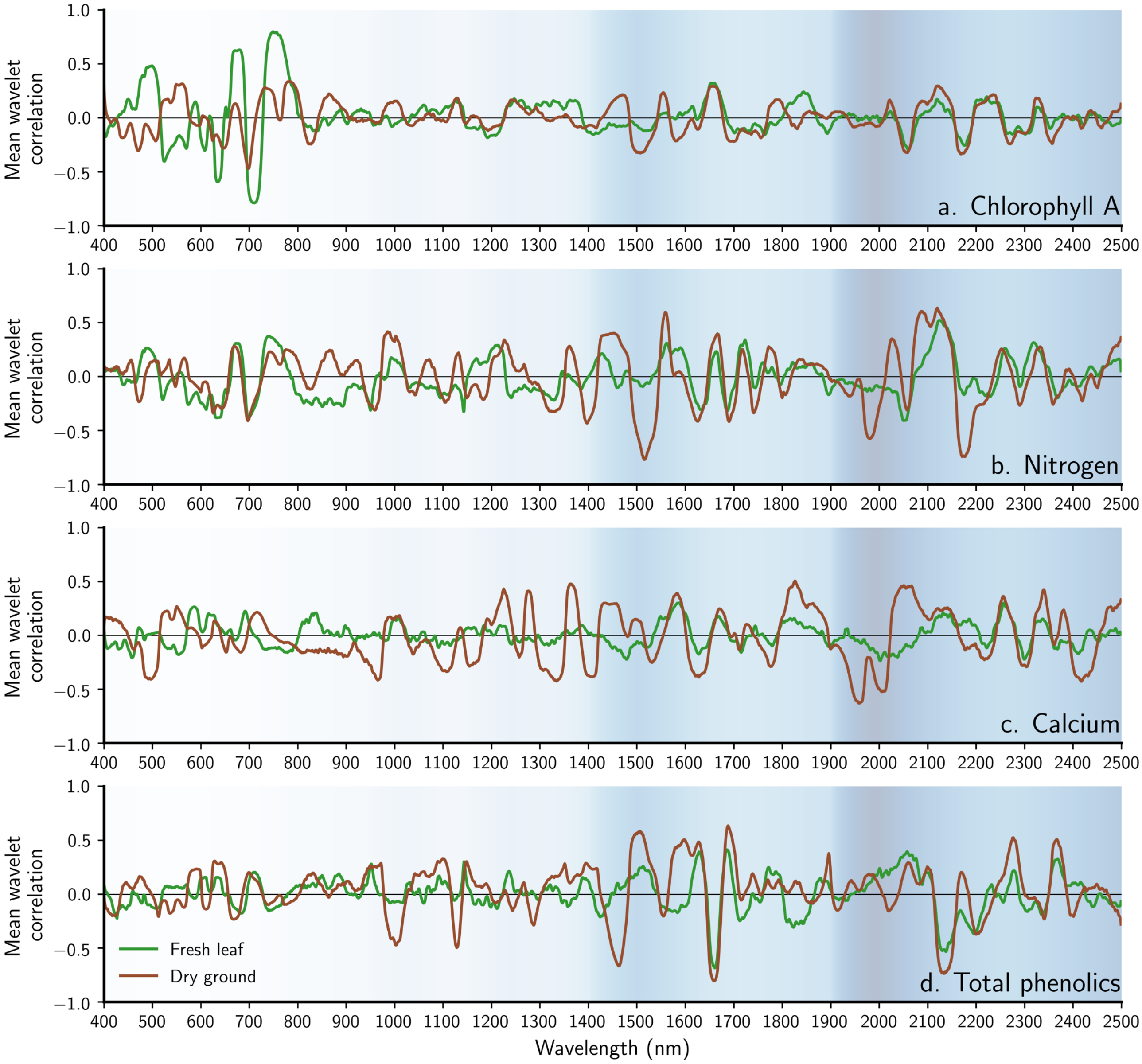

Figure 1.8 Mean wavelet correlation plots for fresh and dry ground spectra for four traits, chlorophyll A, nitrogen, calcium and total phenolics. Blue shading indicates relative intensity of water absorption at each wavelength, darker blue indicates high water absorption.

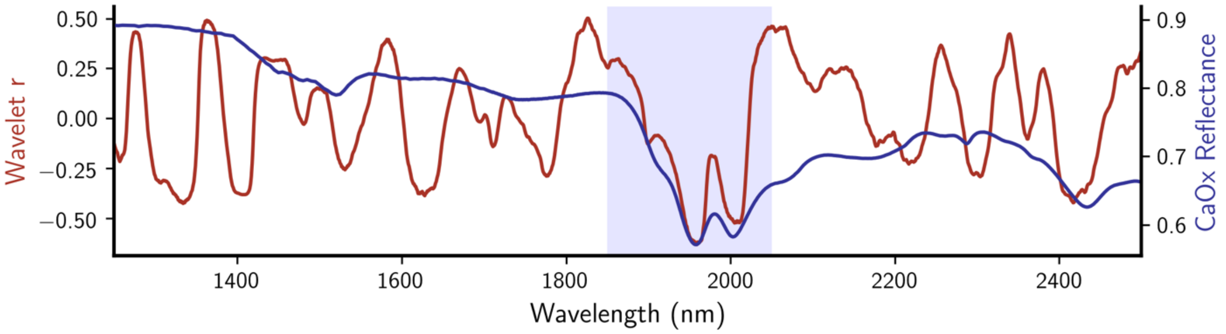

Figure 1.9 . Correlation between dry spectra wavelet features and calcium concentration (red) and calcium oxalate reflectance (blue). Calcium oxalate reflectance spectrum derived from Cloutis (2015).

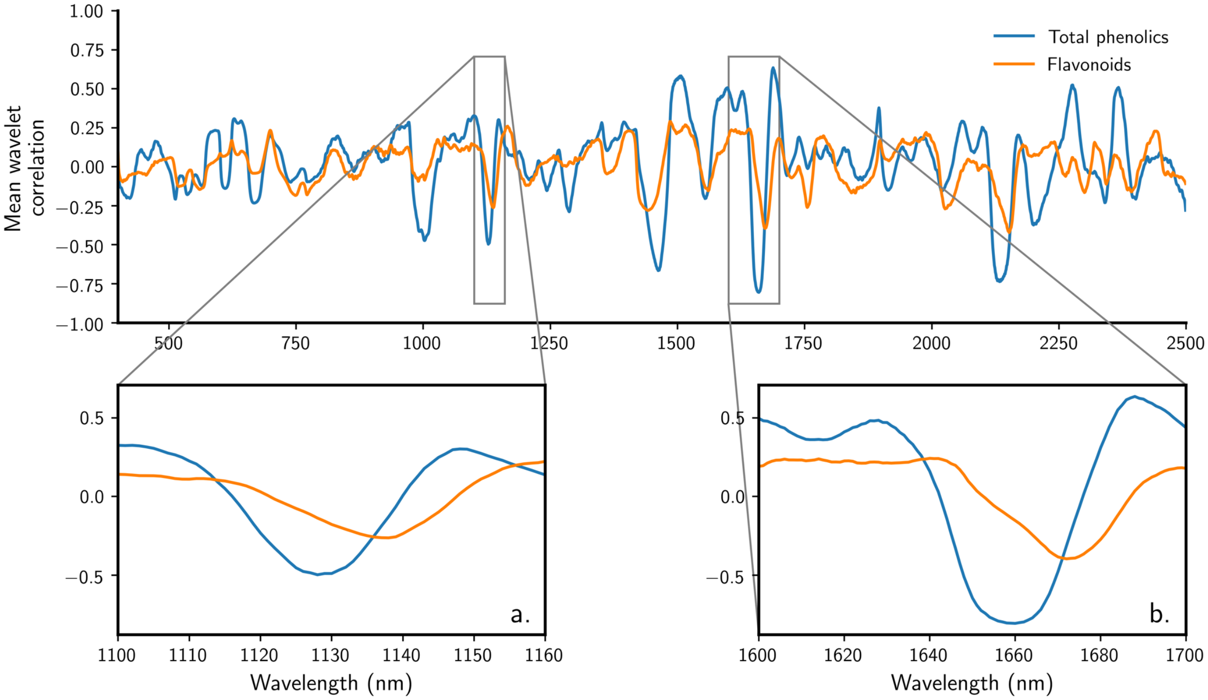

Figure 1.10 Comparison of mean wavelet correlation coefficients for total phenolics and flavonoids. Insets highlight the shift in wavelength of maximum correlation near 1130 nm (a) and 1660 nm (b), flavonoids are shifted approximately 10 nm towards longer wavelengths compared to total phenolics.

Supplemental materials

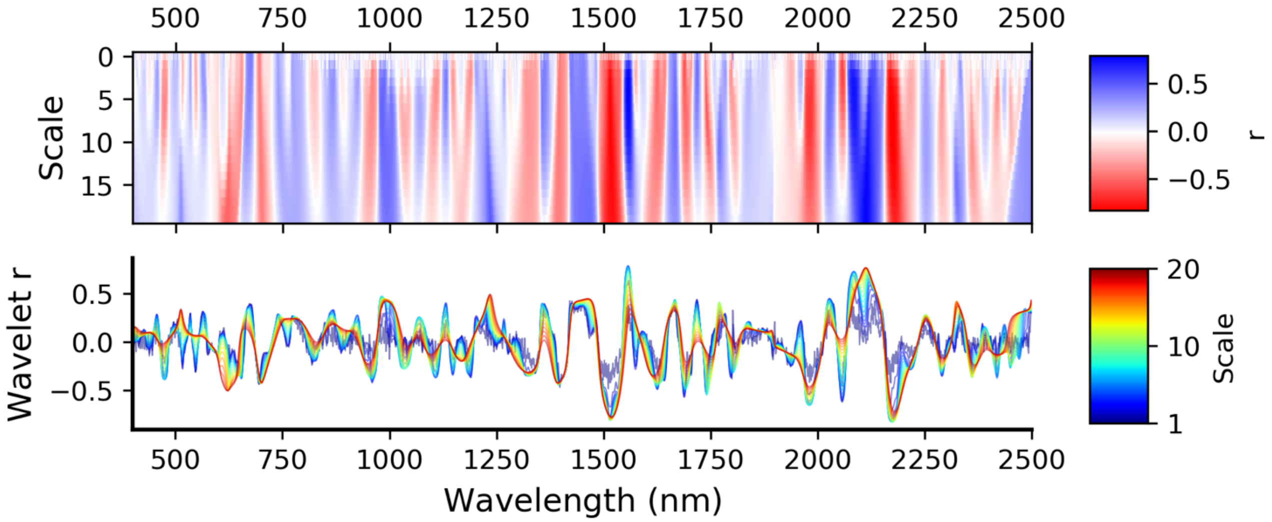

Figure S1.1 Comparison of typical two-dimensional representation of wavelet correlations (top) against one dimensional plot used in this analysis (bottom). Each line in the bottom plot represents a single scale.

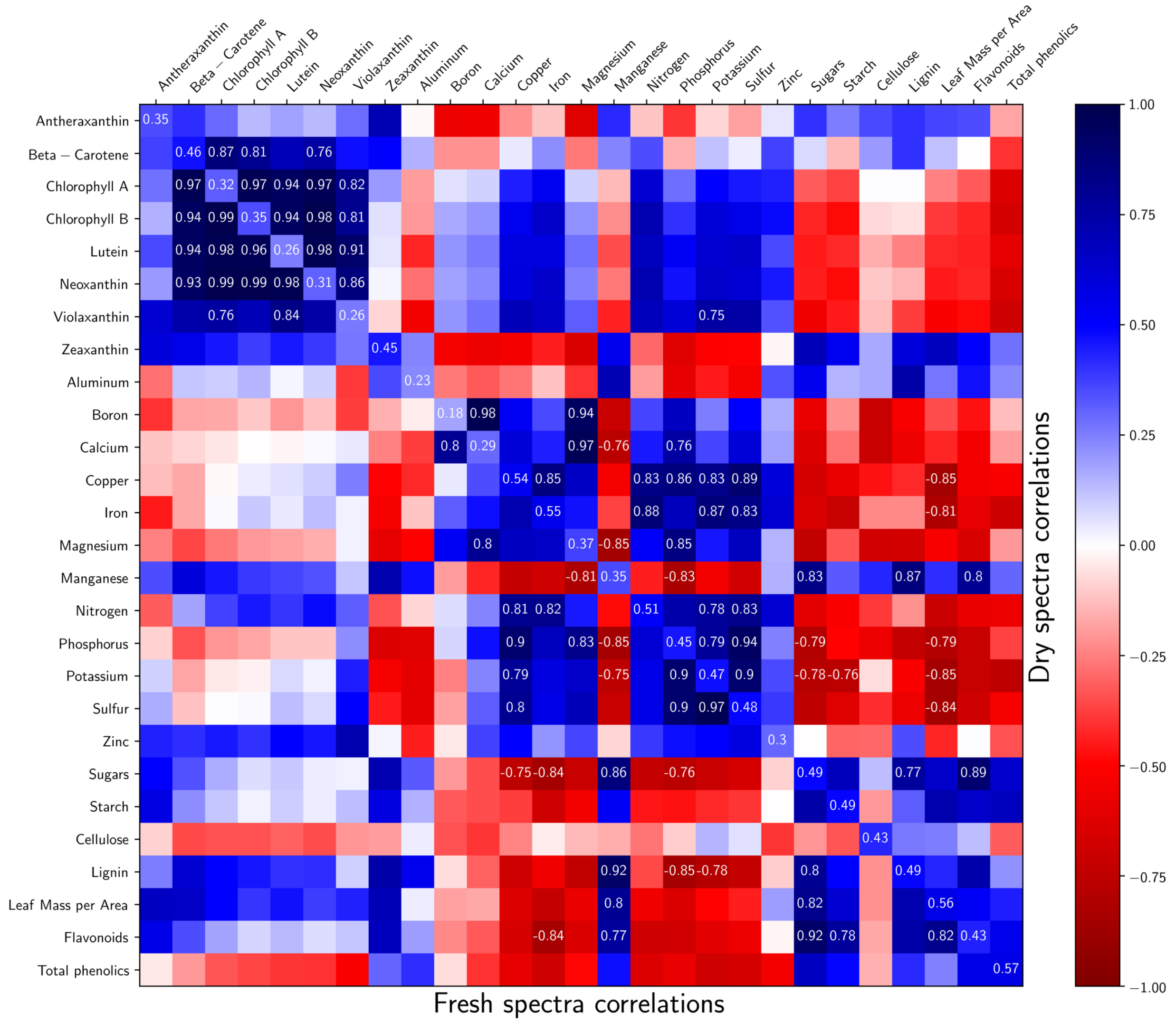

Figure S1.2 Pairwise wavelet correlation (Pearson's r) matrix.

Upper diagonal: correlations between mean dry spectra wavelet correlations. Lower diagonal: correlations between mean fresh spectra wavelet correlations. Diagonal displays correlation between mean wet and dry wavelet correlations between each trait. Labeled correlations indicate p <.01 and absolute r > 0.4. Higher correlations between traits indicate that the pair of traits share common wavelengths whose wavelet transforms correlate with biochemical traits. Strong negative correlations indicate that wavelengths with absorption features for one trait in the pair are matched by reflectance features in the other trait. For example, chlorophyll A and chlorophyll B correlate with nearly identical absorption and reflectance features in foliar spectra, while absorption features in LMA tend to correspond with reflectance features in phosphorus and vice versa.

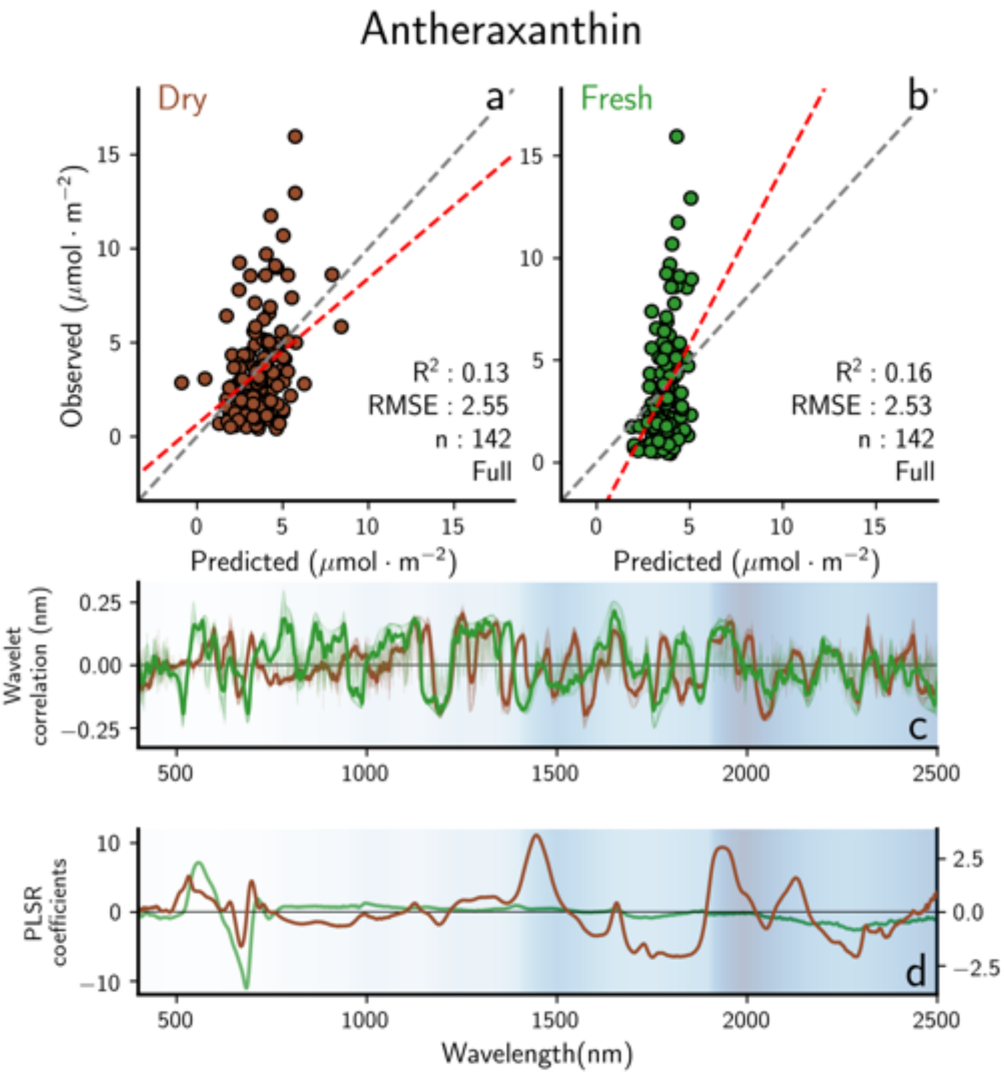

Figure S1.3 Antheraxanthin full results

a) Validation scatterplot and metrics for top performing dry spectra PLSR model. b) Validation scatterplot and metrics for top performing fresh spectra PLSR model. c) Wavelet feature correlation plots for fresh (green) and dry spectra (brown), solid lines indicate mean correlation across all wavelet scales, transparent lines show individual wavelet scales. Blue shading indicates the relative intensity of water absorption at each wavelength, darker blue indicates higher water absorption. The correlation values plotted on c) are the input to the summary plot in Figure 7. Wavelengths where the green and brown lines align indicate common spectral features identified in both fresh and dry spectra. The correlation between the y-axes (wavelet correlations) among all traits (Figures S1.2-S1.28) is the basis for Figure S1.1, with dry spectra (brown line across traits) in the upper diagonal and fresh spectra (green line across traits) in the lower diagonal of S1.1 d) PLSR coefficients for top performing fresh (green) and dry spectra (brown) models. PLSR coefficients cannot be directly compared to wavelet correlations because the number of components (Table 3) strongly influences PLSR. However, ideally, negative wavelet correlations should align with negative PLSR coefficients if an absorption feature associated with the trait is present.

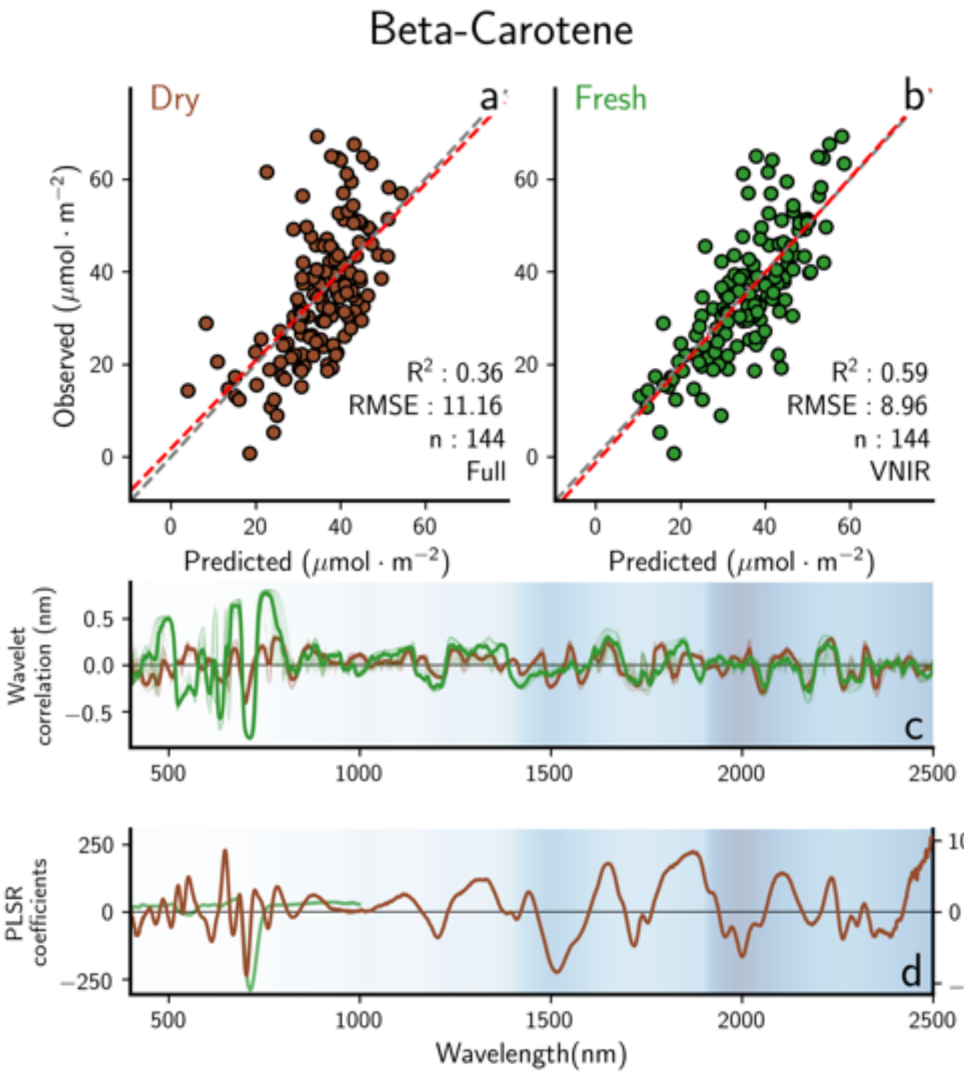

Figure S1.4 Beta-carotene full results

a) Validation scatterplot and metrics for top performing dry spectra PLSR model. b) Validation scatterplot and metrics for top performing fresh spectra PLSR model. c) Wavelet feature correlation plots for fresh (green) and dry spectra (brown), solid lines indicate mean correlation across all wavelet scales, transparent lines show individual wavelet scales. Blue shading indicates the relative intensity of water absorption at each wavelength, darker blue indicates higher water absorption. The correlation values plotted on c) are the input to the summary plot in Figure 7. Wavelengths where the green and brown lines align indicate common spectral features identified in both fresh and dry spectra. The correlation between the y-axes (wavelet correlations) among all traits (Figures S1.2-S1.28) is the basis for Figure S1.1, with dry spectra (brown line across traits) in the upper diagonal and fresh spectra (green line across traits) in the lower diagonal of S1.1 d) PLSR coefficients for top performing fresh (green) and dry spectra (brown) models. PLSR coefficients cannot be directly compared to wavelet correlations because the number of components (Table 3) strongly influences PLSR. However, ideally, negative wavelet correlations should align with negative PLSR coefficients if an absorption feature associated with the trait is present.

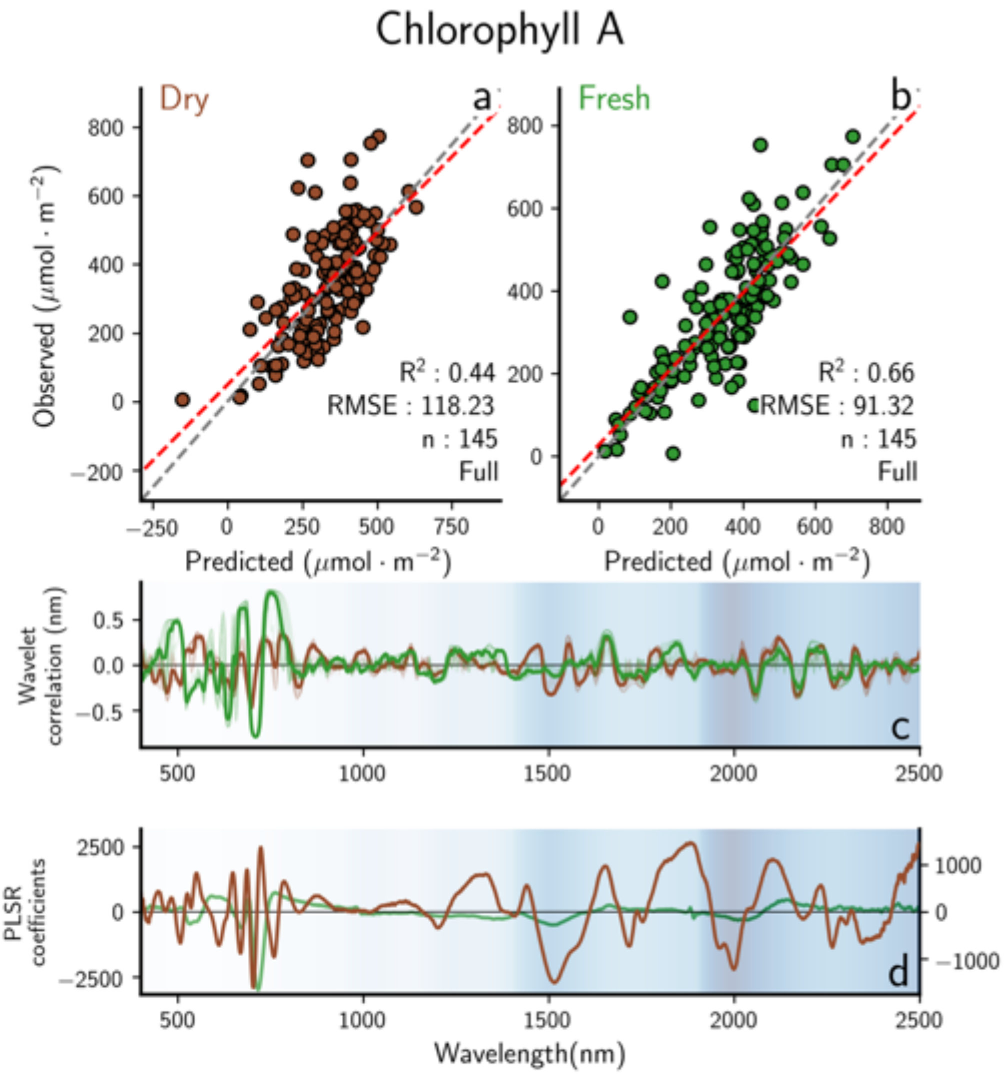

Figure S1.5 Chlorophyll A full results

a) Validation scatterplot and metrics for top performing dry spectra PLSR model. b) Validation scatterplot and metrics for top performing fresh spectra PLSR model. c) Wavelet feature correlation plots for fresh (green) and dry spectra (brown), solid lines indicate mean correlation across all wavelet scales, transparent lines show individual wavelet scales. Blue shading indicates the relative intensity of water absorption at each wavelength, darker blue indicates higher water absorption. The correlation values plotted on c) are the input to the summary plot in Figure 7. Wavelengths where the green and brown lines align indicate common spectral features identified in both fresh and dry spectra. The correlation between the y-axes (wavelet correlations) among all traits (Figures S1.2-S1.28) is the basis for Figure S1.1, with dry spectra (brown line across traits) in the upper diagonal and fresh spectra (green line across traits) in the lower diagonal of S1.1 d) PLSR coefficients for top performing fresh (green) and dry spectra (brown) models. PLSR coefficients cannot be directly compared to wavelet correlations because the number of components (Table 3) strongly influences PLSR. However, ideally, negative wavelet correlations should align with negative PLSR coefficients if an absorption feature associated with the trait is present.

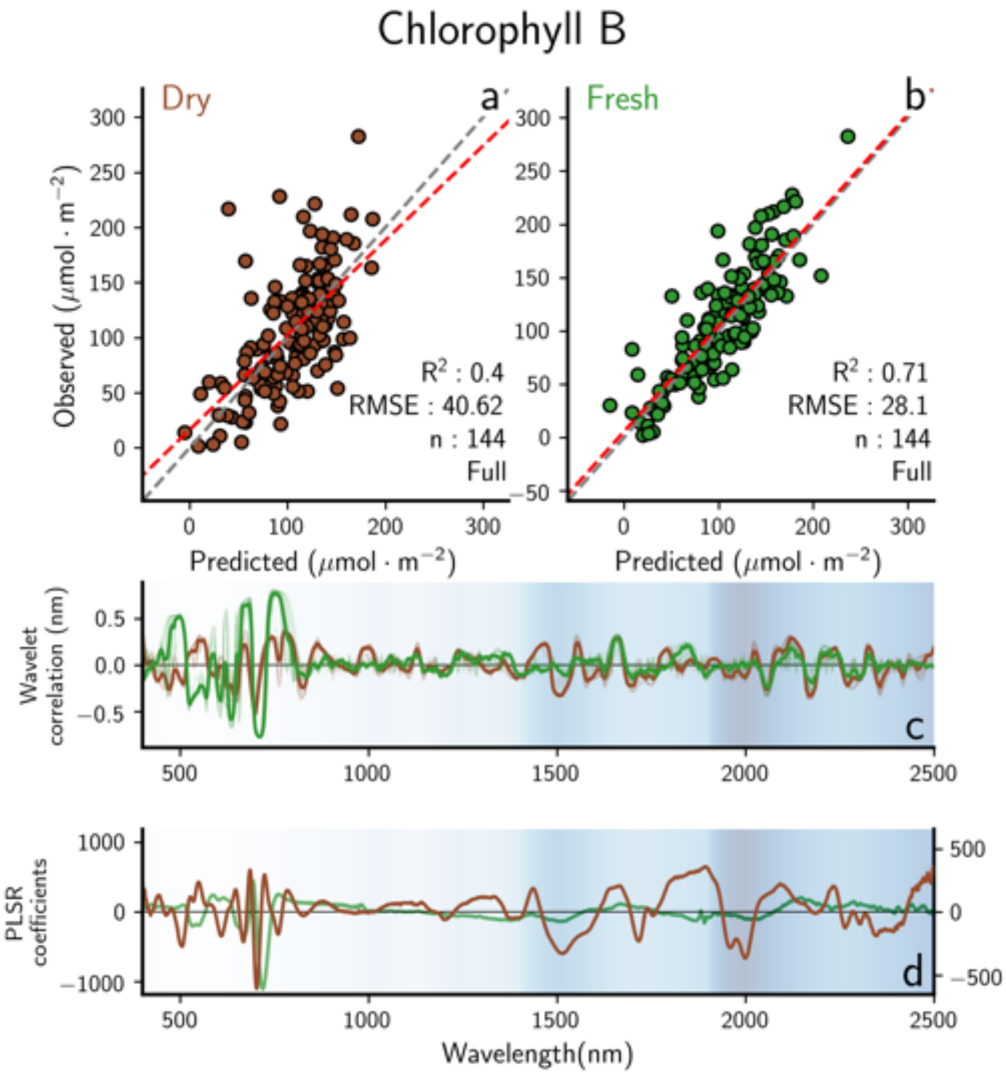

Figure S1.6 Chlorophyll B full results

a) Validation scatterplot and metrics for top performing dry spectra PLSR model. b) Validation scatterplot and metrics for top performing fresh spectra PLSR model. c) Wavelet feature correlation plots for fresh (green) and dry spectra (brown), solid lines indicate mean correlation across all wavelet scales, transparent lines show individual wavelet scales. Blue shading indicates the relative intensity of water absorption at each wavelength, darker blue indicates higher water absorption. The correlation values plotted on c) are the input to the summary plot in Figure 7. Wavelengths where the green and brown lines align indicate common spectral features identified in both fresh and dry spectra. The correlation between the y-axes (wavelet correlations) among all traits (Figures S1.2-S1.28) is the basis for Figure S1.1, with dry spectra (brown line across traits) in the upper diagonal and fresh spectra (green line across traits) in the lower diagonal of S1.1 d) PLSR coefficients for top performing fresh (green) and dry spectra (brown) models. PLSR coefficients cannot be directly compared to wavelet correlations because the number of components (Table 3) strongly influences PLSR. However, ideally, negative wavelet correlations should align with negative PLSR coefficients if an absorption feature associated with the trait is present.

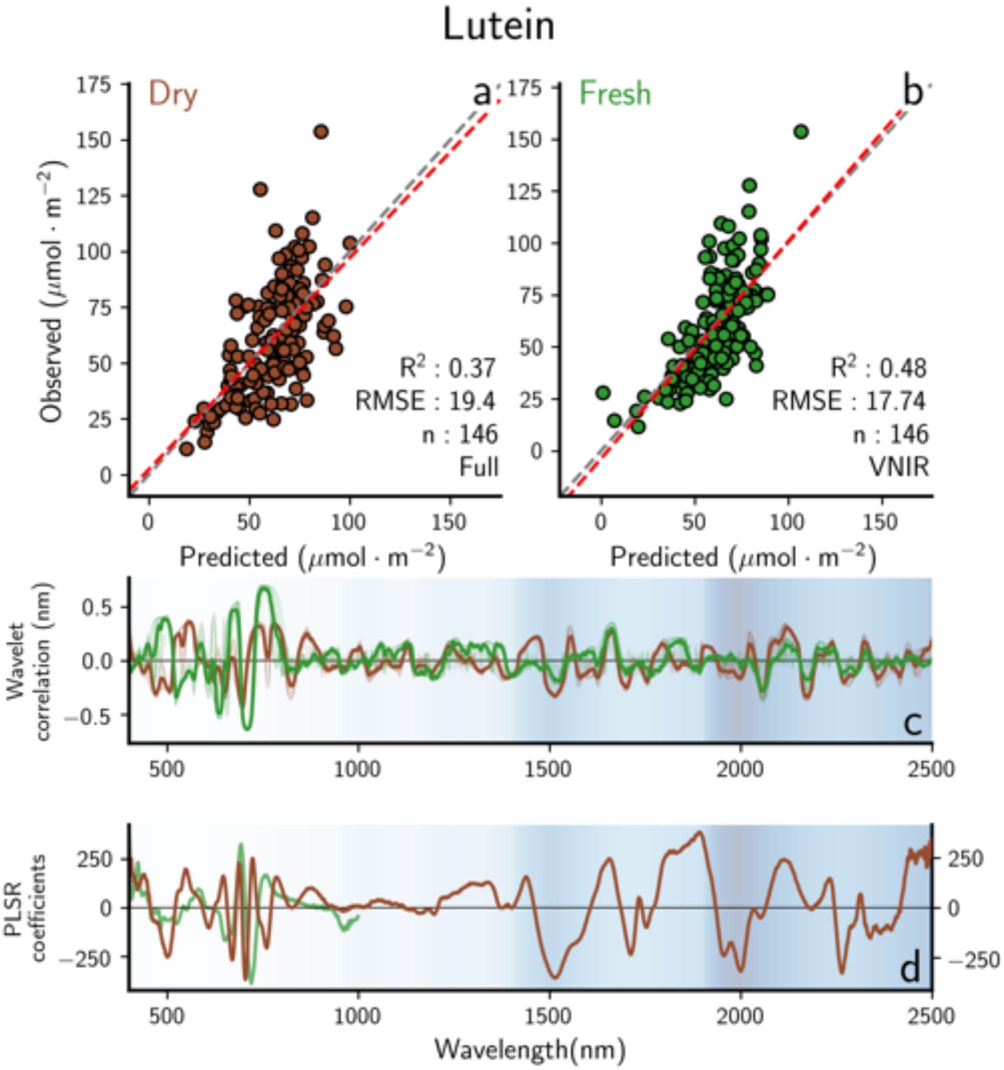

Figure S1.7 Lutein full results

a) Validation scatterplot and metrics for top performing dry spectra PLSR model. b) Validation scatterplot and metrics for top performing fresh spectra PLSR model. c) Wavelet feature correlation plots for fresh (green) and dry spectra (brown), solid lines indicate mean correlation across all wavelet scales, transparent lines show individual wavelet scales. Blue shading indicates the relative intensity of water absorption at each wavelength, darker blue indicates higher water absorption. The correlation values plotted on c) are the input to the summary plot in Figure 7. Wavelengths where the green and brown lines align indicate common spectral features identified in both fresh and dry spectra. The correlation between the y-axes (wavelet correlations) among all traits (Figures S1.2-S1.28) is the basis for Figure S1.1, with dry spectra (brown line across traits) in the upper diagonal and fresh spectra (green line across traits) in the lower diagonal of S1.1 d) PLSR coefficients for top performing fresh (green) and dry spectra (brown) models. PLSR coefficients cannot be directly compared to wavelet correlations because the number of components (Table 3) strongly influences PLSR. However, ideally, negative wavelet correlations should align with negative PLSR coefficients if an absorption feature associated with the trait is present.

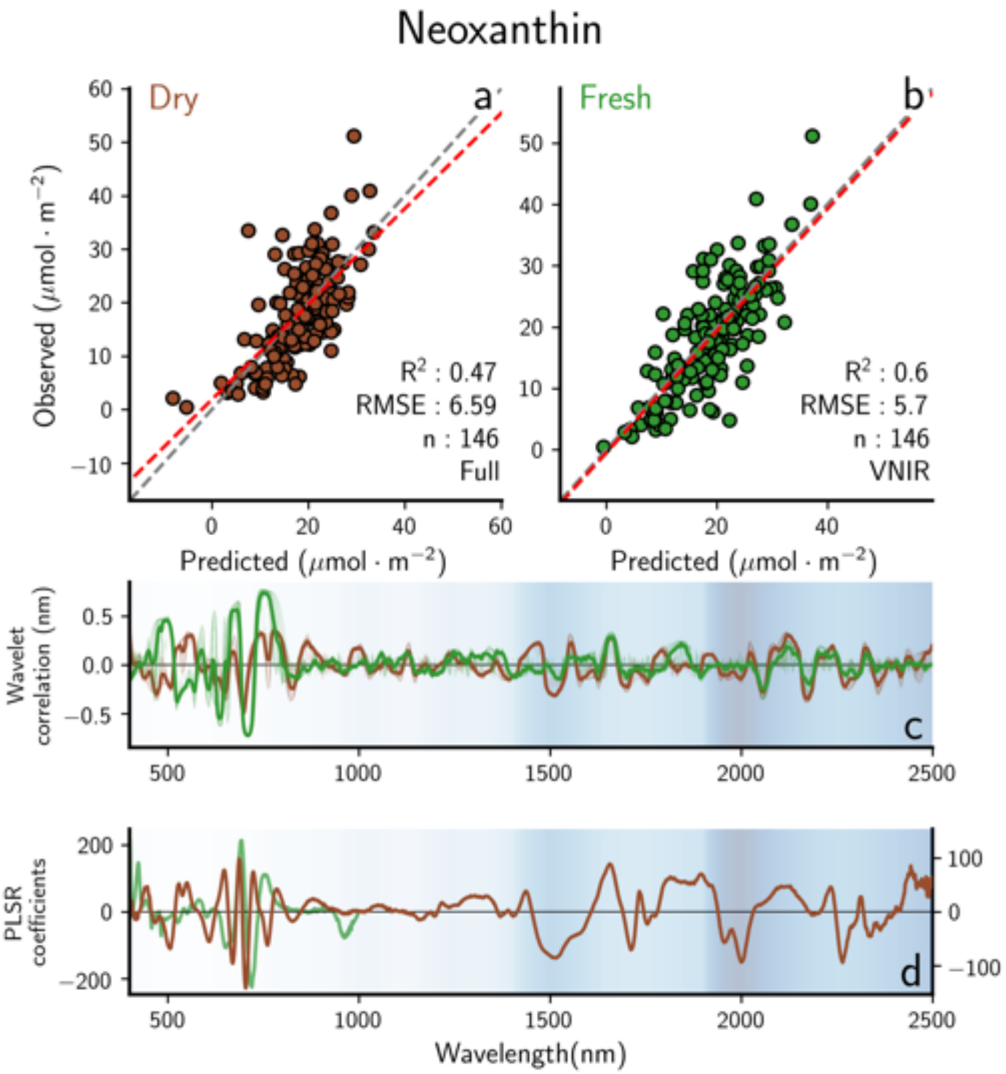

Figure S1.8 Neoxanthin full results

a) Validation scatterplot and metrics for top performing dry spectra PLSR model. b) Validation scatterplot and metrics for top performing fresh spectra PLSR model. c) Wavelet feature correlation plots for fresh (green) and dry spectra (brown), solid lines indicate mean correlation across all wavelet scales, transparent lines show individual wavelet scales. Blue shading indicates the relative intensity of water absorption at each wavelength, darker blue indicates higher water absorption. The correlation values plotted on c) are the input to the summary plot in Figure 7. Wavelengths where the green and brown lines align indicate common spectral features identified in both fresh and dry spectra. The correlation between the y-axes (wavelet correlations) among all traits (Figures S1.2-S1.28) is the basis for Figure S1.1, with dry spectra (brown line across traits) in the upper diagonal and fresh spectra (green line across traits) in the lower diagonal of S1.1 d) PLSR coefficients for top performing fresh (green) and dry spectra (brown) models. PLSR coefficients cannot be directly compared to wavelet correlations because the number of components (Table 3) strongly influences PLSR. However, ideally, negative wavelet correlations should align with negative PLSR coefficients if an absorption feature associated with the trait is present.

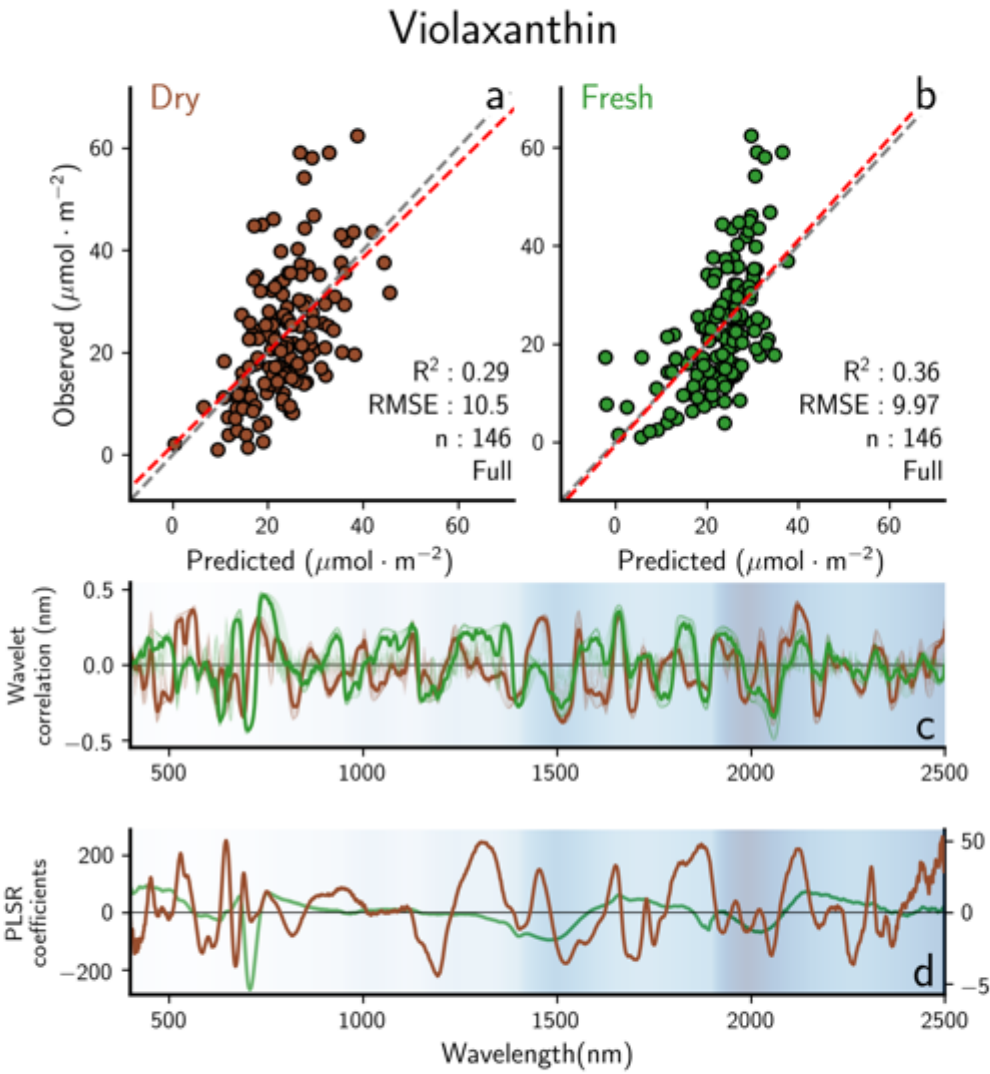

Figure S1.9 Violaxanthin full results

a) Validation scatterplot and metrics for top performing dry spectra PLSR model. b) Validation scatterplot and metrics for top performing fresh spectra PLSR model. c) Wavelet feature correlation plots for fresh (green) and dry spectra (brown), solid lines indicate mean correlation across all wavelet scales, transparent lines show individual wavelet scales. Blue shading indicates the relative intensity of water absorption at each wavelength, darker blue indicates higher water absorption. The correlation values plotted on c) are the input to the summary plot in Figure 7. Wavelengths where the green and brown lines align indicate common spectral features identified in both fresh and dry spectra. The correlation between the y-axes (wavelet correlations) among all traits (Figures S1.2-S1.28) is the basis for Figure S1.1, with dry spectra (brown line across traits) in the upper diagonal and fresh spectra (green line across traits) in the lower diagonal of S1.1 d) PLSR coefficients for top performing fresh (green) and dry spectra (brown) models. PLSR coefficients cannot be directly compared to wavelet correlations because the number of components (Table 3) strongly influences PLSR. However, ideally, negative wavelet correlations should align with negative PLSR coefficients if an absorption feature associated with the trait is present.

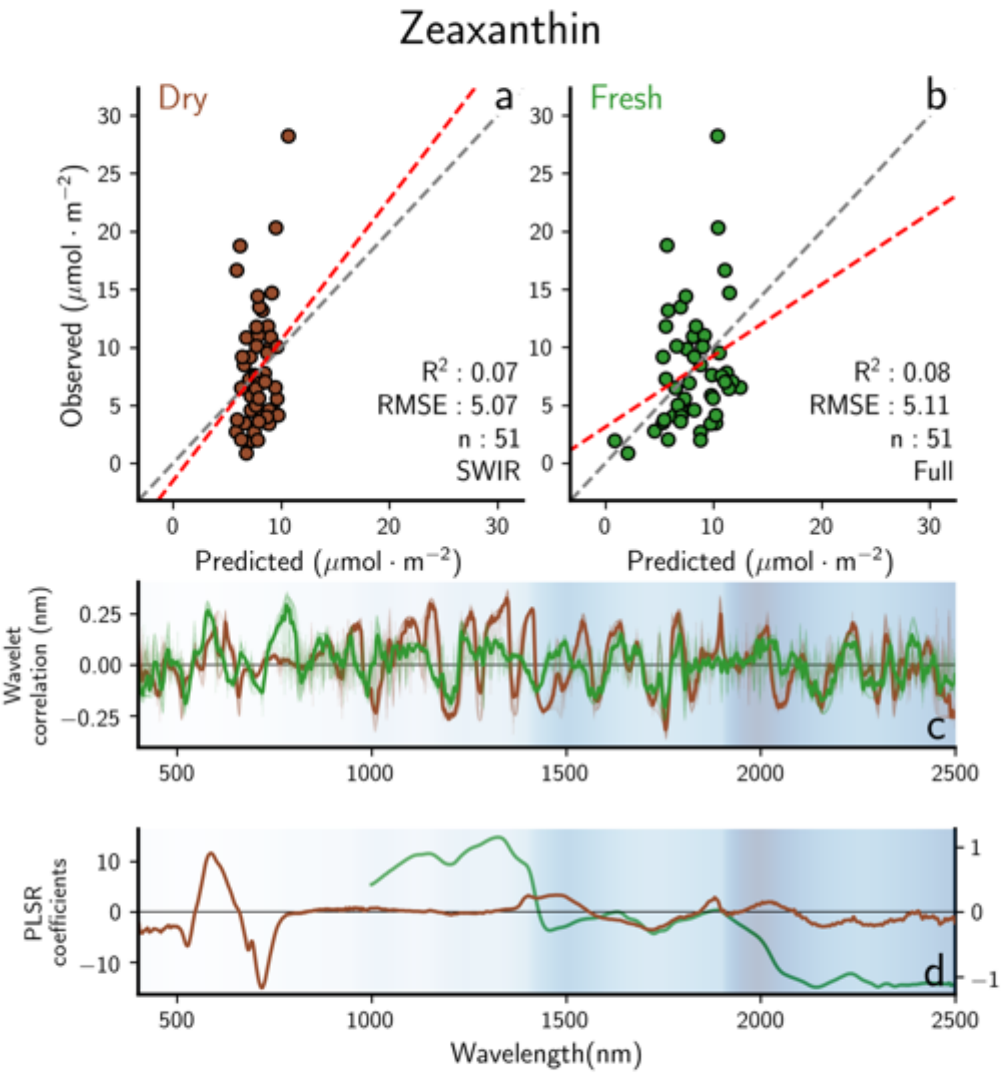

Figure S1.10 Zeaxanthin full results

a) Validation scatterplot and metrics for top performing dry spectra PLSR model. b) Validation scatterplot and metrics for top performing fresh spectra PLSR model. c) Wavelet feature correlation plots for fresh (green) and dry spectra (brown), solid lines indicate mean correlation across all wavelet scales, transparent lines show individual wavelet scales. Blue shading indicates the relative intensity of water absorption at each wavelength, darker blue indicates higher water absorption. The correlation values plotted on c) are the input to the summary plot in Figure 7. Wavelengths where the green and brown lines align indicate common spectral features identified in both fresh and dry spectra. The correlation between the y-axes (wavelet correlations) among all traits (Figures S1.2-S1.28) is the basis for Figure S1.1, with dry spectra (brown line across traits) in the upper diagonal and fresh spectra (green line across traits) in the lower diagonal of S1.1 d) PLSR coefficients for top performing fresh (green) and dry spectra (brown) models. PLSR coefficients cannot be directly compared to wavelet correlations because the number of components (Table 3) strongly influences PLSR. However, ideally, negative wavelet correlations should align with negative PLSR coefficients if an absorption feature associated with the trait is present.

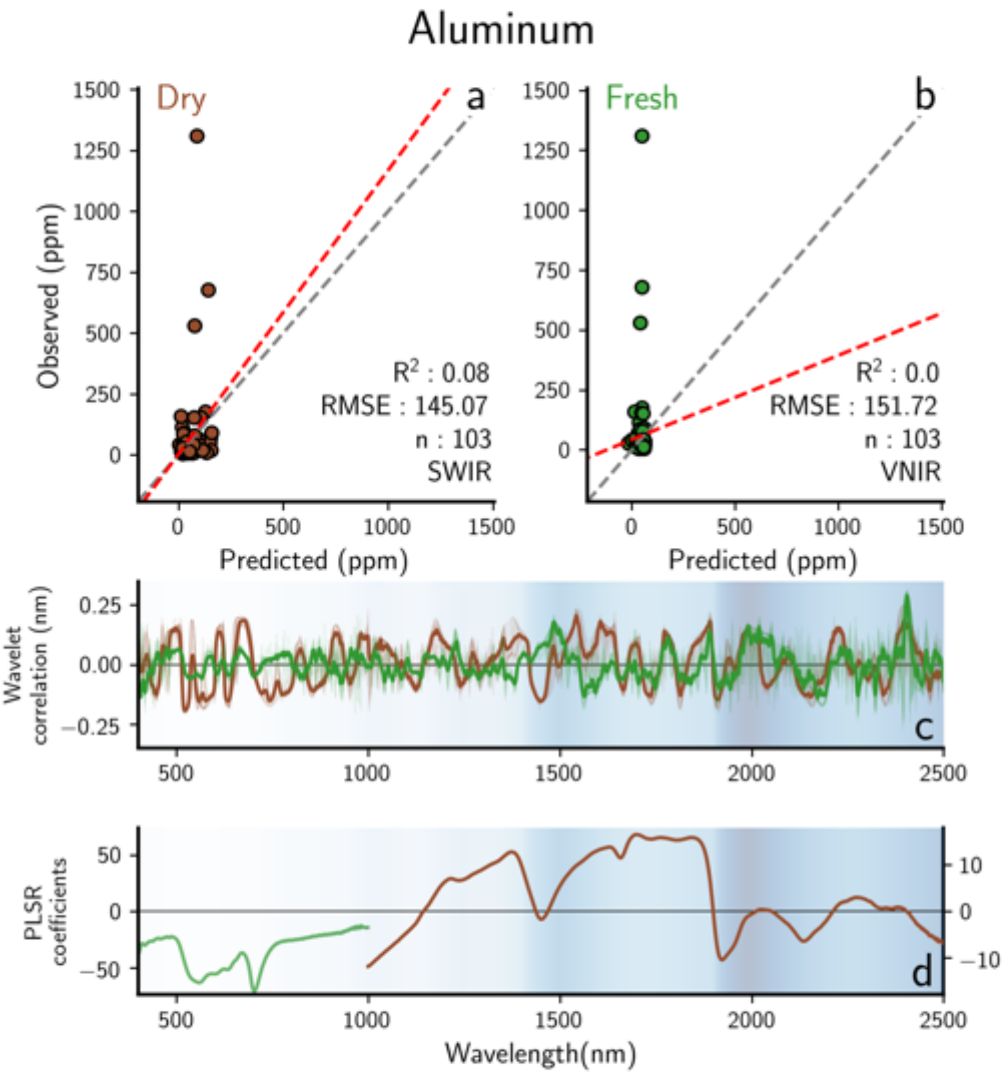

Figure S1.11 Aluminum full results

a) Validation scatterplot and metrics for top performing dry spectra PLSR model. b) Validation scatterplot and metrics for top performing fresh spectra PLSR model. c) Wavelet feature correlation plots for fresh (green) and dry spectra (brown), solid lines indicate mean correlation across all wavelet scales, transparent lines show individual wavelet scales. Blue shading indicates the relative intensity of water absorption at each wavelength, darker blue indicates higher water absorption. The correlation values plotted on c) are the input to the summary plot in Figure 7. Wavelengths where the green and brown lines align indicate common spectral features identified in both fresh and dry spectra. The correlation between the y-axes (wavelet correlations) among all traits (Figures S1.2-S1.28) is the basis for Figure S1.1, with dry spectra (brown line across traits) in the upper diagonal and fresh spectra (green line across traits) in the lower diagonal of S1.1 d) PLSR coefficients for top performing fresh (green) and dry spectra (brown) models. PLSR coefficients cannot be directly compared to wavelet correlations because the number of components (Table 3) strongly influences PLSR. However, ideally, negative wavelet correlations should align with negative PLSR coefficients if an absorption feature associated with the trait is present.

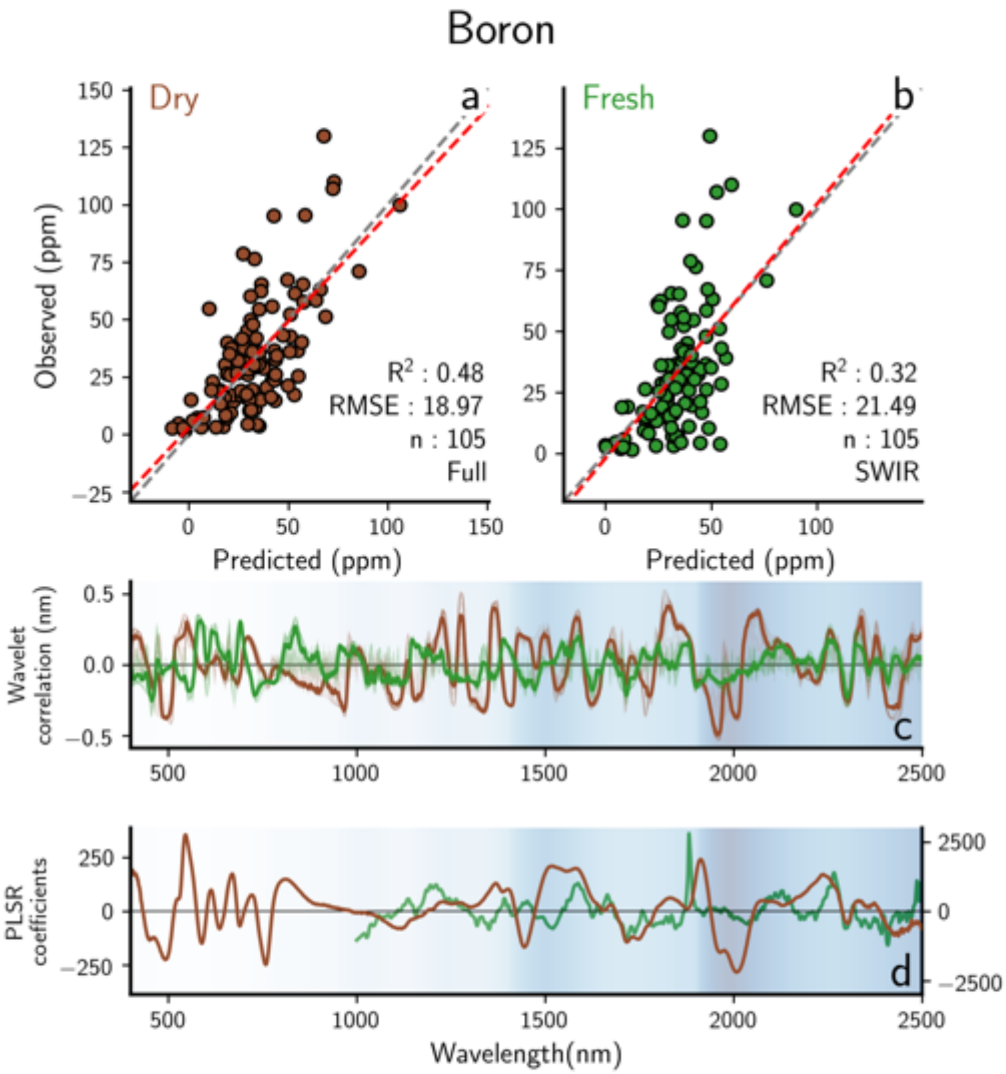

Figure S1.12 Boron full results

a) Validation scatterplot and metrics for top performing dry spectra PLSR model. b) Validation scatterplot and metrics for top performing fresh spectra PLSR model. c) Wavelet feature correlation plots for fresh (green) and dry spectra (brown), solid lines indicate mean correlation across all wavelet scales, transparent lines show individual wavelet scales. Blue shading indicates the relative intensity of water absorption at each wavelength, darker blue indicates higher water absorption. The correlation values plotted on c) are the input to the summary plot in Figure 7. Wavelengths where the green and brown lines align indicate common spectral features identified in both fresh and dry spectra. The correlation between the y-axes (wavelet correlations) among all traits (Figures S1.2-S1.28) is the basis for Figure S1.1, with dry spectra (brown line across traits) in the upper diagonal and fresh spectra (green line across traits) in the lower diagonal of S1.1 d) PLSR coefficients for top performing fresh (green) and dry spectra (brown) models. PLSR coefficients cannot be directly compared to wavelet correlations because the number of components (Table 3) strongly influences PLSR. However, ideally, negative wavelet correlations should align with negative PLSR coefficients if an absorption feature associated with the trait is present.

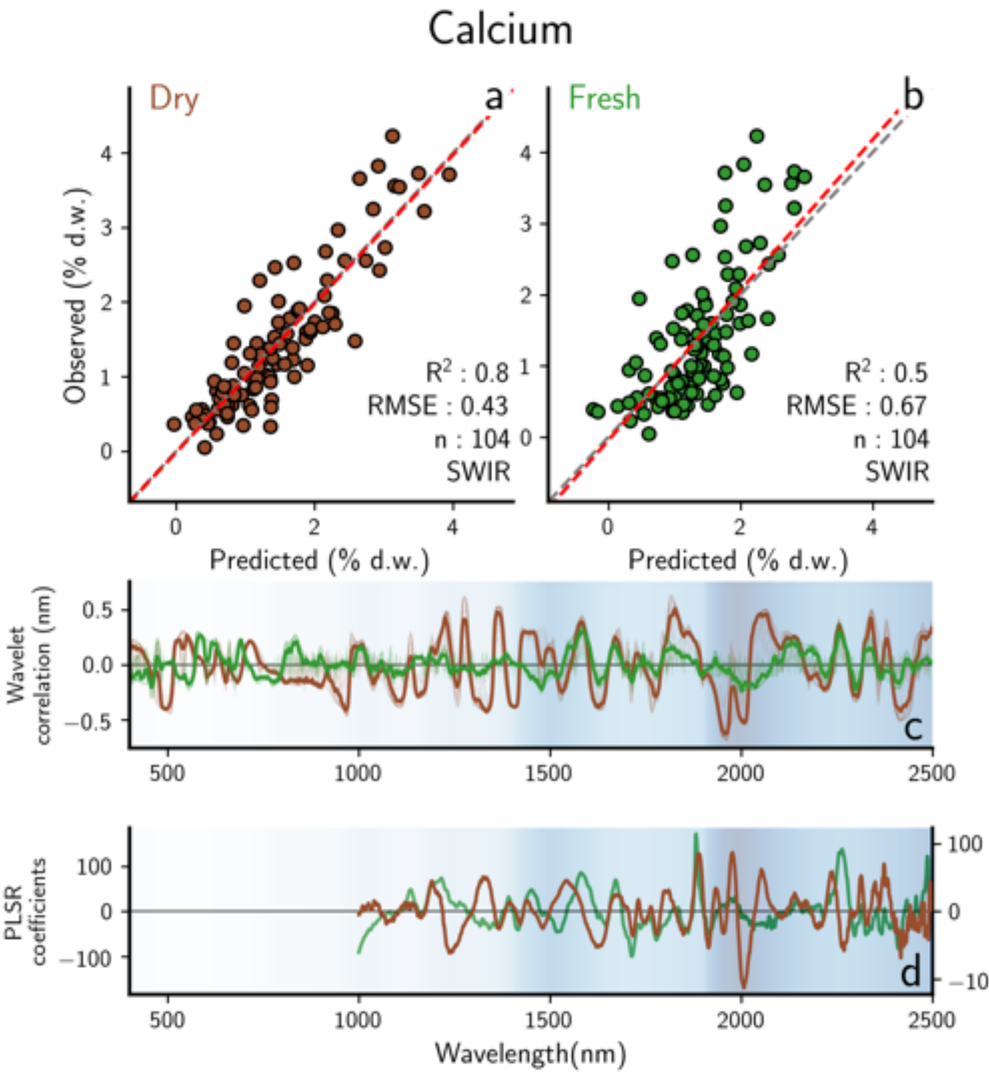

Figure S1.13 Calcium full results

a) Validation scatterplot and metrics for top performing dry spectra PLSR model. b) Validation scatterplot and metrics for top performing fresh spectra PLSR model. c) Wavelet feature correlation plots for fresh (green) and dry spectra (brown), solid lines indicate mean correlation across all wavelet scales, transparent lines show individual wavelet scales. Blue shading indicates the relative intensity of water absorption at each wavelength, darker blue indicates higher water absorption. The correlation values plotted on c) are the input to the summary plot in Figure 7. Wavelengths where the green and brown lines align indicate common spectral features identified in both fresh and dry spectra. The correlation between the y-axes (wavelet correlations) among all traits (Figures S1.2-S1.28) is the basis for Figure S1.1, with dry spectra (brown line across traits) in the upper diagonal and fresh spectra (green line across traits) in the lower diagonal of S1.1 d) PLSR coefficients for top performing fresh (green) and dry spectra (brown) models. PLSR coefficients cannot be directly compared to wavelet correlations because the number of components (Table 3) strongly influences PLSR. However, ideally, negative wavelet correlations should align with negative PLSR coefficients if an absorption feature associated with the trait is present.

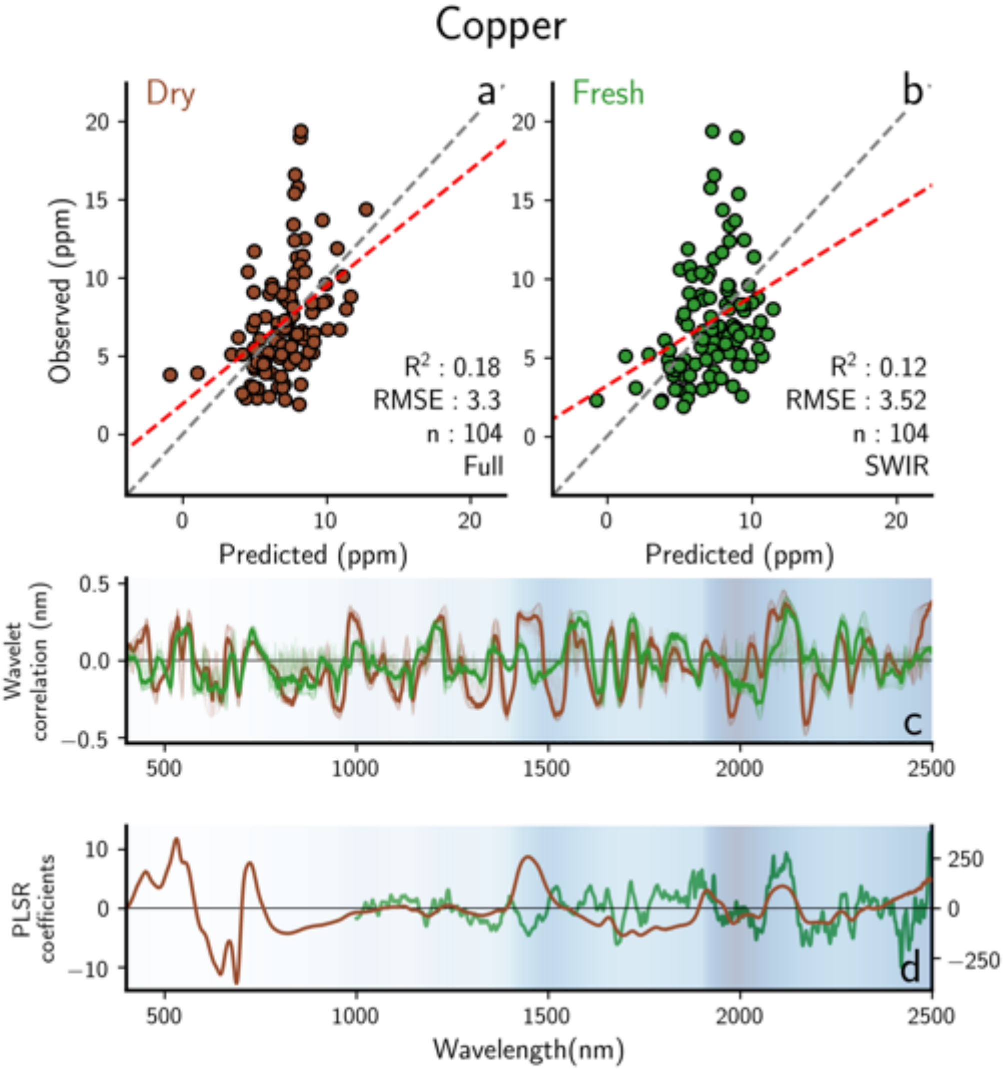

Figure S1.14 Copper full results

a) Validation scatterplot and metrics for top performing dry spectra PLSR model. b) Validation scatterplot and metrics for top performing fresh spectra PLSR model. c) Wavelet feature correlation plots for fresh (green) and dry spectra (brown), solid lines indicate mean correlation across all wavelet scales, transparent lines show individual wavelet scales. Blue shading indicates the relative intensity of water absorption at each wavelength, darker blue indicates higher water absorption. The correlation values plotted on c) are the input to the summary plot in Figure 7. Wavelengths where the green and brown lines align indicate common spectral features identified in both fresh and dry spectra. The correlation between the y-axes (wavelet correlations) among all traits (Figures S1.2-S1.28) is the basis for Figure S1.1, with dry spectra (brown line across traits) in the upper diagonal and fresh spectra (green line across traits) in the lower diagonal of S1.1 d) PLSR coefficients for top performing fresh (green) and dry spectra (brown) models. PLSR coefficients cannot be directly compared to wavelet correlations because the number of components (Table 3) strongly influences PLSR. However, ideally, negative wavelet correlations should align with negative PLSR coefficients if an absorption feature associated with the trait is present.

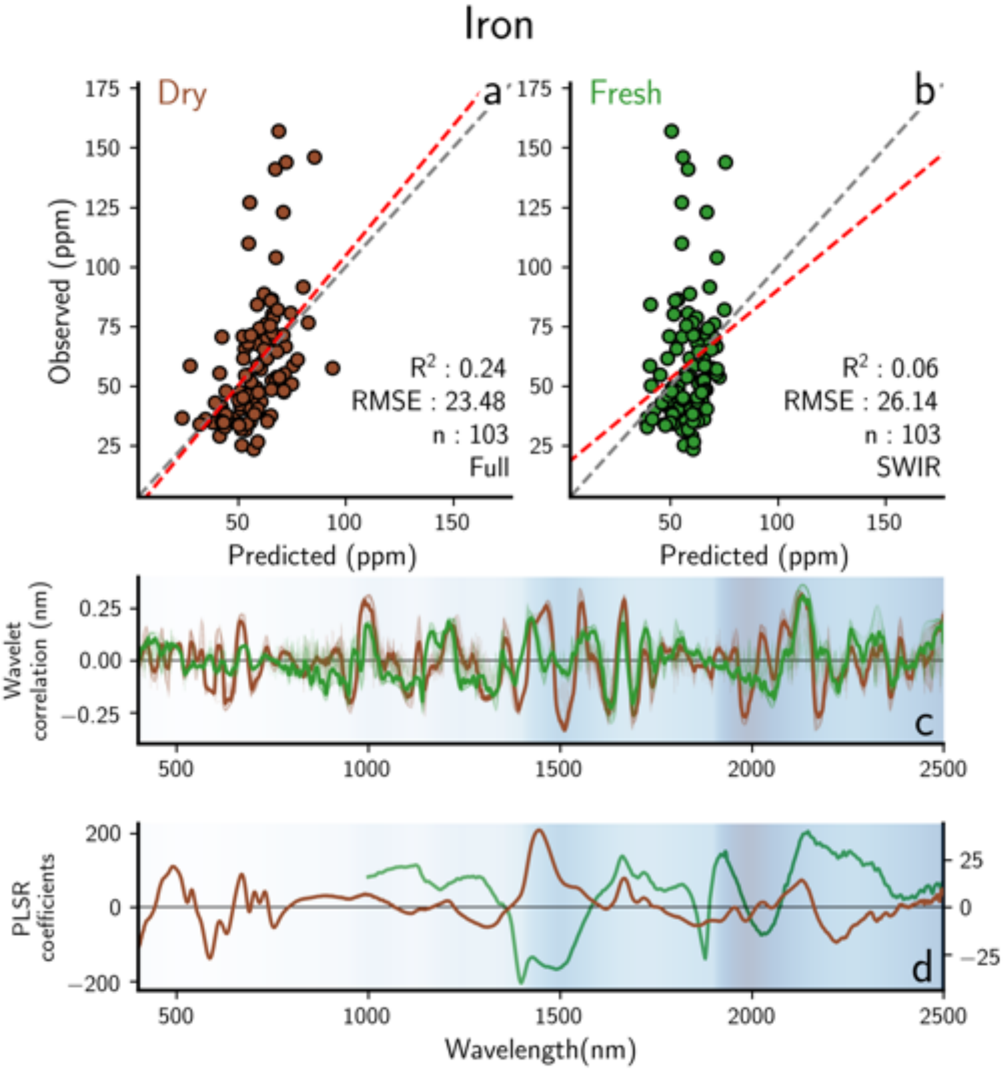

Figure S1.15 Iron full results

a) Validation scatterplot and metrics for top performing dry spectra PLSR model. b) Validation scatterplot and metrics for top performing fresh spectra PLSR model. c) Wavelet feature correlation plots for fresh (green) and dry spectra (brown), solid lines indicate mean correlation across all wavelet scales, transparent lines show individual wavelet scales. Blue shading indicates the relative intensity of water absorption at each wavelength, darker blue indicates higher water absorption. The correlation values plotted on c) are the input to the summary plot in Figure 7. Wavelengths where the green and brown lines align indicate common spectral features identified in both fresh and dry spectra. The correlation between the y-axes (wavelet correlations) among all traits (Figures S1.2-S1.28) is the basis for Figure S1.1, with dry spectra (brown line across traits) in the upper diagonal and fresh spectra (green line across traits) in the lower diagonal of S1.1 d) PLSR coefficients for top performing fresh (green) and dry spectra (brown) models. PLSR coefficients cannot be directly compared to wavelet correlations because the number of components (Table 3) strongly influences PLSR. However, ideally, negative wavelet correlations should align with negative PLSR coefficients if an absorption feature associated with the trait is present.

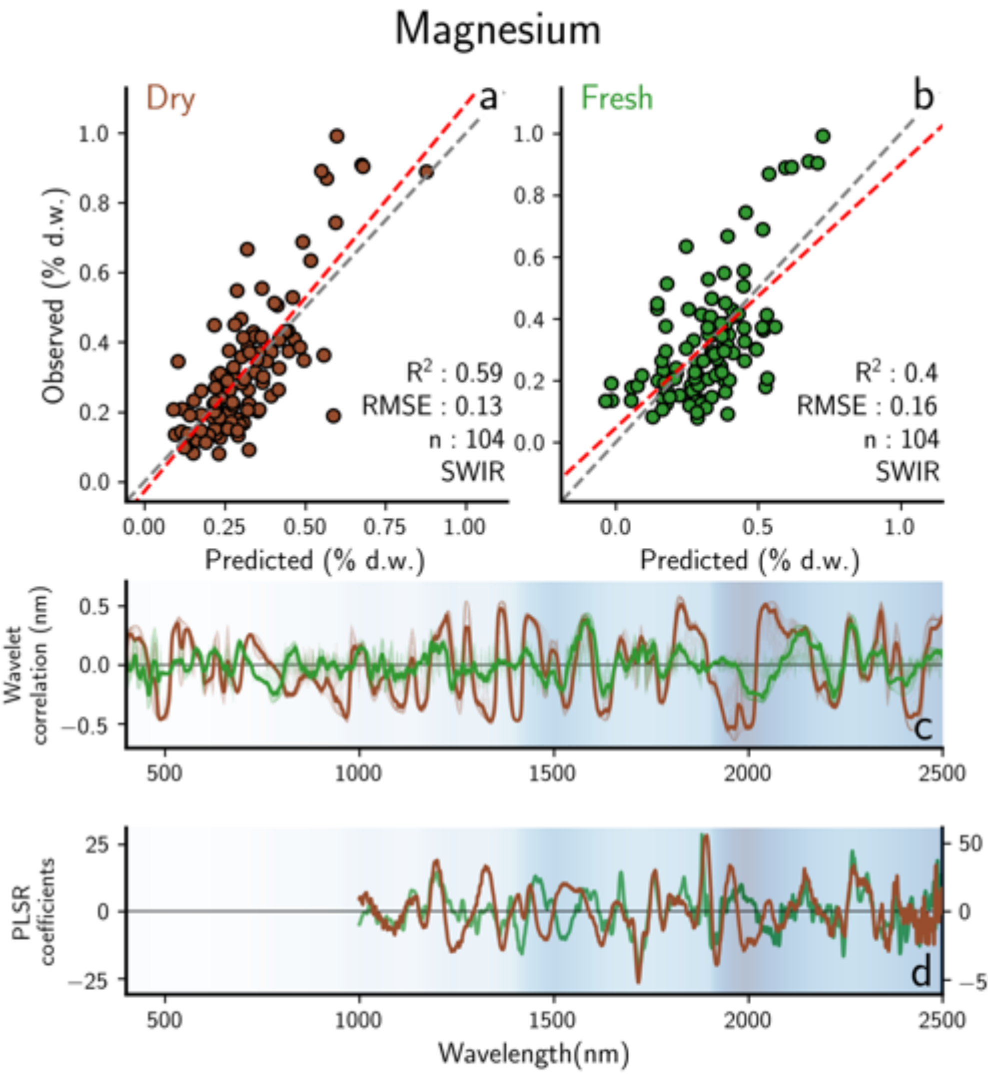

Figure S1.16 Magnesium full results

a) Validation scatterplot and metrics for top performing dry spectra PLSR model. b) Validation scatterplot and metrics for top performing fresh spectra PLSR model. c) Wavelet feature correlation plots for fresh (green) and dry spectra (brown), solid lines indicate mean correlation across all wavelet scales, transparent lines show individual wavelet scales. Blue shading indicates the relative intensity of water absorption at each wavelength, darker blue indicates higher water absorption. The correlation values plotted on c) are the input to the summary plot in Figure 7. Wavelengths where the green and brown lines align indicate common spectral features identified in both fresh and dry spectra. The correlation between the y-axes (wavelet correlations) among all traits (Figures S1.2-S1.28) is the basis for Figure S1.1, with dry spectra (brown line across traits) in the upper diagonal and fresh spectra (green line across traits) in the lower diagonal of S1.1 d) PLSR coefficients for top performing fresh (green) and dry spectra (brown) models. PLSR coefficients cannot be directly compared to wavelet correlations because the number of components (Table 3) strongly influences PLSR. However, ideally, negative wavelet correlations should align with negative PLSR coefficients if an absorption feature associated with the trait is present.

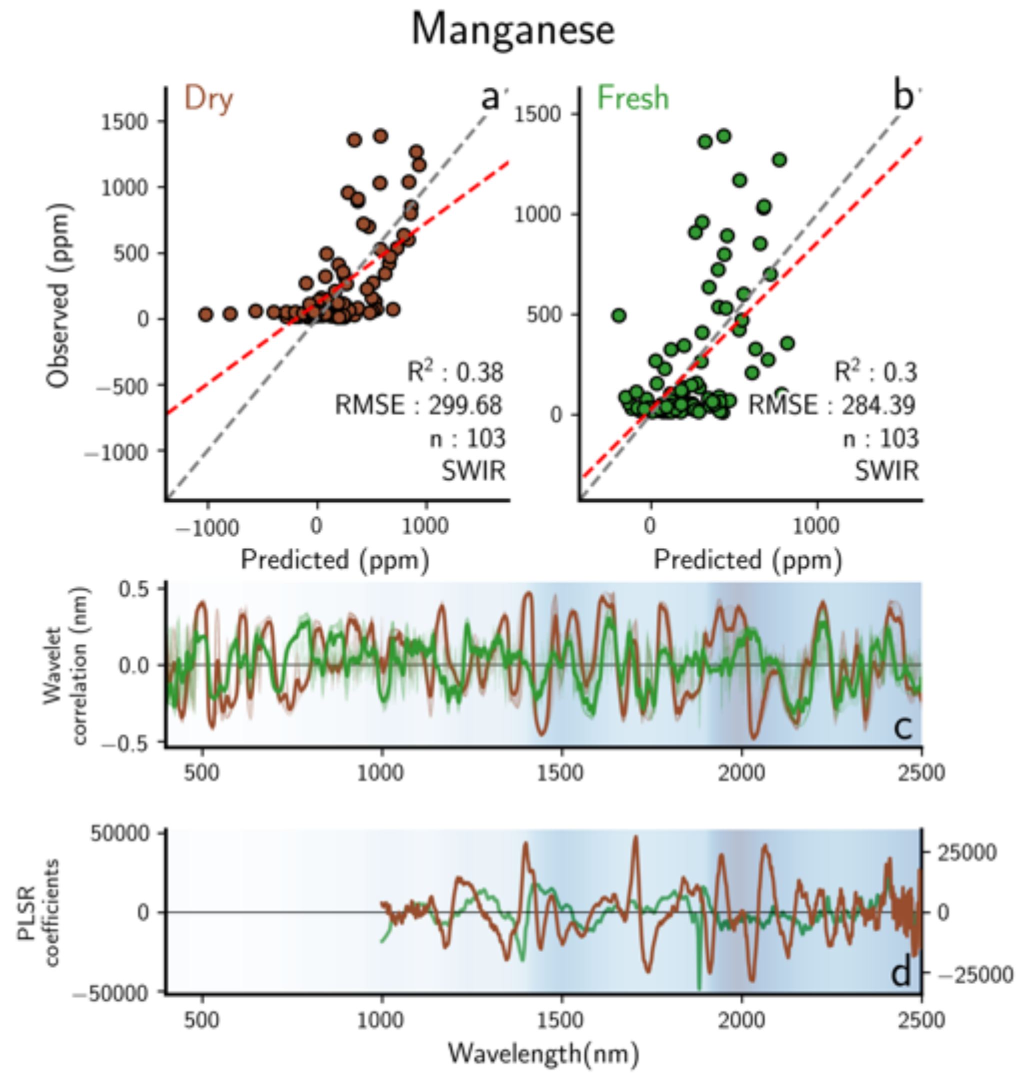

Figure S1.17 Manganese full results

a) Validation scatterplot and metrics for top performing dry spectra PLSR model. b) Validation scatterplot and metrics for top performing fresh spectra PLSR model. c) Wavelet feature correlation plots for fresh (green) and dry spectra (brown), solid lines indicate mean correlation across all wavelet scales, transparent lines show individual wavelet scales. Blue shading indicates the relative intensity of water absorption at each wavelength, darker blue indicates higher water absorption. The correlation values plotted on c) are the input to the summary plot in Figure 7. Wavelengths where the green and brown lines align indicate common spectral features identified in both fresh and dry spectra. The correlation between the y-axes (wavelet correlations) among all traits (Figures S1.2-S1.28) is the basis for Figure S1.1, with dry spectra (brown line across traits) in the upper diagonal and fresh spectra (green line across traits) in the lower diagonal of S1.1 d) PLSR coefficients for top performing fresh (green) and dry spectra (brown) models. PLSR coefficients cannot be directly compared to wavelet correlations because the number of components (Table 3) strongly influences PLSR. However, ideally, negative wavelet correlations should align with negative PLSR coefficients if an absorption feature associated with the trait is present.

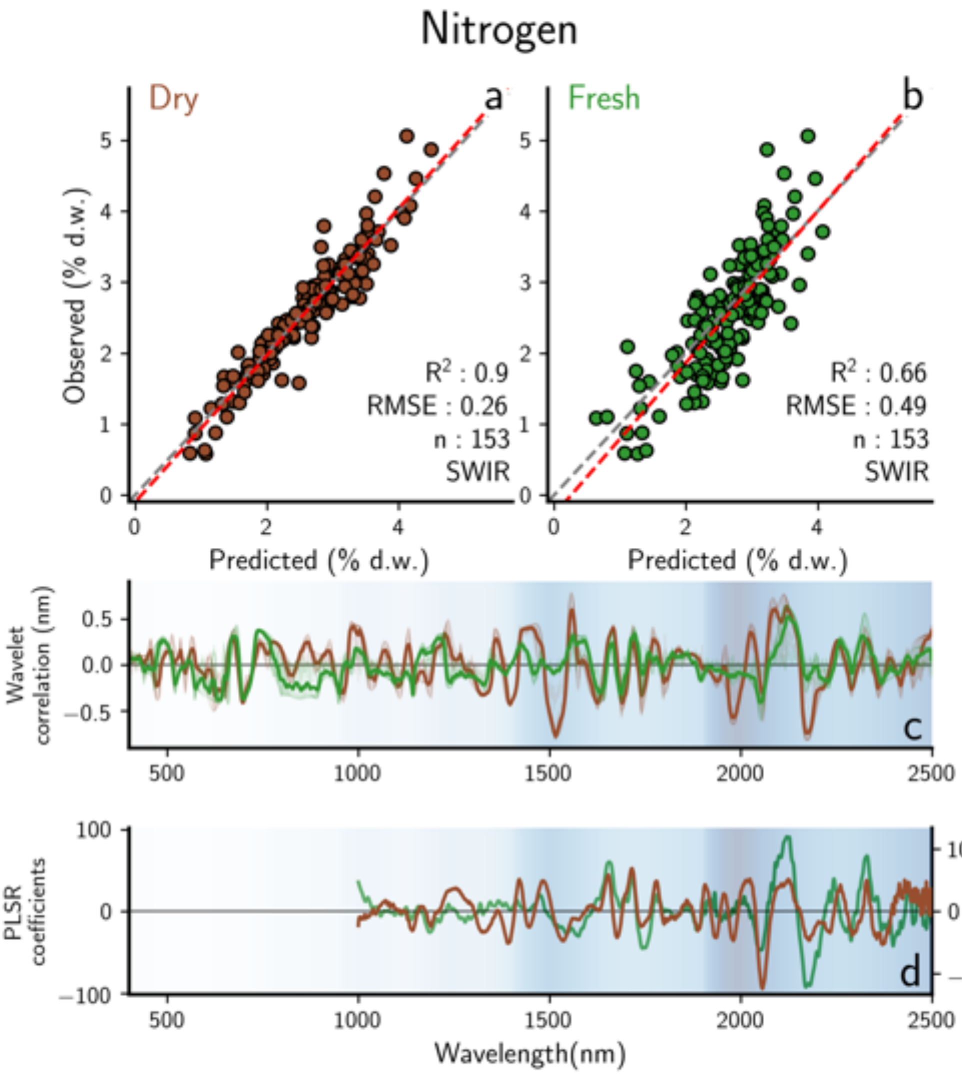

Figure S1.18 Nitrogen full results

a) Validation scatterplot and metrics for top performing dry spectra PLSR model. b) Validation scatterplot and metrics for top performing fresh spectra PLSR model. c) Wavelet feature correlation plots for fresh (green) and dry spectra (brown), solid lines indicate mean correlation across all wavelet scales, transparent lines show individual wavelet scales. Blue shading indicates the relative intensity of water absorption at each wavelength, darker blue indicates higher water absorption. The correlation values plotted on c) are the input to the summary plot in Figure 7. Wavelengths where the green and brown lines align indicate common spectral features identified in both fresh and dry spectra. The correlation between the y-axes (wavelet correlations) among all traits (Figures S1.2-S1.28) is the basis for Figure S1.1, with dry spectra (brown line across traits) in the upper diagonal and fresh spectra (green line across traits) in the lower diagonal of S1.1 d) PLSR coefficients for top performing fresh (green) and dry spectra (brown) models. PLSR coefficients cannot be directly compared to wavelet correlations because the number of components (Table 3) strongly influences PLSR. However, ideally, negative wavelet correlations should align with negative PLSR coefficients if an absorption feature associated with the trait is present.

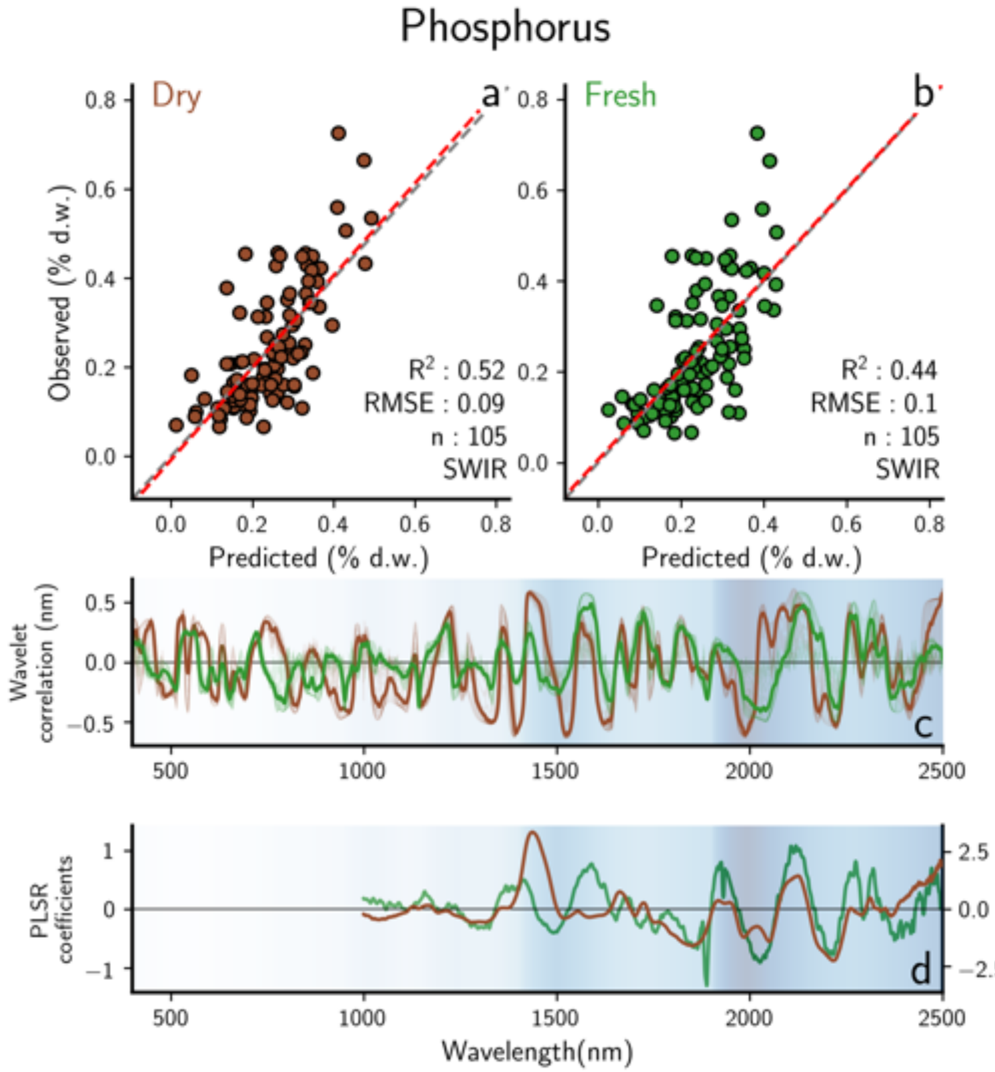

Figure S1.19 Phosphorus full results

a) Validation scatterplot and metrics for top performing dry spectra PLSR model. b) Validation scatterplot and metrics for top performing fresh spectra PLSR model. c) Wavelet feature correlation plots for fresh (green) and dry spectra (brown), solid lines indicate mean correlation across all wavelet scales, transparent lines show individual wavelet scales. Blue shading indicates the relative intensity of water absorption at each wavelength, darker blue indicates higher water absorption. The correlation values plotted on c) are the input to the summary plot in Figure 7. Wavelengths where the green and brown lines align indicate common spectral features identified in both fresh and dry spectra. The correlation between the y-axes (wavelet correlations) among all traits (Figures S1.2-S1.28) is the basis for Figure S1.1, with dry spectra (brown line across traits) in the upper diagonal and fresh spectra (green line across traits) in the lower diagonal of S1.1 d) PLSR coefficients for top performing fresh (green) and dry spectra (brown) models. PLSR coefficients cannot be directly compared to wavelet correlations because the number of components (Table 3) strongly influences PLSR. However, ideally, negative wavelet correlations should align with negative PLSR coefficients if an absorption feature associated with the trait is present.

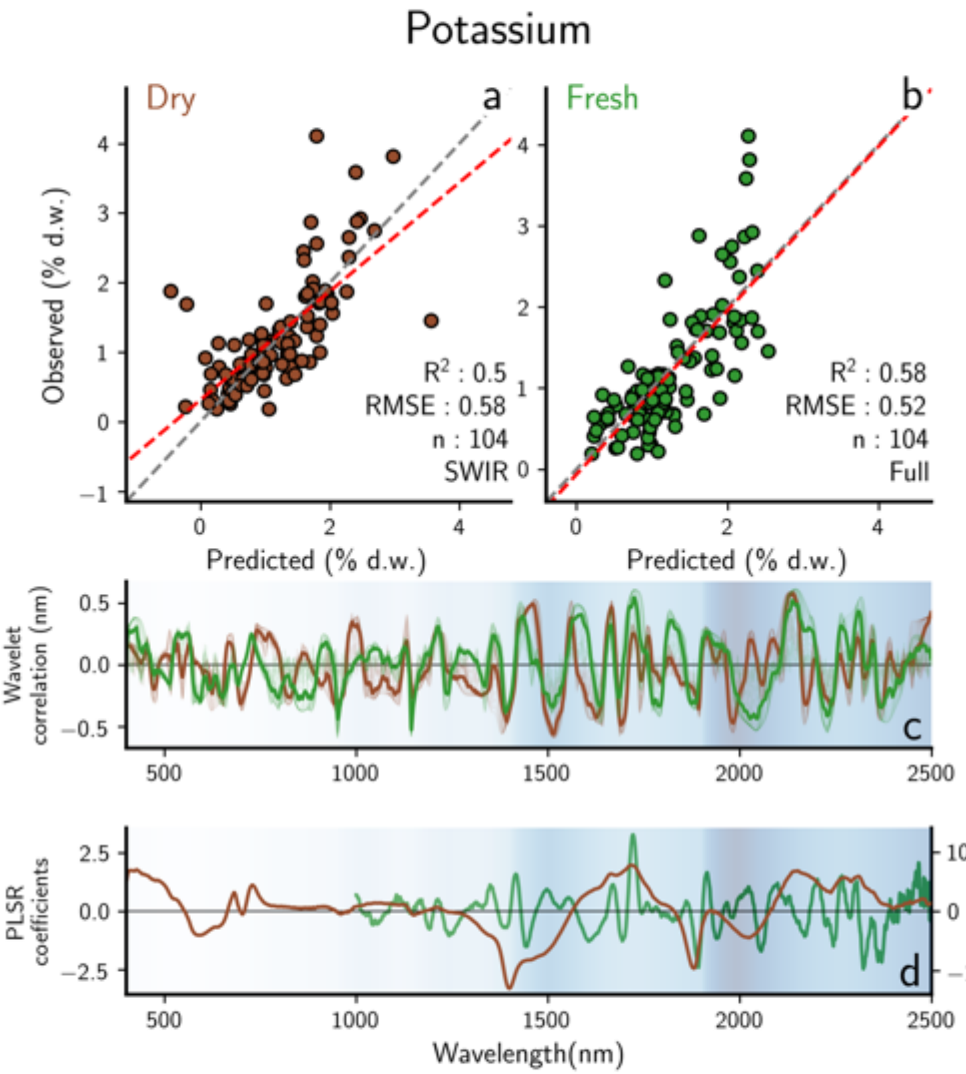

Figure S1.20 Potassium full results

a) Validation scatterplot and metrics for top performing dry spectra PLSR model. b) Validation scatterplot and metrics for top performing fresh spectra PLSR model. c) Wavelet feature correlation plots for fresh (green) and dry spectra (brown), solid lines indicate mean correlation across all wavelet scales, transparent lines show individual wavelet scales. Blue shading indicates the relative intensity of water absorption at each wavelength, darker blue indicates higher water absorption. The correlation values plotted on c) are the input to the summary plot in Figure 7. Wavelengths where the green and brown lines align indicate common spectral features identified in both fresh and dry spectra. The correlation between the y-axes (wavelet correlations) among all traits (Figures S1.2-S1.28) is the basis for Figure S1.1, with dry spectra (brown line across traits) in the upper diagonal and fresh spectra (green line across traits) in the lower diagonal of S1.1 d) PLSR coefficients for top performing fresh (green) and dry spectra (brown) models. PLSR coefficients cannot be directly compared to wavelet correlations because the number of components (Table 3) strongly influences PLSR. However, ideally, negative wavelet correlations should align with negative PLSR coefficients if an absorption feature associated with the trait is present.

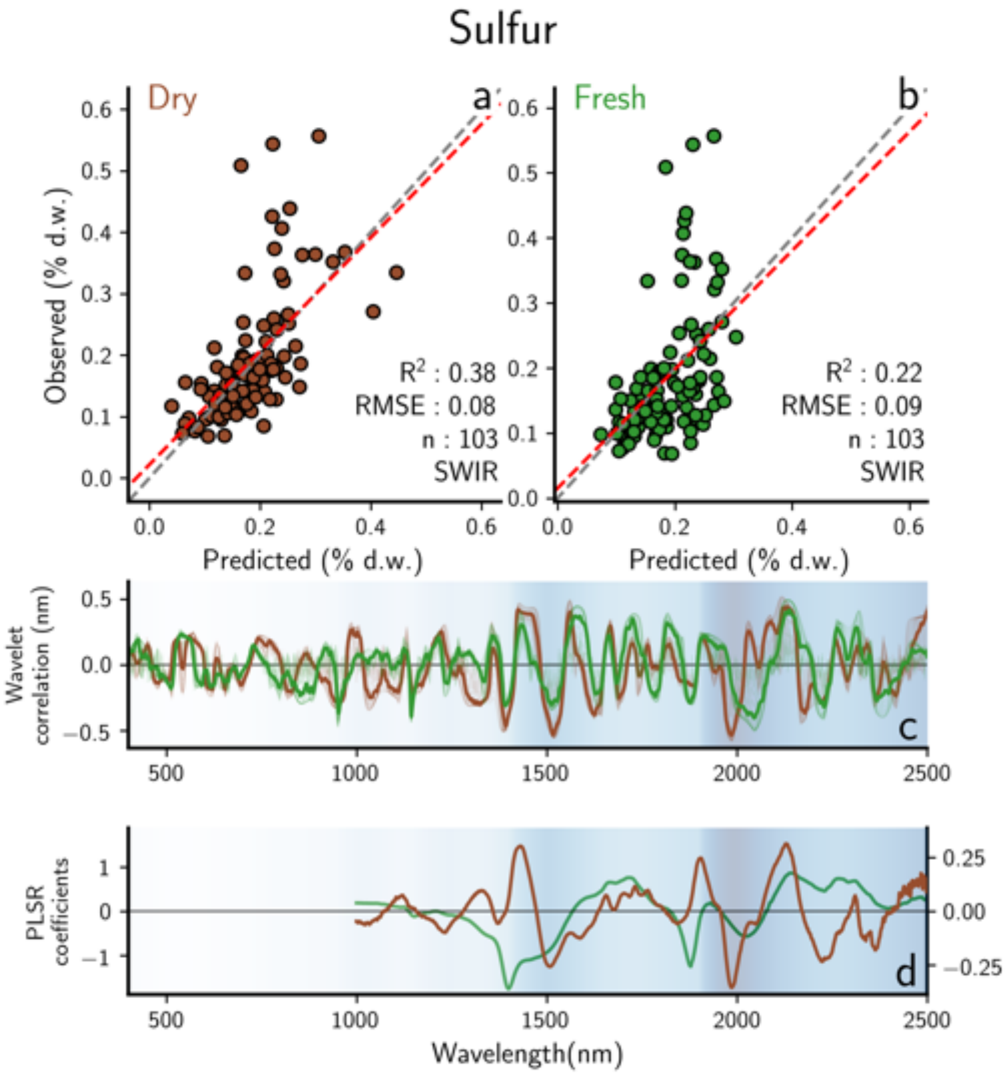

Figure S1.21 Sulfur full results

a) Validation scatterplot and metrics for top performing dry spectra PLSR model. b) Validation scatterplot and metrics for top performing fresh spectra PLSR model. c) Wavelet feature correlation plots for fresh (green) and dry spectra (brown), solid lines indicate mean correlation across all wavelet scales, transparent lines show individual wavelet scales. Blue shading indicates the relative intensity of water absorption at each wavelength, darker blue indicates higher water absorption. The correlation values plotted on c) are the input to the summary plot in Figure 7. Wavelengths where the green and brown lines align indicate common spectral features identified in both fresh and dry spectra. The correlation between the y-axes (wavelet correlations) among all traits (Figures S1.2-S1.28) is the basis for Figure S1.1, with dry spectra (brown line across traits) in the upper diagonal and fresh spectra (green line across traits) in the lower diagonal of S1.1 d) PLSR coefficients for top performing fresh (green) and dry spectra (brown) models. PLSR coefficients cannot be directly compared to wavelet correlations because the number of components (Table 3) strongly influences PLSR. However, ideally, negative wavelet correlations should align with negative PLSR coefficients if an absorption feature associated with the trait is present.

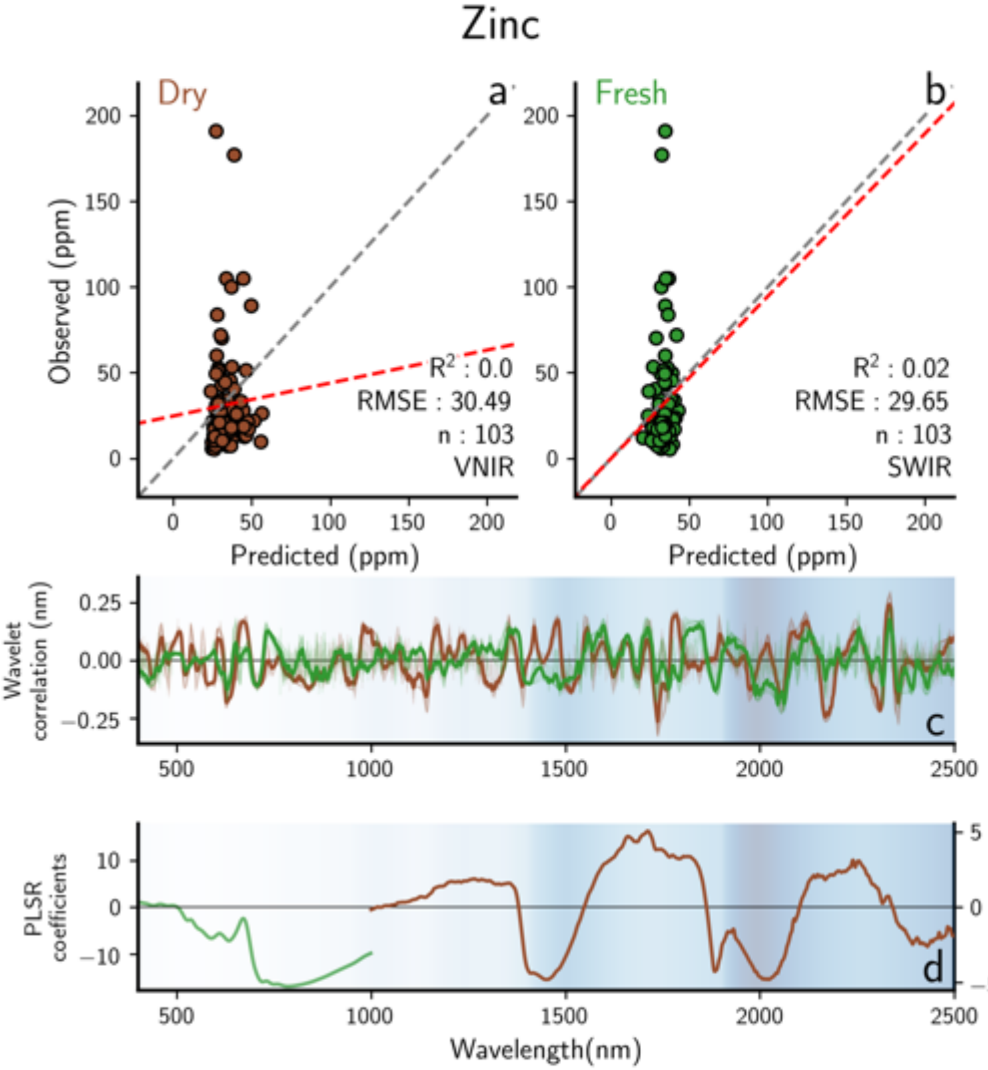

Figure S1.22 Zinc full results

a) Validation scatterplot and metrics for top performing dry spectra PLSR model. b) Validation scatterplot and metrics for top performing fresh spectra PLSR model. c) Wavelet feature correlation plots for fresh (green) and dry spectra (brown), solid lines indicate mean correlation across all wavelet scales, transparent lines show individual wavelet scales. Blue shading indicates the relative intensity of water absorption at each wavelength, darker blue indicates higher water absorption. The correlation values plotted on c) are the input to the summary plot in Figure 7. Wavelengths where the green and brown lines align indicate common spectral features identified in both fresh and dry spectra. The correlation between the y-axes (wavelet correlations) among all traits (Figures S1.2-S1.28) is the basis for Figure S1.1, with dry spectra (brown line across traits) in the upper diagonal and fresh spectra (green line across traits) in the lower diagonal of S1.1 d) PLSR coefficients for top performing fresh (green) and dry spectra (brown) models. PLSR coefficients cannot be directly compared to wavelet correlations because the number of components (Table 3) strongly influences PLSR. However, ideally, negative wavelet correlations should align with negative PLSR coefficients if an absorption feature associated with the trait is present.

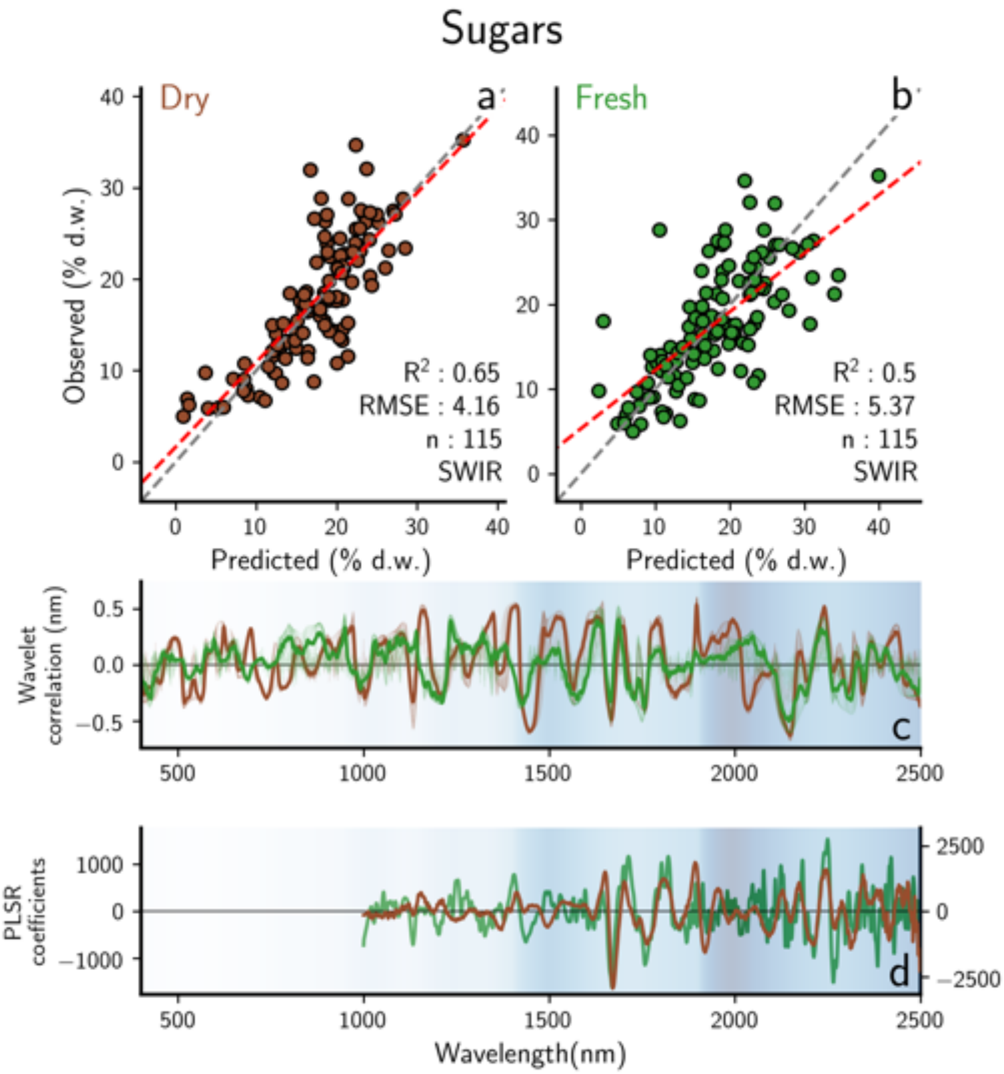

Figure S1.23 Sugars full results

a) Validation scatterplot and metrics for top performing dry spectra PLSR model. b) Validation scatterplot and metrics for top performing fresh spectra PLSR model. c) Wavelet feature correlation plots for fresh (green) and dry spectra (brown), solid lines indicate mean correlation across all wavelet scales, transparent lines show individual wavelet scales. Blue shading indicates the relative intensity of water absorption at each wavelength, darker blue indicates higher water absorption. The correlation values plotted on c) are the input to the summary plot in Figure 7. Wavelengths where the green and brown lines align indicate common spectral features identified in both fresh and dry spectra. The correlation between the y-axes (wavelet correlations) among all traits (Figures S1.2-S1.28) is the basis for Figure S1.1, with dry spectra (brown line across traits) in the upper diagonal and fresh spectra (green line across traits) in the lower diagonal of S1.1 d) PLSR coefficients for top performing fresh (green) and dry spectra (brown) models. PLSR coefficients cannot be directly compared to wavelet correlations because the number of components (Table 3) strongly influences PLSR. However, ideally, negative wavelet correlations should align with negative PLSR coefficients if an absorption feature associated with the trait is present.

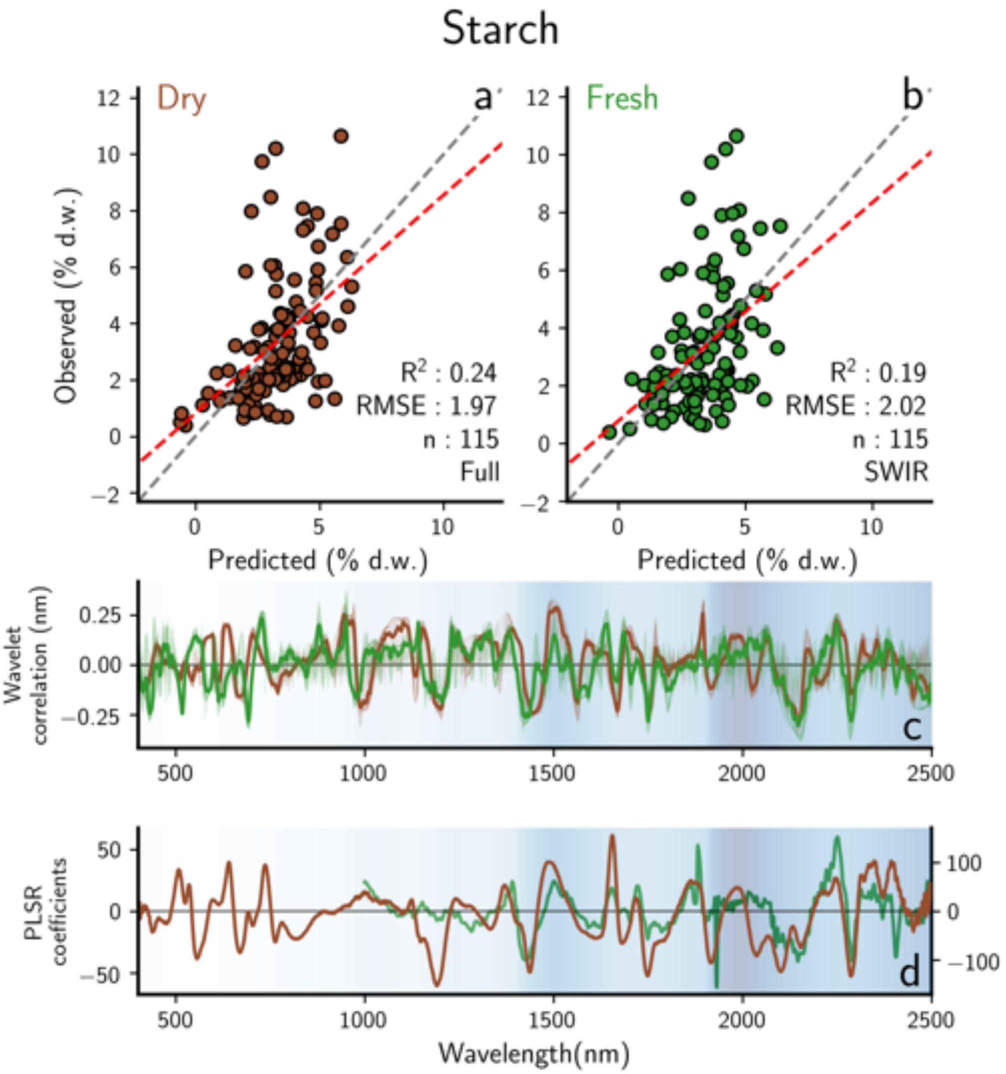

Figure S1.24 Starch full results

a) Validation scatterplot and metrics for top performing dry spectra PLSR model. b) Validation scatterplot and metrics for top performing fresh spectra PLSR model. c) Wavelet feature correlation plots for fresh (green) and dry spectra (brown), solid lines indicate mean correlation across all wavelet scales, transparent lines show individual wavelet scales. Blue shading indicates the relative intensity of water absorption at each wavelength, darker blue indicates higher water absorption. The correlation values plotted on c) are the input to the summary plot in Figure 7. Wavelengths where the green and brown lines align indicate common spectral features identified in both fresh and dry spectra. The correlation between the y-axes (wavelet correlations) among all traits (Figures S1.2-S1.28) is the basis for Figure S1.1, with dry spectra (brown line across traits) in the upper diagonal and fresh spectra (green line across traits) in the lower diagonal of S1.1 d) PLSR coefficients for top performing fresh (green) and dry spectra (brown) models. PLSR coefficients cannot be directly compared to wavelet correlations because the number of components (Table 3) strongly influences PLSR. However, ideally, negative wavelet correlations should align with negative PLSR coefficients if an absorption feature associated with the trait is present.

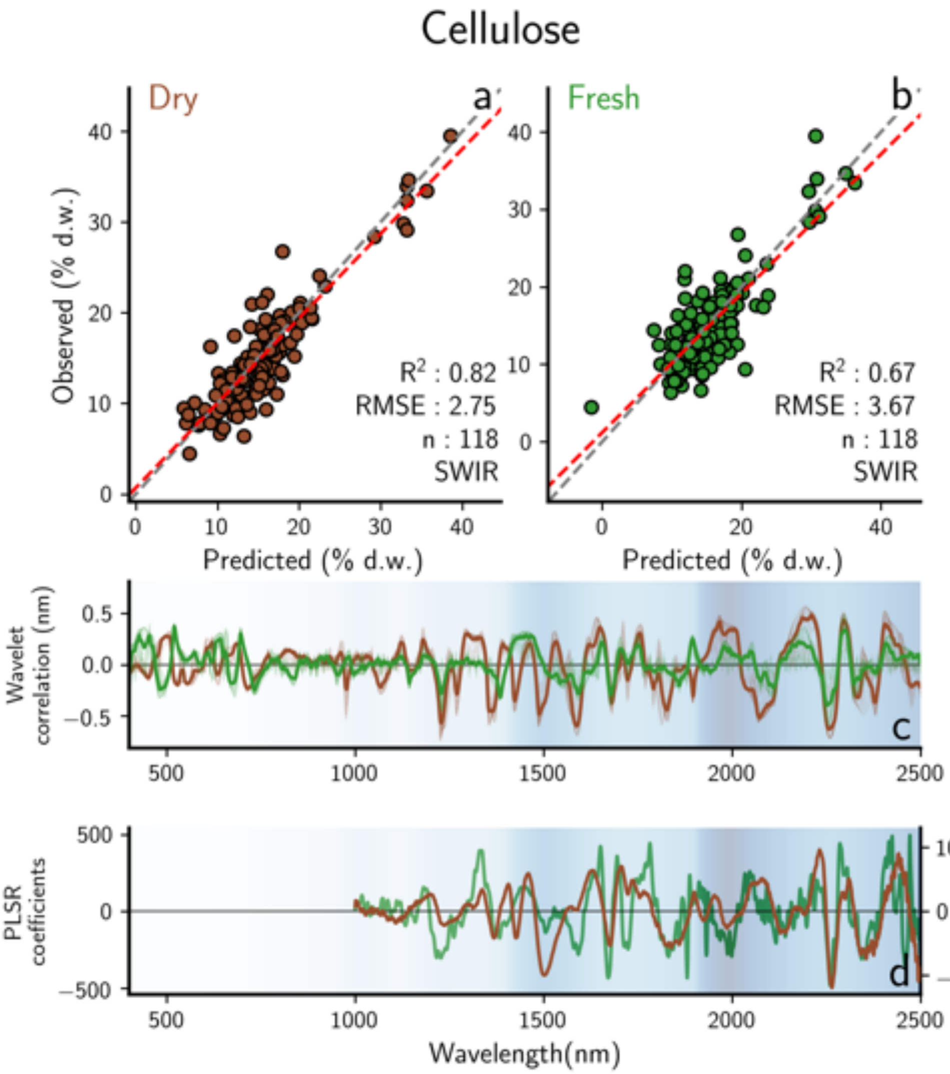

Figure S1.25 Cellulose full results

a) Validation scatterplot and metrics for top performing dry spectra PLSR model. b) Validation scatterplot and metrics for top performing fresh spectra PLSR model. c) Wavelet feature correlation plots for fresh (green) and dry spectra (brown), solid lines indicate mean correlation across all wavelet scales, transparent lines show individual wavelet scales. Blue shading indicates the relative intensity of water absorption at each wavelength, darker blue indicates higher water absorption. The correlation values plotted on c) are the input to the summary plot in Figure 7. Wavelengths where the green and brown lines align indicate common spectral features identified in both fresh and dry spectra. The correlation between the y-axes (wavelet correlations) among all traits (Figures S1.2-S1.28) is the basis for Figure S1.1, with dry spectra (brown line across traits) in the upper diagonal and fresh spectra (green line across traits) in the lower diagonal of S1.1 d) PLSR coefficients for top performing fresh (green) and dry spectra (brown) models. PLSR coefficients cannot be directly compared to wavelet correlations because the number of components (Table 3) strongly influences PLSR. However, ideally, negative wavelet correlations should align with negative PLSR coefficients if an absorption feature associated with the trait is present.

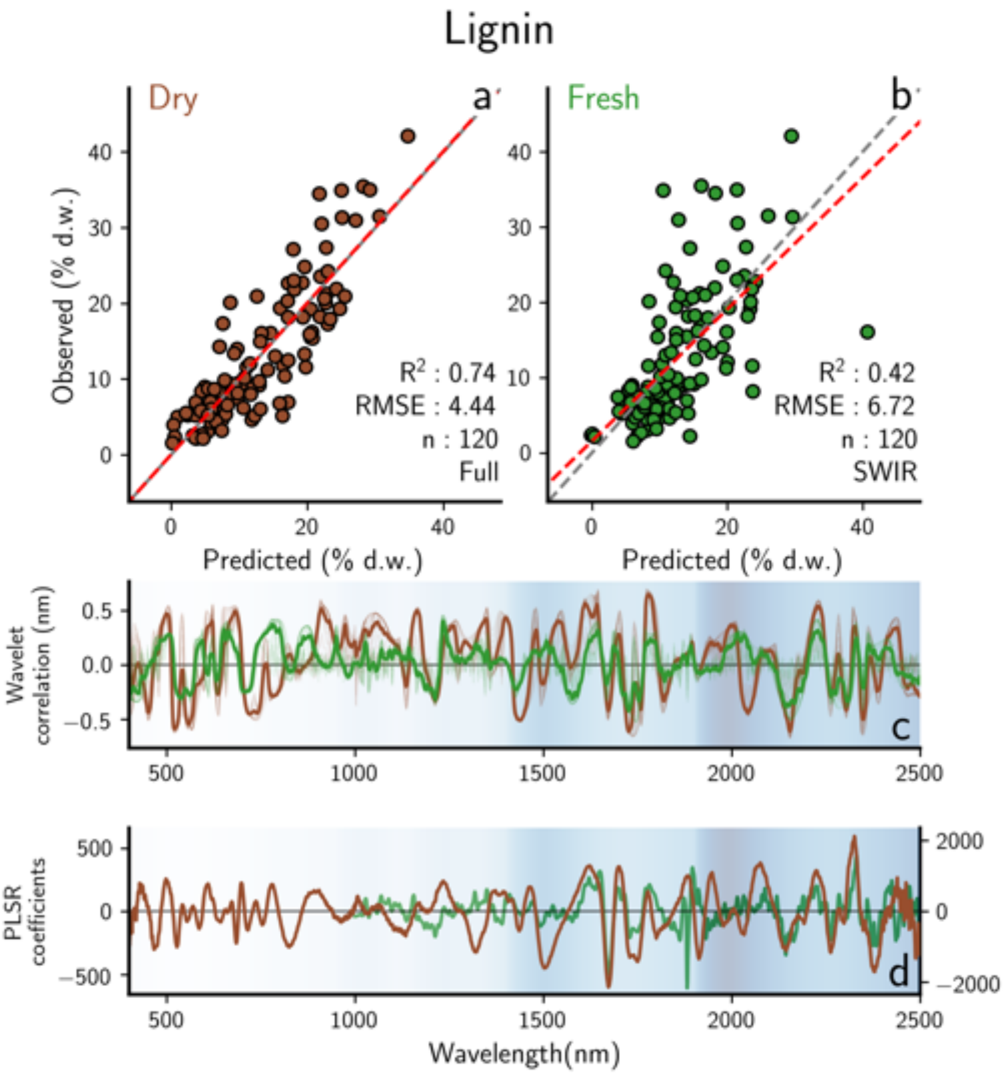

Figure S1.26 Lignin full results

a) Validation scatterplot and metrics for top performing dry spectra PLSR model. b) Validation scatterplot and metrics for top performing fresh spectra PLSR model. c) Wavelet feature correlation plots for fresh (green) and dry spectra (brown), solid lines indicate mean correlation across all wavelet scales, transparent lines show individual wavelet scales. Blue shading indicates the relative intensity of water absorption at each wavelength, darker blue indicates higher water absorption. The correlation values plotted on c) are the input to the summary plot in Figure 7. Wavelengths where the green and brown lines align indicate common spectral features identified in both fresh and dry spectra. The correlation between the y-axes (wavelet correlations) among all traits (Figures S1.2-S1.28) is the basis for Figure S1.1, with dry spectra (brown line across traits) in the upper diagonal and fresh spectra (green line across traits) in the lower diagonal of S1.1 d) PLSR coefficients for top performing fresh (green) and dry spectra (brown) models. PLSR coefficients cannot be directly compared to wavelet correlations because the number of components (Table 3) strongly influences PLSR. However, ideally, negative wavelet correlations should align with negative PLSR coefficients if an absorption feature associated with the trait is present.

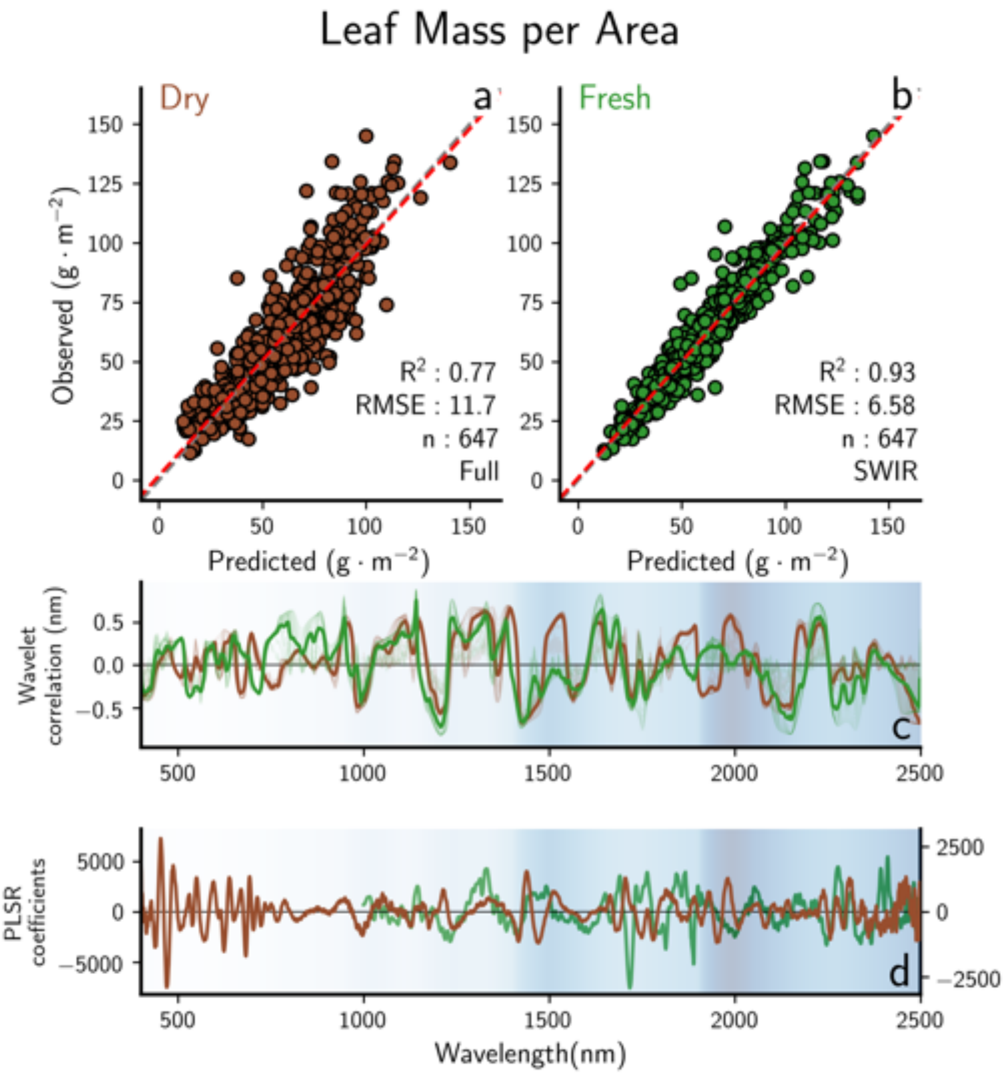

Figure S1.27 LMA full results

a) Validation scatterplot and metrics for top performing dry spectra PLSR model. b) Validation scatterplot and metrics for top performing fresh spectra PLSR model. c) Wavelet feature correlation plots for fresh (green) and dry spectra (brown), solid lines indicate mean correlation across all wavelet scales, transparent lines show individual wavelet scales. Blue shading indicates the relative intensity of water absorption at each wavelength, darker blue indicates higher water absorption. The correlation values plotted on c) are the input to the summary plot in Figure 7. Wavelengths where the green and brown lines align indicate common spectral features identified in both fresh and dry spectra. The correlation between the y-axes (wavelet correlations) among all traits (Figures S1.2-S1.28) is the basis for Figure S1.1, with dry spectra (brown line across traits) in the upper diagonal and fresh spectra (green line across traits) in the lower diagonal of S1.1 d) PLSR coefficients for top performing fresh (green) and dry spectra (brown) models. PLSR coefficients cannot be directly compared to wavelet correlations because the number of components (Table 3) strongly influences PLSR. However, ideally, negative wavelet correlations should align with negative PLSR coefficients if an absorption feature associated with the trait is present.

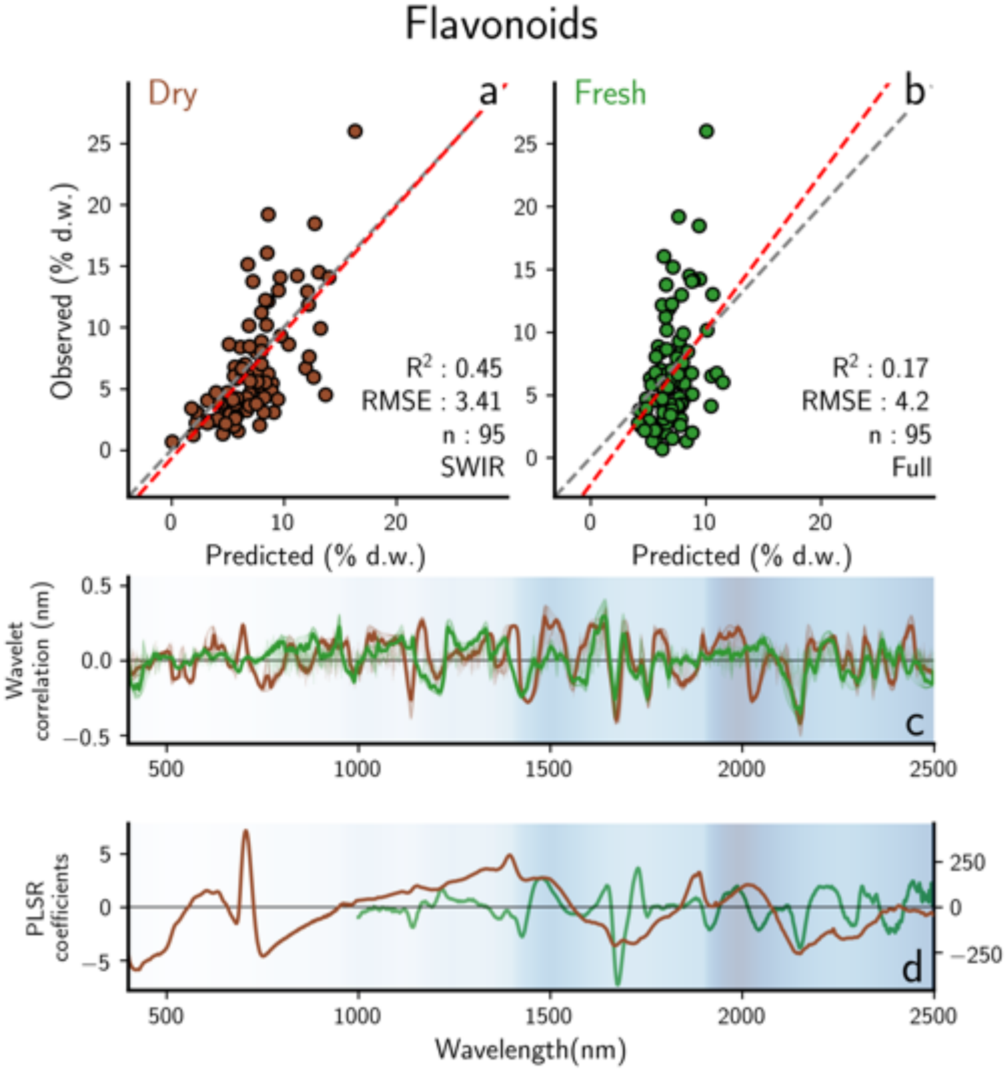

Figure S1.28 Flavonoids full results

a) Validation scatterplot and metrics for top performing dry spectra PLSR model. b) Validation scatterplot and metrics for top performing fresh spectra PLSR model. c) Wavelet feature correlation plots for fresh (green) and dry spectra (brown), solid lines indicate mean correlation across all wavelet scales, transparent lines show individual wavelet scales. Blue shading indicates the relative intensity of water absorption at each wavelength, darker blue indicates higher water absorption. The correlation values plotted on c) are the input to the summary plot in Figure 7. Wavelengths where the green and brown lines align indicate common spectral features identified in both fresh and dry spectra. The correlation between the y-axes (wavelet correlations) among all traits (Figures S1.2-S1.28) is the basis for Figure S1.1, with dry spectra (brown line across traits) in the upper diagonal and fresh spectra (green line across traits) in the lower diagonal of S1.1 d) PLSR coefficients for top performing fresh (green) and dry spectra (brown) models. PLSR coefficients cannot be directly compared to wavelet correlations because the number of components (Table 3) strongly influences PLSR. However, ideally, negative wavelet correlations should align with negative PLSR coefficients if an absorption feature associated with the trait is present.

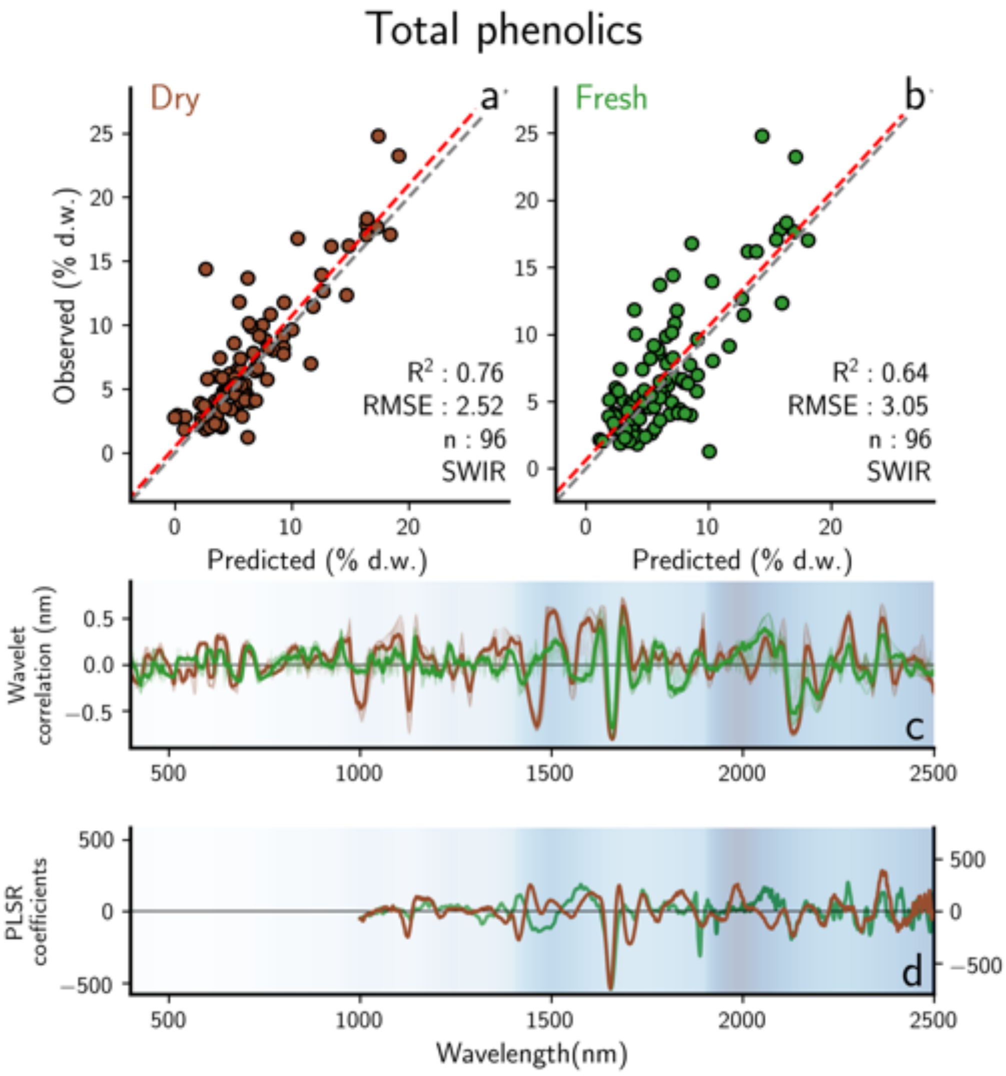

Figure S1.29 Total phenolics full results

a) Validation scatterplot and metrics for top performing dry spectra PLSR model. b) Validation scatterplot and metrics for top performing fresh spectra PLSR model. c) Wavelet feature correlation plots for fresh (green) and dry spectra (brown), solid lines indicate mean correlation across all wavelet scales, transparent lines show individual wavelet scales. Blue shading indicates the relative intensity of water absorption at each wavelength, darker blue indicates higher water absorption. The correlation values plotted on c) are the input to the summary plot in Figure 7. Wavelengths where the green and brown lines align indicate common spectral features identified in both fresh and dry spectra. The correlation between the y-axes (wavelet correlations) among all traits (Figures S1.2-S1.28) is the basis for Figure S1.1, with dry spectra (brown line across traits) in the upper diagonal and fresh spectra (green line across traits) in the lower diagonal of S1.1 d) PLSR coefficients for top performing fresh (green) and dry spectra (brown) models. PLSR coefficients cannot be directly compared to wavelet correlations because the number of components (Table 3) strongly influences PLSR. However, ideally, negative wavelet correlations should align with negative PLSR coefficients if an absorption feature associated with the trait is present.

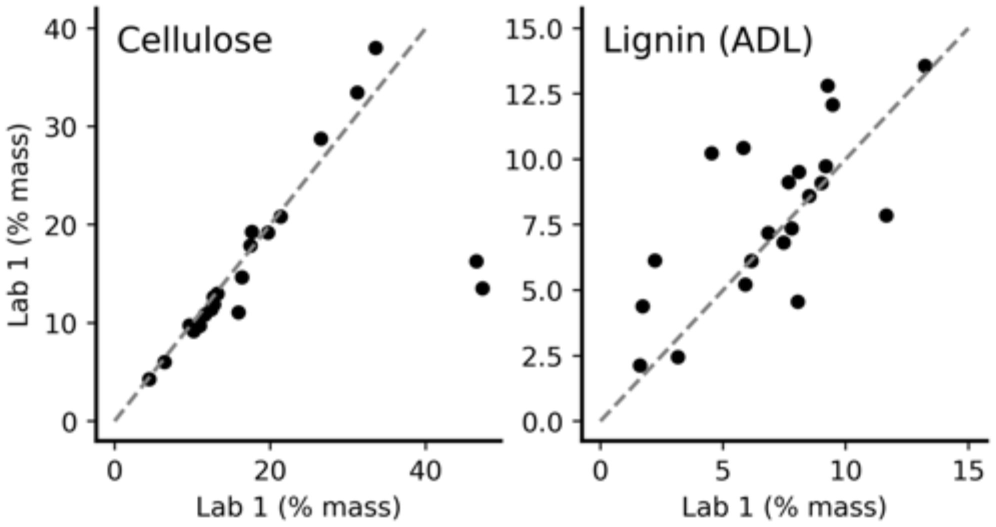

Figure S1.30 Comparison of cellulose (left) and lignin (right) measurements from two separate labs on the same samples using acid detergent extraction. Grey dashed line is 1:1 line.

2. Mapping three-dimensional variation in leaf mass per area with imaging spectroscopy and lidar in a temperate broadleaf forest

Contributors: Adam Chlus, Eric L. Kruger & Philip A. Townsend

Abstract

Imaging spectroscopy is a valuable tool for mapping canopy foliar traits in forested ecosystems at landscape and larger scales. Most efforts to date have involved two-dimensional mapping of traits, typically representing top-of-canopy conditions. However, traits and their associated biological functions vary through the canopy vertical profile, such that incorporating information about vertical patterns may improve modeling of ecosystem processes like primary productivity. In 2016 and 2017, we collected extensive field data in forests in Domain 5 (Great Lakes) of the National Ecological Observatory Network (NEON) to characterize the vertical variation in leaf mass per area (LMA), an important foliar trait related to plant growth and defense. Fieldwork was coincident with NEON Airborne Observation Platform (AOP) overflights which collected imaging spectroscopy and lidar data. Using imaging spectroscopy to map top-of-canopy LMA and lidar to model vertical gradients of transmittance, we developed a method to map three-dimensional patterns in LMA in temperate broadleaf forests. Partial least squares regression (PLSR) was used to estimate top-of-canopy LMA (R^2: 0.57, RMSE 10.8 g m^{-2}), which, along with lidar-derived metrics of light transmittance and height, was used in a multilevel regression to model within-canopy LMA (R^2: 0.78, RMSE 8.3 g m^{-2}). The coupled models accurately estimated LMA throughout the canopy without taking into account species composition (R^2 : 0.82, RMSE: 8.5 g m^{-2}).

Introduction

The world's forest ecosystems are changing rapidly, and extensive data is necessary to better understand corresponding implications for ecosystem function and to accurately model future scenarios. However, traditional field-scale sampling techniques may not provide information at scales sufficient for characterizing landscape and broader-scale variation needed for accurate modeling. Remote sensing has long offered the potential to extrapolate sparse field measurements to generate inputs needed to drive models, especially of two-dimensional patterns across the land surface (Roughgarden et al., 1991; Cohen and Goward, 2004). However, forest ecosystems are inherently three-dimensional (3D) and multiple studies have highlighted the need to accurately characterize vertical patterns in structural and biophysical properties for parametrizing ecosystem process and forecasting models (Cavaleri et al., 2010; Coble et al., 2016; Rogers et al., 2017). For the most part, remote sensing products and ecosystem models ignore vertical variability in traits important to understanding forest processes.

A number of ecologically important structural, morphological and chemical properties vary throughout the vertical extent of forest canopies, including leaf area density (LAD), leaf angle distribution (LAD) and foliar chemical composition (e.g., concentrations of lignin and phosphorus, and δ^{13}C) (Vose et al., 1995; Niinemets, 2015; Leuning et al., 1991). Among the most widely studied and characterized biophysical properties in the context of within-canopy patterns is leaf mass per area (LMA), the ratio between the projected leaf area and dry mass, which is largely comprised of structural and nonstructural carbohydrates, proteins, lignin and minerals (Poorter et al., 2009). LMA—or its inverse, specific leaf area (SLA)—is a central component of the leaf economic spectrum (LES) representing the tradeoff between growth and defense (Wright et al., 2004; Poorter et al., 2009). For example, relatively thin leaves with low LMA tend to have high rates of photosynthesis per unit mass compared to denser, thicker and more durable leaves with high LMA (Niinemets, 1999; Wright et al., 2004). The drivers of LMA variation differ across scales. Broadly, LMA variation is largely driven by taxonomy, while local environment and site conditions can explain a large proportion of LMA variation at finer scales (Messier et al., 2010; Messier et al., 2017).

LMA decreases with depth into the canopy, owing primarily to the attenuation of light and a decrease in height-mediated hydraulic constraints (Cavaleri et al., 2010; Niinemets, 2015). Microclimatic variables including temperature, wind exposure and humidity, which co-vary with incident radiation and height, also influence within-canopy LMA (Niinemets, 2001; Poorter et al. 2009; Petter et al., 2016; Wu et al., 2016). The degree to which within-canopy gradients in LMA are driven by irradiance or height is not universal and can vary as a function of species, local environmental conditions and seasonality (Koch et al., 2004; Coble and Cavaleri 2014; Coble et al. 2016). While numerous studies have explored within-canopy patterns in LMA through individual tree canopies (Ellsworth and Reich, 1993; Aranda et al., 2004), few studies have explored patterns of LMA in vertically heterogenous canopies where both species composition and architecture vary within the vertical profile. The ability to understand these patterns in three dimensions may provide insights into spatial patterns of forest responses to change, ranging from successional responses to disturbances at local scales to landscape-level responses to broad-scale stresses such as drought or the cumulative impacts of climate change. As well, 3D profiles of canopy traits may also enable more accurate parameterization of landscape- and larger-scale process models that do not typically represent spatial variation of the vertical distribution of canopy traits.

Here we present a remote sensing approach that utilizes imaging spectroscopy and lidar to characterize the 3D variation in LMA in broadleaf canopies (Figure 2.1). Our approach is based on the large body of research that has demonstrated that LMA decreases through the canopy from top to bottom and that decrease is largely driven by incident irradiance and/or height mediated hydraulics constraints (Ellsworth and Reich 1993; Koch et al. 2001; Poorter et al. 2009). We posit that if we are able to estimate LMA at the top of the canopy and model the within-canopy environmental gradients that are known to drive top-down decreases in LMA, we should be able estimate within-canopy (top-down) patterns in LMA. Our method uses airborne imaging spectroscopy to estimate LMA at the top of the canopy and lidar to model within-canopy environmental gradients driving top down patterns in LMA. Imaging spectroscopy provides the most direct approach to foliar trait estimation at large scales, including LMA (Asner et al., 2015; Singh et al., 2015; Chadwick and Asner, 2016; Wang et al., 2019, 2020). While lidar provides the ability to penetrate the canopy and enables characterization of the 3D light environment (Lefsky et al., 2002; Todd et al. 2003; Olpenda et al. 2018). Our method builds on the work of Parker et al. (2001) who demonstrated that estimates of vertical light transmittance derived from lidar follow vertical patterns in photosynthetically active radiation (PAR) and Fleck et al. (2004) who found with-canopy LMA tracked with-canopy irradiance estimated using terrestrial lidar. We demonstrate this approach with airborne imaging spectroscopy and lidar data from the U.S. National Ecological Observatory Network (NEON) coupled with coincidence field measurements that we use to parameterize our model.

Methods

Study area

Our study area consisted of hardwood-dominated forests in northern Wisconsin and Michigan's Upper Peninsula (89.5 W, 46.0 N). The area is characterized by a mix of managed and unmanaged stands of various age classes, species composition and structure. Common broadleaf deciduous species include trembling and bigtooth aspen (*Populus tremuloides* and *P. grandidentata),* sugar and red maple (*Acer saccharum* and *A. rubrum*), red oak (*Quercus rubra)*, black and white ash (*Fraxinus nigra and F. americana*), basswood (*Tilia americana*) and paper and yellow birch (*Betula papyrifera and B. alleghaniensis*). Fieldwork was conducted in sites within the Great Lakes ecoregion of the National Ecological Observatory Network. NEON is a continental scale network of long-term monitoring sites distributed across ecoregions within the United States. Each ecoregion contains multiple sites that are the focus of environmental monitoring activities including plant and animal surveys, soil characterization and airborne remote sensing data collection. Sampling took place within three NEON sites in the ecoregion: UNDE, CHEQ, and STEI (Figure 2.2). Sites range in size from 40-200 km^2 and comprise a mix of private, municipal, state and federally-owned land.

Remote sensing data

Remote sensing data were collected between September 2-12, 2016 and September 1-12, 2017 by NEON's Airborne Observatory Platform (AOP). AOP is a multi-sensor system which includes an imaging spectrometer, lidar sensor and a high resolution RGB camera. The imaging spectrometer is an AVIRIS-NG-like sensor built by NASA's Jet Propulsion Laboratory that measures radiation from 380-2510 nm in 420 bands, with a spectral sampling width of approximately 6 nm (Kampe et al., 2010; Kampe et al., 2011). Lidar data were collected using an

Optech ALTM 3500 Gemini, which is a dual sensor instrument consisting of a full waveform digitizer and discrete return sensor transmitting at 1064 nm. The instrument was operated at a pulse frequency of 100 Hz and recorded up to four returns. The AOP system was flown on a DeHavilland DHC-6 Twin Otter at 1000 m above ground level (a.g.l.), resulting in 1 m resolution imaging spectroscopy data and a discrete return density of ~4 pts m^{-2}. The full waveform lidar and RGB camera data were not used in this study.

Orthorectification of the imaging spectroscopy data and co-location with the lidar data was performed by NEON using a ray tracing algorithm coupled with measurements from an onboard inertial measurement unit (IMU) and GPS (Kampe et al. 2016). Surface reflectance was generated using ATCOR 4 (ReSe, Wil, Switzerland), which approximates atmospheric conditions including water vapor and aerosol content using the MODTRAN radiative transfer code (Richter and Schläpfer, 2015). The surface reflectance imagery exhibited strong cross-track gradients in brightness due to varying viewing and solar geometry. To remove the brightness gradients, we applied a semi-empirical bidirectional reflectance distribution function (BRDF) correction employing the widely used Ross-Li kernel combination to model the volumetric, geometric and isometric scattering components (Colgan et al., 2012; Schläpfer et al., 2015). A single set of BRDF correction coefficients was generated for each site and date by randomly sampling 10% of the pixels from each flightline and pooling the sampled data before fitting the BRDF correction model. Because scattering properties are dependent on surface type, we limited the BRDF correction model to vegetated pixels using an NDVI threshold of 0.6. Following the BRDF correction, all images were resampled to an interval of 5 nm (ex. 400 nm, 405 nm, …) using a Gaussian approximation of the spectral response function. Resampling was performed to harmonize interannual images which had different wavelength centers due to annual radiometric calibrations. Before analyses, water absorption features (1330-1430 nm and 1800-1960 nm) and spectrum tails (< 400 nm and > 2450 nm) were removed from the imagery due to low signal to noise.

Discrete lidar data were normalized against a 1 m digital elevation model (DEM) to derive height above ground for each return. The DEM was created by NEON from the discrete return lidar data using a triangulated irregular network of ground returns interpolated to a surface (Goulden, 2019).

Field sampling

Field sampling occurred within 10 days of AOP overflights in 2016 and 2017 and involved plot-level collection of leaves throughout the vertical profile of the canopy. Plot locations were manually chosen to capture the range of forest types within the ecoregion and were distributed throughout the study area. Prior to sampling, a comprehensive survey of each plot was conducted. Species, diameter at breast height (DBH), crown class (dominant, codominant or suppressed) and location within the plot were recorded for all trees with DBH greater than 5 cm that had foliage within the plot. Trees were labeled dominant or codominant if their crowns were in the exposed upper canopy, that is they were visible from above, had sunlit foliage and were not completely obstructed by other trees, while all other trees were designated suppressed. Because GPS positions are known to have large errors under closed canopy conditions, all plots were revisited to survey the plot center coordinates during the fall of the sampling year once the trees had dropped their leaves (Sigrist et al., 1999). GPS measurements were made using a Geo7x with an external Zephyr 2 antenna (Trimble Inc., Sunnyvale, CA, USA) mounted on a 2 m range pole and were differentially corrected after collection to an accuracy of < 2m.

Following the plot survey, branches were sampled throughout the vertical profile of the canopy, independent of species or individual tree. The number of branches within the canopy that were sampled depended on the number of species present in the plot and structural complexity of the canopy. Branches were sampled using a variety of tools depending their location in the canopy. Branches less than 15 m a.g.l. were collected using extendable pole pruners. Between 15 m and the top of the canopy, a Big Shot throw weight launcher (Sherrill Tree, Greensboro, NC, USA) was used to launch a line into the canopy, from which a custom-built cutting device (à la Poulter et al., 1991) was raised to retrieve branches. For sun exposed branches (i.e., top-of-canopy) greater than 15 m, either a shotgun or a second custom cutter (Supplemental Figure S2.1) was used to retrieve the top-of-canopy branch. Whenever possible, we attempted to sample every tree with foliage in the plot at multiple heights. In some plots, whether due to the number of trees within the plot or inaccessibility, not every tree was sampled.

The height (a.g.l.) of all branches, except those collected using a shotgun, were measured directly using a measuring tape that was attached to the cutting device. For branches sampled with a shotgun, the branch height was either measured using a laser hypsometer (Haglöf, Sweden), measuring tape, or, in a select few cases, was estimated from the lidar data. For each sampled branch, we calculated its relative height in the canopy, which was defined as the ratio between the field-measured branch height and maximum lidar return height within the plot.

The only differences in sampling between years were: 1) in 2016, 5-m diameter circular plots were used versus 5 x 5 m square plots in 2017, and 2) 3 and 10 leaves per height were sampled in 2016 and 2017, respectively. Plot shape was changed between years to increase plot size and to simplify sampling. The number of leaves collected per height was increased to better capture within branch variability in LMA.

After leaves were collected, reflectance measurements were made using a full-range (350 – 2500 nm) field spectrometer equipped with a leaf clip to estimate LMA using spectroscopic models. Leaf measurements were referenced against a measurement on a 99% white Spectralon panel (Labsphere, North Sutton, NH, USA) to derive relative reflectance. Measurements were typically taken immediately after collection; when that was not possible, leaves were placed in a plastic bag with a damp paper towel and stored in a cooler on ice until measurements could be made, within 2 hr. Reflectance spectra were measured in 2016 with a Fieldspec 3 spectrometer (Analytical Spectral Devices, Boulder, CO, USA) and in 2017 with a PSR 3500+ spectrometer (Spectral Evolution, Boston, MA, USA). After reflectance measurements were complete, leaf samples were stored in a cooler until leaf area measurements were made later the same day. Leaf area was measured on three leaves per branch using a LI-3100 leaf area meter (LI-COR Biosciences, Lincoln, NE, USA), after which samples were frozen and stored for further analysis. Once the samples were returned to the lab, they were dried to constant mass in a freeze dryer (> 120 hours) and weighed. Dry weights were divided by the projected fresh leaf area to calculate LMA.

LMA has shown to be robustly measurable from fresh leaf spectroscopy across a wide range of leaf types using spectrometers from multiple manufacturers (Serbin et al., 2019). As such, LMA was estimated for leaves that were not directly measured using spectroscopic models. Models were developed using partial least squares regression (PLSR), a common chemometric technique (Wold et al., 2001), in Python using the package 'scikit-learn' (Pedregosa et al., 2011). Spectroscopic models were built using linked reflectance and LMA measurements made during this study, and separate models were generated for each year to account for spectrometer-specific differences in reflectance measurements. Prior to model development, we removed spurious data points using a Bonferroni-corrected outlier detection test (Dupuis and Hamilton, 2000), less than 1% of data points were identified as outliers. Following outlier removal, the dataset was split randomly 50:50 into calibration and validation datasets. Using the calibration data, we then computed the optimal number of model components using the cross-validated predicted residual sum of squares (PRESS) statistic using the adjusted Wold's R as a selection criterion (p=0.05) (Li et al., 2002). The calibration dataset was used to build a series of 500 models, each model was built using a random 70 percent split of the calibration dataset. The 500 models were applied to the validation dataset and the mean predictions were compared to observed LMA values and model performance was assessed using the root mean squared error (RMSE), coefficient of determination (R^2) and bias. Following the accuracy assessment, 500 new permuted models were built using the entire dataset and were applied to the spectra of unmeasured leaves to estimate leaf-level LMA. Branch-level LMA was calculated as the average leaf-level LMA of the 3 or 10 leaves from each branch.

Top-of-canopy LMA

Branch-level LMA was scaled to the canopy level by averaging LMA from all sunlit branches from each plot. Predictive models linking field-measured canopy-level LMA and imaging spectroscopy data were developed using the same modeling approach, PLSR, that was used for developing leaf-level spectroscopic models. Plot spectra were extracted from a 7 x 7 pixel window around each plot center, which was a slightly larger window than the field plot area, to account for GPS and image registration error. All pixels within the 7 x 7 window were averaged, not discriminating between sunlit and shaded pixels, resulting in a single spectrum per plot. This approach makes our method more transferable to spaceborne imagers with larger pixel sizes in which shaded and sunlit portions of tree crowns will be mixed in pixels. When a plot was covered by multiples lines owing to flightline overlap, we averaged pixels from all flightlines to produce a single reflectance spectrum.

A range of regions of the reflectance spectrum have been used to develop predictive models for LMA from spectroscopy data in the literature. At the leaf level, the full spectrum (Yang et al., 2016), spectral region subsets (Ourcival et al., 1999; Serbin et al., 2014) and variable selection techniques (Le Maire et al., 2008; Zhao et al., 2013) have been employed. At the canopy level, the full spectrum (400-2500 nm) is generally used (Singh et al., 2015; Chadwick and Asner, 2016; Wang et al., 2019). However Ali et al. (2016) found that the SWIR region from 1500-2500 nm exhibited the strongest correlation with canopy-level LMA, which is consistent with research showing that the shortwave infrared (SWIR) contains a number of absorption features related to dry matter content (Peterson el al. 1988; Curran et al. 1989; Jacquemoud et al., 1996). To assess the impact of spectral region selection on estimating top-of-canopy LMA, we compared the results of models built using four spectral regions moving to progressively longer wavelengths: 1) full spectrum (400-2450 nm), 2) NIR and SWIR (800-2450 nm), 3) the full SWIR (1600-2450 nm), and 4) far SWIR (2000-2450 nm).

Prior to model development, we performed a Bonferroni-corrected outlier test and identified a single plot as a significant outlier, which was removed from further analysis. The optimal number of PLSR model components was selected by minimizing the cross-validated PRESS statistic using the adjusted Wold's R as a selection criterion ($p = 0.05$).

Transmittance

Lidar transmittance was calculated following the same form used by Parker et al. (2001) to model photosynthetically active radiation (PAR) transmittance from full-waveform lidar:

$$\tau(h) = 1 - \frac{N_{\geq h}}{N_{total}} \quad (2.1)$$

where τ is the lidar transmittance metric at height h above ground, $N_{\geq h}$ is the number of returns at or above height h and N_{total} is the total number of returns within the plot window. The fraction in equation 1 is equivalent to the interception/reflection rate of pulses above a given height. All returns were used when calculating transmittance metrics. Transmittance metrics were calculated at 1 m intervals throughout the canopy and were interpolated using a linear function to estimate transmittance at sampled branch heights in each plot.

Shallow lidar pulse penetration is a common issue in dense canopies where pulse energy may not reach the lower canopy, understory and ground (Figure 2.3). A lack of returns from within the canopy can result in an underestimation of transmittance. We compared a range of window sizes from 5-100 m and found that, with increasing window size, model performance rapidly increased up until 20 m, after which the model performance stabilized, followed by a rapid decline with window sizes greater than 50 m (Supplemental Figure S2.2). Based on these results we used a 20 m wide window around each plot to extract lidar returns for calculating transmittance.

Within-canopy LMA

Vertical gradients in LMA were modeled using multilevel linear regression (MLR). MLR was used to account for the hierarchical structure of the dataset in which variables could be divided into two levels: group (top-of-canopy LMA) and individual (transmittance and absolute and relative heights), where individual-level variables are nested within groups. MLR models present a compromise between complete and no-pooling of data within groups and result in lower standard errors compared to traditional linear regression modeling (Gelman and Hill, 2007). In addition, MLR models can be formulated such that coefficients, intercepts and slopes are modeled as a function of group-level predictors. Models were fit in R using the package 'lmer' (Bates et al., 2015), group- and individual-level predictors were fit as fixed effects, and plot ID was treated as a random effect. We compared a range of models, beginning with univariate models and sequentially increasing model complexity by including additional individual-level predictors and a group-level predictor along with interaction terms. Note that we reverse the values of relative height and transmittance such that values range from 0 at the top of the canopy to 1 at ground level, this has benefits for fitting no-intercept regression models based on top-of-canopy LMA; that is, LMA predicted at a the top of the canopy where both relative height and transmittance are equal to zero will be simply the prediction of top-of-canopy LMA derived from imaging spectroscopy because any modifiers in our model based on these two metrics will be multiplied by zero.

Model evaluation

The performance of both top-of-canopy LMA and within-canopy LMA models were assessed using a 5 by 5-fold repeated cross-validation. Data splits were performed at the plot level to ensure that test and training datasets were independent. For each training-test split, the training data were first used to develop a PLSR model to predict top-of-canopy LMA on the training dataset. These top-of-canopy LMA estimates were then used as inputs to the within-canopy MLR model along with the within-canopy training data. The derived top-of-canopy and within-canopy models were then applied to the test dataset in the same fashion, keeping the same test and training sets separate for each iteration. We report R^2, RMSE and %RMSE for both the training and test datasets.

Full-canopy LMA mapping

Following top-of-canopy and within-canopy model evaluation, we developed 3D maps of LMA across the entire study area using the best performing combination of models as determined by the out-of-sample performance metrics. The final model for implementation was generated using a permutation based approach whereby we generated 500 models each built using a random 70% of the data, we recorded the mean estimate predicted from the 500 models. Models were applied on 5 x 5 m horizontal pixel scale corresponding to the scale of field sampling and at 1 m intervals vertically. Downscaling of the imaging spectroscopy data utilized 5 x 5 pixel aggregation and averaging. Transmittance metrics were calculated at 1 m intervals using the 5 m pixel center for determining the neighborhood window center.

Results

Our dataset consisted of 59 plots, 18 sampled in 2016 and 41 in 2017. Fewer branches were sampled on average per plot in 2017 vs 2016 (12 vs 18 branches) to increase the number of plots sampled. A total of 14 broadleaf species were sampled during the study, 12 of which were present in the top of the canopy in at least one plot. Sugar maple (*A. saccharum*) was the most commonly sampled species accounting for 37% of the branches. Sugar maple is shade tolerant and is a ubiquitous understory species in the study area (Table 2.1). On average, 5.9 trees were sampled per plot and 84% of those had branches sampled at multiple heights with the canopy.

Independent validation of leaf-level spectroscopic models exhibited high accuracies for estimating LMA from fresh spectra for both years of measurements (ASD 2016: R^2: 0.98, RMSE: 2.9 g m^{-2}; PSR 2017: R^2: 0.96, RMSE 4.5 g m^{-2}, Supplemental Figures S2.3, S2.4). Branch-level LMA ranged from 20.2 - 120.7 g m^{-2}, while sampled branch heights ranged from 0.25 - 27.7 m a.g.l. (Figure 2.4). The number of species in each plot varied from 1-7, with a mean of 2.5; multiple species were sampled in 44 of 59 plots.

Top-of-canopy LMA

Cross-validated results of PLSR models for top-of-canopy LMA from imaging spectroscopy data varied in performance depending on spectral interval (Table 2.2). Model performance increased with narrower spectral ranges from full spectrum (400 - 2450 nm: R^2: 0.39, RMSE 12.7 g m^{-2}) to the far SWIR (2000 - 2450 nm: R^2: 0.57, RMSE 10.7 g m^{-2}) (Figure 2.5). We used the top performing model, far SWIR, for the remainder of the analysis.

Within-canopy LMA

Within-canopy variables—height, relative height and lidar transmittance—all correlated positively with LMA (Figure 2.6). Univariate models which considered only within-canopy variables ranged widely in predictive performances: transmittance (R^2: 0.61, RMSE: 10.9 g m^{-2}) was the best performing, followed by relative height (R^2: 0.43, RMSE 13.2 g m^{-2}) and height (R^2: 0.14, RMSE 16.3 g m^{-2}).

Among the model forms tested, we found Eq. 2.2 exhibited the best results based on metrics of model performance, parsimony and interpretability (R^2: 0.78, RMSE 8.3 g m^{-2}, Figure

2.7), using a no-intercept model as described above. (See supplemental Table S2.1. for results of all tested models).

$$LMA(h) = LMA_{toc} + \tau_{inv_{20m}}(h) \cdot (\beta_0 + LMA_{toc} \cdot \beta_1 + rh_{inv}(h) \cdot \beta_2) \tag{2.2}$$

where

$$h = height\ above\ ground\ (m)$$

$$LMA_{toc} = Top\ of\ canopy\ LMA$$

$$\tau_{inv_{20m}} = Inverted\ transmittance\ of\ window\ width\ 20\ m\ at\ height\ h$$

$$rh_{inv} = Inverted\ relative\ height\ at\ height\ h$$

Functionally, this model estimates LMA within a canopy as a function of top-of-canopy LMA, relative position in the canopy and transmittance. Regression coefficients modify the slope of transmittance as a function of relative height and top-of-canopy LMA.

Cross validation metrics varied across species (R^2: 0.35 – 0.9; RMSE: 5.6 – 11.1 g m^{-2} ; Table 2.4). With the exception of *Ostrya virginiana*, which displayed little variation in LMA (23.5 - 36.3 g m^{-2}), the within-canopy model was able to explain at least 50% of the variation in within-canopy LMA and at least 70% for 8 of the 14 species sampled. Normalized RMSE was less than or equal to 15% for all but 4 species (*O. virginiana, C. cornuta, P. tremuloides, Prunus spp.).* In an analysis of residuals, means for sugar maple, river birch, ironwood, red oak and bigtooth and trembling aspen showed small but significant differences from 0 ($p < 0.01$, Figure 2.8a). The mean and median residuals for all species were within +/- 7 g m^{-2}, which is lower than the RMSE of the top-of-canopy LMA model. Likewise, the residuals for canopy dominant trees differed from 0 ($p < 0.01$), but by less than 4 g m^{-2} on average (Figure 2.8b).

Three-dimensional LMA mapping

Three-dimensional maps of LMA were generated using the combination of the far SWIR PLSR model to estimate top-of-canopy LMA and Eq 2.2. to estimate within-canopy LMA. Overall accuracy of the coupled model considering both top-of-canopy LMA and within-canopy LMA estimates was high ($R^2 = 0.82$; RMSE: 8.5 g m^{-2}).

We applied the model to entire study area and highlight a subset of the CHEQ site in three different visualizations of the 3D patterns in LMA: a horizontal map (Figure 2.9a), a profile view across a transect (Figure 2.9b) and vertical profiles for several forest types along the transect (Figure 2.9d).

The horizontal map displays LMA at three heights: top-of-canopy, 5 m into the canopy and 10 m into the canopy, in the red, blue and green channels, respectively. Areas with relatively high LMA throughout the canopy are colored white, and include an open-grown oak stand (Oo) and aspen stand (Ta) annotated on the map. Purple regions, like the thinned oak stand (To), indicate relatively high LMA in the lower canopy, while the darkly colored maroon regions indicate relatively low LMA throughout the canopy and are generally representative of sugar maple stands (Sm).

Discussion

Here we demonstrate a novel method using imaging spectroscopy to estimate top-of-canopy LMA and lidar-derived metrics of within-canopy environmental gradients to map 3D profiles of within-canopy LMA. Our model works within northern temperate broadleaf forests and is independent of information on horizontal or vertical species composition. Prior studies have used imaging spectroscopy to map top-of-canopy LMA or scaled whole-canopy LMA, but this study is the first of its kind to map LMA at discrete intervals throughout the canopy.

The straightforward and computationally efficient lidar transmittance metric we used captured a large portion of the variation in within-canopy LMA. From a technical perspective, our comparison of transmittance window sizes highlights the importance of sufficient lidar beam penetration to accurately characterize understory conditions through the depth of the canopy. In addition to increasing the number of lower canopy returns increasing the window size also accounts for the neighboring canopy structure which impacts the local light environment. For our dataset a window size of 20 m enabled measurement of enough discrete lidar returns to accurately represent 3D variation in canopy structure as it controls vertical distribution in LMA. We found increasing window beyond 20 m provided no benefit to modeling within-canopy LMA because of decreasing spatial autocorrelation in canopy structure, thus providing less horizontal detail in the vertical structure of canopies. For data collected under different sensor configurations this may differ as the ability of a lidar sensor adequately characterize canopy structure is not only a function of characteristics of the canopy itself, but also the lidar sensor properties, including wavelength, beam power, divergence and return density (Lim et al. 2003; Morsdorf 2009; Jakubowski et al. 2013).

Other methods exist for estimating transmittance from discrete return lidar, but usually require *a priori* knowledge of species composition and age classes to define light extinction coefficients (Parker et al., 2002). We developed our method explicitly to operate independent of species composition information, which potentially makes it more flexible for application in new study areas lacking such information. Full waveform lidar offers the potential to provide greater detail on structural characteristics of forest canopies driving within-canopy radiation regimes compared to discrete return lidar, but was not used in this study due to a sensor malfunction. Waveform processing methods such as deconvolution and decomposition offer the ability to extract a greater number of returns (Zhou et al., 2017) or estimate backscattering cross sections (Wagner et al., 2006), that may relate more specifically to leaf/plant area.

Our modeling results highlight the importance of an accurate estimate of top-of-canopy LMA to characterize within-canopy vertical variation in LMA. We found that restricting the wavelength region to the far SWIR (2000 – 2450 nm) resulted in the best performing model, this region of the spectrum is known to contain absorption features related to dry matter content including proteins, starch, sugars and cellulose (Curran 1989; Jacquemoud et al., 1996). Conversely models built using the full VNIR-SWIR range performed poorly, possibly a result of overfitting to pigment absorption features or canopy structure induced effects that are not generalizable across the entire dataset. Inclusion of top-of-canopy LMA as a predictor improved within-canopy model performance compared to models using only height and transmittance metrics as predictors (R^2: 0.69 vs. 0.78; Supplemental Table S2.1). The top-of-canopy LMA serves two roles in the 3D model: first, it acts as a starting point for the within-canopy gradient of decreasing LMA and, second, it defines the slope of the relationship between LMA and transmittance, as plots with higher top-of-canopy LMA show steeper LMA declines within the canopy—i.e., larger values for the $\tau_{inv_{20m}}(h) \cdot (\beta_0 + LMA_{toc} \cdot \beta_1 + rh_{inv}(h) \cdot \beta_2)$ term in Equation 1 (see β coefficients in Table 2.3). The interaction terms in Eq. 2.2 modify the transmittance slope to account for the fact that LMA largely converges to a small range of values at the bottom of the canopy (~20-40 g m^{-2}) irrespective of the value at the top of the canopy, where the range of LMA is large (~50-120 g m^{-2}). Interestingly, our results suggest a generalized relationship describing within-canopy decreases in LMA in these temperate broadleaf deciduous forests, independent of either canopy species or subcanopy species identity (Figures 2.6b and 2.6c). Our field data demonstrate that in multi-species plots, where species vary through the vertical profile, trends in LMA generally follow a continuous pattern regardless of species turnover (illustrated for individual plots in Fig. S2.6). Moreover not only do we see LMA decline within a given tree of a species, there is also vertical species-turnover that corresponds to shade tolerance, and these shade tolerant species also have lower LMA as well. The fact that these patterns can be modeled using remote sensing may enable testing the generality of the relationship across a range of broadleaf forest types.

Our model used relative rather than absolute height above ground as an independent variable, and moreover we show that absolute height had a weaker explanatory power than relative height (Supplemental Table S2.1). While others have shown a strong relationship between LMA and absolute height (Koch et al., 2004; Cavaleri et al., 2010), these studies have focused on much taller trees than in our study area. We expect that hydraulic constraints may play a weaker role in regulating LMA through the canopy in these northern temperate forests, and expect that a similar model may need to leverage absolute height for taller forests in which absolute height plays a more significant hydraulic role on leaf development. It is not clear what physiological process relative height captures in our model, although it may simply be compensating for limitations in characterizing lower canopy vertical structure due to lidar beam attenuation or covarying with other environmental conditions driving LMA variation like temperature, humidity or windspeed.

Ultimately, the utility in our new approach will be the generation of voxels to represent 3D trait variation, potentially applicable for modeling canopy processes. However, our 2-dimensional maps of 3D patterns in LMA reveal unique patterns not visible from the visible imagery (Figure 2.9a,c). In particular, the maps highlight the legacies of logging, selective logging and other disturbances. This results in highly variable, but spatially coherent patterns in within-canopy LMA that is otherwise obscured by relatively dense stands. Of note are the variable patterns seen in the three oak stands highlighted in Figure 2.9, a thinned oak stand (To), a closed canopy oak stand (Co) and an open-grown oak stand (Oo). At the top of the canopy the thinned and closed stands show similar values in LMA, 104 and 105 g m^{-2}, respectively, while the open-grown stand is much higher at 119 g m^{-2}. This difference may be a result of site-specific differences in local microclimate and/or soil moisture in the open-grown site relative to the closed and thinned sites, resulting in higher LMA (Potter et al., 2001; Abrams et al., 1994). However, when comparing within-canopy gradients in LMA the closed and thinned sites quickly diverge. The closed stand shows a sharp decline in LMA through the canopy while the within-canopy gradient of LMA in the thinned stand is shallower owing to increased light penetration, a pattern that is consistent with experimental treatments (Chiang and Brown, 2010). A key insight from this effort is not only that canopy structure is spatially heterogeneous and hence so is full-canopy LMA, but that this variation may be significant to our understanding of within-canopy processes. This also important for understanding patterns of forest function, as the majority of temperate forests in this region have undergone some level of stand management or disturbance that is not apparent in passive imaging.

While this study focused on within-canopy patterns of LMA, other physiologically and ecologically relevant foliar traits also vary along canopy environmental gradients, including concentrations of total non-structural carbohydrates (Niinemets 1997) and phosphorus (Leuning et al., 1991), and chlorophyll to nitrogen ratios (Koike et al., 2001). Although not included in this study due to a lack of validation data, we also estimated a suite of traits using fresh-leaf and dry-ground spectroscopic models and found significant within-canopy patterns in several traits correlated with lidar transmittance including sugar concentration, chlorophyll A content and xanthophyll cycle pigment content (violaxanthin, antheraxanthin and zeaxanthin (VAZ)) (Supplemental Figure S2.5). VAZ, which play a photoprotective role in leaves and are known to correlate positively with light levels/transmittance, showed the strongest relationship with transmittance among the traits estimated ($R^2 = 0.49$) (Niyogi 1997; Hansen et al., 2002).

Here we focused on a single period of the growing season, but LMA is known to vary through the course of the growing season (Reich 1991; Yang et al. 2016). In addition to seasonal variation in absolute values of LMA, there may also be phenological variations in the relationship between top-of-canopy LMA and within-canopy LMA as it relates to forest vertical structure. For example, Coble et al. (2016) found that drivers of within-canopy variability in LMA in sugar maples varied during the growing season, driven by height early in the growing season and light environment later in the growing season. This suggests future directions of research in both ecological and remote sensing research testing the extent to which the relationships we describe are generalizable throughout the course of the growing season. This may also necessitate further testing the extent to which species identity conditions temporal patterns in 3D LMA.

As well, this study is specific to northern temperate broadleaf forests, and was not tested on similar species in other biomes, nor on physiognomically or physiologically different tree types such as conifers and evergreen broadleaves. We expect that different forest types will exhibit a generalizable pattern, a decrease in LMA with depth into the canopy, but due to differences in resource allocation strategies and canopy structure, the shapes of the relationships will differ. Future testing of the generality of our model could apply the model to different forest types to identify how model coefficients change by taxa.

Our mapping of 3D patterns in LMA has the potential to be coupled with recent efforts to model vertical LAI profiles and leaf area density using lidar (Tang et al., 2012; Kamoske et al., 2019) as a basis to estimate full canopy foliar biomass and nutrient content for use as inputs into fire (Perry et al., 2004), nutrient cycling (Grimm et al., 2003) and carbon accounting models (Hudiburg et al., 2009). Extensive airborne and spaceborne lidar (e.g., GEDI) combined with imaging spectroscopy may enable better characterization of the distribution of within-canopy processes, even if wall-to-wall mapping is not yet possible. Multi-layer canopy photosynthesis models that incorporate expected variation in physiologically important traits throughout the canopy can provide more accurate estimates of assimilation rates than more generalized methods like big-leaf models (Raulier et al.,1999). However, at present, most models do not explicitly include 3D variation in foliar traits.

Conclusion

This study is the first to employ imaging spectroscopy and lidar together to map 3D patterns in LMA, an important canopy functional trait that is widely used to characterize photosynthetic capacity of forests. Our method accurately estimated horizontal and vertical variation in LMA in broadleaf forests without taking into account species composition ($R^2 = 0.82$; RMSE: 8.5 g m^{-2}). Our work is an initial step, with further research into the generality of the relationships needed across different sensors, ecosystems and through time. As well, the integration of these data products into ecosystem process models requires testing. Critical to this research was the availability of coincident free and open high-resolution leaf-on lidar and imaging spectroscopy data, which until the NEON AOP was deployed was rare. Separately, each technology addresses different needs, but the true value of imaging spectroscopy and lidar may be in their combined, complementary use. Finally, new or planned spaceborne hyperspectral (ie. PRISMA, HISUI, CHIME and SBG) and lidar systems (GEDI) will provide opportunities to build on our work and quantify full-canopy physiological variation on a global scale.

Acknowledgments

Thank you to Andrew Jablonski, Aidan Mazur, Benjamin Spaier, John Clare, Brendan Heberlein, Ittai Herrmann, Abigail Ernst, Hannah Manninen and Alex Brito for providing field assistance. I am also grateful to Tedward Erker for providing valuable insights into the statistical analysis and Tristan Goulden for guidance on NEON data processing.

References

Abrams, M. D., Kubiske, M. E., Mostoller, S. A. 1994. Relating wet and dry year ecophysiology to leaf structure in contrasting temperate tree species. Ecology. 75(1), 123-133.

Ali, A. M., Skidmore, A. K., Darvishzadeh, R., van Duren, I., Holzwarth, S., Mueller, J. 2016. Retrieval of forest leaf functional traits from HySpex imagery using radiative transfer models and continuous wavelet analysis. ISPRS Journal of Photogrammetry and Remote Sensing. 122, 68-80.

Aranda, I., Pardo, F., Gil, L., Pardos, J. A. 2004. Anatomical basis of the change in leaf mass per area and nitrogen investment with relative irradiance within the canopy of eight temperate tree species. Acta Oecologica. 25(3), 187-195.

Asner, G. P., Anderson, C. B., Martin, R. E., Tupayachi, R., Knapp, D. E., & Sinca, F. 2015. Landscape biogeochemistry reflected in shifting distributions of chemical traits in the Amazon forest canopy. *Nature Geoscience*, *8*(7), 567-573.

Bates, D., Maechler, M., Bolker, B., Walker, S., Christensen, R. H. B., Singmann, H., ... Grothendieck, G. 2011. Package ‘lme4’. Linear mixed-effects models using S4 classes. R package version, 1-1.

Cavaleri, M. A., Oberbauer, S. F., Clark, D. B., Clark, D. A., Ryan, M. G. 2010. Height is more important than light in determining leaf morphology in a tropical forest. Ecology. 91(6), 1730-1739.

Chadwick, K., Asner, G. 2016. Organismic-scale remote sensing of canopy foliar traits in lowland tropical forests. Remote Sensing. 8(2), 87.

Chiang, J. M., Brown, K. J. 2010. The effects of thinning and burning treatments on within-canopy variation of leaf traits in hardwood forests of southern Ohio. Forest Ecology and Management. 260(6), 1065-1075.

Coble, A. P., Cavaleri, M. A. 2014. Light drives vertical gradients of leaf morphology in a sugar maple (Acer saccharum) forest. Tree Physiology. 34(2), 146-158.

Coble, A. P., VanderWall, B., Mau, A., Cavaleri, M. A. 2016. How vertical patterns in leaf traits shift seasonally and the implications for modeling canopy photosynthesis in a temperate deciduous forest. Tree Physiology. 36(9), 1077-1091.

Cohen, W. B., Goward, S. N. 2004. Landsat's role in ecological applications of remote sensing. Bioscience. 54(6), 535-545.

Colgan, M., Baldeck, C., Féret, J. B., Asner, G. 2012. Mapping savanna tree species at ecosystem scales using support vector machine classification and BRDF correction on airborne hyperspectral and LiDAR data. Remote Sensing. 4(11), 3462-3480.

Curran, P. J. 1989. Remote sensing of foliar chemistry. *Remote sensing of Environment*, *30*(3), 271-278.

Du, L., Gong, W., Shi, S., Yang, J., Sun, J., Zhu, B., Song, S. 2016. Estimation of rice leaf nitrogen contents based on hyperspectral LIDAR. International journal of applied earth observation and geoinformation. 44, 136-143.

Dupuis, D. J., Hamilton, D. C. 2000. Regression residuals and test statistics: Assessing naive outlier deletion. Canadian Journal of Statistics. 28(2), 259-275.

Ellsworth, D. S., Reich, P. B. 1993. Canopy structure and vertical patterns of photosynthesis and related leaf traits in a deciduous forest. Oecologia. 96(2), 169-178.

Fleck, S., Van Der Zande, D., Schmidt, M., Coppin, P. 2004. Reconstructions of tree structure from laser-scans and their use to predict physiological properties and processes in canopies. International Archives of Photogrammetry, Remote Sensing and Spatial Information Sciences. 36(8), W2

Gelman, A., Hill, J. 2007. Data analysis using regression and hierarchical/multilevel models. New York, NY: Cambridge.

Goulden, T. 2019. Neon algorithm theoretical basis document (ATBD): Neon elevation (DTN and DSM). Technical Report NEON.DOC.002390, NEON.

Grimm, N. B., Gergel, S. E., McDowell, W. H., Boyer, E. W., Dent, C. L., Groffman, P., ...McClain, M. E. 2003. Merging aquatic and terrestrial perspectives of nutrient biogeochemistry. Oecologia. 137(4), 485-501.

Hakala, T., Suomalainen, J., Kaasalainen, S., Chen, Y. 2012. Full waveform hyperspectral LiDAR for terrestrial laser scanning. Optics Express. 20(7), 7119-7127.

Hansen, U., Fiedler, B., Rank, B. 2002. Variation of pigment composition and antioxidative systems along the canopy light gradient in a mixed beech/oak forest: a comparative study on deciduous tree species differing in shade tolerance. Trees. 16(4-5), 354-364.

Hudiburg, T., Law, B., Turner, D. P., Campbell, J., Donato, D., Duane, M. 2009. Carbon dynamics of Oregon and Northern California forests and potential land-based carbon storage. Ecological Applications. 19(1), 163-180.

Jacquemoud, S., Ustin, S. L., Verdebout, J., Schmuck, G., Andreoli, G., & Hosgood, B. 1996. Estimating leaf biochemistry using the PROSPECT leaf optical properties model. *Remote sensing of environment*, *56*(3), 194-202.

Jakubowski, M. K., Guo, Q., & Kelly, M. 2013. Tradeoffs between lidar pulse density and forest measurement accuracy. *Remote Sensing of Environment*, *130*, 245-253.

Kamoske, A. G., Dahlin, K. M., Stark, S. C., Serbin, S. P. 2019. Leaf area density from airborne LiDAR: Comparing sensors and resolutions in a temperate broadleaf forest ecosystem. Forest Ecology and Management. 433, 364-375.

Kampe, T. U., Johnson, B. R., Kuester, M. A., Keller, M. 2010. NEON: the first continental-scale ecological observatory with airborne remote sensing of vegetation canopy biochemistry and structure. Journal of Applied Remote Sensing. 4(1), 043510.

Kampe, T. U., McCorkel, J., Hamlin, L., Green, R. O., Krause, K. S., Johnson, B. R. 2011. Progress in the development of airborne remote sensing instrumentation for the National Ecological Observatory Network. In Remote Sensing and Modeling of Ecosystems for Sustainability VIII. International Society for Optics and Photonics. 8156, 81560A.

Kampe, T., Gallery W., Goulden T., Leisso K., Krause K. 2016. NEON Imaging Spectrometer Geolocation Algorithm Theoretical Basis Document. Technical Report NEON.DOC.001290, NEON.

Koch, G. W., Sillett, S. C., Jennings, G. M., Davis, S. D. 2004. The limits to tree height. Nature. 428(6985), 851.

Koike, T., Kitao, M., Maruyama, Y., Mori, S., Lei, T. T. 2001. Leaf morphology and photosynthetic adjustments among deciduous broad-leaved trees within the vertical canopy profile. Tree Physiology. 21(12-13), 951-958.

Lefsky, M. A., Cohen, W. B., Parker, G. G., Harding, D. J. 2002) Lidar remote sensing for ecosystem studies: Lidar, an emerging remote sensing technology that directly measures the three-dimensional distribution of plant canopies, can accurately estimate vegetation structural attributes and should be of particular interest to forest, landscape, and global ecologists. BioScience. 52(1), 19-30.

Leuning, R., Cromer, R. N., Rance, S. 1991. Spatial distributions of foliar nitrogen and phosphorus in crowns of Eucalyptus grandis. Oecologia. 88(4), 504-510.

Li, B., Morris, J., Martin, E. B. 2002. Model selection for partial least squares regression. Chemometrics and Intelligent Laboratory Systems. 64(1), 79-89.

Lim, K., Treitz, P., Wulder, M., St-Onge, B., & Flood, M. 2003. LiDAR remote sensing of forest structure. *Progress in physical geography*, *27*(1), 88-106.

Le Maire, G., François, C., Soudani, K., Berveiller, D., Pontailler, J. Y., Bréda, N., ... Dufrêne, E. 2008. Calibration and validation of hyperspectral indices for the estimation of broadleaved forest leaf chlorophyll content, leaf mass per area, leaf area index and leaf canopy biomass. Remote Sensing of Environment. 112(10), 3846-3864.

Martinez-Ramirez, D., Buller, G., McCarthy, A., Ren, X., Morak, A. W. S., Nichol, C., Woodhouse, I. 2012. Developing hyperspectral lidar for structural and biochemical analysis of forest data. In Proc. EARSEL Conf. Adv. Geosci. 1-11.

Messier, J., McGill, B. J., & Lechowicz, M. J. 2010) How do traits vary across ecological scales? A case for trait-based ecology. Ecology Letters, 13(7), 838-848.

Messier, J., McGill, B. J., Enquist, B. J., & Lechowicz, M. J. 2017. Trait variation and integration across scales: is the leaf economic spectrum present at local scales?. Ecography. 40(6), 685-697.

Morsdorf, F., Nichol, C., Malthus, T., & Woodhouse, I. H. (2009). Assessing forest structural and physiological information content of multi-spectral LiDAR waveforms by radiative transfer modelling. *Remote Sensing of Environment*, *113*(10), 2152-2163.

Nevalainen, O., Hakala, T., Suomalainen, J., Mäkipää, R., Peltoniemi, M., Krooks, A., Kaasalainen, S. 2014. Fast and nondestructive method for leaf level chlorophyll estimation using hyperspectral LiDAR. Agricultural and Forest Meteorology. 198, 250-258.

Niinemets, Ü. 1997. Role of foliar nitrogen in light harvesting and shade tolerance of four temperate deciduous woody species. Functional Ecology. 11(4), 518-531.

Niinemets, Ü. 1999. Research review. Components of leaf dry mass per area–thickness and density–alter leaf photosynthetic capacity in reverse directions in woody plants. The New Phytologist. 144(1), 35-47.

Niinemets, Ü. 2001. Global-scale climatic controls of leaf dry mass per area, density, and thickness in trees and shrubs. Ecology. 82(2), 453-469.

Niinemets, Ü., Keenan, T. F., & Hallik, L. 2015. A worldwide analysis of within-canopy variations in leaf structural, chemical and physiological traits across plant functional types. New Phytologist, 205(3), 973-993.

Niyogi, K. K., Björkman, O., Grossman, A. R. 1997. The roles of specific xanthophylls in photoprotection. Proceedings of the National Academy of Sciences, 94(25). 14162-14167.

Olpenda, A. S., Stereńczak, K., & Będkowski, K. 2018. Modeling solar radiation in the forest using remote sensing data: a review of approaches and opportunities. *Remote Sensing*, *10*(5), 694.

Ourcival, J. M., Joffre, R., Rambal, S. 1999. Exploring the relationships between reflectance and anatomical and biochemical properties in Quercus ilex leaves. New Phytologist, 143(2), 351-364.

Parker, G. G., Lefsky, M. A., Harding, D. J. 2001. Light transmittance in forest canopies determined using airborne laser altimetry and in-canopy quantum measurements. Remote Sensing of Environment. 76(3), 298-309.

Parker, G. G., Davis, M. M., Chapotin, S. M. 2002. Canopy light transmittance in Douglas-fir–western hemlock stands. Tree physiology. 22(2-3), 147-157.

Pedregosa, Fabian, Gaël Varoquaux, Alexandre Gramfort, Vincent Michel, Bertrand Thirion, Olivier Grisel, Mathieu Blondel…. 2011. Scikit-learn: Machine learning in Python. Journal of Machine Learning Research. 12, 2825-2830.

Perry, D. A., Jing, H., Youngblood, A., Oetter, D. R. 2004. Forest structure and fire susceptibility in volcanic landscapes of the Eastern High Cascades, Oregon. Conservation Biology. 18(4), 913-926.

Peterson, D. L., Aber, J. D., Matson, P. A., Card, D. H., Swanberg, N., Wessman, C., & Spanner, M. 1988. Remote sensing of forest canopy and leaf biochemical contents. *Remote Sensing of Environment*, *24*(1), 85-108.

Petter, G., Wagner, K., Wanek, W., Sánchez Delgado, E. J., Zotz, G., Cabral, J. S., Kreft, H. 2016. Functional leaf traits of vascular epiphytes: vertical trends within the forest, intra-and interspecific trait variability, and taxonomic signals. Functional Ecology. 30(2), 188-198.

Poorter, H., Niinemets, Ü., Poorter, L., Wright, I. J., Villar, R. 2009. Causes and consequences of variation in leaf mass per area (LMA): a meta-analysis. New Phytologist. 182(3), 565-588.

Potter, B. E., Teclaw, R. M., Zasada, J. C. 2001. The impact of forest structure on near-ground temperatures during two years of contrasting temperature extremes. Agricultural and Forest Meteorology. 106(4), 331-336.

Poulter, A. G., Olbrich, B. W., Dye, P. J. 1991. Sampling shoots from tall canopies with a balloon-hoisted cutting device. Australian Forestry. 54(1-2), 109-110.

Raulier, F., Bernier, P. Y., Ung, C. H. 1999. Canopy photosynthesis of sugar maple (*Acer saccharum*): comparing big-leaf and multilayer extrapolations of leaf-level measurements. Tree Physiology. 19(7), 407-420.

Reich, P. B., Walters, M. B., & Ellsworth, D. S. 1991. Leaf age and season influence the relationships between leaf nitrogen, leaf mass per area and photosynthesis in maple and oak trees. *Plant, Cell & Environment*, *14*(3), 251-259.

Richter, R., Schläpfer, D. 2015. Atmospheric/topographic correction for airborne imagery. ATCOR-4 user guide. Version 7.0.0.

Rogers, A., Medlyn, B. E., Dukes, J. S., Bonan, G., Von Caemmerer, S., Dietze, M. C., ...Prentice, I. C. 2017. A roadmap for improving the representation of photosynthesis in Earth system models. New Phytologist. 213(1), 22-42.

Roughgarden, J., Running, S. W., Matson, P. A. 1991. What does remote sensing do for ecology?. Ecology, 72(6). 1918-1922.

Schläpfer, D., Richter, R., Feingersh, T. 2014. Operational BRDF effects correction for wide-field-of-view optical scanners (BREFCOR). IEEE Transactions on Geoscience and Remote Sensing. 53(4), 1855-1864.

Serbin, S. P., Singh, A., McNeil, B. E., Kingdon, C. C., Townsend, P. A. 2014. Spectroscopic determination of leaf morphological and biochemical traits for northern temperate and boreal tree species. Ecological Applications. 24(7), 1651-1669.

Serbin, S. P., Wu, J., Ely, K. S., Kruger, E. L., Townsend, P. A., Meng, R., ... Rogers, A. 2019. From the Arctic to the tropics: multi-biome prediction of leaf mass per area using leaf reflectance. New Phytologist. 224(4), 1557-1568.

Sigrist, P., Coppin, P., Hermy, M. 1999. Impact of forest canopy on quality and accuracy of GPS measurements. International Journal of Remote Sensing. 20(18), 3595-3610.

Singh, A., Serbin S.P. , McNeil D.E, Kingdon C.C., Townsend P.A. 2015. Imaging spectroscopy algorithms for mapping canopy foliar chemical and morphological traits and their uncertainties. Ecological Applications. 25(8), 2180-2197.

Tang, H., Dubayah, R., Swatantran, A., Hofton, M., Sheldon, S., Clark, D. B., Blair, B. 2012. Retrieval of vertical LAI profiles over tropical rain forests using waveform lidar at La Selva, Costa Rica. Remote Sensing of Environment. 124, 242-250.

Todd, K. W., Csillag, F., & Atkinson, P. M. 2003. Three-dimensional mapping of light transmittance and foliage distribution using lidar. *Canadian Journal of Remote Sensing*, *29*(5), 544-555.

Vauhkonen, J., Hakala, T., Suomalainen, J., Kaasalainen, S., Nevalainen, O., Vastaranta, M., ... Hyyppä, J. 2013. Classification of spruce and pine trees using active hyperspectral LiDAR. IEEE Geoscience and Remote Sensing Letters. 10(5), 1138-1141.

Vose, J. M., Clinton, B. D., Sullivan, N. H., Bolstad, P. V. 1995. Vertical leaf area distribution, light transmittance, and application of the Beer–Lambert Law in four mature hardwood stands in the southern Appalachians. Canadian Journal of Forest Research. 25(6), 1036-1043.

Wagner, W., Ullrich, A., Ducic, V., Melzer, T., Studnicka, N. 2006. Gaussian decomposition and calibration of a novel small-footprint full-waveform digitising airborne laser scanner. ISPRS journal of Photogrammetry and Remote Sensing. 60(2), 100-112.

Wagner, W., Hollaus, M., Briese, C., Ducic, V. 2008. 3D vegetation mapping using small-footprint full-waveform airborne laser scanners. International Journal of Remote Sensing. 29(5), 1433-1452.

Wang, Z., Townsend, P. A., Schweiger, A. K., Couture, J. J., Singh, A., Hobbie, S. E., Cavender-Bares, J. 2019. Mapping foliar functional traits and their uncertainties across three years in a grassland experiment. Remote Sensing of Environment. 221, 405-416.

Wang, Z., Chlus, A., Geygan, R., Ye, Z., Zheng, T., Singh, A., Couture, J.J., Cavender-Bares, J., Kruger, E.L., Townsend, P.A. 2020. Foliar functional traits from imaging spectroscopy across biomes in eastern North America. New Phytologist.

Wold, S., Sjöström, M., Eriksson, L. 2001. PLS-regression: a basic tool of chemometrics. Chemometrics and Intelligent Laboratory Systems. 58(2), 109-130.

Wright, I. J., Reich, P. B., Westoby, M., Ackerly, D. D., Baruch, Z., Bongers, F., ...Flexas, J. 2004. The worldwide leaf economics spectrum. Nature. 428(6985), 821.

Wu, T., Zhang, P., Zhang, L., Wang, G. G., Yu, M. 2016. Morphological response of eight Quercus species to simulated wind load. PloS one. 11(9).

Yang, X., Tang, J., Mustard, J. F., Wu, J., Zhao, K., Serbin, S., Lee, J. E. 2016. Seasonal variability of multiple leaf traits captured by leaf spectroscopy at two temperate deciduous forests. Remote Sensing of Environment. 179, 1-12.

Zhao, K., Valle, D., Popescu, S., Zhang, X., Mallick, B. 2013. Hyperspectral remote sensing of plant biochemistry using Bayesian model averaging with variable and band selection. Remote Sensing of Environment. 132, 102-119.

Zhou, T., Popescu, S. C., Krause, K., Sheridan, R. D., Putman, E. 2017. Gold–A novel deconvolution algorithm with optimization for waveform LiDAR processing. ISPRS Journal of Photogrammetry and Remote Sensing. 129, 131-150.

Tables

Table 2.1 Field sampling summary

Species	Plots	Branches	Top-of-canopy branches	Mean Branch LMA (g m^{-2})	Range Branch LMA (g m^{-2})
Acer rubrum	10	33	2	52.6	33.0 - 86.1
Acer saccharum	39	301	22	40.5	23.2 - 94.9
Betula alleghaniensis	4	24	1	41.5	25.0 - 90.1
Betula papyrifera	7	30	4	51.5	29.7 - 102.6
Corylus cornuta	9	12	0	35.9	26.1 - 49.8
Fraxinus americana	8	24	7	61.2	20.2 - 102.8
Fraxinus nigra	7	51	7	51.8	26.2 - 100.4
Ostrya virginiana	8	17	0	28.5	23.5 - 36.3
Populus grandidentata	7	44	8	72	49.4 - 102.0
Populus tremuloides	13	64	21	74.1	52.9 - 102.1
Prunus spp.	6	13	2	56.4	36.6 - 88.6
Quercus rubra	18	144	21	71.7	32.2 - 120.7
Tilia americana	9	43	6	49.1	20.2 - 87.4
Ulmus americana	1	11	1	43.5	25.3 - 68.9

Table 2.2 Cross-validated PLSR top-of-canopy LMA results

Wavelengths (nm)	Components	Training			Test		
		R^2	RMSE	%RMSE	R^2	RMSE	%RMSE
400 - 2450	7	0.71	8.75	12.6	0.39	12.68	18.27
800 - 2450	6	0.7	8.84	12.74	0.46	11.91	17.15
1600 - 2450	6	0.73	8.49	12.24	0.54	10.99	15.83
2000 - 2450	6	0.73	8.39	12.08	0.57	10.67	15.37

Table 2.3 Within-canopy mean permuted model coefficients

Coefficient	Estimate
β_0	40.19
β_1	-0.80
β_2	-34.83

Table 2.4 Within-canopy LMA cross-validation metrics by species

Species	R^2	RMSE	NRMSE
Acer rubrum	0.69	8.13	0.15
Acer saccharum	0.5	7.02	0.13
Betula alleghaniensis	0.8	8.53	0.13
Betula papyrifera	0.86	5.62	0.09
Corylus cornuta	0.7	5.72	0.24
Fraxinus americana	0.78	9.37	0.11
Fraxinus nigra	0.63	8.37	0.14
Ostrya virginiana	0.35	6.08	0.47
Populus grandidentata	0.84	6.38	0.15
Populus tremuloides	0.5	8.6	0.3
Prunus spp.	0.51	9.71	0.27
Quercus rubra	0.77	11.14	0.13
Tilia americana	0.75	7.33	0.13
Ulmus americana	0.91	6.5	0.15

Figures

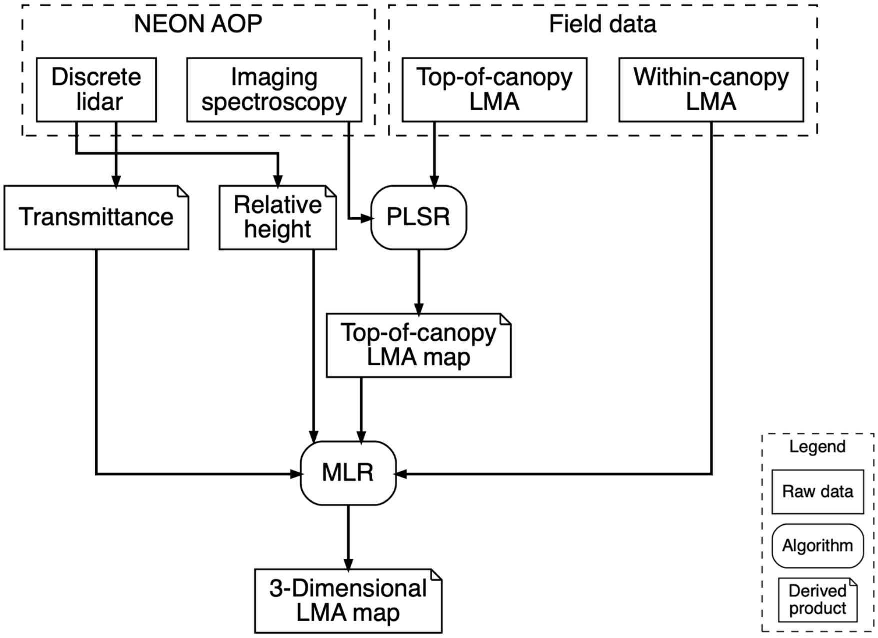

Figure 2.1 Three-dimensional LMA modeling workflow.

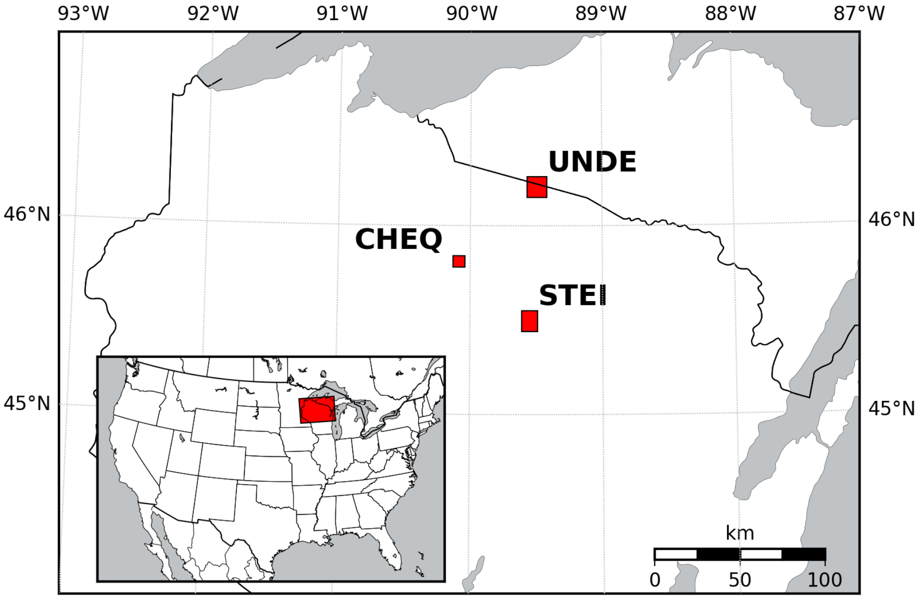

Figure 2.2 Flight boxes and sampling boundaries for the three sites within the NEON Great Lakes ecoregion.

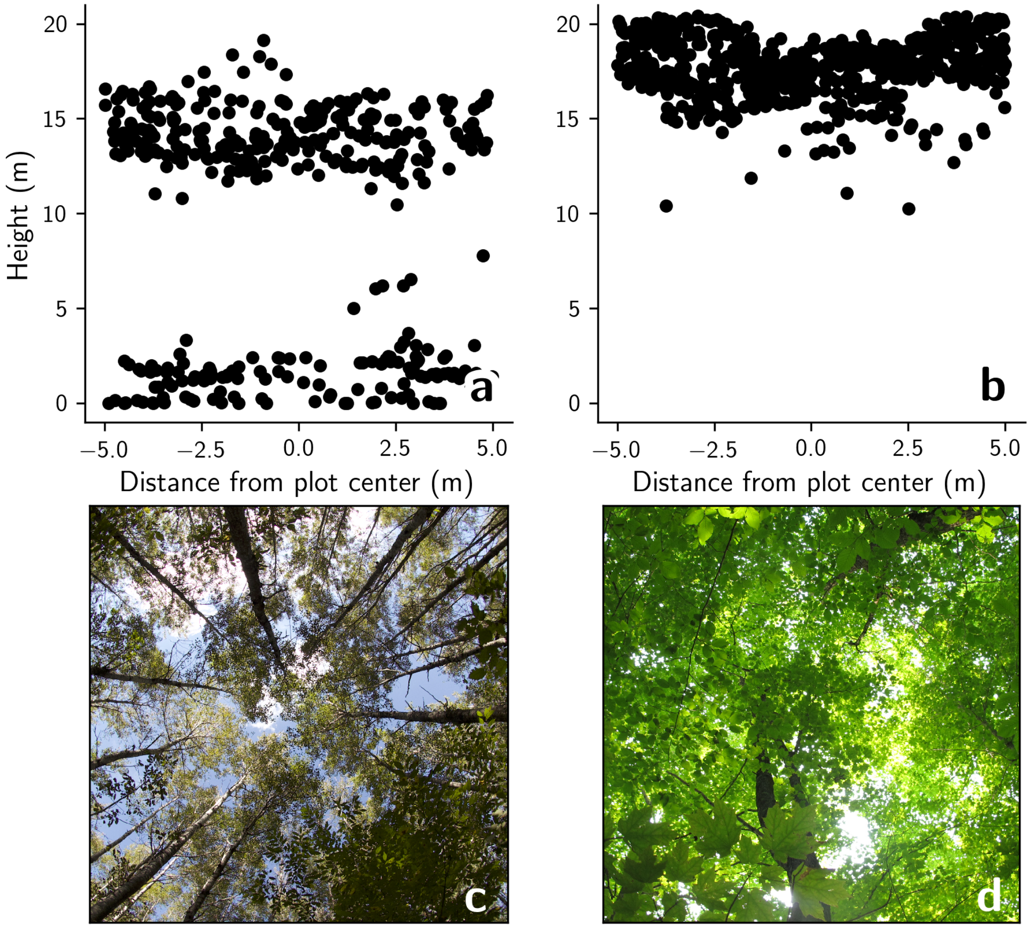

Figure 2.3 Example of varying lidar penetration depth from two plots: a trembling aspen stand (a,c) and sugar maple stand (b,d); a-b) profile view of all returns; c-d) upward looking field photos from each plot. Both plots have a large number of returns from the upper canopy and few to no returns from the middle of the canopy. In the aspen stand the lack of returns from the middle canopy is consistent with branching structure seen in the field photos, while the lack of returns in the maple stand is the result of near complete beam attenuation in the upper canopy.

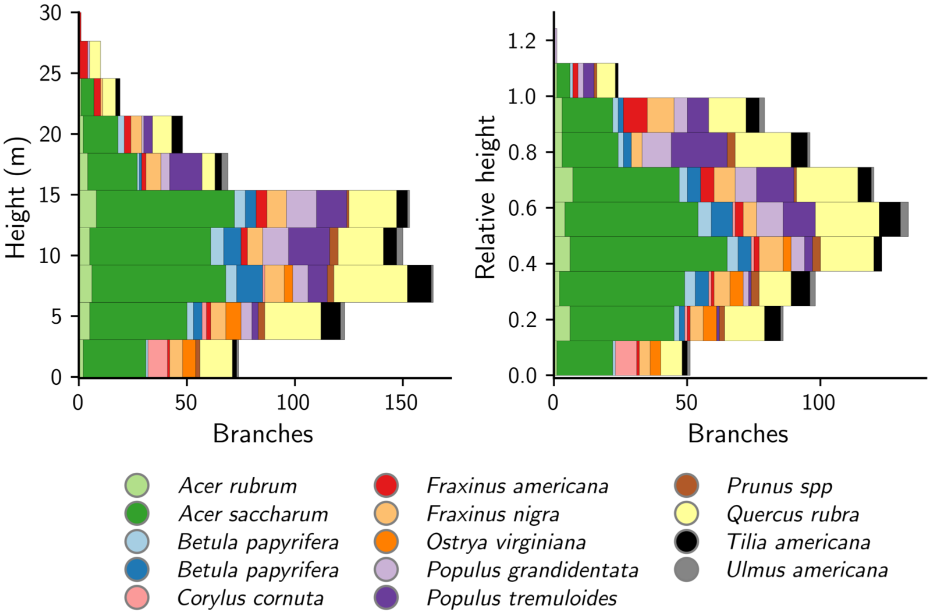

Figure 2.4 Distribution of sampled branches as a function of height and relative height. Note: some branches have relative heights slightly greater than 1 as a result of an underestimation of maximum canopy height by the lidar sensor.

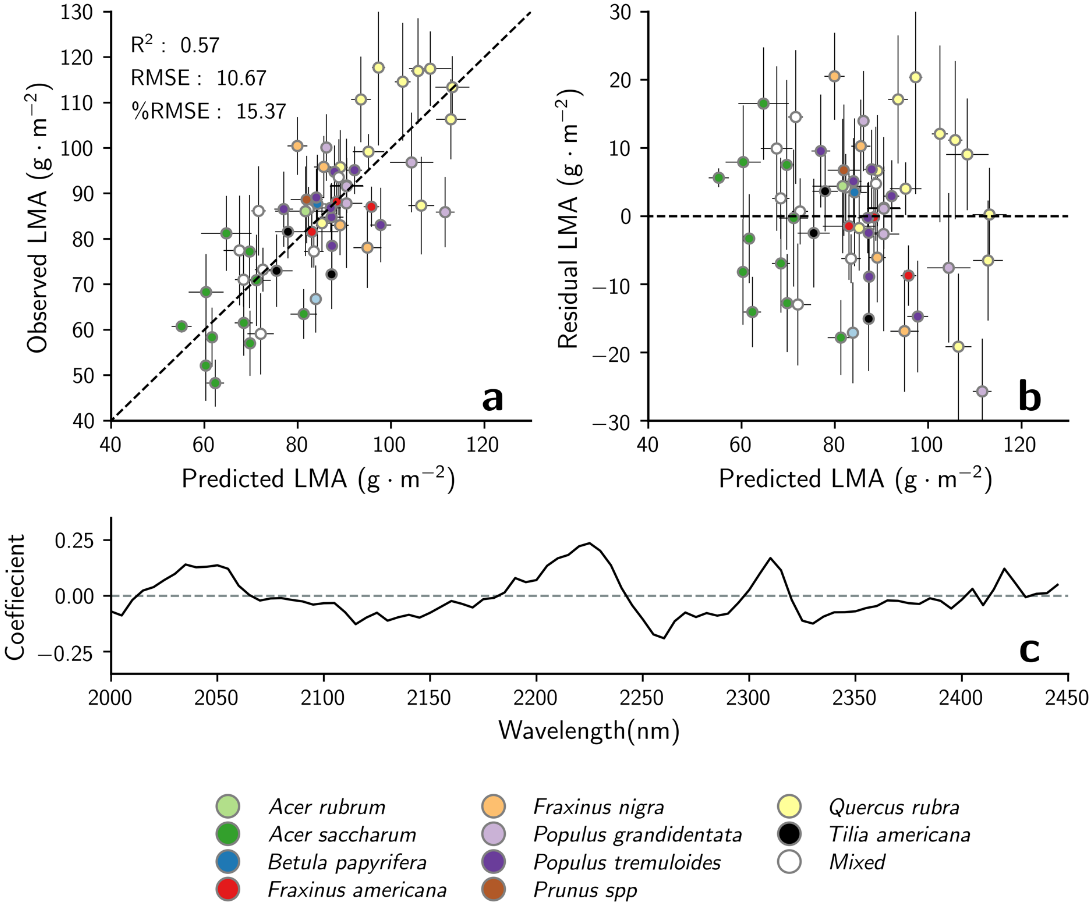

Figure 2.5 Out-of-sample validation results for the top preforming top-of-canopy PLSR model using wavelengths 2000-2450 nm. a) Mean predicted versus observed; b) residuals; c) PLSR model coefficients; X-axis error bars on a and b indicate +/- 1 standard deviation of out-sample LMA estimates across five cross-validation iterations; Y-axis error bars indicate +/- 1 standard deviation of within-branch field measured LMA. Dot colors indicate top-of-canopy species composition.

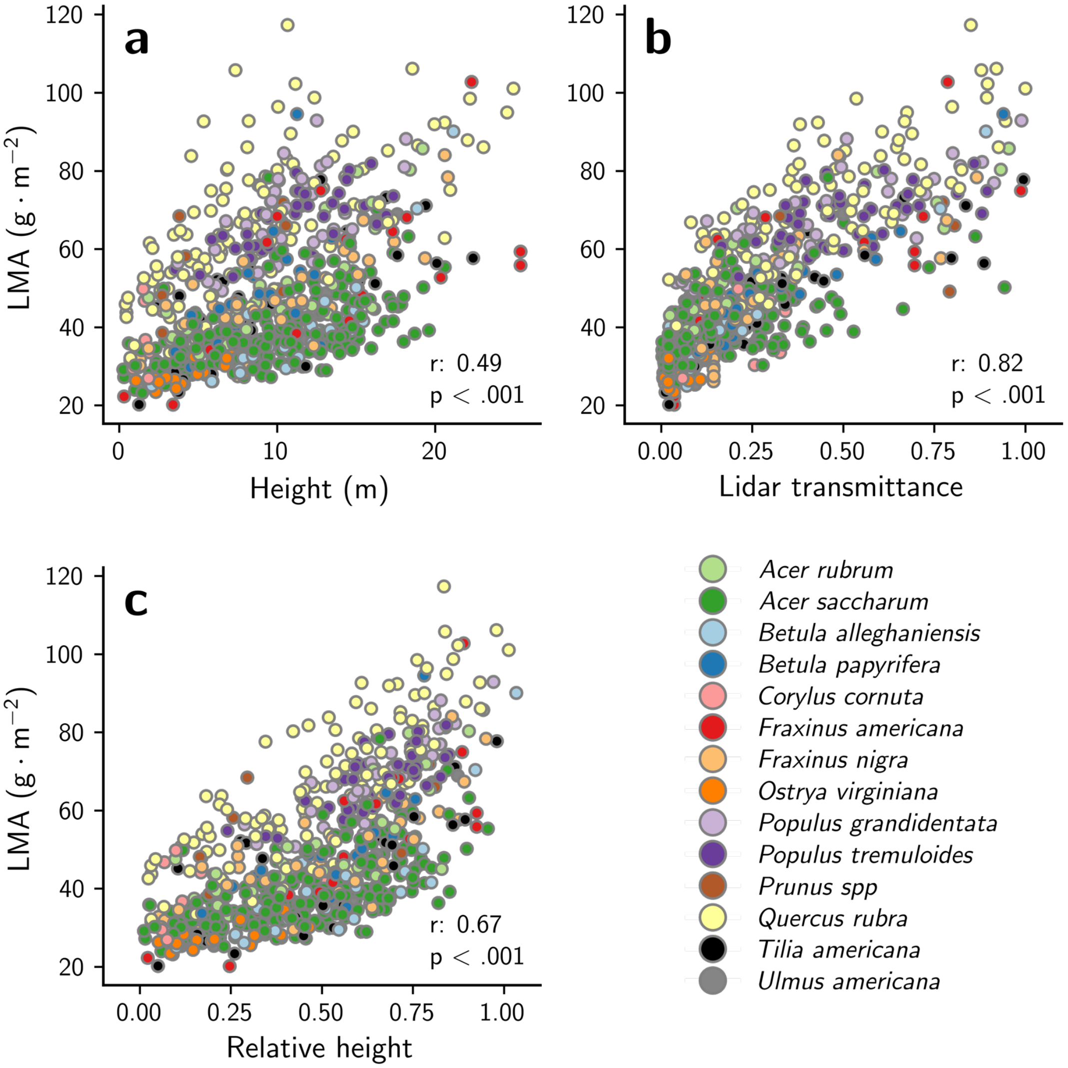

Figure 2.6 Comparison of field-measured within-canopy LMA against the three within-canopy covariates: a) height, b) transmittance and c) relative height.

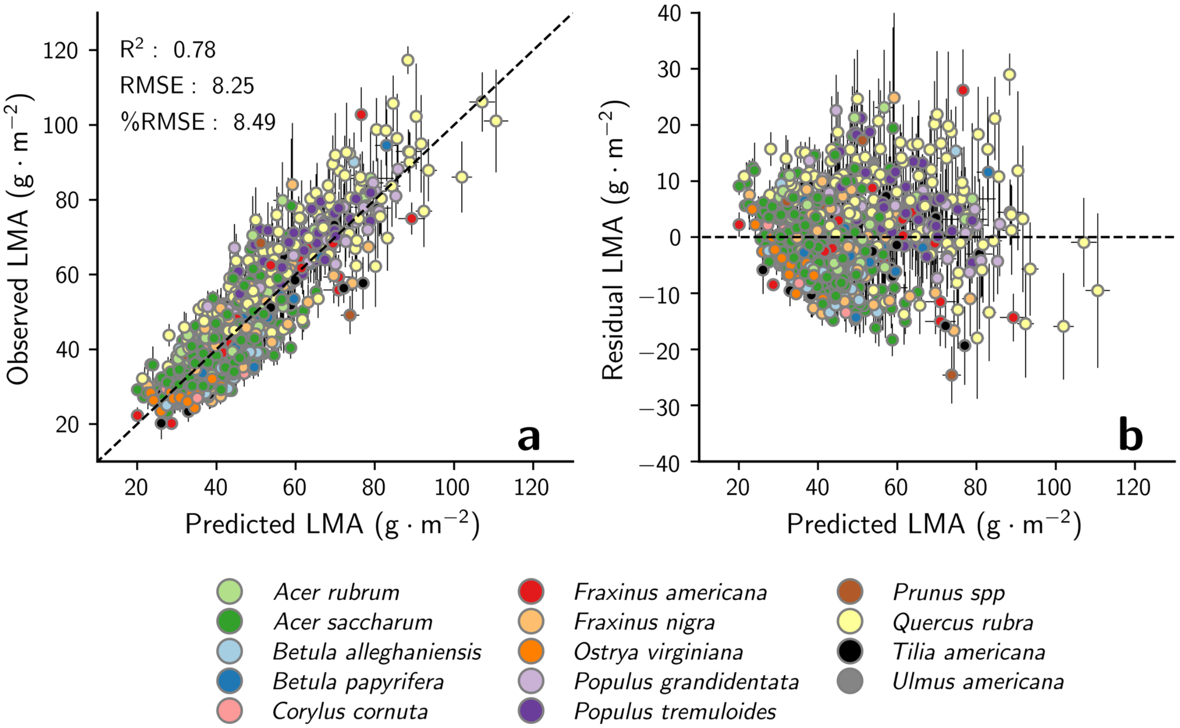

Figure 2.7 Out-of-sample results for best-performing within-canopy LMA model. a) Predicted versus observed scatter plot; b) Residual plot; X-axis error bars indicate +/- 1 standard deviation of out-of-sample LMA estimates across 5 cross-validation iterations; Y-axis error bars indicate +/- 1 standard deviation of within-sample field measured LMA

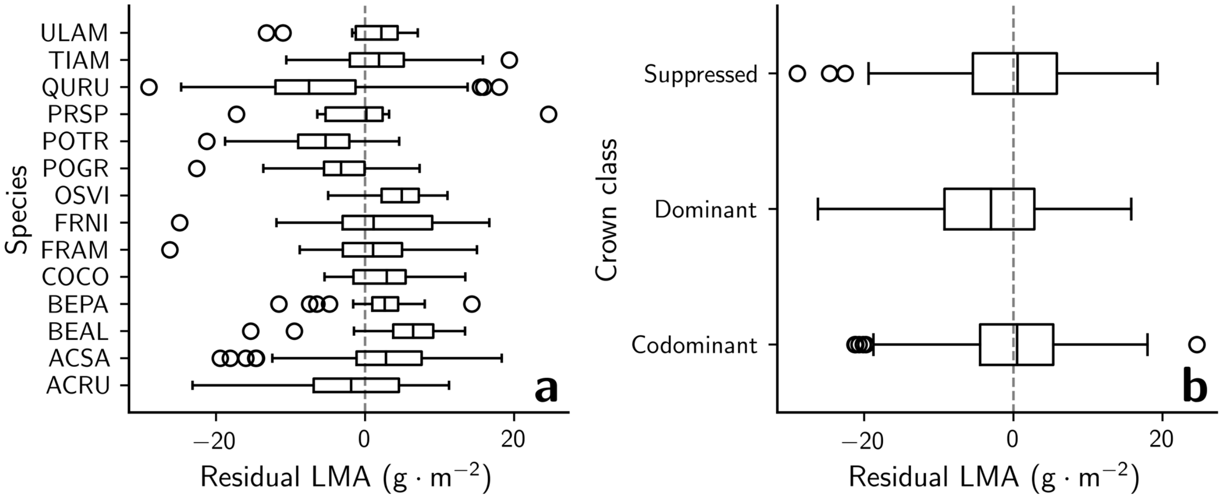

Figure 2.8 Distribution of within-canopy residuals grouped by a) species and b) crown class.

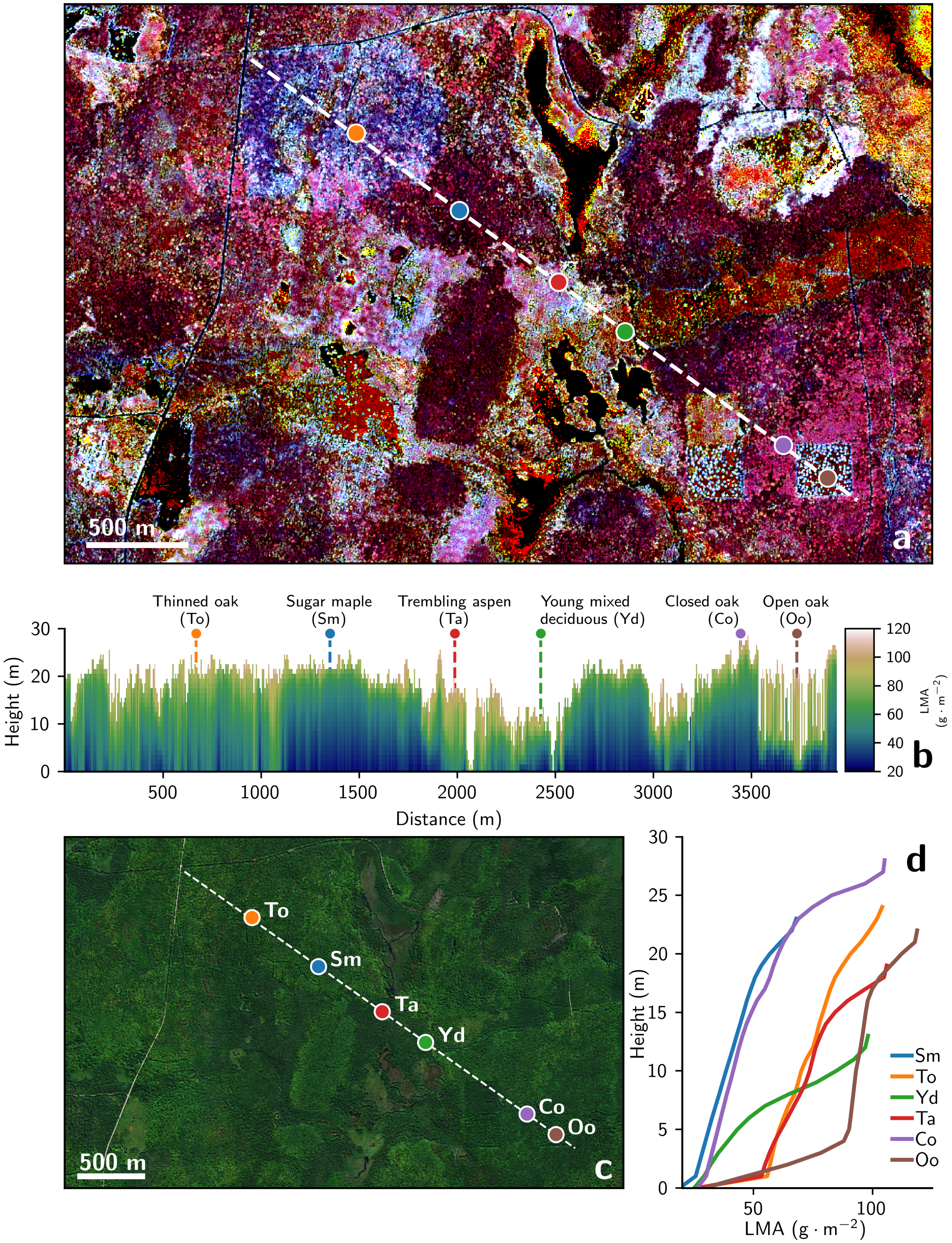

Figure 2.9 Results of three-dimensional LMA model applied to CHEQ (90.069 °W, 45.795° N). a) Two-dimensional RGB representation of three-dimensional patterns in LMA, R: Top-of-canopy LMA, G: LMA 5m into canopy, B: LMA 10m into canopy. b) Profile view of LMA transect; c) True color RGB image d) Height versus LMA for a set of individual 5 m pixels from forest types located on transect. Forest types: Thinned oak (To), Sugar maple (Sa), Trembling aspen (Ta), Young mixed deciduous (Yd), Closed canopy oak (Co), Open- grown oak (Oo).

Supplemental materials

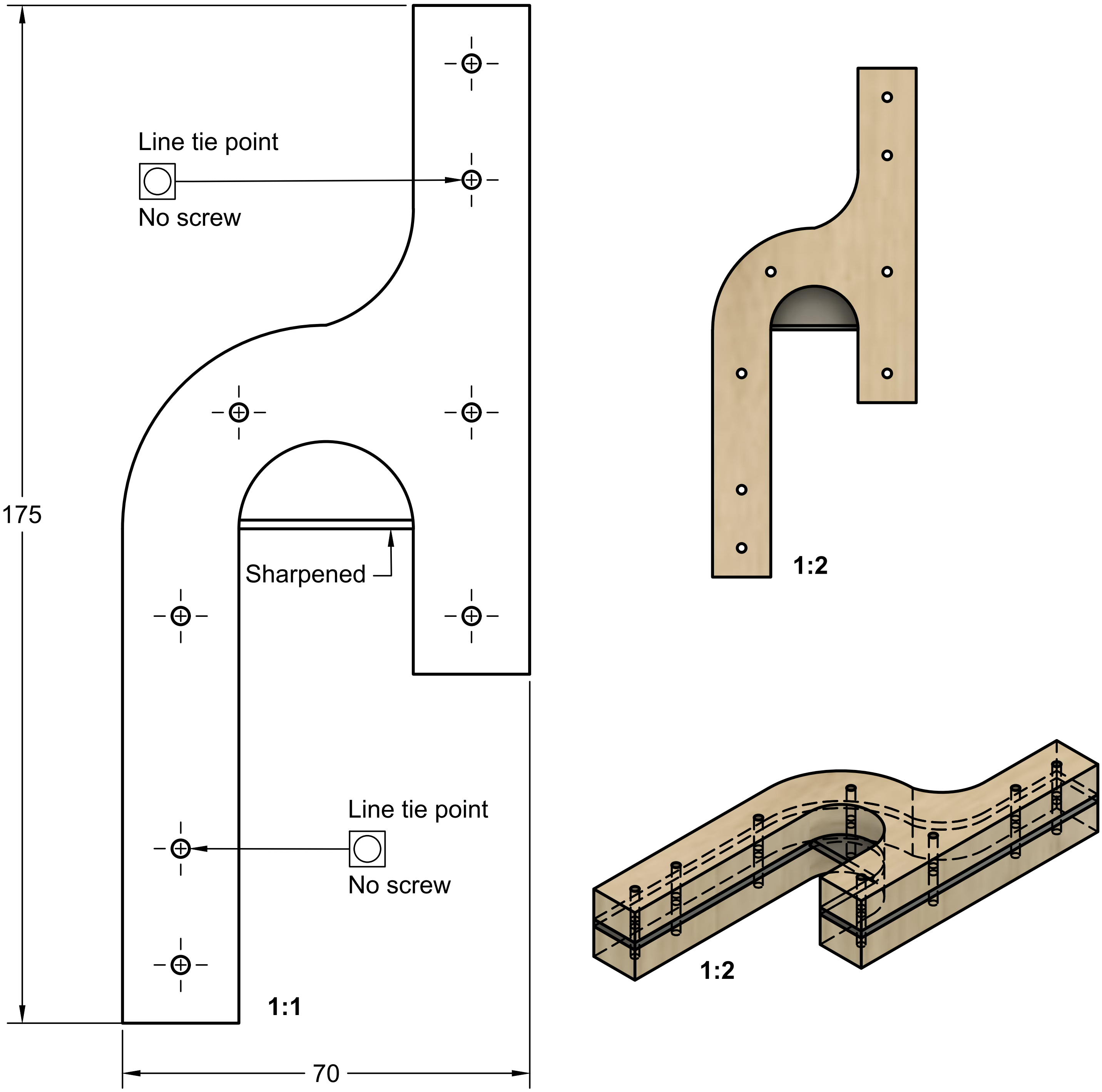

Figure S2.1 Top-of-canopy sampling device schematic

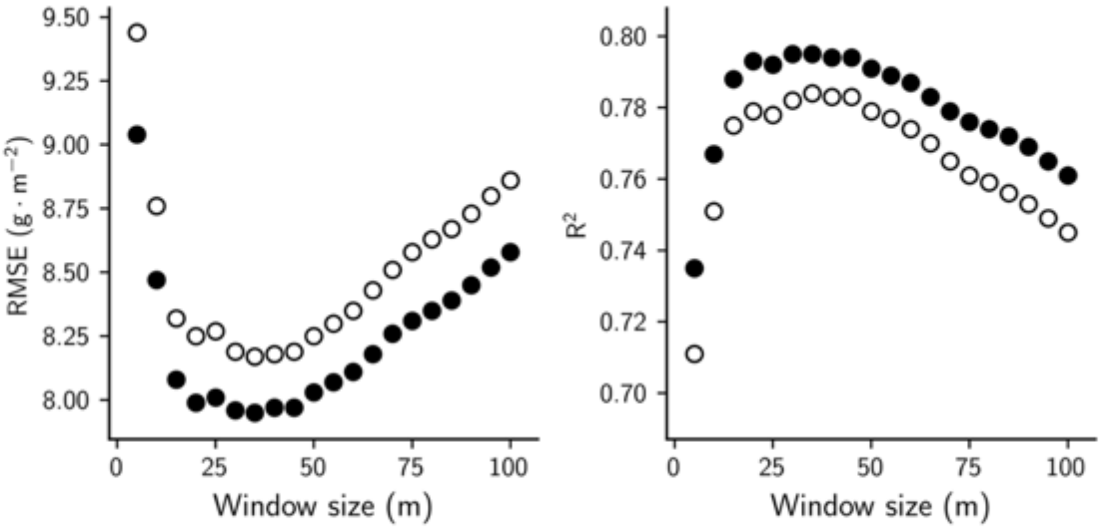

Figure S2.2 Comparison of lidar transmittance window width and performance metrics RMSE and R^2 for within-canopy LMA model (Eq. 2); (●) In-sample metric, (○) out-of-sample metric.

Trait	Leaf Mass per Area
Units	$g \cdot m^{-2}$
Components	15
Iterations	500
Samples	947
Spectrometer	ASD-FS3
Description	2016 LMA model

	n	Percent
Outliers	7	0.0073
Calibration	474	0.5
Validation	473	0.5

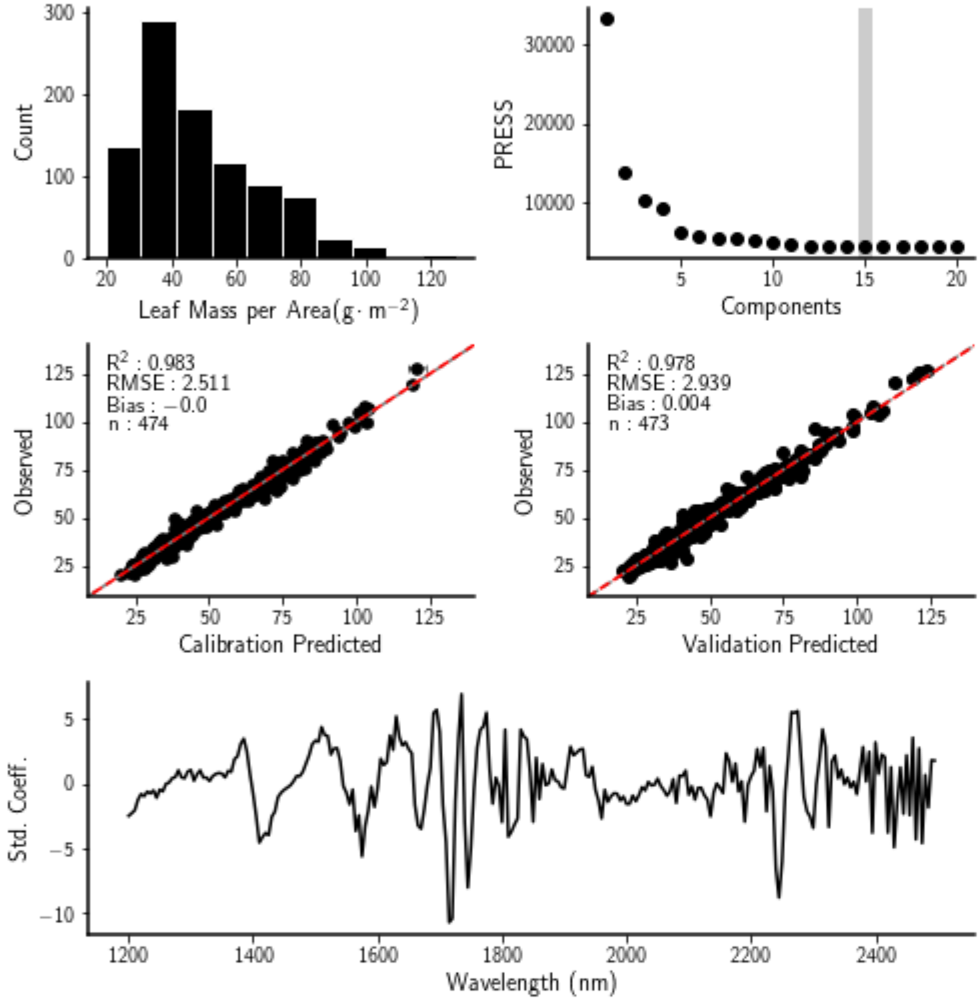

Figure S2.3 Leaf-level spectroscopic model calibration results for 2016 data collected with an ASD Field Spec 3

Trait	Leaf Mass per Area
Units	$g \cdot m^{-2}$
Components	10
Iterations	500
Samples	1473
Spectrometer	SE-PSR
Description	2017 LMA model

	n	Percent
Outliers	12	0.0081
Calibration	737	0.5
Validation	736	0.5

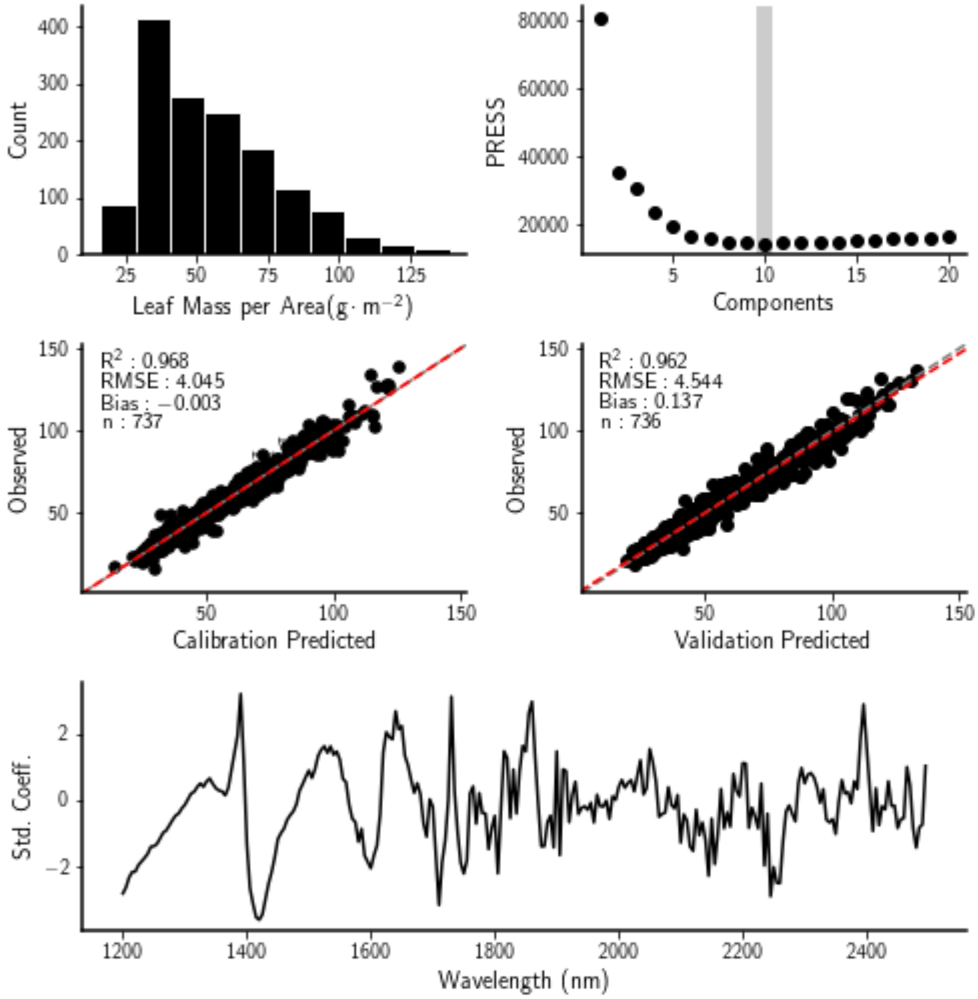

Figure S2.4 Leaf-level spectroscopic model calibration results for 2016 data collected with a Spectral Evolution PSR-3500+

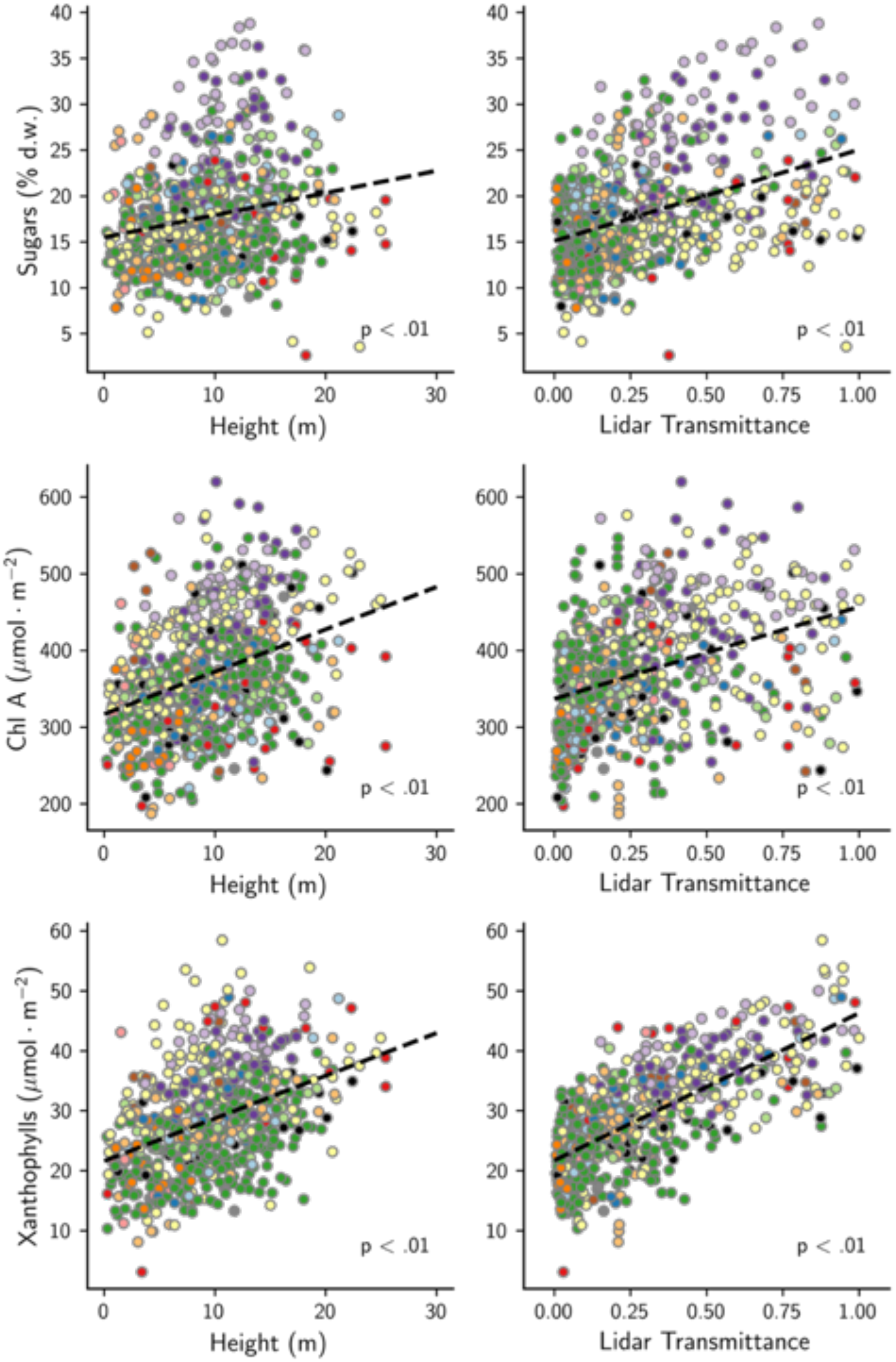

Figure S2.5 Linear regressions between within-canopy variables height (left column) and transmittance (right column) and fresh-leaf and dry-ground spectroscopic trait estimates.

Table S2.1 Cross validated within-canopy LMA results for all tested models, shaded row indicates model used in final analysis.

Model formula	Train			Test		
	R^2	RMSE	%RMSE	R^2	RMSE	%RMSE
$\beta_0 + \tau * \beta_1$	0.63	10.75	11.07	0.61	10.93	11.25
$\beta_0 + rh * \beta_1$	0.45	13.08	13.46	0.43	13.24	13.63
$\beta_0 + h * \beta_1$	0.16	16.13	16.61	0.14	16.31	16.8
$\beta_0 + \tau * \beta_1 + h * \beta_2 + \tau * h * \beta_3$	0.68	9.99	10.29	0.66	10.23	10.53
$\beta_0 + \tau * \beta_1 + rh * \beta_2 + \tau * rh * \beta_3$	0.7	9.61	9.9	0.69	9.82	10.11
$\beta_0 + rh * \beta_1 + h * \beta_2 + h * h * \beta_3$	0.52	12.13	12.49	0.51	12.35	12.72
$LMA_{toc} + \tau * (\beta_0 + LMA_{toc} * \beta_1)$	0.67	10.14	10.44	0.65	10.33	10.63
$LMA_{toc} + rh * (\beta_0 + LMA_{toc}\beta_1)$	0.57	11.47	11.81	0.54	11.87	12.22
$LMA_{toc} * \beta_0 + h * (\beta_1 + LMA_{toc} * \beta_2)$	0.29	14.81	15.25	0.24	15.32	15.77
$LMA_{toc} + \tau * \beta_0 + rh * \beta_1$	0.52	12.17	12.53	0.48	12.62	13
$LMA_{toc} + \tau * (\beta_0 + LMA_{toc} * \beta_1) + rh * (\beta_0 + LMA_{toc} * \beta_1)$	0.73	9.08	9.35	0.71	9.43	9.71
$LMA_{toc} + \tau \cdot (\beta_0 + LMA_{toc} \cdot \beta_1 + rh \cdot \beta_2)$	0.79	7.99	8.22	0.78	8.25	8.49
$LMA_{toc} + rh \cdot (\beta_0 + LMA_{toc} \cdot \beta_1 + \tau \cdot \beta_2) + \tau \cdot \beta_3$	0.56	11.66	12	0.52	12.2	12.56
$LMA_{toc} + \tau \cdot (\beta_0 + LMA_{toc} \cdot \beta_1 + rh \cdot \beta_2) + rh \cdot \beta_3$	0.8	7.91	8.14	0.78	8.28	8.53
$LMA_{toc} + rh \cdot (\beta_0 + LMA_{toc} \cdot \beta_1 + \tau \cdot \beta_2) + \tau \cdot \beta_3$	0.79	8.14	8.38	0.76	8.65	8.91

3. Characterizing seasonal variation in foliar biochemistry in a temperate broadleaf forest using imaging spectroscopy

Contributors: Adam Chlus, Eric L. Kruger & Philip A. Townsend

Abstract

Foliar biochemical traits are important indicators of ecosystem functioning and health that are difficult to characterize at large spatial and temporal scales using traditional measurements. However, comprehensive inventories of foliar traits are important to understanding ecosystem responses to anthropogenic and natural disturbances, as inputs into ecosystem process models, and for quantifying spatial variation in functional diversity. Imaging spectroscopy has been demonstrated as a valuable tool for developing maps of ecologically important foliar traits at large scales, but its application to mapping foliar traits over the course of the growing season has been limited. We collected high-resolution imaging spectroscopy data over Blackhawk Island, Wisconsin, USA at eight time points during the 2018 growing season (May - October). Using partial least squares regression (PLSR) we developed predictive models applicable to all dates to produce canopy-level maps of nine traits related to ecophysiological function: chlorophyll content, leaf mass per area and concentrations of nitrogen, lignin, fiber, phenolics, calcium, phosphorus and potassium. The accuracy of our models varied across traits (R^2: 0.55-0.93), traits with well-defined absorption features were retrieved with the highest accuracy including chlorophyll (R^2: 0.93; %RMSE: 8.0) and total phenolics (R^2: 0.86; %RMSE: 11.0). We tested the primary drivers of trait variation and found that phenology (date) explained the greatest amount of variation for all traits with the exception of total phenolics for which species explained 75% of the variation. Macronutrients (N, P and K) showed general trends of decreasing concentration over the course of the year, reflecting dilution by carbon-rich compounds during the growing season and resorption during senescence. Conversely, recalcitrant compounds including lignin, fiber and calcium increased until late summer, after which they stabilized. Using this data-driven approach, some traits required data collected across the entire growing season to develop general predictive models, indicating that trait-spectra relationships may vary across the growing season. These results demonstrate the potential of current and proposed spaceborne imaging spectroscopy missions for mapping seasonal foliar biochemistry at a global scale.

Introduction

Foliar biochemical traits are dynamic properties of plants that vary through space and time and are linked to a multiple ecosystem processes, including primary productivity and nutrient cycling (de Bello et al. 2010). Foliar traits include biochemical properties related to photosynthesis, such as chlorophyll and nitrogen, structure and decomposition, including fiber and lignin, and defense, like condensed tannins and other phenolic compounds. Understanding how these functional traits vary through space and time is important for developing accurate ecosystem process models, for predicting ecosystem response to change and understanding patterns in community assembly (Ito et al. 2006; Reichstein et al. 2014). In general, studies that use functional traits to assess patterns in community composition and ecological function make use of mean trait values for species (Albert et al. 2011). However, variability in functional traits is known to be scale dependent and driven by both taxonomic and environmental factors (Albert et al. 2010; Messier et al. 2010, 2017). Moreover, ecosystems with strong seasonal patterns, like temperate deciduous forests, display significant variation in foliar traits as leaves develop and senesce; this variation in turn drives intra-annual patterns in ecosystem processes (Reich et al. 1991; Salminen et al. 2004; Noda et al. 2015).

Studies dating to the early 20th century have reported on the seasonal variation in foliar biochemical traits and demonstrated that interannual patterns vary between species, within species, and across locations (McHargue and Roy 1932; Alway et al. 1934; Sampson and Samisch 1935; Chandler 1939). In a review of more than 20 studies, Turner et al. (1977) found that the direction of intra-annual trends (increasing, decreasing or stable) in foliar nutrient concentrations was not universal. In general, with elemental concentrations, calcium and manganese increase during the growing season, while nitrogen, phosphorus and potassium decrease, and boron, copper and magnesium (Mg) are stable throughout the year. Other studies have reported on seasonal patterns in more complex compounds including pigments (Schertz 1929; Sanger 1971), phenolics (Schultz et al. 1982; Salminen et al. 2004; Zehnder et al. 2009), nonstructural carbohydrates (McLaughlin et al. 1980; Flower 2007) and lignin (Martin and Aber 1997; Zehnder et al. 2009).

Trait-based ecology has emerged due the relative ease with which functional traits can be measured compared to their underlying physiological processes. This has led to the development of trait databases such as TRY (Kattge et al. 2020), which have enabled global-scale analyses of the variation in and drivers of ecosystem function (Díaz et al. 2016). Despite their relative ease of measurement, there are limits to the density of measurements, spatial extent and temporal richness at which functional traits can be quantified using in-situ sampling and laboratory analysis before efforts become prohibitively costly. Leaf-level spectroscopy represents a viable alternative for rapidly and nondestructively measuring foliar functional traits (Asner and Martin 2011; Serbin et al. 2014, 2019; Couture et al. 2016), which in turn has vastly increased the amount of data available to characterize evolutionary, taxonomic and environmental sources of trait variation (Asner et al. 2014; Nunes et al. 2017; Mereiles et al. 2020). Imaging spectroscopy has now also emerged as a valuable technology for further expanding the scale at which foliar functional traits can be measured. By developing relationships between canopy spectra and field measured leaf traits, maps of these traits can be generated at large spatial scales. These maps have been used characterize relationships between canopy traits and precipitation (Asner et al. 2005), geomorphology (Chadwick and Asner 2016), soil chemistry (Chadwick and Asner 2018), and land use (Swinfield et al. 2020). However most studies using imaging spectroscopy to map foliar traits have largely focused on a single point in time, namely the peak of the growing season (Martin and Aber 1997; Asner et al. 2008; Asner et al. 2015; Singh et al. 2015; Wang et al. 2020), whereas foliar traits are known to vary throughout the course of the growing season and are most dynamic during shoulder seasons following leaf out and over the course of senescence (Reich et al. 1991; Yang et al. 2016).

Remote sensing of phenology has historically been studied within the context of greenness using the normalized difference vegetation index (NDVI), or similar indices like the enhanced vegetation index (EVI), as metrics of vegetative vigor (Duchemin et al. 1999). Greenness indices are valuable for representing large-scale phenological patterns due their ease of computation and compatibility with a wide variety of remote sensing platforms (e.g. Landsat, MODIS, Sentinel). However, these indices are largely capturing variation in pigment content and leaf/canopy structure, whereas other ecologically relevant foliar traits may not exhibit the same temporal patterns (Wu et al. 2009). With its high spectral resolution, full-range (400-2500 nm) imaging spectroscopy provides the ability to resolve narrowband absorption features associated with biochemical traits not discernible from broadband sensors (Curran 1989). Few studies have used imaging spectroscopy to study phenological patterns of foliar biochemistry of natural ecosystems (Matson et al. 1994), mostly due to lack of data. At the leaf level, trait-spectra relationships vary across the course of the growing season, and predictive models developed using leaves from on time point and introduce biases in prediction on leaves from a different point in the growing season (Yang et. al. 2016). This is expected to transfer to the canopy level, but the magnitude of the effect remains untested.

In this paper, we demonstrate the application of imaging spectroscopy to track changes in foliar biochemistry across a growing season in the temperate deciduous forest on Blackhawk Island, Wisconsin. Using data from eight airborne imaging spectroscopy acquisitions in 2018 combined with field data, we map variation in nine canopy traits related to growth (chlorophyll, nitrogen), structure (fiber, LMA, lignin), defense (total phenolics) and mineral acquisition (calcium, phosphorus and potassium). We also test the temporal sensitivity of our data-driven trait mapping algorithms to time of year. Finally, we apply our model to the entire time series of imagery and characterize the spatiotemporal patterns in canopy biochemistry across the course of the growing season.

Methods

Study area

Blackhawk Island is a 73-ha island located in the Wisconsin River near Wisconsin Dells, WI, USA (43.65° N, 89.79° W). Blackhawk Island has a long history of ecological research, including some of the earliest studies linking decomposition processes, species composition and primary productivity (Pastor et al. 1984). The island has variable topography, with steep slopes along the river edge and relatively flat terrain in the center of the island, at its highest point it rises 33 m above the river. Five soil orders are present on the island, including Alfisols, Entisols, Incepticols, Histosols and Spodosols (Pastor et al. 1984). Forest community composition on Blackhawk Island is closely related to soil properties (Pastor et al. 1982). Canopy dominant species are primarily oaks (*Quercus alba and Q. rubra*), pines (*Pinus resinosa and P. strobus*), and maples (*Acer rubrum and A. saccharum*), with seven other species present to a lesser extent as canopy dominants (Figure 3.6). Aboveground production is driven by soil texture and N mineralization, with mineralization rates a function of N and P return to the soil in leaf litter and litter quality variation due to species (Pastor et al. 1984, 1982). As a consequence of these and other studies, Blackhawk Island has also been the site of numerous studies that have used imaging spectroscopy to map canopy biochemistry (Martin and Aber 1997; Singh et al. 2015), and is the site where Wessman and colleagues first demonstrated the potential for hyperspectral imagery to map ecosystem-relevant foliar traits (Wessman et al. 1988), especially as drivers of decomposition processes.

Remote sensing data

Imaging spectroscopy data was collected using a HySpex airborne imaging system (Norsk Elektro Optikk As, Skedsmokorset, Norway). The system consists of two cameras, a VNIR-1800 camera, which measures radiation between 400-997 nm across 186 channels with a spectral sampling interval of 3.26 nm, and a SWIR-384 camera, which covers 975-2500 nm and measures radiation at 288 channels with a spectral sampling interval of 5.45 nm. The cameras were mounted on a vibration-dampening platform with an iTraceRT F400-E GPS/IMU (iMAR Navigation GmbH, St. Ingbert, Germany). The imaging system was flown aboard a Cessna 180 at a nominal altitude of 700 m above ground level, resulting in a spatial resolution of 0.5 m for the VNIR camera and 1.0 m for the SWIR camera. Each overflight consisted of nine flightlines with 60% sidelap. A total of eight overflights were flown between 16 May and 17 October, 2018, and all flights were conducted +/- 2 hours of solar noon (Table 3.1).

Raw image data were converted to radiance using manufacturer-provided calibration coefficients. A spectral calibration was performed using a feature-matching algorithm to correct wavelength shifts (Gao et al. 2004). Camera alignment and geometric registration were performed using PARGE 6.0 orthorectification software (RESE, Wil SG, Switzerland). Calculation of apparent surface reflectance from at-sensor radiance was performed using an inverse algebraic atmospheric correction algorithm with the 'libRadtran' radiative transfer code (Emde et al. 2016) based on the method of Adler-Golden et al. (1999). Total column water vapor was estimated by flightline using the depth of the water vapor feature at 940 nm (Carrere and Conel 1993). Visibility, which was high during all overflights, was set to a constant of 50 km. Following atmospheric correction, a bidirectional reflectance distribution function (BRDF) correction was applied to remove brightness gradients resulting from varying sun and sensor geometry using the approach described in Chlus et al. (2020). Briefly, using sensor and sun geometry, we modeled the volumetric, geometric and isometric scattering components using the Ross-Li scattering kernel (Colgan et al. 2012; Schläpfer et al. 2014). For each date we pooled data across all flightlines and generated a single set of BRDF correction coefficients by regressing the resulting kernels against the uncorrected reflectance data for each wavelength. The VNIR imagery was aggregated and averaged to 1 m to match the spatial resolution of the SWIR camera. Image data from both cameras were combined at 980 nm to create a single full range (400-2500 nm) image for each flightline. Spectrum tails (<450 nm and >2300 nm) and water absorption bands were excluded from analysis due to low signal-to-noise ratios. Individual flightlines were merged to create a mosaic of the island for each date; in overlapping regions the pixel with the smallest viewing zenith angle (i.e. closest to nadir) was selected (Figure 3.2).

Foliar sampling

Within eight days of each overflight we collected foliage from 7-11 trees. To ensure that our field-derived foliar measurements were from trees identifiable in the imagery we sampled trees that had crowns greater than 5 m in diameter. From each tree we sampled two large (~1 m) branches from the sun exposed top of the canopy. Branches were sampled using either extendable pole pruners or a custom-built cutting device (described in Chlus et al. 2020). From each branch we measured the reflectance of 20 leaves with a PSR 3500+ spectrometer (Spectral Evolution, Boston, MA, USA) equipped with a leaf clip to estimate leaf-level foliar traits using spectroscopic models. Of those 20 leaves, we measured the one-sided area of three leaves using a flatbed scanner to calculate leaf mass per area (LMA) and retained a single leaf for pigment analysis to validate the spectral models. We combined the remaining 16 leaves with an additional 20-30 leaves from each branch for bulk chemical analyses. All foliar samples were stored in plastic bags with a damp paper towel in coolers with ice until the end of each day when they were frozen in liquid nitrogen and stored in a -20° C freezer until further processing. In addition to foliar sampling, we also recorded the species, diameter at breast height (DBH), crown shape of each tree sampled and made a general site characterization. We recorded tree locations with a differentially corrected GeoXM or Geo7x GPS receiver (Trimble Inc., Sunnyvale, CA, USA). Over the course of the study period, a total of 80 trees were sampled representing 11 broadleaf species (Table S3.1).

Sample processing

Bulk foliar samples were dried in a lyophilizer (> 120 hr) and ground using a Wiley Mill (Thomas Scientific, Swedesboro, NJ, USA) equipped with a #20 mesh (0.841 mm). Spectral measurements were then made on the dried and ground samples with an ASD Fieldspec 3 spectrometer (Analytical Spectral Devices, Boulder, CO, USA) following Serbin et al. (2014). A subset of ground samples was analyzed for concentraations of elements (N, P, K, Ca) (n=27), total phenolics (n=48) and acid-digested lignin, cellulose and fiber (n=27). Elemental concentration was determined using combustion analysis (N) and inductively coupled plasma emission spectroscopy (Ca, K, P) (Gavlak et al. 2004). Total phenolics concentration was determined using the Folin-Ciocalteu method (Ainsworth and Gillepsie 2007), and fiber and lignin concentrations were determined using a hot-acid detergent extraction (Couture et al. 2012). Leaves measured for leaf area were dried for >72 hr in a 68° C oven and weighed on a precision balance (0.0001 g) to determine dry mass. LMA was calculated by dividing measured dry mass by leaf area. Chlorophyll A content was measured on a subset of samples (n= 61) using high performance liquid chromatography (HPLC) following Schweiger et al. (2018).

Spectroscopic models were then used to estimate foliar biochemistry for all samples. Estimation of foliar traits from reflectance spectra is a well-established method for rapidly and accurately estimating foliar biochemical properties (Asner et al. 2008; Serbin et al. 2014; Yang et al. 2016). Fresh leaf-level reflectance spectra were used to estimate LMA and chlorophyll A content, while spectra of dried and ground samples were used for the estimation all other traits. Models were built using partial least squares regression (PLSR) using ‘scikit-learn’ in Python (Pedrogosa et al. 2011). PLSR models were calibrated with data from three independent datasets: Serbin et al. (2014), Wang et al. (2020) and Chlus et al. (Chapter 1: Chlus et al. 2020) and validated against the subset of samples from Blackhawk Island described above that were measured using laboratory techniques. Models for all traits were built using the SWIR region of the spectrum (1200-2500 nm), with the exception of chlorophyll A models that used the VNIR (400-800 nm). Prior to model building, each spectrum was normalized to its mean to remove brightness differences, similar to normalization used in other studies (Feilhauer et al. 2010; Kim et al. 2013). The optimal number of model components was determined by minimizing the cross-validated predicted residual sum of squares (PRESS). A series of 500 calibration models was generated, each built using a random 70 percent of the calibration data. These models were then applied to the independent (fully withheld) validation dataset and the mean trait value across the 500 models was calculated for each sample and compared against the observed trait value. Model performance was assessed using the coefficient of determination (R^2), root mean squared error (RMSE) and normalized RMSE (NRMSE) (Table S3.2). Following the accuracy assessment, 500 new permuted models were built using the entire dataset and were applied to all fresh and ground spectra. Any negative trait predictions were truncated to zero.

Canopy trait mapping

Trait maps were generated using PLSR, predicting canopy-level traits as a function of HySpex imaging spectroscopy. Canopy-level traits were derived by simple averaging of all leaf-level trait estimates from each crown. Canopy spectra of sampled trees were extracted from the imagery using manually digitized crown polygons and averaged, resulting in a single spectrum per tree. We used all pixels from a crown, including both sunlit and shaded components, as this is more representative of canopy spectra than using sun-facing pixels exclusively, and also better facilitates comparison with coarser-resolution data expected from forthcoming satellite missions. Similar to the leaf-level models we mean-normalized the canopy spectra prior to analysis.

To test the impact of phenology on the predictive ability of our models, we split the growing season into three periods: early (May 16 - July 25), middle (June 29-Sept 10) and end of season (Aug 13 - Oct 17). We chose overlapping periods to ensure sufficient sample size for calibration and so that each period had approximately the same number of samples. We kept track of the percent overlap in trait values between each seasonal period to use as a diagnostic of cross-season PLSR model performance. For each period we developed a PLSR model using data from the within-period dates and applied the model to the out-of-period dates, we then calculated the R^2, RMSE and NRMSE of the predicted values. The optimal number of model components was determined by minimizing the cross-validated PRESS statistic calculated on the calibration dataset. This analysis was conducted to evaluate whether trait/spectra relationships change through time, and to assess the consequences of using trait models built using data from a season that differs from the season of the imagery.

Finally, we built a model using data from all dates by randomly dividing the data 70:30 into calibration and validation and repeated the same model building steps used for generating permuted leaf-level models. The resulting permuted models were applied to all images in the time series and the mean trait estimates and their standard deviations were calculated for each pixel. For analysis, we masked pixels whose values were outside +/-15% of the range of field measured traits.

All image models were built using the SWIR region of the of the spectrum (1200-2300 nm), with the exception of chlorophyll A (450 - 750 nm; Gitelson and Merzylyak 1996) for which we aimed to exploit pigment absorption features, and total phenolics (1600-1700 nm), in which we aimed to exploit a 1660 nm phenolics feature (Kokaly and Skidmore 2015). The remaining traits were predicted using only the SWIR spectrum because the primary absorption features associated with those traits are located in the SWIR (Curran 1989), but also to reduce confounding influence of pigment-related spectral features in the visible that may correlate with non-pigment traits and to limit the influence of canopy structure in the NIR wavelengths.

Species classification

Species classification was performed using an object-oriented (segmentation) classification approach, in which both spatial context and spectral signatures are used to delineate trees. Image segmentation was performed using the Shepherd segmentation algorithm (Shepherd et al. 2019) implemented using the Python library 'RSGISLib' (Bunting et al. 2014). Shepherd segmentation uses an iterative process of grouping spectrally similar regions of pixels until all regions reach a user-defined minimum mapping size, which we established as 25 pixels (25 m^2) to correspond to the minimum crown size sampled. The segmentation was performed on a five band composite of principal component (PC) images from three dates 16 May (PC bands: 2, 4, 5), 04 June (PC band: 4) and 29 June (PC band: 4). We used multiple dates to exploit phenological and spectral differences among canopy trees. The PC transformation was performed to reduce the dimensionality of the data, thus improving processing time and limiting data redundancy. We visually inspected the PCs and chose for segmentation those that showed the greatest amount of contrast between neighboring crowns. Late season images were not used as testing demonstrated that they provided no improvement in segmentation results.

After segmentation, species classification was performed using a random forest classifier built with 100 trees using the 'scikit-learn' library in Python (Pedrogosa et al. 2011). For each segment we calculated the mean value of all contained pixels for each band across seven dates, this resulted in 2821 features per segment (403 bands x 7 dates). Imagery from October 17 was excluded due to irregular senescence of deciduous species across the island. To reduce the dimensionality of the data we applied a PC transformation and retained as predictor variables the first 99 components, which explained 99.99% of the variance in the data. Species labels for training and testing of the classifier were derived from a combination of field data collected in 2018 and 2019 and photointerpretation, yielding a total of 347 individual trees representing 13 species. We excluded species for which there were less than three individuals found on the island, including yellow birch (*Betula alleghaniensis*), cottonwood (*Populus deltoides*) and elm (*Ulmus sp.).* We used the crown center locations associated with the identified trees to select the corresponding image segments. The data were then split 50:50 into training and testing data, stratified by species. A classification model was built with the training dataset and used to label the testing dataset, on which we calculated accuracy metrics. After accuracy assessment the classifier was rebuilt using all of the data and applied to all image segments to make a map to intersect with the trait maps. We retained the classification probability of each segment to use in subsequent analyses to filter data based on confidence of its species label.

Variance partitioning

We performed a variance component analysis to identify sources of variation in foliar traits derived from the imaging spectroscopy data. Variance components were extracted using a linear mixed-effects model fit in R using the package ‘lme4’ (Bates et al. 2018) as follows:

$$T = \mu + Species/Segment + Date + Soil\ type + \varepsilon$$

where T is the observed trait value, μ is the trait mean, *Species*, *Segment*, *Date*, *Soil* are random effects and ε is the unexplained variance which also includes within-segment variance. Segment refers to the unique crown or crown element mapped during the species classification and includes numerous pixels of which trait estimates that are classified as a single species. The nested effects *Species/Segment* account for interspecific and intraspecific variance. *Soil* refers to soil type derived from a soils map of Blackhawk Island by Pastor et al. (1982). The soil map was manually digitized using a combination of a hig- resolution (1 m) lidar DEM collected in 2010 and historical aerial photography (See Figure S3.1). *Date* refers to each image acquisition date for which traits are estimated (Table 3.1). Image segments were used to extract pixel-wise foliar trait estimates from trait maps. We excluded edge pixels between segments to reduce edge-effect mixing of pixels from neighboring trees (Figure S3.2). To reduce computational complexity, ten pixels were randomly selected from each segment. To reduce uncertainty in the variance partitioning, only segments whose species classification probability was greater than 0.5 in the random forest classification were used. Here we treat segments as individual tree crowns. However, we note that in many cases large individual trees were divided into multiple segments in the object-oriented portion of the classification, and are therefore best described as crown elements.

Results

Canopy trait models

The results of the full-season PLSR model validation exhibited strong predictive performances for most traits (R^2: 0.47-0.93), and, with the exception of fiber, the NRMSE was less than or equal to 20% (Figure 3.3; Table 3.2; see Table S3.2 for detailed metrics).

Performance of models developed for one season and applied to different seasons varied across traits (Table 3.2). Total phenolics was estimated with high accuracy regardless of the date (R^2: 0.8-0.9, NRMSE < 15%), whereas nitrogen models calibrated using data from seasonal subsets all performed poorly ($R^2 \leq 0.07$). In contrast, the full-season nitrogen model performed considerably better (R^2 : 0.79). Structural traits including fiber, LMA and lignin exhibited generally similar patterns in model performances and showed the highest accuracies when calibrated with mid-season data (R^2: 0.64-0.7). Conversely, chlorophyll A model performance was best for the early and end of the season models where values spanned 80-100% of the range of the validation data, compared to mid-summer where chlorophyll content values were captured only 50% of the range. Calcium, phosphorus and potassium showed inconsistent patterns across the season, but all three improved substantially with the full-season model, especially calcium. Across all traits, model performance metrics (NRMSE and R^2) did not correlate with percent of overlap in trait values between the time periods being compared ($p > 0.5$). For example, the data range of LMA for the early time period (16 May- 25 July) overlaps 77% with the other two time periods (i.e., LMA generally lower earlier and higher later in the growing season), but the fact that the data ranges were unequal was unrelated to the relatively poor performance of the early season LMA model on mid- and late-season data (R^2: 0.02) (Table 3.2).

Species classification

The accuracy of the classifier was high (Overall accuracy: 87.9%; Cohen's kappa: 0.86; see Table S3.3 for details). All of the most common species on Blackhawk Island were accurately classified (both producer's and user's accuracy), while uncommon species such as white ash and silver maple had lower accuracies. Red oak (*Q. rubra*) was the most common tree species on Blackhawk Island (43% cover), followed by white pine (*P. strobus*) (18%) and sugar maple (*A. saccharum*) (13%), with all other species having less than 10% cover.

Variance partitioning

Species and date (i.e., phenology) were the primary drivers of differences among the 10 mapped traits (Figure 3.4), but the relative importance of each among traits was highly variable. For chlorophyll, fiber, lignin, LMA, phosphorus and potassium, phenology accounted for the greatest proportion of variance (55% on average). Species accounted for the majority of variance in total phenolics (76%), while for all other traits it accounted for less than 32% of the total variance, although species did account for the largest amount of explained variance in calcium, and nitrogen. A majority of the variance was unexplained for nitrogen (53%). The amount of variance explained by soil type was low for all traits (mean: 0.43%) and was highest for potassium (1.03%) and lowest for total phenolics (0.0%). Similarly, within-species effects accounted for a small proportion of the total variance (mean: 3.1%) with calcium having the largest proportion (4.6%). Interestingly, across all traits the amount of unexplained variance was positively correlated with the number latent vectors used in building the PLSR model (r: 0.85, p < .01). Models with a larger number of components, despite validating similarly or better than lower-component models, resulted in noisier trait maps. This noise resulted in an increase in within-canopy variability which is captured in the residual variance.

Seasonal patterns

Species-averaged trait trajectories varied across the course of the growing season (Figure 3.5). Traits associated with leaf structure, including LMA, lignin and fiber, displayed similar species ordering from low to high values on all dates, and followed a generally similar trend of increasing values until leveling off in the late summer. Calcium displayed a similar trend, but species ordering differed from LMA, lignin and fiber, with *T. americana* and *C. cordiformis* accumulating calcium at the fastest rate among the five broadleaf species. Chlorophyll A content trajectories showed the greatest dynamic range among all traits with a two-fold increase and decrease across the growing season. All species had similar seasonal trends but showed differences in phenological timing. Nitrogen, potassium and phosphorus decreased in concentration as the season progressed, but rates of decrease varied among traits and species. After full leaf expansion, nitrogen concentration was stable during the peak of the growing season before declining in late September, while phosphorus and potassium exhibited a gradual and continuous decline across the growing season. Seasonal trajectories of phenolics varied most widely across species in both magnitude and direction. *A. rubrum* had the highest phenolics concentration among the common species on Blackhawk Island, and gradually increased until mid-summer after which it exhibited a gradual decrease. Non-*Acer* species displayed a U-shaped seasonal pattern, with the highest concentrations of phenolics early and late in the season.

We visualized the trait maps by generating three band composite images across four dates in the growing season and summarized the species-average patterns in the six most common broadleaf species on the island (Figure 3.6). We displayed total phenolics, LMA and potassium in the red, green and blue bands, respectively, as these traits have different seasonal trajectories and show distinct patterns in species sorting (Figure 3.5). For visualization, each trait value was first normalized to 5-95 percentile range across all four dates, then for each date and pixel, traits values were normalized to their sum. On 16 May broadleaf species are characterized by relatively high concentrations of total phenolics and potassium and low LMA. Beginning on 04 June, non-maple species exhibit a relative decrease in total phenolics content captured by the shift in color from purple to blue. As the season progressed, LMA increased across all species resulting in an island-wide shift towards green on the map. In both the July and September composite images there are distinct groupings in tri-variate trait space of species: those with high LMA, low phenolics and low potassium (red and white oak), those with low LMA, high phenolics and low potassium (red and sugar maple) and species with low LMA, low phenolics and high potassium (basswood and bitternut hickory).

Discussion

Using a time series of imaging spectroscopy data over a single growing season, we developed maps of canopy foliar traits to characterize phenological variation in a temperate broadleaf forest. We demonstrate that accurate maps of canopy traits can be derived using a single cross-seasonal model per trait and that these models accurately characterize interspecific trait trajectories (Figure 3.5). The performance of the full-season models closely matches the "peak-season" models of Wang et al. (2020), who used imaging spectroscopy to map canopy traits in biomes across the eastern United States. Models that performed best included those with strong absorption features in the VSWIR spectrum (400-2500 nm), including chlorophyll (R^2:

0.93) and total phenolics (R^2: 0.86). Other traits, like calcium, despite performing comparatively poorly (R^2: 0.55), still accurately captured interannual trends and species ordering as reported in the literature (Chandler 1939; Chandler 1941; Insley et al. 1981; Cote and Fyles 1994).

We tested the sensitivity of canopy-level PLSR models to seasonality and found that the influence of seasonality on relationships between spectra and traits is not universal across traits. For example, models for estimating total phenolics performed well at other times of year regardless of the time of year for which the model was built, in contrast to nitrogen which performed poorly except when built using data from the entire growing season. We also found that model performance was not correlated with the amount of variation represented in the data used for model calibration. We performed this analysis under the assumption that trait data from one time of the season may not be representative of the trait data range for other parts of the season. This suggests that seasonal variation in the trait data range does not drive model performance, but rather that for some traits there is a seasonally dependent trait-spectra relationship that is not directly related to the range of trait measurements. Specifically, other factors – presumably unmeasured – confound the predictive relationship unless they are captured in the dataset. Unlike leaf-level spectroscopy, which allows for the collection reflectance measurements under controlled conditions (i.e. leaf clip or integrating sphere), imaging spectroscopy presents a number of external factors that introduce errors and biases in canopy reflectance retrievals. These include radiometric calibration, atmospheric correction and BRDF correction (Weyermann et al. 2013; Thompson et al. 2018), as well as other factors such as the crown architecture and the presence and relative density of understory vegetation. These impacts can be seen in our data where on certain dates trait retrievals appear systematically biased across all species, however, these biases are not universal across traits and are likely a function of model wavelength weightings (Figure 3.5).

Coupling our trait maps with species composition and soil type maps, we were able to characterize the sources of variation in foliar traits. Past studies use field measurements to examine the variance structure of foliar traits, while our study is the first to our knowledge to demonstrate the utility of imaging spectroscopy for variance partitioning of foliar traits seasonally. Variance component analysis showed that the dominant source of variation for most traits was phenology. An exception was total phenolics, for which species explained 75% of the variation, compared to just 5% for phenology. This illustrates that phenolics are strongly phylogenetically controlled, in contrast to seasonal variation being more prominent in the other traits we studied. We found that soil class explained little to no variance in canopy traits. This result does not indicate that soils do not impact canopy traits but that relative to other drivers like taxonomy and phenology, the effect was small on Blackhawk Island. Moreover, the lack variation may be a result of the coarse nature of the soil maps, which do not capture fine-scale variation in soil properties that may exist within soil classes that may affect individual trees. We expect that soils would likely have a greater impact with finer detail and over greater spatial scales. Nevertheless, data-driven approaches require adequately capturing the expected range of trait variability, including sampling through time and across species, as was shown for leaf level studies by Yang et al. (2016).

The trends in mapped chlorophyll content reflect the well documented phenological patterns of green-up and senescence observed from spaceborne platforms (Melaas et al. 2013; Li et al. 2019). However, with the high spatial resolution of the HySpex airborne sensor, we also detected variation in phenological phenomena among species, which can be seen in basswood (*T.*

americana) (Figure 3.5). After an early peak, on 29 June chlorophyll content decreased in basswood as a result of the formation of yellow-green bracts during the flowering phase which obscured green foliage (See Figure S3.3). These bracts act as wings aiding in seed dispersal (Scholtz 1958) and detach at the end of the fruiting stage, after which chlorophyll content once again increased (Figure 3.5). Our maps also captured the variability in phenological timing between species, most notably the delayed development of bitternut hickory and early senescence of sugar maple.

Phenological patterns in total phenolics closely matched those reported in the literature for the same or similar species. Rossiter et al. (1988) and Louis et al. (2009) both observed that phenolic concentrations in *Quercus* species were highest immediately following leaf emergence and stabilized at low levels after full leaf expansion, mirroring the patterns observed in *Quercus* species at Blackhawk Island. High concentrations of phenolics early in the growing season may inhibit herbivory before the development of unpalatable structural compounds like lignin (Lambers and Poorter 1992). Similar to our results, Shultz et al. (1982) found that sugar maple reached a maximum level of total phenolics in June and remained relatively steady through the growing season. While phenolic compounds are generally studied within the context of plant-herbivore interactions, the analytical method we used to measure total phenolics is sensitive to a broad range of phenolic compounds that differ in identity both among species and within a species during a single growing season (Nicol 1997; Appel et al. 2001). As such, it is difficult to interpret the causation underlying intra-annual patterns or interspecific differences; however beyond their role in plant-herbivore interactions phenolics are also associated with photoprotection, nutrient stress, cold acclimation and litter decomposition rates (Dixon and Paiva 1995; Close and MacArthur 2002; Pennycooke et al. 2006; Hattenschwiler and Jorgensen 2010)

Nutrients related to growth, including nitrogen, potassium and phosphorus, all decreased in concentration during the course of the growing season, as a consequence of dilution by increased content of carbon-rich structural compounds as leaves develop (Chapin 1980), and resorption at the end of the growing season (Killingbeck 1996). In contrast, calcium, which plays an important role in cell wall formation, increased as the growing season progressed, but is not resorbed due to its low mobility in phloem (Guha and Mitchell 1966; Zipkin 1973; Day and Monk 1977). Similar patterns were observed in fiber, lignin and LMA, which increase in concentration during the season, reflecting an investment in structural compounds as leaves develop (Groenevel et al. 1998; Poorter et al. 2009).

Our results demonstrate that imaging spectroscopy can be used to accurately map a suite of foliar biochemicals traits across the course of the growing season. While our study site was small, maps over larger areas with more significant gradients in soils, topography and climate may provide clearer insights into drivers of variation in foliar biochemistry than field measurements alone. These maps can also provide a framework to understand the impacts of phenology on estimates of functional diversity and its contribution to a range of ecological functions (Duran et al. 2019). Moreover, seasonal maps of traits may act as inputs into the next generation of vegetation models that are able to take advantage of rich information provided by imaging spectroscopy beyond basic plant functional types (Berzaghi et al. 2020).

In this study we focused on broadleaved deciduous species, and continued work is needed to assess the ability of imaging spectroscopy to characterize seasonal variation across a range of species and ecosystems. For example, needleleaf species also display seasonal variation in canopy biochemistry associated with the development of new needles and remobilization of nutrients into existing foliage (Wyttenbach and Tobler 1988; Billow et al. 1994). As well, foliar traits can vary significantly in grasslands, for example where species relative dominance changes over the course of the growing season such as from C_3 to C_4 and back to C_3 species (Dickinson and Dodd 1976). Outside of temperate ecosystems, there is also considerable seasonal variability in tropical systems. For example, species in dry deciduous systems would be expected to show variability in traits related to leaf structure and water conservation (Ishida et al., 2006; Kenzo et al. 2016). Moist tropical systems also exhibit variability, since leaf turnover occurs year-round (Hikosaka 2005) and seasonality in Mediterranean systems is likewise variable due to climate drivers (Sperlich et al. 2015).

Our work focused on a single growing season, but foliar biochemistry also varies from year-to-year (Mitchell 1936; Taylor and Parkinson 1987). Plant phenology is known to be driven by climatic variation, which thus affects allocation of resources at the leaf level (Shen et al. 2011; Liu et al. 2016). For instance, long-term trends of increasing temperatures are associated with earlier spring green-up (Cleland et al. 2007; Dai et al. 2019), for which imaging spectroscopy could provide an approach to document resulting impacts on foliar traits. Numerous other factors likewise alter phenological timing and could be expressed in foliar traits, including biotic forcings, such as herbivory (Lemoine et al. 2017) as well as plant development stage and ontogeny (Augspurger and Bartlett 2003; Grassi et al. 2005). However, our understanding of patterns and drivers interannual variation in seasonal dynamics of foliar biochemistry is limited to few species or localized areas, largely due to the challenges of making in-situ measurements. Continued long-term imaging with airborne and future spaceborne spectroscopy missions will provide a better understanding of the role of climate, environment and ontogeny in driving intra-annual variability in foliar biochemistry and subsequent impacts on ecological processes.

The launch of future spaceborne imaging spectroscopy missions will provide the opportunity to map seasonal variation in foliar biochemistry on a global scale. However continued research is needed into the impacts of spatial resolution on biochemistry retrievals. For example, the high spatial resolution of our imagery allowed us to develop and apply our models on individual trees and mask non vegetated areas. The lower spatial resolution (20-30m) pixels of current and future spaceborne imagers will be composed of species mixes, as well as canopy gaps (possibly with understory vegetation present), shadows and non-vegetated areas in addition to vegetation. In particular, the presence of multiple species in a single pixel may make interpretation of spatiotemporal patterns in foliar biochemistry and functional diversity challenging.

Our study site had relatively low species diversity (< 15 broadleaf species), whereas highly diverse ecosystems like tropical forests can have hundreds of species in a comparable area (Keil and Chase 2019). Globally, there are over 300,000 vascular plant species (Christenhusz and Byng 2016) and over 60,000 tree species (Beech et al. 2017), which has been a strong justification for utilizing a trait- rather than species-based approach to characterizing ecosystems and their function. However, given the diversity of plants on Earth, further investigation is needed into the feasibility of a developing global, cross-seasonal predictive models to map foliar traits or whether locally-optimized models are more appropriate. Models for some traits like chlorophyll and total phenolics, which have relatively well characterized absorption features, may be well suited for a global model approach. In contrast, traits like calcium, for which the underlying relationship between trait and spectra remains unclear, may require ecosystem-specific modeling. Moreover, the choice of predictive algorithm on seasonal trait retrievals warrants further investigation. We chose PLSR, a data-driven approach, for developing our mapping algorithms. However, other empirical methods have also been used mapping foliar traits from imaging spectroscopy including Gaussian process models (Verrelst et al. 2012; Wang et al. 2019) and neural networks (Mutanga and Skidmore 2004). Radiative transfer models (RTM), like 4SAIL (Verhoef et al., 2007) and INFORM (Atzberger 2000), provide an alternative method for trait retrieval using a physically-based approach to model light transmission as a function of canopy and leaf properties (Schlerf and Atzberger 2006). RTMs also have been used to estimate traits across the growing season at the leaf level (Gara et al. 2019), however the catalog of biochemical traits retrieved using RTMs is limited to those with well-defined absorbance properties.

Conclusion

In this study we used imaging spectroscopy to characterize the variation in foliar biochemistry in nine traits across the course a growing season in a temperate broadleaf deciduous forest. Our method used a single cross-seasonal model to map foliar biochemistry at eight time points from May to October, but we also tested the consequences of using models from one part of the growing season to map traits in another. We demonstrate that seasonal patterns in foliar traits are highly variable, both spatially and temporally, and highlight that date of image collection can significantly impact inferences made about ecosystem processes. Our research illustrates that when using data-driven methods to map canopy traits, models will generally need to be developed using data representing all of the seasons being mapped. Our analyses show that phenology (date of acquisition) accounted for the greatest proportion of variation in foliar traits at Blackhawk Island, followed by taxonomy (species). Continued work is needed to assess this approach across a broader range of ecosystems and with other ecologically relevant biochemical traits, as well as at the scale of spaceborne imaging spectroscopy. This work demonstrates the potential for future spaceborne imaging spectrometers to map ecologically important seasonal variations in foliar biochemistry. Trait maps from imaging spectroscopy which will provide spatial context to both inform and complement databases of field measurements (e.g. Kattge et al. 2020) and modeled predictions of global traits (e.g. Butler et al. 2017, Moreno-Martinez et al. 2018), while potentially also providing inputs to drive and/or validate earth system models.

Acknowledgments

Thank you to the members of the Townsend lab for their help with fieldwork, image collection and sample processing, especially Abigail Walther, Anghad Dhariwal, Benjamin Spaier, Dewi Radin Umar and Raina Eddy. I am also grateful to the pilots and staff at the Wisconsin Department of Natural Resources and the staff at Upham Woods for providing operational and logistical support.

References

Adler-Golden, S. M., Matthew, M. W., Bernstein, L. S., Levine, R. Y., Berk, A., Richtsmeier, S. C., ... & Hoke, M. L. (1999, October). Atmospheric correction for shortwave spectral imagery based on MODTRAN4. In *Imaging Spectrometry V* (Vol. 3753, pp. 61-69). International Society for Optics and Photonics.

Ainsworth, E. A., & Gillespie, K. M. (2007). Estimation of total phenolic content and other oxidation substrates in plant tissues using Folin–Ciocalteu reagent. *Nature protocols*, *2*(4), 875-877.

Albert, C. H., Thuiller, W., Yoccoz, N. G., Douzet, R., Aubert, S., & Lavorel, S. (2010). A multi-trait approach reveals the structure and the relative importance of intra-vs. interspecific variability in plant traits. *Functional Ecology*, *24*(6), 1192-1201.

Albert, C. H., Grassein, F., Schurr, F. M., Vieilledent, G., & Violle, C. (2011). When and how should intraspecific variability be considered in trait-based plant ecology?. *Perspectives in Plant Ecology, Evolution and Systematics*, *13*(3), 217-225.

Alway, F. J., Maki, T. E., & Methley, W. J. (1934). Composition of the leaves of some forest trees. *Soil Science Society of America Journal*, *15*(2001), 81-84.

Appel, H. M., Govenor, H. L., D'ascenzo, M., Siska, E., & Schultz, J. C. (2001). Limitations of Folin assays of foliar phenolics in ecological studies. *Journal of chemical ecology*, *27*(4), 761-778.

Asner, G. P., Carlson, K. M., & Martin, R. E. (2005). Substrate age and precipitation effects on Hawaiian forest canopies from spaceborne imaging spectroscopy. *Remote sensing of environment*, *98*(4), 457-467.

Asner, G. P., & Martin, R. E. (2008). Spectral and chemical analysis of tropical forests: Scaling from leaf to canopy levels. *Remote Sensing of Environment*, *112*(10), 3958-3970.

Asner, G. P., & Martin, R. E. (2011). Canopy phylogenetic, chemical and spectral assembly in a lowland Amazonian forest. *New Phytologist*, *189*(4), 999-1012.

Asner, G. P., Martin, R. E., Carranza-Jiménez, L., Sinca, F., Tupayachi, R., Anderson, C. B., & Martinez, P. (2014). Functional and biological diversity of foliar spectra in tree canopies throughout the Andes to Amazon region. *New Phytologist*, *204*(1), 127-139.

Asner, G. P., Martin, R. E., Anderson, C. B., & Knapp, D. E. (2015). Quantifying forest canopy traits: Imaging spectroscopy versus field survey. *Remote Sensing of Environment*, *158*, 15-27.

Atzberger, C. (2000). Development of an invertible forest reflectance model: The INFOR-Model. *A decade of trans-European remote sensing cooperation*, 39-44.

Augspurger, C. K., & Bartlett, E. A. (2003). Differences in leaf phenology between juvenile and adult trees in a temperate deciduous forest. *Tree Physiology*, *23*(8), 517-525.

Bates, D., Maechler, M., Bolker, B., Walker, S., Christensen, R. H. B., Singmann, H., ... & Green, P. (2018). Package 'lme4'. *Version*, *1*, 17.

Berzaghi, F., Wright, I. J., Kramer, K., Oddou-Muratorio, S., Bohn, F. J., Reyer, C. P., ... & Hartig, F. (2020). Towards a new generation of trait-flexible vegetation models. *Trends in Ecology & Evolution*, *35*(3), 191-205.

Billow, C., Matson, P., & Yoder, B. (1994). Seasonal biochemical changes in coniferous forest canopies and their response to fertilization. *Tree Physiology*, *14*(6), 563-574.

Bunting, P., Clewley, D., Lucas, R. M., & Gillingham, S. (2014). The remote sensing and GIS software library (RSGISLib). *Computers & geosciences*, *62*, 216-226.

Butler, E. E., Datta, A., Flores-Moreno, H., Chen, M., Wythers, K. R., Fazayeli, F., ... & Blonder, B. (2017). Mapping local and global variability in plant trait distributions. *Proceedings of the National Academy of Sciences*, *114*(51), E10937-E10946.

Carrère, V., & Conel, J. E. (1993). Recovery of Atmospheric Water Vapor Total Column Abundance from Imaging Spectrometer Data Around 940 nm-Sensitivity Analysis and Application to Airborne Visible/Infrared Imaging Spectrometer (AVIRIS).

Chadwick, K. D., & Asner, G. P. (2016). Tropical soil nutrient distributions determined by biotic and hillslope processes. *Biogeochemistry*, *127*(2-3), 273-289.

Chadwick, K. D., & Asner, G. P. (2018). Landscape evolution and nutrient rejuvenation reflected in Amazon forest canopy chemistry. *Ecology letters*, *21*(7), 978-988.

Chandler, R. F. (1939). The calcium content of the foliage of forest trees. *Cornell University Agriculture Experiment Station*. Memo 228. Ithaca, NY.

Chandler Jr, R. F. (1941). Amount and mineral nutrient content of freshly fallen leaf litter in the hardwood forests of central New York. *Journal of the American Society of Agronomy*.

Chapin III, F. S. (1980). The mineral nutrition of wild plants. *Annual review of ecology and systematics*, *11*(1), 233-260.

Chlus, A., Kruger, E. L., & Townsend, P. A. (2020). Mapping three-dimensional variation in leaf mass per area with imaging spectroscopy and lidar in a temperate broadleaf forest. *Remote Sensing of Environment*, *250*, 112043.

Christenhusz, M. J., & Byng, J. W. (2016). The number of known plants species in the world and its annual increase. *Phytotaxa*, *261*(3), 201-217.

Cleland, E. E., Chuine, I., Menzel, A., Mooney, H. A., & Schwartz, M. D. (2007). Shifting plant phenology in response to global change. *Trends in ecology & evolution*, *22*(7), 357-365.

Close, D. C., & McArthur, C. (2002). Rethinking the role of many plant phenolics–protection from photodamage not herbivores?. *Oikos*, *99*(1), 166-172.

Colgan, M. S., Baldeck, C. A., Féret, J. B., & Asner, G. P. (2012). Mapping savanna tree species at ecosystem scales using support vector machine classification and BRDF correction on airborne hyperspectral and LiDAR data. *Remote Sensing*, *4*(11), 3462-3480.

Côté, B., & Fyles, J. W. (1994). Nutrient concentration and acid–base status of leaf litter of tree species characteristic of the hardwood forest of southern Quebec. *Canadian journal of forest research*, *24*(1), 192-196.

Couture, J. J., Meehan, T. D., & Lindroth, R. L. (2012). Atmospheric change alters foliar quality of host trees and performance of two outbreak insect species. *Oecologia*, *168*(3), 863-876.

Couture, J. J., Singh, A., Rubert-Nason, K. F., Serbin, S. P., Lindroth, R. L., & Townsend, P. A. (2016). Spectroscopic determination of ecologically relevant plant secondary metabolites. *Methods in Ecology and Evolution*, *7*(11), 1402-1412.

Curran, P. J. (1989). Remote sensing of foliar chemistry. *Remote sensing of environment*, *30*(3), 271-278.

Dai, W., Jin, H., Zhang, Y., Liu, T., & Zhou, Z. (2019). Detecting temporal changes in the temperature sensitivity of spring phenology with global warming: Application of machine learning in phenological model. *Agricultural and Forest Meteorology*, *279*, 107702.

Day Jr, F. P., & Monk, C. D. (1977). Seasonal nutrient dynamics in the vegetation on a southern Appalachian watershed. *American Journal of Botany*, *64*(9), 1126-1139.

de Bello, F., Lavorel, S., Díaz, S., Harrington, R., Cornelissen, J. H., Bardgett, R. D., ... & da Silva, P. M. (2010). Towards an assessment of multiple ecosystem processes and services via functional traits. *Biodiversity and Conservation*, *19*(10), 2873-2893.

Díaz, S., Kattge, J., Cornelissen, J. H., Wright, I. J., Lavorel, S., Dray, S., ... & Garnier, E. (2016). The global spectrum of plant form and function. *Nature*, *529*(7585), 167-171.

Dickinson, C. E., & Dodd, J. L. (1976). Phenological pattern in the shortgrass prairie. *American Midland Naturalist*, 367-378.

Dixon, R. A., & Paiva, N. L. (1995). Stress-induced phenylpropanoid metabolism. *The plant cell*, *7*(7), 1085.

Duchemin, B., Goubier, J., & Courrier, G. (1999). Monitoring phenological key stages and cycle duration of temperate deciduous forest ecosystems with NOAA/AVHRR data. *Remote Sensing of Environment*, *67*(1), 68-82.

Durán, S. M., Martin, R. E., Díaz, S., Maitner, B. S., Malhi, Y., Salinas, N., ... & Bentley, L. P. (2019). Informing trait-based ecology by assessing remotely sensed functional diversity across a broad tropical temperature gradient. *Science advances*, *5*(12), eaaw8114.

Emde, C., Buras-Schnell, R., Kylling, A., Mayer, B., Gasteiger, J., Hamann, U., ... & Bugliaro, L. (2015). The libRadtran software package for radiative transfer calculations (Version 2.0). *Geoscientific model development discussions*, *8*(12).

Feilhauer, H., Asner, G. P., Martin, R. E., & Schmidtlein, S. (2010). Brightness-normalized partial least squares regression for hyperspectral data. *Journal of Quantitative Spectroscopy and Radiative Transfer*, *111*(12-13), 1947-1957.

Flower, C. E. (2007). *Seasonal carbohydrate allocation in big tooth aspen (Populus grandidentata Michx.) and northern red oak (Quercus rubra L.) from northern lower Michigan* (Doctoral dissertation, The Ohio State University).

Gao, B. C., Montes, M. J., & Davis, C. O. (2004). Refinement of wavelength calibrations of hyperspectral imaging data using a spectrum-matching technique. *Remote Sensing of Environment*, *90*(4), 424-433.

Gara, T. W., Darvishzadeh, R., Skidmore, A. K., Wang, T., & Heurich, M. (2019). Evaluating the performance of PROSPECT in the retrieval of leaf traits across canopy throughout the growing season. *International Journal of Applied Earth Observation and Geoinformation*, *83*, 101919.

Gavlak, R., Horneck, D., Miller, R. O., & Kotuby-Amacher, J. (2003). Soil, plant and water reference methods for the western region. *WCC-103 Publication, Fort Collins, CO*.

Gitelson, A. A., & Merzlyak, M. N. (1996). Signature analysis of leaf reflectance spectra: algorithm development for remote sensing of chlorophyll. *Journal of plant physiology*, *148*(3-4), 494-500.

Grassi, G., Vicinelli, E., Ponti, F., Cantoni, L., & Magnani, F. (2005). Seasonal and interannual variability of photosynthetic capacity in relation to leaf nitrogen in a deciduous forest plantation in northern Italy. *Tree Physiology*, *25*(3), 349-360.

Groeneveld, H. W., Bergkotte, M., & Lambers, H. (1998). Leaf growth in the fast-growing Holcus lanatus and the slow-growing Deschampsia flexuosa: tissue maturation. *Journal of experimental botany*, 1509-1517.

Guha, M. M., & Mitchell, R. L. (1966). The trace and major element composition of the leaves of some deciduous trees. *Plant and Soil*, *24*(1), 90-112

Hättenschwiler, S., & Jørgensen, H. B. (2010). Carbon quality rather than stoichiometry controls litter decomposition in a tropical rain forest. *Journal of Ecology*, *98*(4), 754-763.

Hikosaka, K. (2005). Leaf canopy as a dynamic system: ecophysiology and optimality in leaf turnover. *Annals of Botany*, *95*(3), 521-533.

Insley, H., Boswell, R. C., & Gardiner, J. B. H. (1981). Foliar macronutrients (N, P, K, Ca and Mg) in lime (Tilia spp.). *Plant and Soil*, *61*(3), 391-401.

Ishida, A., Diloksumpun, S., Ladpala, P., Staporn, D., Panuthai, S., Gamo, M., ... & Puangchit, L. (2006). Contrasting seasonal leaf habits of canopy trees between tropical dry-deciduous and evergreen forests in Thailand. *Tree Physiology*, *26*(5), 643-656.

Ito, A., Muraoka, H., Koizumi, H., Saigusa, N., Murayama, S., & Yamamoto, S. (2006). Seasonal variation in leaf properties and ecosystem carbon budget in a cool-temperate deciduous broad-leaved forest: simulation analysis at Takayama site, Japan. *Ecological Research*, *21*(1), 137-149.

Kattge, J., Bönisch, G., Díaz, S., Lavorel, S., Prentice, I. C., Leadley, P., ... & Acosta, A. T. (2020). TRY plant trait database–enhanced coverage and open access. *Global change biology*, *26*(1), 119-188.

Keil, P., & Chase, J. M. (2019). Global patterns and drivers of tree diversity integrated across a continuum of spatial grains. *Nature ecology & evolution*, *3*(3), 390-399.

Kenzo, T., Iida, S. I., Shimizu, T., Tamai, K., Kabeya, N., Shimizu, A., & Chann, S. (2016). Seasonal and height-related changes in leaf morphological and photosynthetic traits of two dipterocarp species in a dry deciduous forest in Cambodia. *Plant Ecology & Diversity*, *9*(5-6), 505-520.

Killingbeck, K. T. (1996). Nutrients in senesced leaves: keys to the search for potential resorption and resorption proficiency. *Ecology*, *77*(6), 1716-1727.

Kim, G., Kim, D. Y., Kim, G. H., & Cho, B. K. (2013). Applications of discrete wavelet analysis for predicting internal quality of cherry tomatoes using VIS/NIR spectroscopy. *J. Biosyst. Eng*, *38*(1), 48-54.

Kokaly, R. F., & Skidmore, A. K. (2015). Plant phenolics and absorption features in vegetation reflectance spectra near 1.66 μm. *International Journal of Applied Earth Observation and Geoinformation*, *43*, 55-83.

Lambers, H. A. N. S., & Poorter, H. (1992). Inherent variation in growth rate between higher plants: a search for physiological causes and ecological consequences. In *Advances in ecological research* (Vol. 23, pp. 187-261). Academic Press.

Lemoine, N. P., Doublet, D., Salminen, J. P., Burkepile, D. E., & Parker, J. D. (2017). Responses of plant phenology, growth, defense, and reproduction to interactive effects of warming and insect herbivory. *Ecology*, *98*(7), 1817-1828.

Li, X., Zhou, Y., Meng, L., Asrar, G. R., Lu, C., & Wu, Q. (2019). A dataset of 30 m annual vegetation phenology indicators (1985–2015) in urban areas of the conterminous United States. *Earth System Science Data*, *11*(PNNL-SA-144732).

Liu, Q., Fu, Y. H., Zeng, Z., Huang, M., Li, X., & Piao, S. (2016). Temperature, precipitation, and insolation effects on autumn vegetation phenology in temperate China. *Global change biology*, *22*(2), 644-655.

Martin, Mary E., and John D. Aber. "High spectral resolution remote sensing of forest canopy lignin, nitrogen, and ecosystem processes." *Ecological applications* 7, no. 2 (1997): 431-443.

Matson, P., Johnson, L., Billow, C., Miller, J., & Pu, R. (1994). Seasonal patterns and remote spectral estimation of canopy chemistry across the Oregon transect. *Ecological Applications*, *4*(2), 280-298.

McHargue, J. S., & Roy, W. R. (1932). Mineral and nitrogen content of the leaves of some forest trees at different times in the growing season. *Botanical Gazette*, *94*(2), 381-393.

McLaughlin, S. B., McConathy, R. K., Barnes, R. L., & Edwards, N. T. (1980). Seasonal changes in energy allocation by white oak (Quercus alba). *Canadian Journal of Forest Research*, *10*(3), 379-388.

Meireles, J. E., Cavender-Bares, J., Townsend, P. A., Ustin, S., Gamon, J. A., Schweiger, A. K., ... & Schrodt, F. (2020). Leaf reflectance spectra capture the evolutionary history of seed plants. *New Phytologist*.

Melaas, E. K., Friedl, M. A., & Zhu, Z. (2013). Detecting interannual variation in deciduous broadleaf forest phenology using Landsat TM/ETM+ data. *Remote Sensing of Environment*, *132*, 176-185.

Messier, J., McGill, B. J., & Lechowicz, M. J. (2010). How do traits vary across ecological scales? A case for trait-based ecology. *Ecology letters*, *13*(7), 838-848.

Messier, J., McGill, B. J., Enquist, B. J., & Lechowicz, M. J. (2017). Trait variation and integration across scales: is the leaf economic spectrum present at local scales?. *Ecography*, *40*(6), 685-697.

Mitchell, H. L. (1936). Trends in the nitrogen, phosphorus, potassium and calcium content of the leaves of some forest trees during the growing season. *Black Rock Forest Papers*, *1*(6), 30-44.

Moreno-Martínez, Á., Camps-Valls, G., Kattge, J., Robinson, N., Reichstein, M., van Bodegom, P., ... & Niinemets, Ü. (2018). A methodology to derive global maps of leaf traits using remote sensing and climate data. *Remote Sensing of Environment*, *218*, 69-88.

Mutanga, O., & Skidmore, A. K. (2004). Integrating imaging spectroscopy and neural networks to map grass quality in the Kruger National Park, South Africa. *Remote sensing of environment*, *90*(1), 104-115.

Nicol, R. W. (1997). The activity of the phytochemical defenses of red maple (Acer rubrum L.) and sugar maple (Acer saccharum Marsh.) against the forest tent caterpillar (Malacosoma disstria Huebner). University of Ottawa (Canada).

Noda, H. M., Muraoka, H., Nasahara, K. N., Saigusa, N., Murayama, S., & Koizumi, H. (2015). Phenology of leaf morphological, photosynthetic, and nitrogen use characteristics of canopy trees in a cool-temperate deciduous broadleaf forest at Takayama, central Japan. *Ecological Research*, *30*(2), 247-266.

Nunes, M., Davey, M., & Coomes, D. (2017). On the challenges of using field spectroscopy to measure the impact of soil type on leaf traits.

Pastor, J., Aber, J. D., McClaugherty, C. A., & Melillo, J. M. (1982). Geology, soils and vegetation of Blackhawk Island, Wisconsin. *American Midland Naturalist*, 266-277.

Pastor, J., Aber, J. D., McClaugherty, C. A., & Melillo, J. M. (1984). Aboveground production and N and P cycling along a nitrogen mineralization gradient on Blackhawk Island, Wisconsin. *Ecology*, *65*(1), 256-268.

Pedregosa, F., Varoquaux, G., Gramfort, A., Michel, V., Thirion, B., Grisel, O., ... & Vanderplas, J. (2011). Scikit-learn: Machine learning in Python. *the Journal of machine Learning research*, *12*, 2825-2830.

Pennycooke, J. C., Cox, S., & Stushnoff, C. (2005). Relationship of cold acclimation, total phenolic content and antioxidant capacity with chilling tolerance in petunia (Petunia× hybrida). *Environmental and Experimental Botany*, *53*(2), 225-232.

Poorter, H., Niinemets, Ü., Poorter, L., Wright, I. J., & Villar, R. (2009). Causes and consequences of variation in leaf mass per area (LMA): a meta-analysis. *New phytologist*, *182*(3), 565-588.

Reich, P. B., Walters, M. B., & Ellsworth, D. S. (1991). Leaf age and season influence the relationships between leaf nitrogen, leaf mass per area and photosynthesis in maple and oak trees. *Plant, Cell & Environment*, *14*(3), 251-259.

Reichstein, M., Bahn, M., Mahecha, M. D., Kattge, J., & Baldocchi, D. D. (2014). Linking plant and ecosystem functional biogeography. *Proceedings of the National Academy of Sciences*, *111*(38), 13697-13702.

Salminen, J. P., Roslin, T., Karonen, M., Sinkkonen, J., Pihlaja, K., & Pulkkinen, P. (2004). Seasonal variation in the content of hydrolyzable tannins, flavonoid glycosides, and proanthocyanidins in oak leaves. *Journal of Chemical Ecology*, *30*(9), 1693-1711.

Sampson, A. W., & Samisch, R. (1935). Growth and seasonal changes in composition of oak leaves. *Plant physiology*, *10*(4), 739.

Sanger, J. E. (1971). Quantitative investigations of leaf pigments from their inception in buds through autumn coloration to decomposition in falling leaves. *Ecology*, *52*(6), 1075-1089.

Schertz, F. M. (1929). Seasonal variation of the chloroplast pigments in several plants on the mall at Washington, D. C. *Plant physiology*, *4*(1), 135.

Schultz, J. C., Nothnagle, P. J., & Baldwin, I. T. (1982). Seasonal and individual variation in leaf quality of two northern hardwoods tree species. *American Journal of Botany*, *69*(5), 753-759.

Schläpfer, D., Richter, R., & Feingersh, T. (2014). Operational BRDF effects correction for wide-field-of-view optical scanners (BREFCOR). *IEEE Transactions on Geoscience and Remote Sensing*, *53*(4), 1855-1864.

Schlerf, M., & Atzberger, C. (2006). Inversion of a forest reflectance model to estimate structural canopy variables from hyperspectral remote sensing data. *Remote sensing of environment*, *100*(3), 281-294.

Schweiger, A. K., Cavender-Bares, J., Townsend, P. A., Hobbie, S. E., Madritch, M. D., Wang, R., ... & Gamon, J. A. (2018). Plant spectral diversity integrates functional and phylogenetic components of biodiversity and predicts ecosystem function. *Nature Ecology & Evolution*, *2*(6), 976-982.

Scholz, H. F. (1958). *Silvical Characteristics of American Basswood (Tilia Americana)* (No. 62). Lake States Forest Experiment Station, Forest Service, US Department of Agriculture.

Serbin, S. P., Singh, A., McNeil, B. E., Kingdon, C. C., & Townsend, P. A. (2014). Spectroscopic determination of leaf morphological and biochemical traits for northern temperate and boreal tree species. *Ecological Applications*, *24*(7), 1651-1669.

Serbin, S. P., Wu, J., Ely, K. S., Kruger, E. L., Townsend, P. A., Meng, R., ... & Rogers, A. (2019). From the Arctic to the tropics: multibiome prediction of leaf mass per area using leaf reflectance. *New Phytologist*, *224*(4), 1557-1568.

Shen, M., Tang, Y., Chen, J., Zhu, X., & Zheng, Y. (2011). Influences of temperature and precipitation before the growing season on spring phenology in grasslands of the central and eastern Qinghai-Tibetan Plateau. *Agricultural and Forest Meteorology*, *151*(12), 1711-1722.

Singh, A., Serbin, S. P., McNeil, B. E., Kingdon, C. C., & Townsend, P. A. (2015). Imaging spectroscopy algorithms for mapping canopy foliar chemical and morphological traits and their uncertainties. *Ecological Applications*, *25*(8), 2180-2197.

Sperlich, D., Chang, C. T., Peñuelas, J., Gracia, C., & Sabaté, S. (2015). Seasonal variability of foliar photosynthetic and morphological traits and drought impacts in a Mediterranean mixed forest. *Tree physiology*, *35*(5), 501-520.

Swinfield, T., Both, S., Riutta, T., Bongalov, B., Elias, D., Majalap-Lee, N., ... & Jucker, T. (2020). Imaging spectroscopy reveals the effects of topography and logging on the leaf chemistry of tropical forest canopy trees. *Global change biology*, *26*(2), 989-1002.

Taylor, B. R., & Parkinson, D. (1988). Annual differences in quality of leaf litter of aspen (Populus tremuloides) affecting rates of decomposition. *Canadian journal of botany*, *66*(10), 1940-1947.

Thompson, D. R., Natraj, V., Green, R. O., Helmlinger, M. C., Gao, B. C., & Eastwood, M. L. (2018). Optimal estimation for imaging spectrometer atmospheric correction. *Remote Sensing of Environment*, *216*, 355-373.

Turner, J., Dice, S. F., Cole, D. W., & Gessel, S. P. (1977). Variation of nutrients in forest tree foliage: a review.

Verhoef, W., Jia, L., Xiao, Q., & Su, Z. (2007). Unified optical-thermal four-stream radiative transfer theory for homogeneous vegetation canopies. *IEEE Transactions on geoscience and remote sensing*, *45*(6), 1808-1822.

Verrelst, J., Alonso, L., Caicedo, J. P. R., Moreno, J., & Camps-Valls, G. (2012). Gaussian process retrieval of chlorophyll content from imaging spectroscopy data. *IEEE Journal of Selected Topics in Applied Earth Observations and Remote Sensing*, *6*(2), 867-874.

Wang, Z., Townsend, P. A., Schweiger, A. K., Couture, J. J., Singh, A., Hobbie, S. E., & Cavender-Bares, J. (2019). Mapping foliar functional traits and their uncertainties across three years in a grassland experiment. *Remote Sensing of Environment*, *221*, 405-416.

Wang, Z., Chlus, A., Geygan, R., Ye, Z., Zheng, T., Singh, A., ... & Townsend, P. A. (2020). Foliar functional traits from imaging spectroscopy across biomes in eastern North America. *New Phytologist*.

Wessman, C. A., Aber, J. D., Peterson, D. L., & Melillo, J. M. (1988). Remote sensing of canopy chemistry and nitrogen cycling in temperate forest ecosystems. *Nature*, *335*(6186), 154-156.

Weyermann, J., Damm, A., Kneubühler, M., & Schaepman, M. E. (2013). Correction of reflectance anisotropy effects of vegetation on airborne spectroscopy data and derived products. *IEEE transactions on geoscience and remote sensing*, *52*(1), 616-627.

Wu, C., Niu, Z., Tang, Q., Huang, W., Rivard, B., & Feng, J. (2009). Remote estimation of gross primary production in wheat using chlorophyll-related vegetation indices. *Agricultural and Forest Meteorology*, *149*(6-7), 1015-1021.

Wyttenbach, A., & Tobler, L. (1988). The seasonal variation of 20 elements in 1st and 2nd year needles of Norway spruce, Picea abies (L.) Karst. *Trees*, *2*(1), 52-64.

Yang, X., Tang, J., Mustard, J. F., Wu, J., Zhao, K., Serbin, S., & Lee, J. E. (2016). Seasonal variability of multiple leaf traits captured by leaf spectroscopy at two temperate deciduous forests. *Remote Sensing of Environment*, *179*, 1-12.

Zehnder, C. B., Stodola, K. W., Joyce, B. L., Egetter, D., Cooper, R. J., & Hunter, M. D. (2009). Elevational and seasonal variation in the foliar quality and arthropod community of Acer pensylvanicum. *Environmental Entomology*, *38*(4), 1161-1167.

Zipkin, I. (Ed.). (1973). *Biological mineralization*. Krieger Publishing Company.

Tables

Table 3.1 Imaging spectrometer collection summary.

Overflight date	Mean local acquisition time	Local solar noon	Mean solar zenith angle
May 16 2018	12:22	12:55	25°
June 04 2018	11:19	12:57	29°
June 29 2018	12:18	13:02	22°
July 25 2018	13:38	13:05	25°
August 13 2018	14:26	13:03	34°
September 10 2018	12:18	12:56	39°
September 26 2018	12:40	12:50	45°
October 17 2018	12:22	12:44	53°

Table 3.2 PLSR model seasonal sensitivity metrics. Early: May 16 - Jul 25; Middle: June 29 - Sept 10; End: Aug 13 - Oct. 17; Full: May 16 - Oct 17. Overlap indicates the percent the calibration dataset trait values overlap the validation dataset values. R^2 values in parentheses are calibration metrics.

			Time period			
Trait	**Units**	**Metrics**	**Early**	**Middle**	**End**	**Full**
Calcium	% mass	R^2	0.23 (0.7)	0.0 (0.6)	0.01 (0.55)	0.55 (0.69)
		NRMSE	43.99	60.96	39.27	17
		Overlap	0.62	1	0.86	1
		Components	7	5	5	7
Chlorophyll A	μmol •m^2	R^2	0.9 (0.91)	0.57 (0.7)	0.91 (0.91)	0.93 (0.91)
		NRMSE	15.66	23.58	12.85	8
		Overlap	0.8	0.5	1	1
		Components	3	2	3	4
Fiber	% mass	R^2	0.59 (0.76)	0.65 (0.64)	0.55 (0.69)	0.47 (0.76)
		NRMSE	16.17	16.02	20.23	23
		Overlap	0.92	0.77	0.79	0.77
		Components	5	5	4	5
Lignin	% mass	R^2	0.45 (0.77)	0.7 (0.58)	0.29 (0.72)	0.56 (0.74)
		NRMSE	18.5	13.94	24.81	20
		Overlap	0.96	0.77	0.79	0.73
		Components	5	5	5	5
LMA	g •m^2	R^2	0.02 (0.78)	0.64 (0.66)	0.38 (0.57)	0.77 (0.8)
		NRMSE	37.88	16.55	19.4	11
		Overlap	0.82	0.58	0.86	1
		Components	3	5	3	6
Nitrogen	% mass	R^2	0.06 (0.6)	0.07 (0.56)	0.0 (0.79)	0.79 (0.95)
		NRMSE	42.79	36.16	38.22	12
		Overlap	0.7	0.66	0.93	1
		Components	4	3	4	12
Phosphorus	% mass	R^2	0.12 (0.88)	0.29 (0.54)	0.19 (0.61)	0.72 (0.94)
		NRMSE	26.04	30.0	22.02	16
		Overlap	0.95	0.96	0.71	0.8
		Components	7	3	4	10
Potassium	% mass	R^2	0.24 (0.9)	0.4 (0.89)	0.71 (0.85)	0.82 (0.89)
		NRMSE	26.58	28.47	19.19	12
		Overlap	0.94	0.95	0.73	0.8
		Components	8	9	8	9
Total phenolics	% mass	R^2	0.9 (0.9)	0.8 (0.92)	0.89 (0.91)	0.86 (0.91)
		NRMSE	9.57	12.09	9.74	11
		Overlap	1	0.95	0.86	0.92
		Components	3	3	4	3

Figures

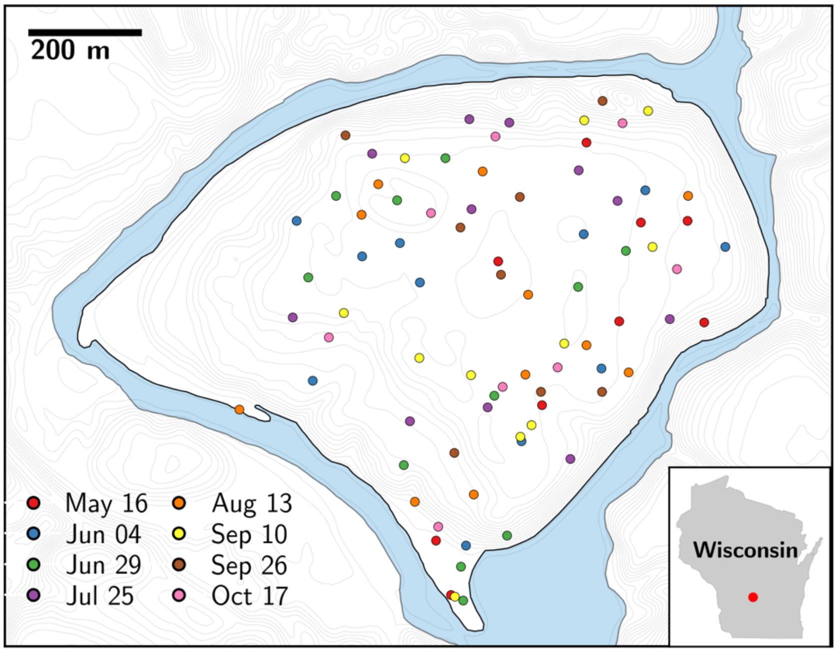

Figure 3.1 Map of Blackhawk Island with locations of sampled trees.

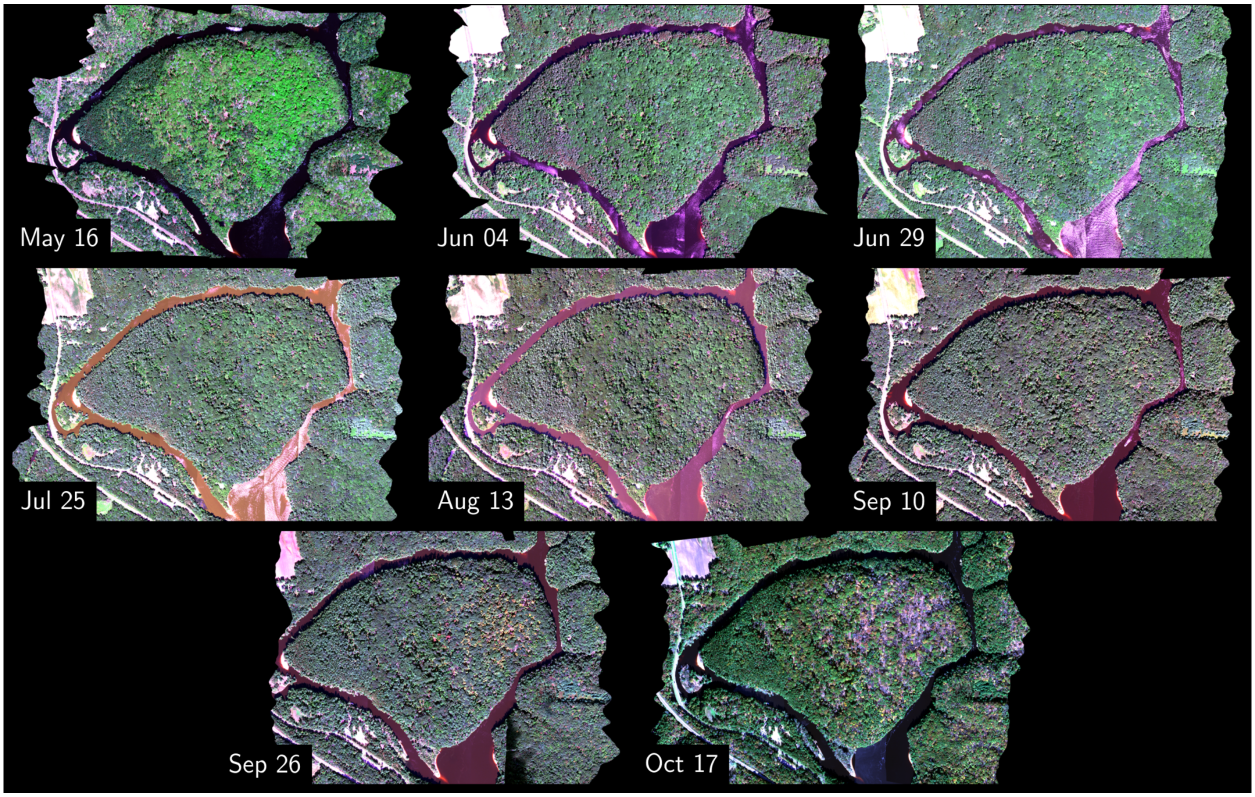

Figure 3.2 True color RGB mosaics of HySpex imaging spectroscopy data for each overflight date.

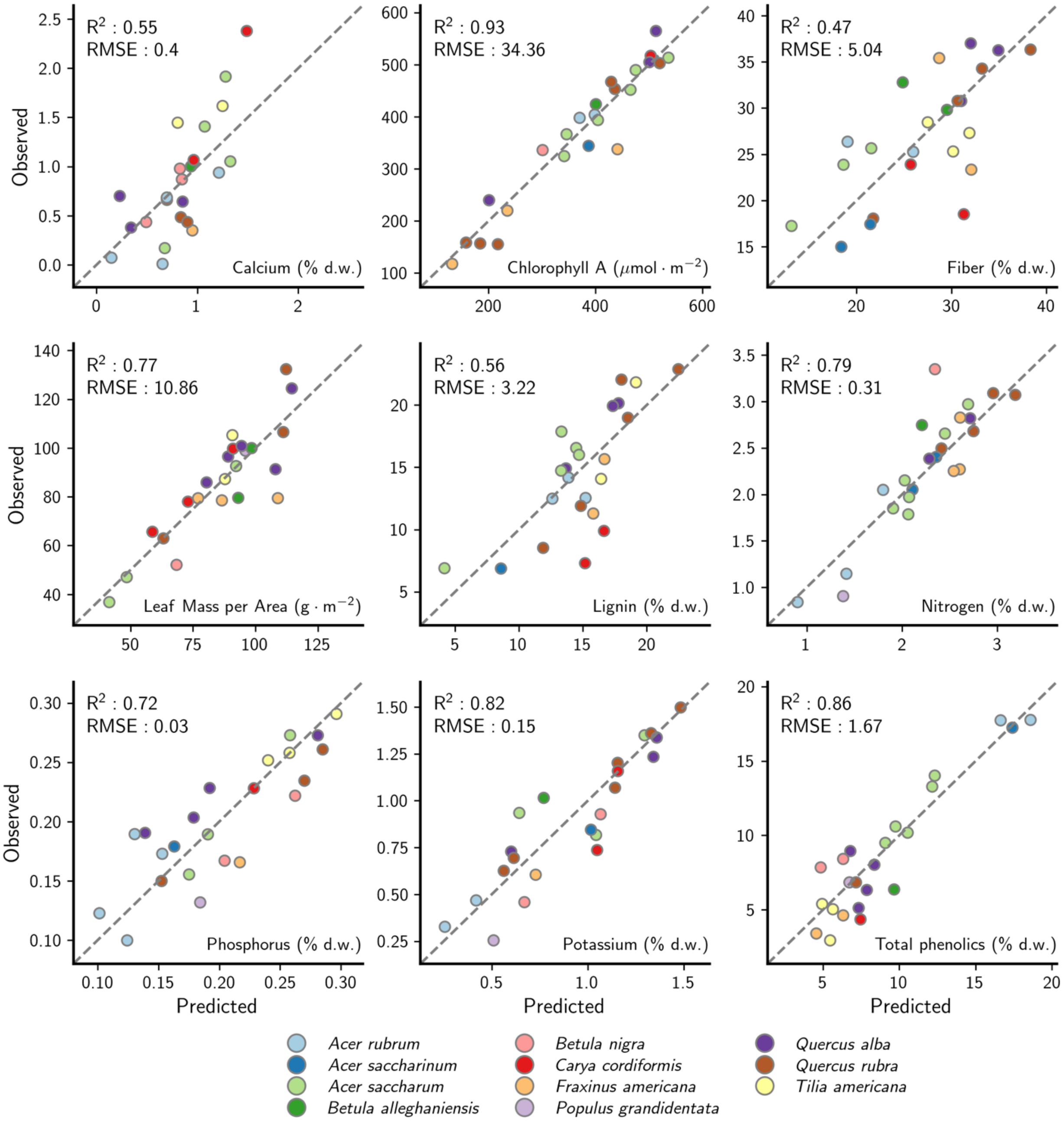

Figure 3.3 Canopy-level PLSR independent validation results, predicted versus observed scatterplots. Note: Validation and calibration splits were repeated for each trait, as such species makeup varies across trait validation data.

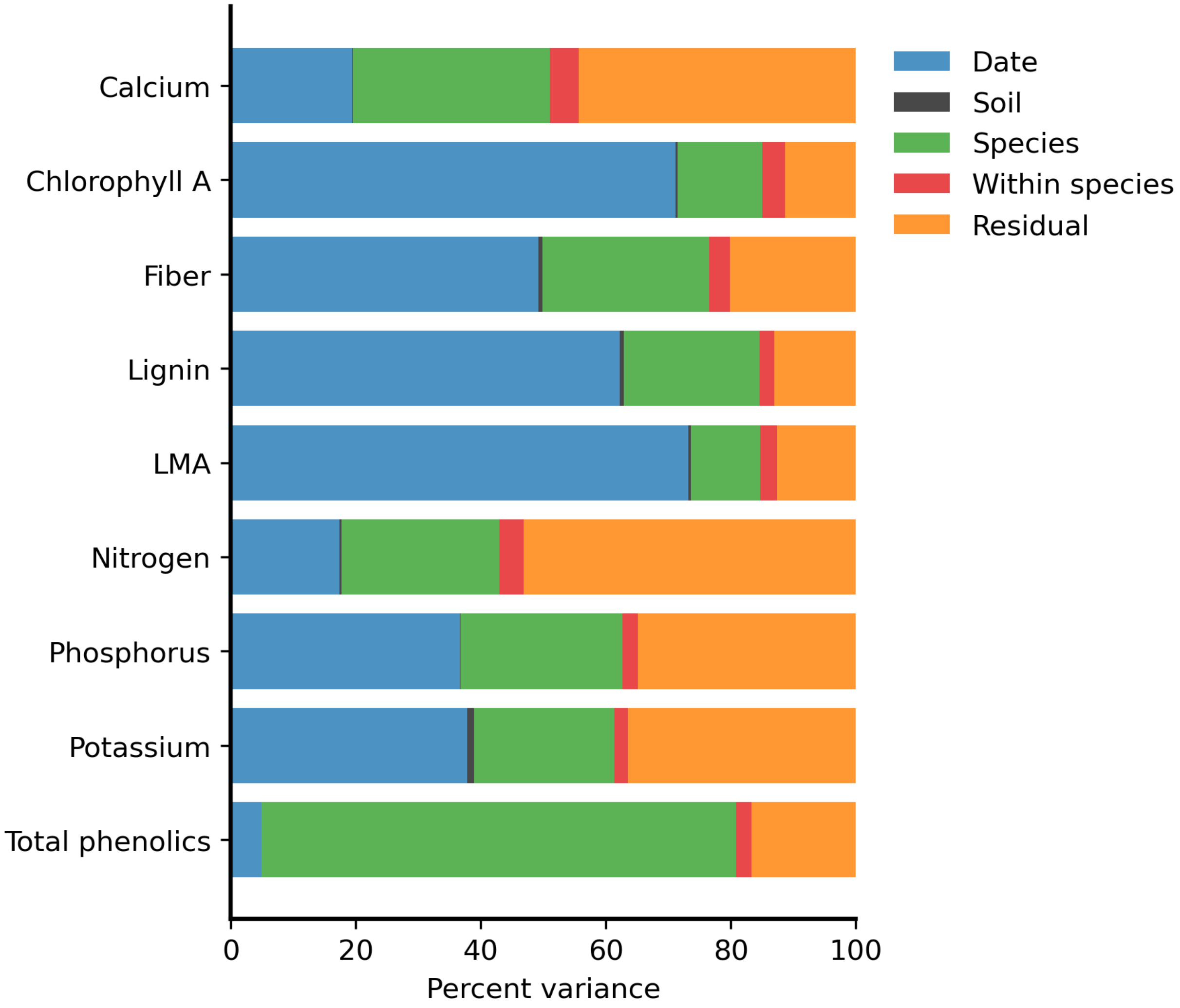

Figure 3.3 Variance partitioning results

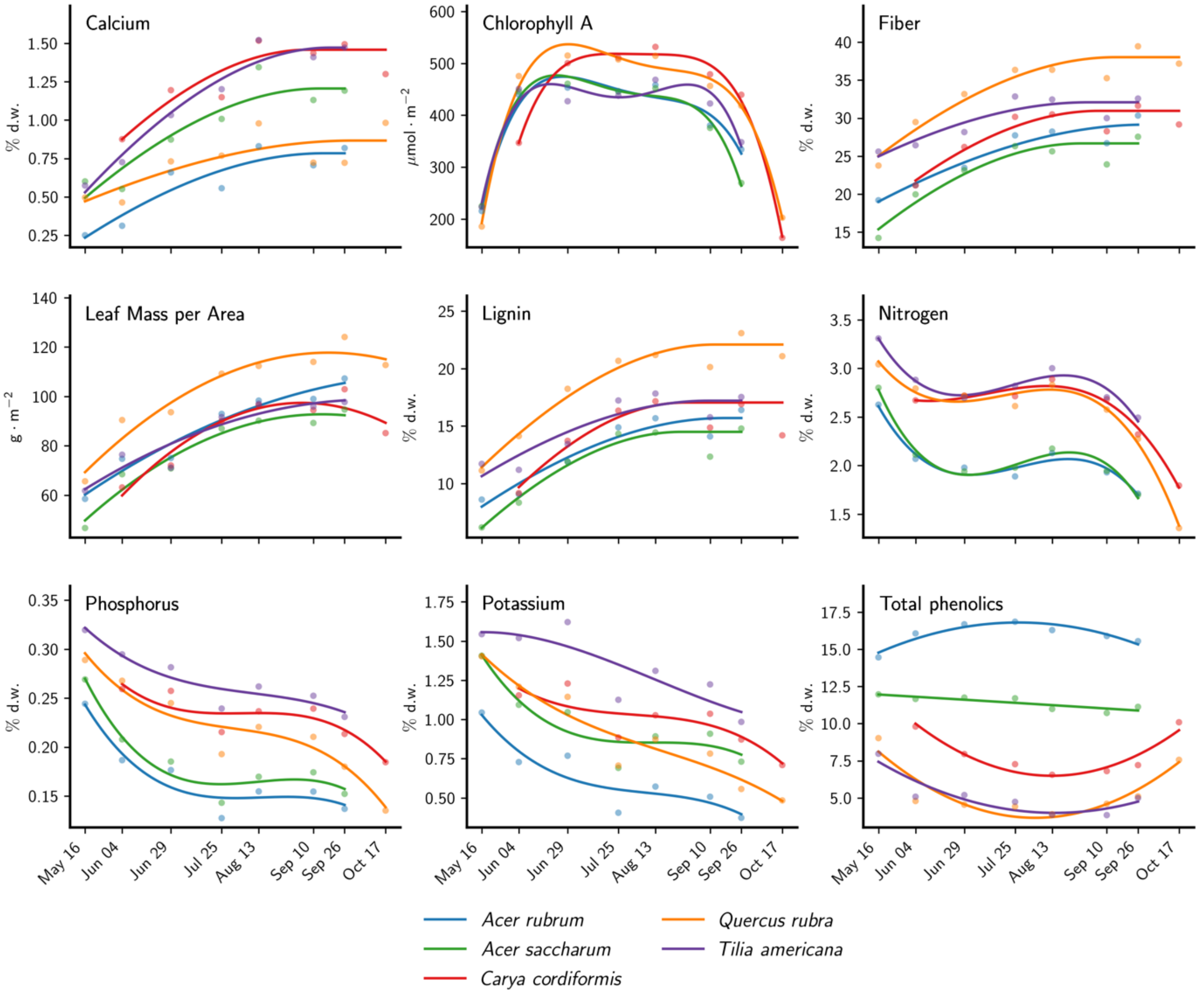

Figure 3.4 Species-wise average foliar traits trajectories derived from imaging spectroscopy for five broadleaf species on Blackhawk Island. Trajectories were fit using 2nd (LMA, total phenolics), 3rd (nitrogen, phosphorus, potassium) and 4th (chlorophyll A) order polynomials or a spherical model (calcium, fiber, lignin). Sugar and red maple (A. saccharum, A. rubrum) and basswood (T. americana) are not shown for October as nearly all trees had dropped all their leaves. Bitternut hickory (C. cordiformis) was not shown for May as most trees had not leafed out.

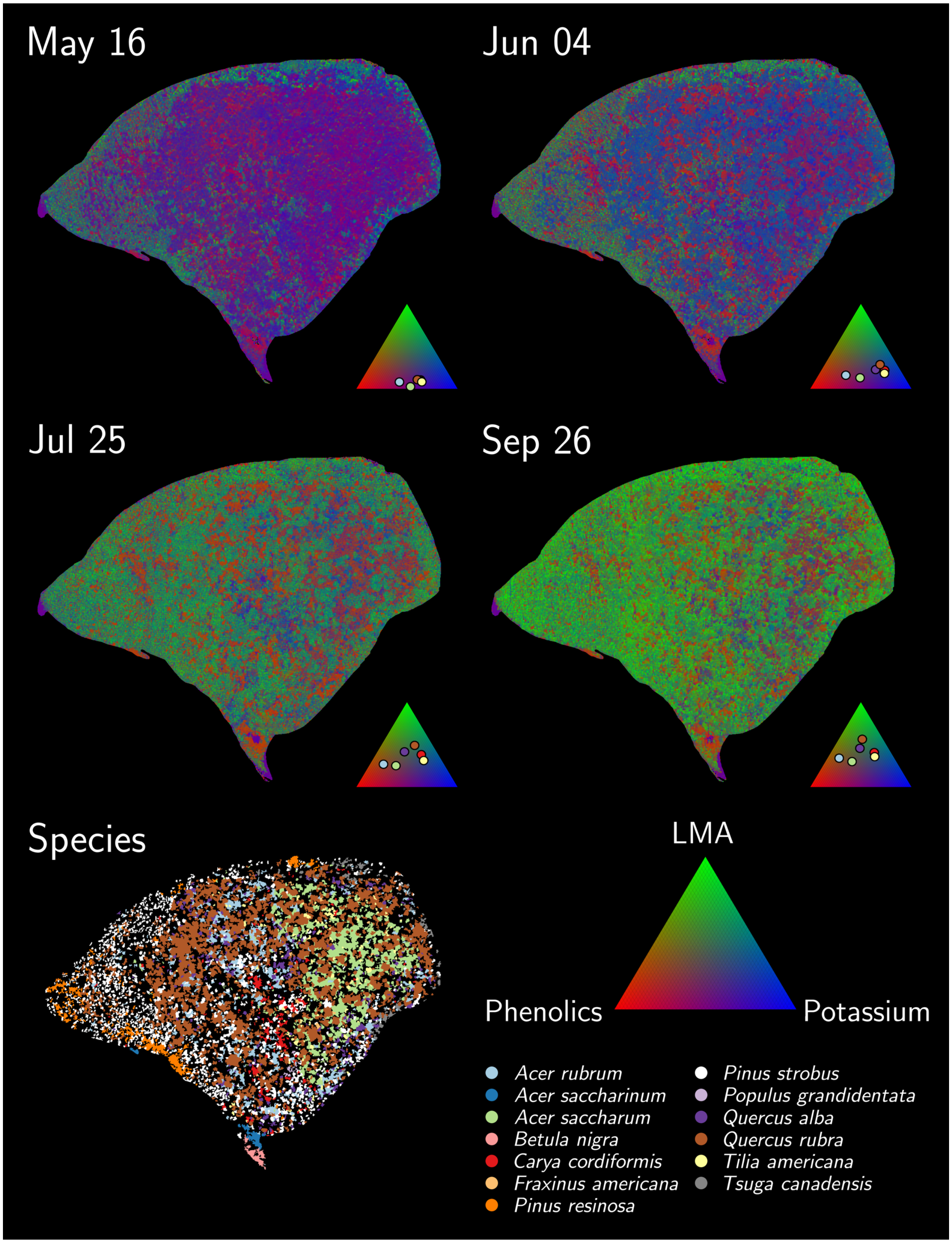

Figure 3.5 Top two rows: RGB composite images of total phenolics (red), LMA (green) and potassium (blue) at four time points during the growing season. For each date the species wise averages of the six most common broadleaf species are shown on the ternary legend. Bottom left: species map, only trees with 30% classification probability are shown, to exclude canopy gaps, shadows and low growing vegetation.

Supplemental materials

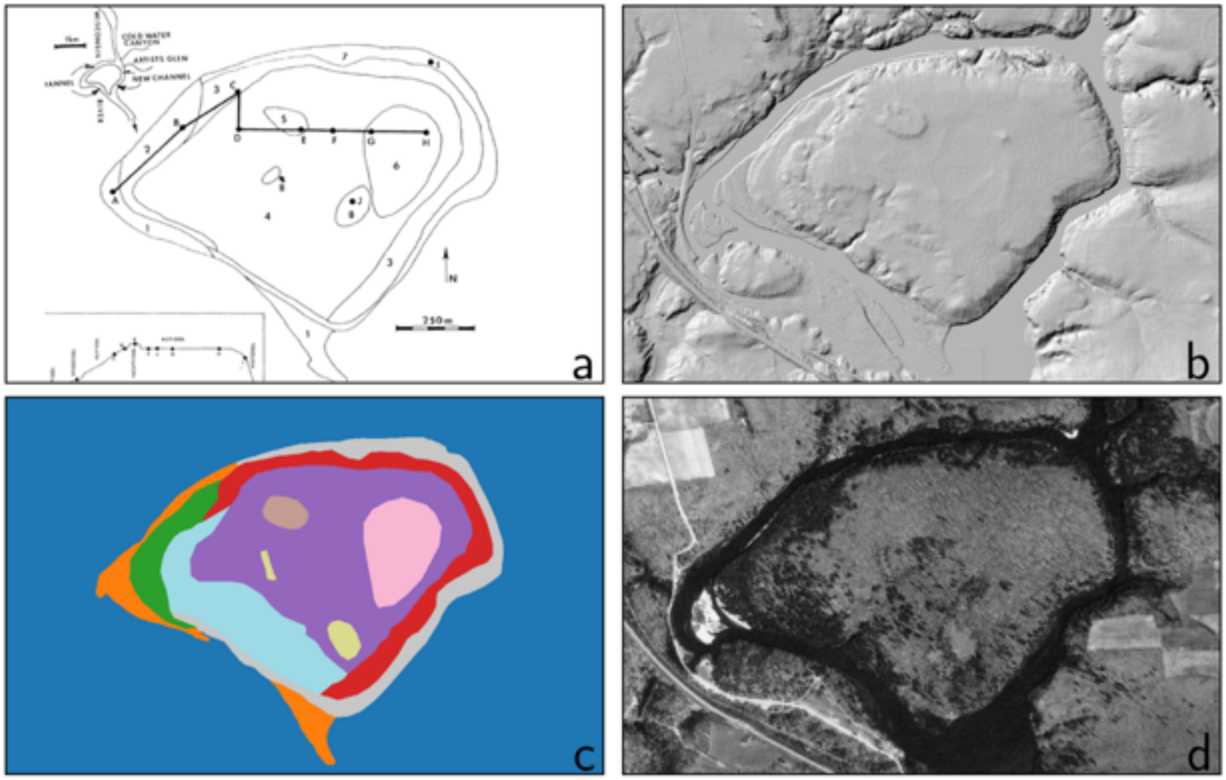

Figure S3.1 Soil map delineation datasets: a) Georeferenced soil map from Pastor et al. 1982; b) Lidar hillshade model; c) Digitized soil map; d) Panchromatic aerial image collected in 1938. We subdivided soil class 4 into two soil classes given the distinct topographic difference on the west side of the island, while the aerial image from 1938 was used to delineate the boundaries of soil class 8.

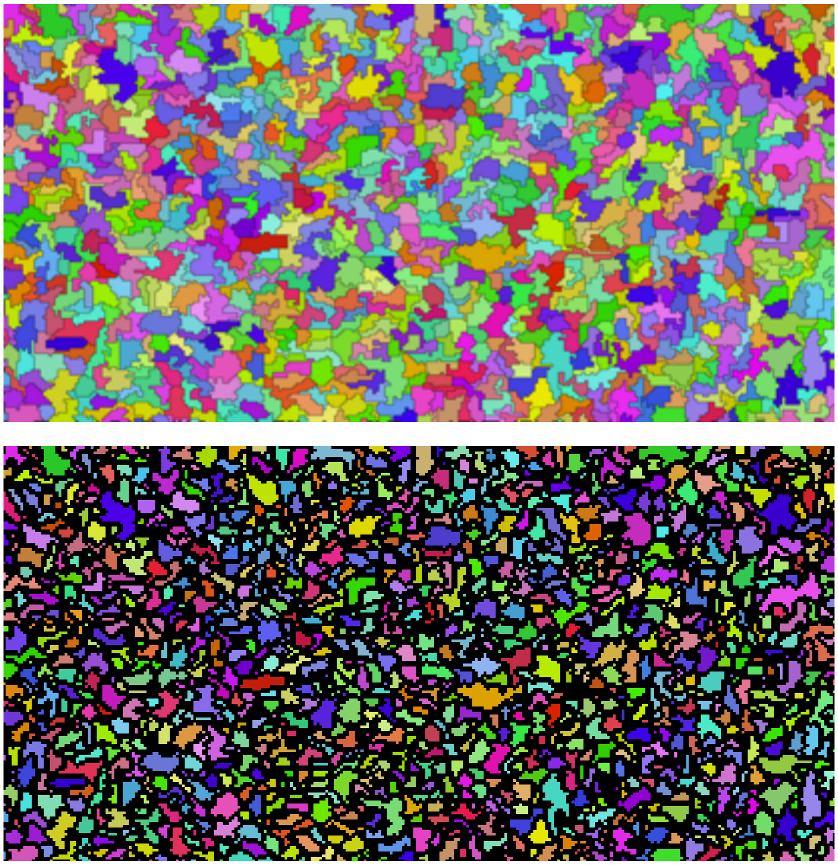

Figure S3.2 Example of segment erosion, top, original segmentation results, bottom, segments after one pixel erosion

Figure S3.3 Examples of bract formation on basswood (*Tilia americana*) trees. Top: Photo of a basswood tree on a residential street in Madison, Wisconsin, USA demonstrating an extreme example of bract coverage on a canopy. Bottom: Branch collected from a basswood tree in this study.

Table S3.1 Summary of sampled species

Species	Code	May 16	Jun 04	Jun 29	Jul 25	Aug 13	Sep 10	Sep 26	Oct 17	Total
Acer rubrum	ACRU	0	2	1	2	0	2	1	0	8
Acer saccharum	ACSA	2	1	1	2	3	1	1	1	12
Acer saccharinum	ACSN	1	0	0	0	1	0	0	0	2
Betula alleghaniensis	BEAL	0	0	0	0	0	1	1	0	2
Betula nigra	BENI	1	0	1	0	0	1	0	0	3
Carya cordiformis	CACO	0	1	1	0	1	1	0	1	5
Fraxinus americana	FRAM	0	1	1	1	1	1	1	1	7
Populus grandidentata	POGR	0	1	0	1	0	1	0	1	4
Quercus alba	QUAL	1	2	2	2	2	1	1	1	12
Quercus rubra	QURU	2	2	2	2	2	1	1	2	13
Tilia americana	TIAM	1	1	1	1	0	1	1	0	6
Total		8	11	10	11	10	11	7	7	80

Table S3.2 Leaf-level fresh and dry ground spectroscopic model metrics.

					Calibration				Validation			
Trait	**Units**	**Type**	**Wavelength (nm)**	**LV**	**R^2**	**RMSE**	**NRMSE**	**Samples**	**R^2**	**RMSE**	**NRMSE**	**Samples**
Calcium	% mass	Dry ground	1200 - 2500	19	0.87	0.35	0.07	500	0.93	0.3	0.11	27
Chlorophyll A	µmol •m^2	Fresh	400 - 800	3	0.84	69.93	0.09	201	0.88	70.92	0.11	47
Fiber	% mass	Dry ground	1200 - 2500	11	0.85	4.72	0.1	416	0.35	11.23	0.35	27
Lignin	% mass	Dry ground	1200 - 2500	11	0.86	3.54	0.1	419	0.3	10.17	0.37	27
LMA	g •m^2	Fresh	1200 - 2499	6	0.92	6.66	0.04	1703	0.89	7.9	0.07	120
Nitrogen	% mass	Dry ground	1200 - 2500	9	0.92	0.24	0.05	1002	0.92	0.34	0.08	27
Phosphorus	% mass	Dry ground	1200 - 2500	13	0.57	0.08	0.12	501	0.63	0.1	0.16	27
Potassium	% mass	Dry ground	1200 - 2500	13	0.68	0.4	0.1	498	0.72	0.27	0.12	27
Total phenolics	% mass	Dry ground	1200 - 2500	14	0.73	2.09	0.09	577	0.9	2.62	0.09	48

Table S3.3 Full-season image spectroscopic model calibration and validation metrics

				Calibration			Validation		
Trait	**Units**	**Wavelength (nm)**	**LV**	**R^2**	**RMSE**	**NRMSE**	**R^2**	**RMSE**	**NRMSE**
Calcium	% mass	1203.5 - 2298.7	7	0.69	0.3	0.12	0.55	0.4	0.17
Chlorophyll A	µmol •m^2	450.4 - 747.4	3	0.91	41.48	0.08	0.93	34.36	0.08
Fiber	% mass	1203.5 - 2298.7	5	0.76	3.42	0.11	0.47	5.04	0.23
Lignin	% mass	1203.5 - 2298.7	4	0.74	2.49	0.11	0.56	3.22	0.2
LMA	g •m^2	1203.5 - 2298.7	5	0.8	8.51	0.09	0.77	10.86	0.11
Nitrogen	% mass	1203.5 - 2298.7	12	0.95	0.14	0.06	0.79	0.31	0.12
Phosphorus	% mass	1203.5 - 2298.7	12	0.94	0.01	0.06	0.72	0.03	0.16
Potassium	% mass	1203.5 - 2298.7	10	0.89	0.11	0.07	0.82	0.15	0.12
Total phenolics	% mass	1601.2 - 1699.3	4	0.91	1.33	0.08	0.86	1.67	0.11

*Wavelength refers to HySpex wavelengths used for model calibration. LV refers to number of latent vectors used in the PLSR model

Table S3.4 Species classification confusion matrix.

Acer rubrum (ACRU), Acer saccharum (ACSA), Acer saccharinum (ACSN), Betula nigra (BENI), Carya cordiformis (CACO), Fraxinus Americana (FRAM), Pinus resinosa (PIRE), Pinus strobus (PIST), Populus grandidentata (POGR), Quercus alba (QUAL), Quercus rubra (QURU), Tilia americana (TIAM), Tsuga canadensis (ACRU).

	ACRU	ACSA	ACSN	BENI	CACO	FRAM	PIRE	PIST	POGR	QUAL	QURU	TIAM	TSCA	Producers accuracy
ACRU	21	1	0	0	1	0	0	0	0	0	2	0	0	84
ACSA	1	24	0	0	0	0	0	0	0	0	0	0	0	96
ACSN	2	0	0	0	0	0	0	0	0	0	1	0	0	0
BENI	0	0	0	2	0	0	0	0	0	0	0	0	0	100
CACO	0	0	0	0	14	0	0	0	0	0	0	0	0	100
FRAM	1	0	0	0	1	1	0	0	0	0	2	0	0	20
PIRE	0	0	0	0	0	0	10	2	0	0	0	0	0	83.3
PIST	0	0	0	0	0	0	0	25	0	0	0	0	0	100
POGR	0	0	0	0	1	0	0	0	4	0	0	0	0	80
QUAL	1	0	0	0	0	0	0	0	0	16	0	0	0	94.1
QURU	0	1	0	0	0	0	0	0	0	0	24	0	0	96
TIAM	1	0	0	0	0	0	0	1	0	0	1	6	0	66.7
TSCA	0	0	0	0	0	0	0	1	0	0	0	0	6	85.7
Users accuracy	77.8	92.3	0	100	82.4	100	100	86.2	100	100	80	100	100	
Total accuracy	87.9													
kappa coefficient	86.3													